

Biomass Representation in Synthetic Aperture Radar Interferometry Data Sets

Dr.-Ing. Kazimierz Becek

The University of Brunei Darussalam

Brunei Darussalam, 1 August 2009

TABLE OF CONTENT

| | |
|---|------|
| LIST OF FIGURES | iii |
| LIST OF TABLES | iv |
| SUMMARY | vi |
| ZUSAMMENFASSUNG | viii |
| 1. INTRODUCTION | 1 |
| 2. RATIONALE | 6 |
| 3. BIOMASS | 8 |
| 3.1. Definitions and Terminology | 8 |
| 3.2. Estimates of Global Biomass | 13 |
| 3.3. Morphology of Biomass | 14 |
| 3.4. Biomass Density | 14 |
| 3.5. Chemical Composition of Biomass | 16 |
| 3.6. Microwave Dielectric Spectrum of Biomass | 16 |
| 3.7. Spatial Variability of Biomass | 16 |
| 3.8. Tree Morphology | 17 |
| 3.9. Stochastic Properties of Vegetation | 18 |
| 3.10. Characterisation of Forest Structure | 18 |
| 3.11. Methods of Quantitative Biomass Assessments | 19 |
| 3.11.1. Ground-based methods | 20 |
| 3.11.2. Photo-interpretation of aerial or satellite imagery | 21 |
| 3.11.3. Remote sensing | 21 |
| 3.12. Conclusion | 23 |
| 4. FUNDAMENTALS OF SYNTHETIC APERTURE RADAR INTERFEROMETRY | 24 |
| 4.1. The Electromagnetic Waves | 24 |
| 4.2. The Radar | 26 |
| 4.3. Synthetic Aperture Radar | 28 |
| 4.4. Synthetic Aperture Radar Interferometry (InSAR) | 31 |
| 4.4.1. Theoretical Background | 31 |
| 4.4.2. Limitations of InSAR method | 33 |
| 4.5. Polarimetric SAR Interferometry (PolInSAR) | 34 |
| 4.6. Differential SAR Interferometry (DInSAR) | 34 |
| 4.7. Permanent Scatterers SAR Interferometry (PSInSAR) | 35 |
| 4.8. Other InSAR solutions | 35 |
| 5. InSAR DATASETS | 36 |
| 5.1. Classification of InSAR datasets | 36 |
| 5.2. Error Budget of InSAR Datasets | 37 |
| 5.3. Accuracy Assessement of InSAR Datasets | 39 |
| 5.4. InSAR Data Acquisition Systems | 41 |
| 5.5. SRTM Digital Elevation Data Product | 46 |
| 6. BIOMASS REPRESENTATION IN InSAR DATASETS | 48 |
| 6.1. Biomass Impenetrability | 49 |
| 6.2. The Frequency Factor | 54 |
| 6.3. Biomass Density | 59 |
| 6.4. Incidence Angle | 62 |
| 6.5. Stochastic Properties of the Biomass | 65 |

| | |
|---|-----|
| 7. STUDIES ON BIOMASS IMPENETRABILITY | 72 |
| 7.1. Modelling a tree and forest | 72 |
| 7.2. Modelling gaps in the canopy cover | 74 |
| 7.3. Modelling the Incidence Angle | 84 |
| 7.4. Simulation study of the biomass impenetrability | 85 |
| 7.5. The Biomass Equation | 96 |
| 7.6. Conclusions | 96 |
| 8. BIOMASS IMPENETRABILITY FOR FOREST CHANGE DETECTION AND ASSESSEMENT | 98 |
| 8.1. The Change Detection Method | 99 |
| 8.2. Problem Formulation | 99 |
| 8.3. Data | 100 |
| 8.4. Data Processing Procedures | 100 |
| 8.5. Results | 101 |
| 8.6. Accuracy Assessment of Forest Depletion | 103 |
| 8.7. Assessment of Forest Resources Using the Depletion Method | 105 |
| 8.8. Biomass Impenetrability versus other Remote Sensing Types of Data | 106 |
| 8.8.1. Impenetrability vs. NDVI | 107 |
| 8.8.2. Impenetrability vs. GRFM data | 107 |
| 8.8.3. Impenetrability vs. TerraSAR-X data | 109 |
| 8.8.4. Impenetrability vs. PALSAR data | 109 |
| 9. OUTLOOK | 111 |
| 10. CONCLUSIONS | 112 |
| 11. REFERENCE | 113 |
| 12. APPENDIX 1: Descriptions of Test Sites | 131 |
| 13. APPENDIX 2: Descriptions of Datasets Used | 148 |
| 14. APPENDIX 3: Formulas | 155 |

LIST OF FIGURES

| | | |
|-------------|--|----|
| Figure 1. | Cumulative density function of average cloud cover (...) | 6 |
| Figure 2. | Forest dieback in the Badas Peat Swamp Forest (...) | 9 |
| Figure 2. | Constituent elements of an ecosystem. | 9 |
| Figure 3. | Relationship between carbon stock, biomass, vegetation and forest. | 11 |
| Figure 4. | Components of the carbon stock. | 12 |
| Figure 6. | Fundamentals of the global carbon cycle. (...) | 13 |
| Figure 7. | An example of vertical distribution of biomass of stems (...) | 15 |
| Figure 8. | Histogram of the aboveground biomass density for country forest areas. (...) | 15 |
| Figure 9. | Dielectric spectrum of biomass. (...) | 16 |
| Figure 10. | Histograms of wood density of tree species (...) | 18 |
| Figure 5. | Biomass (M) as a function of tree diameter (DBH) (...) | 19 |
| Figure 62. | Tree height (H) as a function of tree diameter (DHB) (...) | 20 |
| Figure 13. | Relationship between electric and magnetic waves (...) | 25 |
| Figure 7. | Graph of sinc^2 with argument in units of D/λ (...) | 29 |
| Figure 85. | Right-hand SAR scanning configuration. (...) | 30 |
| Figure 96. | Principle of the SAR interferometry. (...) | 31 |
| Figure 107. | An RMS error caused by discrete representation of a surface. (...) | 39 |
| Figure 118. | GeoSAR system configuration. (...) | 43 |
| Figure 129. | SRTM.X coverage over Borneo. (...) | 46 |
| Figure 20. | A model of an “impenetrable” forest. (...) | 48 |
| Figure 21. | Histogram of differences in DSM <i>minus</i> DTM for the Western USA test site. (...) | 51 |
| Figure 132. | Histogram of differences in SRTM.C <i>minus</i> DTM. (...) | 52 |
| Figure 143. | Histogram of differences in SRTM.C <i>minus</i> reference DTM (...) | 53 |
| Figure 24. | A cross-section of a forest stand and surrounding open space. (...) | 54 |
| Figure 155. | Histogram of differences SRTM.X <i>minus</i> SRTM.C over the Australian test site. (...) | 56 |
| Figure 26. | Histogram of differences in SRTM.X <i>minus</i> reference DTM (...) | 56 |
| Figure 167. | Histogram of differences in SRTM.X <i>minus</i> SRTM.C over the Kalimantan site. (...) | 56 |
| Figure 28. | Histogram of differences in SRTM.X <i>minus</i> SRTM.C (...) | 57 |
| Figure 29. | Histogram of the elevation differences in IFSAR X-band DSM <i>minus</i> SRTM.C (...) | 58 |
| Figure 30. | Histogram of differences in DSM <i>minus</i> SRTM.C (...) over the USA site. (...) | 58 |
| Figure 31. | A parcel-based land cover classification. (...) | 60 |
| Figure 32. | Biomass impenetrability versus percentage of tree cover (...) | 61 |
| Figure 33. | Percentage of tree cover versus biomass impenetrability for the Brunei (...) | 61 |
| Figure 34. | An illustration of the SAR incidence angle Θ . | 63 |
| Figure 35. | Location and orientation of the transect in NSF. (...) | 63 |
| Figure 36. | Differences in SRTM.X <i>minus</i> DTM (...) as functions of slope. (...) | 64 |
| Figure 37. | Illustration of the geometric relationship between slope and radar beam. (...) | 64 |
| Figure 38. | Aerial view of the tree canopy of the Badas Forest. (...) | 66 |
| Figure 39. | Histogram of disparities in tree height as observed by SRTM.C. (...) | 66 |
| Figure 40. | Transect of runway 02-20 at Miri airport, Malaysia. (...) | 68 |
| Figure 41. | A typical bimodal histogram of the pixel density of grey aerial photography (...) | 70 |
| Figure 42. | Average disparity in elevation of the 204 SRTM.C pixels (...) | 70 |
| Figure 43. | Picture of selected 3 by 3 arc-second samples of the canopy. (...) | 71 |
| Figure 44. | A one ha sample of manually delineated crowns. (...) | 72 |
| Figure 45. | Histogram of diameters of manually extracted tree crowns in the Badas Forest. (...) | 73 |
| Figure 46. | A typical power spectrum (...) | 74 |
| Figure 47. | The Menger sponge – 3D fractal. (...) | 75 |
| Figure 48. | Identified gaps in the canopy cover of the Badas test site. (...) | 76 |
| Figure 49. | Cumulative probability density function (...) | 77 |
| Figure 50. | Horizontal cross-section at crown base level. (...) | 78 |
| Figure 51. | Selected shapes of trees crowns used in the simulation study. (...) | 79 |
| Figure 52. | Illustration of the penetrable gaps within the tree canopy. | 81 |
| Figure 53. | Histograms of differences SPOT DEM <i>minus</i> SRTM (...) | 83 |
| Figure 54. | Model of vegetation medium. (...) | 84 |
| Figure 55. | Histogram of areas of simulated triangles. | 86 |

| | | |
|------------|--|-----|
| Figure 56. | The impenetrability vs. type of tree shape (Type 2 gaps). (...) | 86 |
| Figure 57. | The impenetrability vs. crown closure for different crown shapes. (...) | 87 |
| Figure 58. | The impenetrability vs. crown height (...) | 88 |
| Figure 59. | Histograms of impenetrability of a “free forest” | 88 |
| Figure 17. | Impenetrability of a forest plot as a function of the percentage of the Type 1 gaps | 89 |
| Figure 61. | The tree crown gapness, G , of deciduous and evergreen tree species over time. | 90 |
| Figure 62. | Empirical cumulative probability density function for the randomly generated diameter(...) | 92 |
| Figure 63. | Typical histogram of the mean weighted length of gaps (...) | 93 |
| Figure 64. | Mean penetration length versus wavelength, including standard deviation (...) | 94 |
| Figure 65. | Simulation result of the impenetrability of tree crown versus percentage of gaps (...) | 95 |
| Figure 66. | Examples of simulated horizontal cross-sections of a tree crown (...) | 95 |
| Figure 67. | There is no factor clearly responsible for these diebacks in Brunei (...) | 98 |
| Figure 68. | The impenetrability for various forest types (...) | 103 |
| Figure 69. | Mean maximum impenetrability and its standard deviation (...) | 103 |
| Figure 70. | Accuracy assessment of depletion (...) | 104 |
| Figure 71. | Forest parcel with depleted regions (...) | 104 |
| Figure 72. | Scattergram of Impenetrability versus NDVI (...) | 106 |
| Figure 73. | Scattergram showing values of the radar backscatter versus impenetrability (...) | 107 |
| Figure 74. | Scattergrams showing the X-band reflectance vs. impenetrability (...) | 108 |
| Figure 75. | TerraSAR-X (left pane) and weather radar image (right pane). (...) | 109 |
| Figure 76. | Scattergram showing a relationship between the impenetrability (...) | 109 |
| Figure A1 | Location of the Nerang Forest test site. | 123 |
| Figure A2 | Mosaic of orthophotographs (0.15m by 15m pixel) (...) | 123 |
| Figure A3 | Basic climate data for NSF test site. | 124 |
| Figure A4 | Sample of leaves of predominant tree species in the Nerang State Forest (...) | 124 |
| Figure A5 | Open eucalyptus Nerang State Forest from the ground. (...) | 125 |
| Figure A6 | Sun-shadowed DTM over the Nerang test site (...) | 126 |
| Figure A7 | Histogram of elevations (...), and slopes (...) | 126 |
| Figure A8 | Histogram of aspects for the NSF site. | 127 |
| Figure A9 | Location of the Brunei Darussalam and Kalimantan test sites. | 128 |
| Figure A10 | Geographical features of the Brunei Darussalam test site. | 129 |
| Figure A11 | Sun-shadowed digital elevation model of the Badas Forest (...) | 130 |
| Figure A12 | Fringes of the Badas Forest (...) | 131 |
| Figure A13 | Aerial view of the canopy top of the Badas Forest (...) | 131 |
| Figure A14 | Location of transects over SRTM DSM in the Badas test site. | 132 |
| Figure A15 | Cauliflower-like canopy of trees (<i>Shorea albida</i>) in the Badas test site. | 132 |
| Figure A16 | Diebacks in Brunei Muara district. The cause of the destruction is unknown. | 133 |
| Figure A17 | Topography of the Kalimantan test site based on the SRTM.X. | 134 |
| Figure A18 | Histogram of aspect over the Kalimantan test site. | 134 |
| Figure A19 | Sample of leaves of predominant tree species (...) | 135 |
| Figure A20 | Sunshadowed IFSAR X-band dataset for the USA site. (...) | 135 |
| Figure A21 | Histogram of slopes of the West USA test site. (...) | 136 |
| Figure A22 | A QuickBird image of a part of the USA site. (...) | 136 |
| Figure A23 | Douglas fir (...) | 137 |
| Figure A24 | Ground view of the German site. (...) | 137 |
| Figure A25 | The Germany test site. SRTM.X (...) | 138 |
| Figure A26 | Sunshadowed map of the German test site. (...) | 138 |
| Figure A27 | Histogram of elevations for the German test site based on the SRTM.X dataset | 139 |
| Figure A28 | Forest Map of Brunei Darussalam. (...) | 143 |
| Figure A29 | The SPOT DEM dataset used in this project. (...) | 144 |
| Figure A30 | The coverage of the PALSAR dataset used in the project | 145 |
| Figure A31 | TerraSAR-X dataset used in this project. (...) | 146 |

LIST OF TABLES

| | | |
|-----------|--|-----|
| Table 1. | Biomass structural elements influencing propagation of EM waves. (...) | 14 |
| Table 2. | The distribution of biomass among components of a tree. (...) | 17 |
| Table 3. | Contribution of tree components to total biomass for selected boreal forest trees. (...) | 17 |
| Table 4. | Main accuracy indicators obtained from 41 forest stands. (...) | 22 |
| Table 5. | Radar frequency bands and their applications. (...) | 28 |
| Table 6. | Comparison of attributes of the spaceborne vs. airborne InSAR systems. (...) | 33 |
| Table 7. | SRTM Height Error Budget. (...) | 38 |
| Table 8. | Results of the accuracy assessments of SRTM datasets (...) | 41 |
| Table 9. | Selected parameters of the AeS-1 InSAR airborne system. (...) | 42 |
| Table 10. | Basic technical parameters of the DOSAR system (...) | 42 |
| Table 11. | Basic technical parameters of the GeoSAR system (...) | 43 |
| Table 12. | Technical parameters of IFSAR system operated by Intermap Technologies Inc. | 44 |
| Table 13. | Selected parameters of TOPSAR acquisition system. (...) | 44 |
| Table 14. | Selected parameters of E-SAR system. (...) | 45 |
| Table 15. | The Australian test site results. (...) | 50 |
| Table 16. | The Brunei test site results. (...) | 51 |
| Table 17. | Biomass impenetrability as found by various authors (...) | 54 |
| Table 18. | Difference SRTM.X <i>minus</i> SRTM.C by continent. (...) | 55 |
| Table 19. | Comparison of the biomass impenetrability for X- <i>minus</i> C-band (...) | 59 |
| Table 20. | Radar saturation levels of biomass for various frequencies. | 59 |
| Table 21. | SRTM.C elevations including their coordinates (WGS84) selected for analysis..... | 67 |
| Table 22. | Formulas for calculation of volume of crown of various shapes. | 80 |
| Table 23. | Constants used in the first simulation experiment. | 86 |
| Table 24. | Effective forest areas in Brunei Darussalam (...) | 100 |
| Table 25. | Mean maximum impenetrability versus corresponding typical impenetrability (...) | 100 |
| Table A1. | Elevations of the Nerang Forest test site as calculated from various datasets | 127 |
| Table A2. | Parameters of the data takes used in the investigations..... | 140 |
| Table A3. | Basic parameters of SRTM.X elevation data product..... | 141 |
| Table A4. | Forest types as identified on the 1:200,000 forest map (...) | 142 |
| Table A5. | Basic Statistics of forest types in Brunei Darussalam (...) | 144 |

SUMMARY

This work makes an attempt to explain the origin, features and potential applications of the elevation bias of the synthetic aperture radar interferometry (InSAR) datasets over areas covered by vegetation.

The rapid development of radar-based remote sensing methods, such as synthetic aperture radar (SAR) and InSAR, has provided an alternative to the photogrammetry and LiDAR for determining the third dimension of topographic surfaces. The InSAR method has proved to be so effective and productive that it allowed, within eleven days of the space shuttle mission, for acquisition of data to develop a three-dimensional model of almost the entire land surface of our planet. This mission is known as the Shuttle Radar Topography Mission (SRTM). Scientists across the geosciences were able to access the great benefits of uniformity, high resolution and the most precise digital elevation model (DEM) of the Earth like never before for their a wide variety of scientific and practical inquiries.

Unfortunately, InSAR elevations misrepresent the surface of the Earth in places where there is substantial vegetation cover. This is a systematic error of unknown, yet limited (by the vertical extension of vegetation) magnitude. Up to now, only a limited number of attempts to model this error source have been made. However, none offer a robust remedy, but rather partial or case-based solutions. More work in this area of research is needed as the number of airborne and space-based InSAR elevation models has been steadily increasing over the last few years, despite strong competition from LiDAR and optical methods.

From another perspective, however, this elevation bias, termed here as the “biomass impenetrability”, creates a great opportunity to learn about the biomass. This may be achieved due to the fact that the impenetrability can be considered a collective response to a few factors originating in 3D space that encompass the outermost boundaries of vegetation. The biomass, presence in InSAR datasets or simply the biomass impenetrability, is the focus of this research.

The report, presented in a sequence of sections, gradually introduces terminology, physical and mathematical fundamentals commonly used in describing the propagation of electromagnetic waves, including the Maxwell equations. The synthetic aperture radar (SAR) and InSAR as active remote sensing methods are summarised. In subsequent steps, the major InSAR data sources and data acquisition systems, past and present, are outlined. Various examples of the InSAR datasets, including the SRTM C- and X-band elevation products and INTERMAP Inc. IFSAR digital terrain/surface models (DTM/DSM), representing diverse test sites in the world are used to demonstrate the presence and/or magnitude of the biomass impenetrability in the context of different types of vegetation – usually forest. Also, results of investigations carried out by selected researchers on the elevation bias in InSAR datasets and their attempts at mathematical modelling are reviewed.

In recent years, a few researchers have suggested that the magnitude of the biomass impenetrability is linked to gaps in the vegetation cover. Based on these hints, a mathematical model of the tree and the forest has been developed. Three types of gaps were identified; gaps in the landscape-scale forest areas (Type 1), e.g. forest fire scares and logging areas; a gap between three trees forming a triangle (Type 2), e.g. depending on the shape of tree crowns; and gaps within a tree itself (Type 3). Experiments have demonstrated that Type 1 gaps follow the power-law density distribution function. One of the most useful features of the power-law distributed phenomena is their scale-independent property. This property was also used to model Type 3 gaps (within the tree crown) by assuming that these gaps follow the same distribution as the Type 1 gaps. A hypothesis was formulated regarding the penetration depth of the radar waves within the canopy. It claims that the depth of penetration is simply related to the quantisation level of the radar backscattered signal. A higher level of bits per pixels allows for capturing weaker signals arriving from the lower levels of the tree crown.

Assuming certain generic and simplified shapes of tree crowns including cone, paraboloid, sphere and spherical cap, it was possible to model analytically Type 2 gaps. The Monte Carlo simulation method was used to investigate relationships between the impenetrability and various configurations of a modelled forest. One of the most important findings is that impenetrability is largely explainable by the gaps between trees. A much less important role is played by the penetrability into the crown cover.

Another important finding is that the impenetrability strongly correlates with the vegetation density. Using this feature, a method for vegetation density mapping called the mean maximum impenetrability (MMI) method is proposed. Unlike the traditional methods of forest inventories, the MMI method allows for a much more realistic inventory of vegetation cover, because it is able to capture an *in situ* or current situation on the ground, but not for areas that are nominally

classified as a “forest-to-be”. The MMI method also allows for the mapping of landscape variation in the forest or vegetation density, which is a novel and exciting feature of the new 3D remote sensing (3DRS) technique.

Besides the inventory-type applications, the MMI method can be used as a forest change detection method. For maximum effectiveness of the MMI method, an object-based change detection approach is preferred. A minimum requirement for the MMI method is a time-lapsed reference dataset in the form, for example, of an existing forest map of the area of interest, or a vegetation density map prepared using InSAR datasets.

Preliminary tests aimed at finding a degree of correlation between the impenetrability and other types of passive and active remote sensing data sources, including TerraSAR-X, NDVI and PALSAR, proved that the method most sensitive to vegetation density was the Japanese PALSAR - L-band SAR system. Unfortunately, PALSAR backscattered signals become very noisy for impenetrability below 15 m. This means that PALSAR has severe limitations for low loadings of the biomass per unit area.

The proposed applications of the InSAR data will remain indispensable wherever cloud cover obscures the sky in a persistent manner, which makes suitable optical data acquisition extremely time-consuming or nearly impossible.

A limitation of the MMI method is due to the fact that the impenetrability is calculated using a reference DTM, which must be available beforehand. In many countries around the world, appropriate quality DTMs are still unavailable. A possible solution to this obstacle is to use a DEM that was derived using P-band InSAR elevations or LiDAR. It must be noted, however, that in many cases, two InSAR datasets separated by time of the same area are sufficient for forest change detection or similar applications.

ZUSAMMENFASSUNG

Diese Arbeit leistet einen Beitrag zur Erklärung der Ursprünge, Funktionen und möglichen Anwendungen der Höhenfehler von Interferometrischem Synthetic Aperture Radar Datensätzen in vegetationsbedeckten Gebieten.

Die schnelle Entwicklung der radarbasierten Fernerkundung, wie das Synthetic Aperture Radar und Interferometrische Synthetic Aperture Radar (InSAR), stellen eine Alternative zur Photogrammetrie und LiDAR, zur Bestimmung der dritten Dimension von topografischen Oberflächen bereit. Die InSAR- Methode hat sich als so wirksam und produktiv erwiesen, dass sie innerhalb einer elftägigen Space-Shuttle-Mission die Bestimmung von Daten erlaubte, die die Entwicklung eines dreidimensionalen Modells fast der gesamten Topographie unseres Planeten ermöglichte. Diese Mission ist als Shuttle Radar Topography Mission (SRTM) bekannt. Wissenschaftler verschiedener Fachdisziplinen konnten die Vorteile der Gleichförmigkeit und der hohen Auflösung des zur Zeit präzisesten Digitalen Höhenmodells (DHM) der Erde, für eine Vielzahl von wissenschaftlichen und praktischen Untersuchungen nutzen.

Bedauerlicherweise stellen InSAR- Erhebungen die Erdoberfläche an Orten, welche mit viel Vegetation bedeckt sind, falsch dar. Dieser systematische Fehler wird durch die vertikale Ausdehnung der Vegetation hervorgerufen und hat ein begrenztes aber unbekanntes Ausmaß. Bis heute wurden nur wenige Versuche unternommen, diese Fehlerquelle zu modellieren. Es konnte bisher kein allgemeingültiger Ansatz beschrieben werden, da ausschließlich partielle oder fallbasierte Lösungen vorgestellt wurden. Mehr Arbeit auf diesem Forschungsgebiet ist erforderlich, da die Anzahl luft- und satellitenbasierter InSAR- Höhenmodelle über die letzten Jahre, trotz der Konkurrenz von LiDAR und optischen Methoden, ständig zugenommen hat.

Von einer anderen Perspektive jedoch bietet die Undurchlässigkeit der Biomasse, die zu den Höhenfehlern führt, das Potenzial, Erkenntnisse über die Biomasse zu erlangen. Dies könnte durch den Fakt erreicht werden, dass die Undurchlässigkeit als eine gesammelte Reaktion auf einige Faktoren, entstehend im dreidimensionalen Raum, betrachtet werden kann. Diese umfassen die äußeren Grenzen der Vegetation.

Die in InSAR- Datensätzen präsente Biomasse (entsprechend der Undurchlässigkeit der Biomasse), ist der Schwerpunkt dieser Untersuchung.

Die vorliegende Arbeit führt schrittweise in Fachbegriffe und physikalische sowie mathematische Grundlagen ein, welche die theoretische Grundlage zur Beschreibung der Ausbreitung von elektromagnetischen Wellen, einschließlich der Maxwell-Gleichungen, bilden.

Das Synthetic Aperture Radar (SAR) und Interferometrisches Synthetic Aperture Radar (InSAR), als aktive Fernerkundungsmethoden, werden im Folgendem zusammengefasst.

In weiteren Abschnitten werden die hauptsächlichen Quellen für InSAR-Daten und die Datenerfassungssysteme der Vergangenheit und Gegenwart umrissen. Verschiedene Beispiele für InSAR- Datensätze, einschließlich der SRTM C- und X-Band Erhebungsprodukte und INTERMAP Inc. - IFSAR Digitale Gelände- und Oberflächenmodelle (DGM/DOM), welche verschiedene Testgelände in der Welt repräsentieren, werden genutzt, um die Präsenz und/oder das Ausmaß der Undurchlässigkeit der Biomasse im Kontext verschiedener Arten von Vegetation (hauptsächlich aber Wald) zu demonstrieren. Außerdem werden die Ergebnisse ausgewählter wissenschaftlicher Untersuchungen, welche sich mit Höhenfehlern in InSAR- Datensätzen beschäftigen und ihre Versuche diese mathematische zu modellieren, in die Betrachtungen eingebunden.

In den letzten Jahren wurde in verschiedenen Quellen die Auffassung publiziert, dass das Ausmaß der Undurchlässigkeit der Biomasse mit den Lücken in der Vegetationsbedeckung verknüpft sei. Auf der Basis dieser Arbeiten wurde ein mathematisches Modell vom Baum und vom Wald entwickelt. Drei Typen von Lücken wurden identifiziert: Lücken in Waldflächen (Typ 1), zum Beispiel Waldbrandschäden und Rodungsflächen; Lücken zwischen 3 Bäumen, welche ein Dreieck bilden (Typ 2), abhängig von der Form der Baumkronen; und Lücken innerhalb von Baumkronen (Typ 3). Untersuchungen haben gezeigt, dass die Verteilung von Typ 1– Lücken dem Potenzgesetz der Dichteverteilungsfunktion folgt. Ein wesentliches, vom Potenzgesetz abgeleitetes Merkmal ist die Maßstabsfreiheit. Diese Eigenschaft wurde ebenso genutzt um die Typ 3- Lücken (innerhalb der Baumkrone) zu modellieren. Dabei wurde unterstellt, dass diese Lücken derselben Verteilung wie die der Typ 1- Lücken folgen.

Bezüglich der Durchdringungstiefe von Radarwellen innerhalb von Baumkronen, wurde eine Hypothese formuliert, dass die Tiefe der Durchdringung mit dem quantitativen Level der zurückgestreuten Radarsignalen korreliert.

Eine höhere Anzahl von Bits pro Pixel erlaubt das Erfassen von schwächeren Signalen, die aus tieferen Schichten der Baumkrone reflektiert worden.

Mit generalisierten Formen der Baumkronen, einschließlich Kegel, Paraboloid, Kreis und Kreissegment, war es möglich, die Typ 2- Lücken analytisch zu modellieren. Um die Beziehung zwischen der Undurchlässigkeit und verschiedenen Konfigurationen des Waldmodells zu untersuchen, wurde die Monte Carlo Simulationsmethode verwendet. Eines der wichtigsten Erkenntnisse ist, dass die Undurchlässigkeit unter Berücksichtigung der Lücken zwischen den Bäumen weitgehend erfassbar ist. Es zeigte sich, dass die Durchlässigkeit im Kronenschluss eine wesentlich geringere Rolle spielt.

Als weiteres, wichtiges Ergebnis konnte gezeigt werden, dass die Undurchlässigkeit stark mit der Vegetationsdichte korreliert. Unter Verwendung dieser Eigenschaft wurde eine Methode zur Kartierung von Vegetationsdichte, die Mean Maximum Impenetrability-Methode (MMI), angewendet. Anders als bei traditionellen Methoden zur Waldbestandsaufnahme ermöglicht die MMI-Methode eine wesentlich realitätsnähere Bestandsaufnahme der Vegetationsbedeckung, da sie die aktuelle Situation des Geländes erfasst.

Dies gilt aber nicht für Flächen, welche nominal als Aufforstungsflächen klassifiziert sind. Die MMI-Methode ermöglicht außerdem die Kartierung von Landschaftsveränderungen der Wald- und Vegetationsdichte. Dies ist eine neuartige und vielversprechende Funktion der neuen 3D-Fernerkundungstechnik (3DRS).

Neben den Anwendungen zur Bestandsaufnahme kann die MMI-Methode auch zur Erfassung von Waldveränderungen genutzt werden. Für die größtmögliche Effektivität dieser Methode wird eine objektbasierte Herangehensweise vorgeschlagen. Eine minimale Voraussetzung für die MMI-Methode ist ein multitemporaler Referenzdatensatz, zum Beispiel von einer existierenden Waldkarte eines interessanten Bereiches oder eine Karte der Vegetationsdichten, welche unter Benutzung von InSAR-Datensätzen erstellt wurde.

Vorbereitende Tests, die mit dem Ziel durchgeführt wurden, ein Maß der Korrelation zwischen der Undurchlässigkeit und anderen Arten von aktiven und passiven Fernerkundungsdatenquellen, einschließlich TerraSAR-X, NDVI und PALSAR, zu finden, zeigten dass die für Vegetation sensibelste Methode das japanische PALSAR- L-Band SAR System ist. Bedauerlicherweise werden zurückgestreute PALSAR-Signale bei einer Undurchlässigkeit unterhalb von 15 Metern sehr verrauscht. Dies bedeutet, dass mit PALSAR starke Grenzen für niedrige Lasten von Biomasse pro Flächeneinheit gesetzt sind.

Die vorgeschlagenen Anwendungen erlauben den Einsatz von InSAR-Daten in Gebieten, in denen häufige Wolkenbedeckung eine adäquate, optische Datenakquise extrem zeitaufwendig oder gar fast unmöglich macht.

Eine Grenze der MMI Methode ist durch den Umstand gegeben, dass für die Berechnung der Undurchlässigkeit ein Referenz DGM verfügbar sein muss. In vielen Ländern der Welt sind DGMs geeigneter Qualität noch nicht vorhanden. Eine mögliche Lösung für diese Unzulänglichkeit ist die Nutzung eines Digitalen Höhenmodells, welches aus P-Band InSAR Höhen oder LiDAR abgeleitet wurde. Anzumerken ist, dass in den meisten Fällen zwei zeitlich getrennte InSAR Datensätze derselben Fläche für die Detektion von Waldveränderungen und ähnlichen Anwendungen genügen.

1. INTRODUCTION

The term **Radio Detection and Ranging (RADAR)** or radar has been known to the world since 1941. It is the product of many contributors, the first coming from a German, Christian Hülsmeyer, who, in 1904, in Düsseldorf, patented a device for detecting “*the presence of distant metallic objects*” (BAUER, 2005). It is not difficult to conclude that this discovery may be classified as the world’s first remote sensing method. Moreover, because a dedicated source of microwaves was used, in contemporary terminology it would be classified as an active microwave or radar remote sensing technology.

The next important stage in the development of radar-based remote sensing was the invention of the synthetic aperture radar (SAR) technique in the mid-1950’s (CUTRONA *et al.*, 1966; CURLANDER & McDONOUGH, 1991; HANSSEN, 2001). The main advantage of the SAR technique was the fact that it greatly increased the resolution of radar. However, the real breakthrough in the development of active remote sensing came about in 1970 with a technique known as SAR interferometry (InSAR). InSAR allows the measurement of all three coordinates of an object on the surface of the Earth (GRAHAM, 1974).

The microwave range of electromagnetic waves in comparison to the visible part of electromagnetic waves possesses at least two advantages that make it very useful and attractive for remote sensing applications. The first advantage is its all-weather and day-night deployability. These attributes increase the applicability of radar in areas of persistent cloud cover (the tropics), and in the polar regions, where optical data are not available for up to six months every year. The second advantage is that radar is able to penetrate vegetation cover. In the case of dense tropical forests, this seems to be the only reliable way to extract the true location of the Earth’s surface.

Scientific and application-oriented exploration of datasets acquired with microwave frequencies and using SAR methodology commenced on June 28, 1978 with the launch of the SEASAT satellite. This first spaceborne SAR data acquisition system marked a new phase in the investigation of our environment using remote sensing technology (JPL, 2008). Completely new classes of datasets acquired using microwaves allowed for greater spectral “penetration” or resolution of vegetation cover, polar regions, and ocean surfaces. For the first time ever it became possible to collect data related, for example, to wind speed and direction, ocean surface temperature, ocean waves, and polar ice coverage on a global scale, all thanks to the penetrability of the atmosphere by L-band microwaves and day-night radar deployability.

The SEASAT experiment was short-lived. It ended after just 105 days when a massive short circuit destroyed the electronics. However, the legacy of the experiment continues and the datasets are still available from the Jet Propulsion Laboratory (JPL, 1978).

Soon after, the Shuttle Imagine Radar-A (SIR-A) was flown on the space shuttle in 1981. This was followed by an instrument with multilook capabilities (SIR-B), which was carried into space in 1984. In April and October of 1994, a much more comprehensive radar instrument was delivered. It was a joint experiment of the German (DLR), Italian (ASI), and North American (NASA) space agencies. SIR-C/X-SAR operated in the L-, C-, and X-bands, and in multi-look, multi-incidence angle, and multi-polarization modes. NASA and JPL were also conducting experiments with airborne radar systems. AIRSAR and TOPSAR are radar systems operating in the L-, C- and P-bands (FREEMAN, 1996). Experiments and experience gained, thanks to two orbital flights and airborne SAR missions, helped to develop the Shuttle Radar Topography Mission (SRTM), which was flown in February 2000. From many points of view, the SRTM project was one of the most successful global data acquisition missions to date.

The European Space Agency joined the spaceborne “radar club” by launching its ERS-1 satellite on July 17, 1991. One of the instruments on board was the SAR C-band system. The ERS-2, which is very similar in construction to its predecessor, was placed in the same orbit as ERS-1 on April 21, 1995, with its successor ENVISAT (ENVI) launched on March 1, 2002. The instruments on board ENVI differed from those of the ERS-2, but they did include the ASAR system (Advanced SAR) that operates in the C-band.

The Canadian Space Agency (CSA) launched its own C-band SAR satellite, RADARSAT-1, on November 4, 1995. RADARSAT-2, a follow-up to RADARSAT-1, was launched on December 14, 2007. The RADARSAT program has been very useful, especially for Canada, because the northern regions of the country are frequently covered by clouds, and for six months every year are in permanent night conditions.

Prior to RADARSAT-1, Japan successfully launched its own L-band SAR system, the Japanese Earth Resources Satellite (JERS-1), on February 11, 1992. The satellite ceased operations in 1998. However, its legacy still remains strong because the freely available forest cover dataset became the framework for the Global Forest Mapping

Programs, which includes The Global Rain Forest Mapping Program (GRFM) (ROSENQVIST *et al.*, 2000), and the Global Boreal Forest Mapping Program (GBFM) (ROSENQVIST *et al.*, 2004). Continuous commitment to the exploration of land cover using L-band radar has been achieved by the Japan Aerospace Exploration Agency (JAXA) with its launching of the Advanced Land Observing Satellite (ALOS) or 'DAICHI' on January 24, 2006. One of the instruments carried on board of ALOS is the Phased Array type L-band Synthetic Aperture Radar (PALSAR system).

Since July 15, 2007, humankind has been witness to a new, much more technologically advanced radar instrument installed on board the TerraSAR-X satellite. The satellite's payload is an advanced X-band SAR radar system allowing the acquisition of data at selectable resolutions from 1m by 1m – 18m by 18m pixel size. It is planned that in 2009 an additional satellite system will be placed in orbit. Both systems will be orbiting in a tandem configuration. This experiment is referred to as the TanDEM-X mission (FIEDLER *et al.*, 2006). In addition, at least five radar satellite programs are in various stages of planning and/or development which will enhance the data acquisition power of the radar satellite fleet in the near future (STONE, 2004).

The above overview of past and current radar satellite systems clearly confirms the usefulness of radar-based data acquisition technology for a wide range of applications, including environmental studies, defence and mapping.

One of the biggest current scientific challenges is the quantitative modelling of carbon flux between environmental storages. This is because the increased concentration of carbon in the atmosphere is linked to global warming. Such a model of carbon flux would be extremely useful in finding, for example, optimal mitigation strategies for reducing the consequences of global warming. Among the fundamental elements needed to develop such a model is a precise knowledge of carbon quantities stored in the aboveground biomass on the surface of our planet and the rate of its exchange with the atmosphere. Other "must-know" elements for successful modelling of the biomass are the spatiotemporal properties of the biomass, which include variations of carbon flux as a function of daily, seasonal and ecological biomass variations. It is also worthwhile mentioning that the modelling is even more complicated if anthropogenic emissions of CO₂ are taken into consideration.

As a first approximation of the biomass estimate, its horizontal extent can be used. In fact, this is so far the only global method of biomass inventory and has been performed every five years since the 1940s. The results are published as the global forest resources assessment report (GFRA) (FAO, 1997, 2005a). It should be noted, however, that the accuracy and precision of the results are not fully controlled by the Food and Agriculture Organisation (FAO) – one of the United Nations organisations; the data are, in some cases, of poor quality (*ibid*). Regional and local area-based biomass assessments are performed much more frequently (every 10 to 14 days) by spaceborne sensors (DeFRIES *et al.*, 2006; Mollicone *et al.*, 2003). It has also been demonstrated that this remote sensing could have been successfully utilized for verification purposes of the GFRA 2000 (FAO, 2005). However, the GFRA 2005 was not verified in this way because of the prohibitive costs of satellite imagery (DeFRIES *et al.*, 2006). Another problem with the acquisition of global datasets by passive sensors has been the issue of persistent cloud cover in the tropics.

Regarding the climatoeconomic determinants of the biomass estimates, it bears mentioning that the precision of these estimates would increase if the vertical extent of the biomass was considered. Sources of the biomass vertical extent data may include field inventory, deriving the height from aerial stereopair, **Light Detection and Ranging (LiDAR)** technology, and InSAR methods. Despite much progress in 3D biomass modelling, the precision of the estimates is still too low; hence, this modelling is still an active research area. These research efforts are concentrated both on developing formulas for the relationship between the biomass and its third dimension, i.e., *biomass = f(the third dimension)*, and obtaining a sufficient quality of biomass vertical data. Another argument for 3D biomass modelling is that the biomass and biomass change are linked to forest growth (in terms of vertical expansion), but neither of these forest parameters are detectable by passive remote sensing methods (FRANKLIN *et al.*, 1995).

The above remarks regarding the 3D nature of the biomass suggest a new model for remote sensing. Instead of assuming that land cover is a multicolour flat "paint," the cover can and should be considered as something which also has a vertical dimension. The remote sensing with this extended dimensionality can be termed 3D remote sensing (3DRS). It may be suggested that a "soft" launching of the 3DRS came from the works of Leroy C. Graham and included the adoption of the SAR interferometer (GRAHAM, 1974). So far, little has been done to promote the idea of 3DRS, except for, perhaps, the "Workshop on 3D Remote Sensing in Forestry," held in Vienna, February 14-15, 2006. This lack of 3DRS promotion is due to many factors, including the still unresolved issues with an "all-inclusive" remote sensing data model that considers all available data sets (multispectral and vertical) in one coherent data model. This is the same idea that is used in the data assimilation approach used in many geosciences (HOUSER, 2001), including weather forecasting and hydrology (LOEW, 2008). The related techniques performed using remote sensing is known as data fusion and data integration. Expected gains, thanks to this synergic approach, would be a more adequate model of interest leading to more precise and accurate estimates. Some other factors diminishing the promotion of 3DRS include

the track record of applicability of the optical sensors, the human, software and hardware infrastructure in place to support optical data processing, strong marketing of optical data products and big supply of imagery. However, a potential change in the popularity of 3DRS is expected with the arrival of the Global Earth Observation System of Systems, which should be implemented by the year 2015 (GEO, 2007).

The previously mentioned penetrability of vegetation cover by radar is frequency-dependent. Microwaves of longer wavelengths are able to penetrate the vegetation, whereas waves of shorter length do not penetrate vegetation as well. A deciding factor in that is the number of scatterers of the size of the same order the wavelength (~3cm for X-band, and ~5.5cm for C-band, for example). Hence, the response of vegetation to microwave radiation comes, mainly from the tree canopy. This further means that backscattered waves may contain potentially useful data about the vegetation cover which would be valuable in environmental studies.

Forest biomass is not only an important input parameter for environmental models on a global scale, but also on a local scale to monitor and manage the health and productivity of forests (ASKNE *et al.*, 1996). However, analysis of the current status of the biomass estimates in terms of precision and accuracy leads to a conclusion that the precision is too low to be used for any quantitative carbon flux model.

In this work, primary focus is given to the application of the InSAR datasets for biomass studies.

The value of InSAR datasets is fully revealed when the three dimensional picture of an object is needed. Some relatively current examples of InSAR datasets applicability include glacier mass balance studies (BERTHIER *et al.*, 2007), volcano studies, Earth crust deformation studies (LU *et al.*, 2000, 2004; WRIGHT *et al.*, 2006), hydrological studies (SCHUMANN *et al.*, 2007), erosion studies (BAILEY *et al.*, 2007), and vegetation studies (KELLNDORFER *et al.*, 2004).

The InSAR workshop, sponsored by the National Aeronautics and Space Administration (NASA), National Science Foundation (NSF) and the United States Geological Survey (USGS), has identified the fundamental questions that can be potentially answered using datasets acquired using active remote sensing technology. According to ZEBKER, (2004), pp.2 these would include the following:

1. *What is the three-dimensional (3-D) structure of vegetation on the Earth's terrestrial surface that influences habitat, carbon, climate, agricultural and timber resources, fire behaviour, and economic value?*
2. *How does land cover change over time and what are the mechanisms, including the spatial distribution of change, regarding human-driven land-use conversion between urban, forest, agriculture, and wildland natural disturbance including fire, hurricanes/wind, insects/pathogens, landslides, and earthquakes/volcanoes?*
3. *How are biomass/carbon distributed over the surface of the Earth (global carbon cycle)?*
4. *What is the surface topography and change in surface topography under vegetation canopies?*
5. *How does land cover/vegetation control the cycling of carbon, nutrients, and water through ecosystems, and what is the current state of the Earth system?*

Any answer to the above questions requires detailed, quantitative knowledge of the parameters of the biomass. However, at the present time, precise estimates of the absolute quantities of biomass using any method, including field survey, are insufficiently accurate for practical applications. For example, it was found that in the tropical rainforest of Manu in Peru, where biomass ranges from 40 to 500Mg/ha for young and old undisturbed forests, respectively, "*the P-band horizontal and vertical polarization data combined separate biomass classes in good agreement with forest inventory estimates.*" However, for sparse and over-flooded forests, when the radar operates at circular polarization, the errors exceed 100% (RIGNOT *et al.*, 1995).

One of the contributing factors to the poor accuracy of the biomass estimates is the lack of a suitable method of dataset acquisition, which must be applicable at a variety of spatial scales from local to global. Another factor influencing the accuracy of the biomass estimates is the requirement to complete the acquisition in a short period of time to avoid the potential bias of natural changes of forest. These determinants of the biomass estimate accuracy justify an exploration of imaging radar applications for that purpose (*ibid*). These applications include multi-polarization, long wavelength radar imaging among others. Some global and homogenous datasets for this kind of project are already available. Examples of this include the previously mentioned Global Rain Forest Mapping Project datasets and the Shuttle Radar Topography Mission, C-band datasets (SRTM.C). But many more can be expected in the near future.

This study investigates biomass representation in the InSAR datasets and how this knowledge can be utilized in studies on biomass.

Before reporting on the biomass representation in the InSAR datasets, at least three questions have to be answered. The first question is: what kind of physical principles govern the biomass representation in InSAR datasets? An answer to that question lies probably among the physical principles of propagation of electromagnetic waves in random media. The second question is: how is the biomass represented in InSAR datasets? An answer can be reached by theoretical modelling and computer simulations, field experiments, or a combination of both. The third question: how can the representation of biomass in the InSAR datasets be used for biomass modelling and estimates?

These three basic questions need to be focused on topics of contemporary and common concern in order to maintain clarity of presentation, while observing as much as possible universality of the answers. One such topic is forest change detection and assessment. Forest change is usually considered in terms of human activities (deforestation), but it can also be linked to one of the most challenging problems our civilization is currently facing—global warming. Here, the term biomass depletion is used instead of forest or biomass change. The difference between these terms is that biomass depletion means a “permanent departure” of biomass from a certain state of equilibrium maintained within a given envelope of environmental conditions, while biomass change also includes seasonal variations of biomass. The biomass depletion can be sudden or a slow event, and is always a response of biomass to forces of natural or anthropogenic origin (HOLLING, 1973). Biomass depletion is marked by either increases or decreases of biomass density. While a drop in the biomass density is the most frequently investigated issue, an increase in biomass density can also be observed as a result of a high concentration of CO₂ in the atmosphere (more nutrients for plants). This, however, might not be a positive development because the lianas are one of the biggest beneficiaries of that increase, which leads to a permanent change in an ecosystem (MALHI *et al.*, 2002). The term biomass depletion in the context of biomass change was probably used for the first time by Ooi Jin Bee (BEE, 1987).

Biomass in the InSAR datasets is represented as an elevation bias with magnitude controlled by the frequency of the radar waves and the density of biomass. Using that relationship and other reference data, a method of biomass change detection was developed. The method permits the detection of relative changes in biomass caused by any type of depleting force such as logging or slow acting forces such as air pollution or an increase in the mean air temperature. The method requires a homogenous biomass. The degree of biomass depletion is measured as an average elevation bias of that biomass object. The method can be classified as an object-oriented method of change detection. Among already mentioned advantages of radar systems, the InSAR method is simpler to execute when compared with traditional multispectral approaches.

The term biomass is used here as a generic name representing all aboveground organic matter including vegetation, animals and insects. However, because of the economic and ecological role of forest, and because the forest is one of the major carriers of aboveground biomass on earth, the focus is placed on forests. Hence, in almost all cases, the term biomass is to be read as forest.

This work is organized into the following chapters:

After this Introduction, Chapter 2 presents a series of observations and conclusions from the literature. These studies can be considered a rationale for the approach and research presented in this work. In most cases, the references were omitted here for clarity. They can be found in the subsequent, relevant parts of the work.

In Chapter 3, several characteristics of the biomass are presented. Selection of topics was determined by their relevance to radar-based investigations. The purpose of this presentation is to work out the extreme ranges of variety of parameters that characterize the biomass. The idea is to have an envelope of parameters in which the biomass is hosted in the environment.

Chapter 4 introduces fundamental laws of physics that are essential for understanding the radar systems. The radar-based methods and systems discussed include synthetic aperture radar (SAR) and SAR interferometry (InSAR).

Chapter 5 contains a detailed explanation of the InSAR elevation data. This presentation seeks to identify error sources within the data sets and to determine the sensitivity equation of InSAR to the parameters of radar systems, the environment and other factors.

Chapter 6 contains a detailed picture of the biomass representation currently available in InSAR datasets. A conclusion is drawn regarding the applicability of the InSAR datasets for biomass studies. Major analytical and experimental models of the biomass representations in InSAR datasets are summarized in this chapter.

In Chapter 7, a mathematical model of a tree and a forest are gradually developed. A number of simulation experiments are summarised. They chiefly indicate the important role played by gaps in the forest in the process of InSAR data acquisition.

Chapter 8 shows a novel method of forest change detection and assessment using the InSAR elevation data product. The method is tested on the forests of Brunei Darussalam. The results obtained clearly show the usefulness of the method for forest monitoring at various spatial scales.

This report is concluded by the Outlook, Conclusion, a comprehensive list of References, and three Appendices, where technical details of the datasets and other relevant information are presented.

2. RATIONALE

This work has been built on the basis of several conclusions drawn from comprehensive literature studies of the biomass estimation using remote sensing methods. These conclusions define a body of arguments about and proposed solutions to the identified issues of biomass estimation. Detailed references to statements given in this section, in most cases, will be provided in the subsequent chapters.

Biomass, as one of the elements constituting the natural environment, remains in constant interaction with its surroundings, including the adverse forces that cause a certain level of stress on biomass. These adverse forces can potentially influence biomass in a catastrophic way, leading to its total destruction, e.g., forest fires. These forces can also cause low-level but prolonged biomass stress, and in the case of changes in ground water conditions, air pollution and global warming. The origin of adverse forces can be natural and/or anthropogenic. Catastrophic events are normally restricted to a relatively small geographic area, whereas changes in biomass caused by regional or global forces affect much a larger geographical range. Catastrophic events are easy to register and monitor, which is routinely done today using remote sensing technology. Long-term changes are much harder to detect. In fact, there is a lack of literature on remote sensing reporting on quantitative changes in biomass caused by air/water pollution or global warming, despite the existence of rich data sources dating back to the early 1970s (the Landsat platform).

These disturbances, revocable and irrevocable, natural and anthropogenic, are significant for determining the distribution of carbon in the environment, i.e. they influence the natural distribution of carbon between the atmosphere and the biomass. A leading effect of these disturbances is the continuously increasing levels of carbon in the atmosphere, which is linked to global warming.

A reasonable exploration of global warming requires that quantitative models of biomass and carbon flux between carbon storages are available. In this context, the quest to develop more comprehensive biomass models is not yet over. This is because, to date and in the foreseeable future, there is no method for precise biomass estimation on a global or local scale. The current estimates have a relative margin of error of 25% to 100%. These extreme values have been reported on both global and local scales. Obviously, this is too high an error margin to feed any carbon flux model.

The tropical belt of the Earth is the most biologically active and significant ecosystem on the planet in terms of its participation in the global carbon cycle. Hence, continuous and accurate monitoring, assessment and reporting of its variations are of the utmost importance.

The data acquisition capabilities of optical sensors are very much dependent on the transparency of the atmosphere. The most common obstruction to reflected radiation from the surface of the earth is clouds. Optical spaceborne remote sensing in the tropical region of the world is severely affected by this persistent cloud cover. Therefore, acquiring cloud-free imagery in the tropics poses a serious problem.

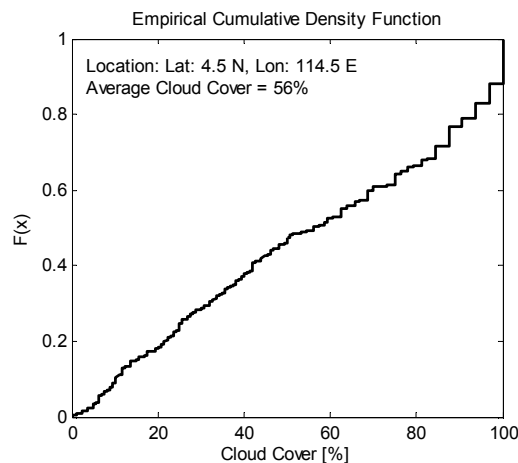


Figure 1: Cumulative density function of average cloud cover as observed by SPOT satellite imagery from January 1, 1986 to January 1, 2007, over Brunei Darussalam. In the calculations, all 498 pictures have been considered.

For example, according to the Brunei Darussalam Meteorological Service, the monthly mean amount of cloud cover for the year 2005 was 6.9 oktas, ranging between 6.3 and 7.1 oktas. This means that, on average, about 86% of days in a

year are cloudy. Encountering cloud-free days, between 9:30 and 10:30 am (satellite passing event) is a seldom occurring phenomenon, mostly taking place during elusive intermonsoon periods. These estimates have been verified by calculating statistics based on the cloud cover data extracted from the SPOT image catalogue. Figure 1 shows the average cloud cover and the empirical cumulative density function of the average cloud cover from SPOT images over Brunei Darussalam (4.5° north of equator) acquired from 1986 to 2007. A nearly one-to-one relationship between the percentage of cloud cover and its probability (in the range of up to 25%) predicts that acquisition of a cloud-free image over Brunei is unlikely. This seems to be confirmed by the local experience, as well. An immediate conclusion drawn from the above observation and analysis is that all-weather spaceborne sensors for biomass observation are absolutely necessary.

In addition to cloud cover, the 2D dogma is another limitation of optical remote sensing. This 2D dogma assumes that biomass is a thin “paint” on the earth’s surface. This assumption certainly oversimplifies any biomass model which is based on remote sensing data only.

Radar-based remote sensing already possesses powerful techniques that include SAR, InSAR, PolInSAR, DInSAR, and differential tomography (MARECHAL, 1995; Reigber *et al.*, 2003; and LOMBARDINI, 2005). It is reasonable to expect that the list of techniques will gradually expand in the future as scientific and technological developments continue to progress. Also, in light of the previously indicated meteorologically- and climatologically-driven restrictions of optical remote sensing, radar sensors with all-weather and day-night data acquisition capabilities are indispensable for biomass-related studies. Multifrequency and full polarimetric radar able to penetrate vegetation cover at different rates will allow the potential for studies of the vertical structure and the density of vegetation.

The digital elevation data such as C- and X-band SRTM reveal an elevation bias which to some extent depends on the interaction between vegetation and microwaves. Therefore, it can be expected that through analysis of the elevation bias some measurable characteristics of biomass could be deduced. This could lead to the development of an InSAR-based methodology that more accurately estimates biomass. The global coverage of the SRTM dataset and the uniform way the data was developed makes the SRTM dataset a unique source of information about the biomass on a global scale. Unfortunately, only one global 3D snapshot of the earth’s surface is insufficient to produce a reliable assessment of biomass quantity. A reference dataset is required to assess the change. However, the availability of similar datasets, possible in the near future because of the upcoming TanDEM-X satellite system, ALOS DEM or ASTER DEM (http://asterweb.jpl.nasa.gov/content/03_data/01_Data_Products/release_DEM_relative.htm), and others, could create an opportunity to mitigate the issue.

3. BIOMASS

Biomass is one of the fundamental components of this planet. Moreover, it is the effect and constituency of life on this planet. However, the current position of the term “biomass” in the collective mind of our civilisation is much more prominent than some two millennia before. This is because one of the greatest ancient philosophers, Aristotle, did not include the concept of biomass on the list of elements the universe is constructed from, i.e., air, fire, earth and water (LLOYD, 1968).

In recent decades, biomass has received special attention in connection with the so-called global carbon flux. The primary function of biomass in this complex chain of biochemical processes is described as carbon sink capacity, but it is also described as a carbon emitter, which especially draws the attention of ecologists if artificially induced (by deforestation, for instance). The fundamental issues and major focus of studies of biomass on a global scale are attempts to find out *how much* biomass there is on the Earth and its variation over space and time. In the following chapter, biomass will be studied as a subject of interest investigated using remote sensing techniques. The following sections are intended to present a comprehensive and coherent discussion of the biophysical/chemical, morphological and structural properties and spatial variability of biomass that are able to significantly influence readings from remote sensing sensors. The fundamental approach is to consider biomass as a three-dimensional medium that has density (measured in gcm^{-3}). A natural extension of this view of biomass is the concept of *biopixel* – a 3D entity comprised of biomass, of a large enough size to be resolved by a remote sensing sensor at a useful SNR level. The aboveground biomass is the focus of this study.

3.1 Definitions and Terminology

One of the key terms in common use in the remote sensing of the environment is *biomass*. Casually, it is understood as all organic matter above the ground. The formal definition of biomass is provided by the IPCC (2003): “*Organic material both aboveground and belowground, and both living and dead, e.g., trees, crops, grasses, tree litter, roots etc. Biomass includes the pool definition for above - and below - ground biomass*”. According to the same source, the aboveground biomass is to be understood as: “*All living biomass above the soil including stem, stump, branches, bark, seeds and foliage*”.

Biomass is measured by “*the total amount of aboveground living organic matter in trees expressed as oven-dry tons per unit area*”¹ which is known as the *biomass density* (FAO, 1997).

It should be noted that this definition excludes dead wood standing or lying and also does not include the forest understorey constituted by grasses, tree litter, roots etc. It also does not reflect the vertical nature and structure of the aboveground biomass, nor its bio-diversity, which is especially rich in multilayer tropical forests.

Contemporary global issues related to climate change require a comprehensive monitoring and quantification regime of all the components of the environment other than those allowed by the above definition of aboveground biomass. The limitations imposed also cannot be overlooked, for example, meteorological (persistent cloud cover) and financial constraints² (GFRA 2005). These limitations of the deployment of the optical remote sensing lead to the following problems with the results of environmental monitoring (MOLLICONE *et al.*, 2003):

1. The true rate of deforestation is unknown.
2. The amount of biomass for different type of forests is unknown.
3. The spatial distribution of these types of forests is also unknown.

This list certainly does not exhaust other significant parameters that can be observed in forests in order to describe the forest’s health and resilience to anthropogenic disturbances. For example, the problems of defragmentation and depletion of biomass (BECEK *et al.* 2005; 2006), which are adverse manifestations of socio-economic development (besides natural variations), would need to be monitored using an additional set of parameters, for example, the herbaceous and chemical composition of the biomass and their spatial and temporal variations. However, these issues, clearly extremely important, are not to be identified and monitored using the above definitions posed in GFRA 2005.

A good summation of the current state of engagement of remote sensing in the observation and measurement of forests could be that “*the present contribution of satellite remote sensing imagery to quantifying the global carbon budget*

¹ The aboveground biomass density is usually expressed in kg/m^2 or in t/ha (tonne/ha), (FAO, 2005).

² Lack of funding was the reason for not deploying remote sensing to verify the Global Forest Resources Assessment 2005 (FAO, 2005).

issue is related to the true level of humid tropical deforestation, and not yet to the amount of forest biomass” (MOLLICONE et al., 2003).



Figure 2: Forest dieback in the Badas Peat swamp Forest (Brunei Darussalam) caused by anthropogenically induced drop in ground water levels in the peat swamp 19/12/2004. Photo: K.Becek

The following is the definition of ‘aboveground biomass’ adopted in this work:

Aboveground biomass is a layer extending above the land surface of the Earth, in which transformation of solar energy and organic and non-organic molecules into organic matter occurs. It contains floral organisms living or dead, commonly known as vegetation. It may also contain fauna organisms including insects and birds.

This way of understanding biomass is currently dominant in the remote sensing community (ZEBKER, 2004). It directly refers to an ecological perception of biomass. Some fundamentals of this ecological approach are shown in Figure 3.

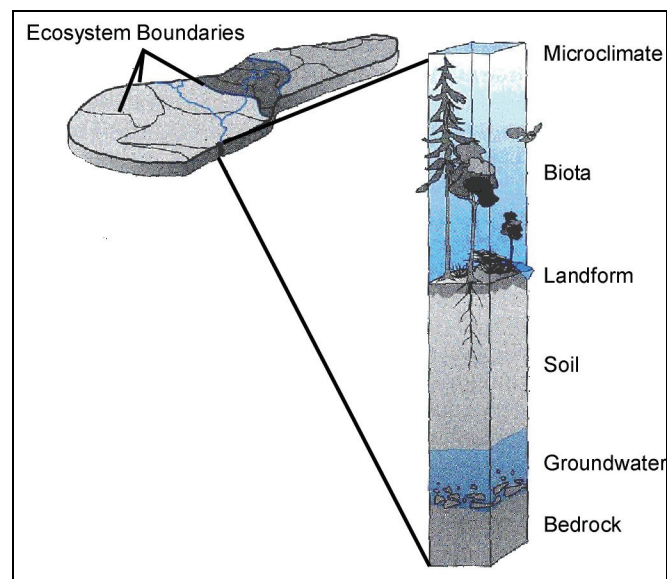


Figure 3: Constituent elements of an ecosystem. Source: (BAILEY, 1996)

The ecological background and character of the definition are manifested in the inclusion of all forms of organic matter relevant to natural carbon flux, rather than being limited solely to the herbaceous part of a forest. Another

distinguishing element of this definition is that, in spatial terms, it covers all land areas, provided that they are at least temporarily covered by vegetation at some point.

The following are the disparities between the GFRA 2005's definition of the aboveground biomass and the one adopted in this work. The current work:

- Does not refer to any particular vegetation type or land cover, i.e. forest;
- Does refer to matter in addition to vegetation;
- Does refer to the 3D nature of vegetation.

It must be noted that biomass and carbon stock are usually associated with floral material, and do not include animals, such as birds and insects. Justification of the exclusion is founded on the assumptions that:

- The non-floral component of biomass is in a state of equilibrium (does not change much over time);
- the total mass of this non-floral component of biomass is much smaller than that of the floral component;
- the spatial resolution of the remote sensing sensors (air/space borne) is too coarse to capture and/or identify individual animals.

However, considering that the estimated total number of insect individuals on Earth is roughly 10^{18} (CHAPMAN, 2005; MAY, 1988), which is equivalent to about 1.8 kg of insects per meter squared of the land masses of Earth, it must be concluded that the non-floral component of biomass (insects only) equals about 15% of the herbaceous biomass (11.9kg/m^2) (FAO, 2005). Some insect species are airborne most of the time, which must have certain implications for propagation of electromagnetic waves (ZRNIC *et al.*, 1998).

Key terms considered in this work are forest, vegetation, biomass and carbon stock. Although they refer, to varying degrees, to the same quality of our reality, e.g. to the living layer of our planet, they have distinct, but not universal meanings across different sciences. The following is an attempt to contrast these terms as they are used within the remote sensing community, and to highlight the meaning of biomass as it is understood within this work.

The meaning of the term 'forest' is greatly influenced by the three major functions a forest performs, that is natural, commercial and ecological.

Since the dawn of civilization, the forest has surrounded humans in one capacity or another, providing them with shelter and a livelihood. This is what is here considered the natural function of a forest. This defacto symbiosis between human civilization and the forest changed very little for a considerable period of human history, despite the agricultural revolution that occurred some 8000 years ago. In fact, the forest was used in a sustainable way until around 1700. During that period, only 7% of the initial forest areas were lost to deforestation. Since the Industrial Revolution beginning around 1770 until 1990, humans managed to deforest up to 30% of the original forest area (DIXON *et al.*, 1994; MALHI *et al.*, 2002), adding an additional 2% in the last 20 years or so (FAO, 2005). Thus, our planet has lost about 39% of its original forest areas due to human activities. This dramatic increase in the deforestation rate over the last 300 years is one of the major suspects on the list of factors adversely influencing current climatic changes. Therefore, the world's forest resources and their dynamics provide some of the most important data related to the planet's ability to control the climate.

During the Industrial Revolution, the commercial value of forests gradually became recognised. Forests became sources of timber and other commodities to which monetary value could be assigned. The monetary appraisal of forests requires regular measurements, which are commonly known as forest inventories. The main goal of forest inventories is to estimate the volume of timber. In addition, the inventories are also helpful in forest fire mitigation, identification of natural disturbances like insect infestations, and other forest management purposes, including ecosystem process modelling (FRANKLIN, 2001).

The development of the 'ecological' consciousness of the human population over the last 40 years or so, which culminated in the signing and ratifying of the United Nations Framework Convention on Climate Change (UNFCCC) by a majority of countries worldwide, and its Kyoto Protocol (DeFRIES *et al.*, 2006), has gradually given additional meaning and relevance to forests. Forests have become the primary component in the attempt to quantify the natural flux of carbon in the environment. The 'carbon cycle' is understood not only as a sink for carbon residing in the atmosphere but also as a source of carbon released into the atmosphere through deforestation and forest depletion (MAYAUX *et al.*, 2005). Therefore, ecologists recognise the ecological function of forests, and perceive it as a bearer of a significant amount of biomass. For this reason, ecologists tend to 'measure' forests in ecological terms, rather than in terms of the stand basal area, which is a commercial approach.

This diversified range of forest functions creates some difficulties in defining the term ‘forest’. As H. G. Laud of Forest Information Services, Manassas, Virginia, USA calculated in 1999, there are more than 240 different definitions of ‘forest’ (UNFCCC, 2006). According to the definition adopted by FAO for the purpose of the Global Forest Assessment 2005 (GFRA 2005) (FAO 2004; 2006a; IPCC, 2003)), ‘forest’ is described as:

“Land spanning more than 0.5 hectares with trees higher than 5 meters and a canopy cover of more than 10 percent, or trees able to reach these thresholds *in situ*. It does not include land that is predominantly under agricultural or urban land use.”

The quantitative parameters used in the above definition allow for a much wider interpretation of the horizontal and/or vertical extent of a forest than is commonly understood. For example, the definition includes areas that one would hardly recognise as a forest, based just on visual observation. It also includes land that can be considered a ‘would-be-forest’ for an unspecified length of time.

These remarks indicate the real source of difficulty, potential discrepancies, errors and omissions in forest inventories conducted for GFRA 2005. This is because the forest inventories conducted according to the above definition of forest should include both data from existing forestry department records and some additional knowledge, like land use maps, cadastral data and planning/zoning information. However, effective and accurate data compilation and the preparation of such a report require a functional nationwide GIS as a part of a well-developed national spatial data infrastructure (NSDI). This proves not to be the case in many, especially tropical, countries, where the state and dynamics of their forest reserves play a fundamental role in the quantitative assessment of the global carbon flux (UNFCCC, 2006).

The requirement for data in addition to what can be acquired visually, imposed by the definition of ‘forest’, restricts the viability of remote sensing as an instrument for independent verification of national methods. Furthermore, the deployment of remote sensing for an assessment of forest reserves and their dynamics on regional and global scales is usually done using sensors with a spatial resolution of $> 70\text{m/pixel}$. This means that all patches of forest around 0.5 ha (about 70 by 70m) are omitted (ZHAN *et al.*, 2000).

This disappointing conclusion means that the national reports that were used to compile GFRA 2005 are unverifiable using independent and transparent methods, which may cast doubt on the quality of the outcome of the report.

However, FAO continuously strives to improve the quality of national reports by program like the Japanese-funded Monitoring, Assessment and Reporting on Sustainable Forest Management (MAR-SFM) in Asia (<http://www.fao.org/forestry/media/13853/0/0/>).

The advantage of this approach to forest classification is that it creates a consistent baseline, allowing for comparison of the results of similar inventories of forest resources conducted every five to ten years, beginning in 1946 (FAO, 2006a).

Figure 4 shows an intuitive interrelationship between carbon, biomass, vegetation and forest (FAO, 2004).

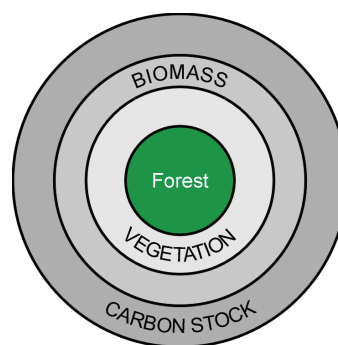


Figure 4: Relationship between carbon stock, biomass, vegetation and forest.

According to Figure 4, the forest is the smallest, yet most important core component of the carbon stock. Forest consists partly of vegetation, which also includes crops, grasses and parks. While biomass encompasses vegetation living or dead, the carbon stock consists of all of the above, and also includes biotic mineral deposits like natural gas, coal, peat, oil, etc.

Figure 5 shows a detailed decomposition of the terms ‘carbon stock’, ‘biomass’ and ‘forest’ as they were used in the most recent and most comprehensive global inventory of forest resources, which was prepared by the United Nations, based on the national reports of participating countries. (FAO, 2005). When discussing the Global Forest Resources Assessment 2005 (GFRA 2005), it is worthwhile noting that the national reports used for GFRA 2005 were prepared using traditional ‘on the ground’ methodology, and they have not been verified using transparent remote sensing methodology due to lack of sufficient financial resources (FAO, 2005).

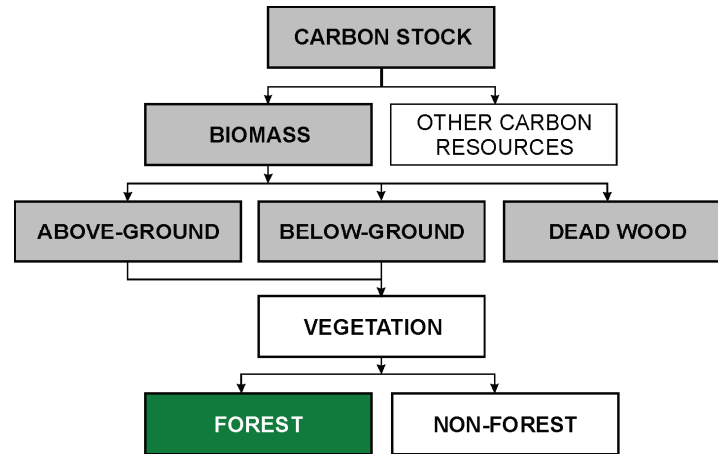


Figure 5: Components of the carbon stock. Note that the term ‘vegetation’ has not been defined by the Food and Agriculture Organisation (FAO, 2004).

This work is concerned with the components above that are coloured grey in Figure 5, while the white boxes represent fossil fuels, such as petroleum, coal or natural gas and non-forest areas like parks and agricultural lands. It must be clarified that the atmospheric pool of CO₂ is included in the bio-carbon stock as it is readily available for participation in the global carbon flux through photosynthesis.

The above definition of forest is concerned with its spatial (horizontal) extent only. This is insufficient, however, if the data are intended to be used to calculate the carbon stock and its fluctuations in the environment. What is omitted in the above definition is the vertical variation of forests. A tree’s height and its vertical structure are continuously changing as functions of the species, natural growth, seasonal defoliation/re-foliation (leaves-on/off). They also change as a combined result of atmospheric, land and ground water pollution or level changes, insect and disease infestations, and catastrophic events including fire.

Often in the literature, the terms ‘forest stand’ and ‘the compartment’ are used. According to HOWARD, (1991) ‘forest stand’ refers to ‘*an aggregation of trees sufficiently uniform in composition, age classes, size classes, etc. The stand is usually the smallest unit of forest management...*’ In this work, the forest class is identical to the forest stand. The compartment is a territorial unit of the forest for administrative purposes (*ibid*).

Various types of vegetation cover the remaining 72% of the land area (excluding inland water bodies) on our planet. Besides forested areas, this also includes steppes, grassland, cultivated vegetation (crops), parks and interurban green areas, and isolated tree groups. Even desert and high mountainous areas are occupied from time to time by some kind of vegetation.

It is obvious that non-forest vegetation also participates to a certain degree in the carbon stock sink and release processes. The carbon-release process is greatly magnified by the fermentation processes of agricultural (crop and animal) products. Through this mechanism, non-forest vegetation is a significant contributor to greenhouse gas emissions (methane), and as such cannot be taken out of the carbon accounting procedures that are strictly specified by the Kyoto Protocol.

The last term that is often mentioned in the context of vegetation and the global climate changes is carbon. Carbon is regarded as a fundamental element of all life forms on Earth. It is also the main component of the greenhouse gases that are emitted when burning carbohydrate fuels, and is released into the atmosphere through deforestation and the depletion of forests.

The formal definition of carbon (IPCC, 2003) directly associates it with biomass. It states that carbon is in all living biomass above the soil, including stems, stumps, branches, bark, seeds, and foliage. For the purpose of GFRA 2005, it was accepted that ‘half the dry weight of biomass is carbon’ (IPCC, 2003).

In this work, carbon is to be understood in the same manner, that is through its association with biomass. Thus, in order to quantify carbon, all living or dead organic material must be considered.

The more generic term ‘carbon stock’ is defined as ‘the quantity of carbon in a “pool”, meaning a reservoir or system which has the capacity to accumulate or release carbon’.

The difference between carbon and biomass is that biomass is a macroscopic, thus observable physical entity, while carbon exists rather as a concept, or, at most, as a (chemical) element.

In remote sensing literature sources, the terms ‘biomass’ and ‘carbon’ are used almost synonymously. This could be because of the 50% rule (biomass contains 50% carbon), which is almost universal across herbaceous life forms. Therefore, in this work, the commonly accepted approach will be adopted wherever possible.

3.2 Estimates of Global Biomass

For further discussion on biomass or carbon stock, it would be useful to establish quantitative estimates of their respective quantities on a global scale.

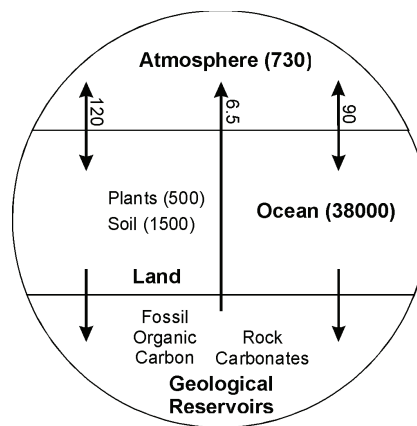


Figure 6: Fundamentals of the global carbon cycle. The arrows with numbers represent gross primary production and absorption of carbon by the biomass and ocean-atmosphere exchange. The arrow from the Geological Reservoirs to the atmosphere indicates fossil-fuel combustion. The units for all fluxes are Pg per year, Pg yr^{-1} , ($1\text{Pg} = 10^{15}\text{g}$). The numbers in brackets indicate an estimated size of a particular carbon reservoir in PgC. Source: Adopted from MALHI *et al.* (2002).

Figure 6 shows the main global carbon stocks and routes of natural carbon flux (MALHI *et al.*, 2002). Major carbon exchange occurs between the ocean and the atmosphere (90Pg yr^{-1}) and the atmosphere and vegetation (120Pg yr^{-1}), and as a result of burning carbohydrate fuel (6.5Pg yr^{-1}). The vegetation-atmosphere and the geological-atmosphere routes are identified as unbalanced releases of carbon. Therefore, they are considered to be one of the reasons for climate changes.

The net increase of carbon released into the atmosphere since the Industrial Revolution (deforestation and fossil-fuel burning) has resulted in an increase in the concentration of CO_2 in the atmosphere from 260-285 ppm to about 365 ppm at present, which is the primary contributor to the greenhouse effect (MALHI *et al.*, 2002).

According to MALHI *et al.* (2002), the carbon stored in plants amounts to about 500 Pg. However, FAO estimate of the total carbon content of forest ecosystems for 2005 is 638 Pg. Roughly half of the total carbon is found in forest biomass and dead wood, while the rest can be found in soil and litter (FAO, 2005a). Even higher discrepancies in this assessment are to be found in DIXON *et al.* (1994). According to DIXON *et al.* (1994), “Globally, forest vegetation and soils contain about 1,146 petagrams of carbon”. Moreover, it is assumed that “over two-thirds of the carbon in forest ecosystems is contained in soils and associated peat deposits” (*ibid*). The discrepancy in figures, 500 vs. 319

(50% of 638) vs. 1,146 Pg, clearly indicates that an accurate method of biomass assessment on a global scale does not exist. In Chapter 8, a novel method of change detection and assessment of the aboveground biomass on a nearly global scale will be presented.

In the following discussion, we shall consider in detail the properties of biomass that appear to be relevant for a researcher interested in using the InSAR technology for vegetation studies.

3.3 Morphology of Biomass

Understandably, biomass density is different from location to location. Moreover, for any given point the biomass density changes over time at various time-scales including annual, seasonal or even fractions of a second, which is due to wind.

The morphology or structure of biomass describes the type, shape, dimensions, composition and spatial distribution of forest components. The forest components include stems, branches and leaves, but also air and light within the forest area (NADKARNI *et al.*, 2008). Pauchard *et al.* (2000) provide other views on forest structure, which they define by vertical structure, horizontal structure and abundance. Therefore, any assessment of forest structure must consider these three parameters. However, those examples certainly do not exhaust all views and definitions of forest structure. According to NADKARNI *et al.* (2008), from 1976 to 2003, the keywords ‘canopy structure’ and/or ‘forest structure’ were mentioned over 9000 times in forest-related citations. A common drawback of definitions of forest structure is the focus on a particular aspect of that structure, such as the shape of the crown, the vertical distribution of canopy components, structural density, and others. However, there are many questions related to forest structure that have not been answered yet. Examples include the influence of climate change on biomass production or the influence of forest depletion on the animal population. Therefore, a more general view about forest structure is needed. NADKARNI *et al.* (2008) proposed a novel framework for categorization of forest structure concepts.

The types of biomass structural components are universal across the Earth. They include stems, branches and leaves. Other structural characteristics of biomass, like arrangement, quantity and size are extremely variable. For example, crown density, the number of stems per hectare, tree heights, DBH (=1.3 m) for a certain forest age, type of leaves and LAI change from place to place and from time to time.

The major factors influencing the structural diversity of biomass include type of species, climatic conditions, and abundance of water and nutrients. Variations in biomass caused by these factors can climb to over 60% for a given species. For example, recent studies on mixed dipterocarp forests - perhaps the single most important rain forest type in the wet tropics - showed that elevation that varied from 100 m to 1200 m amsl was the explanatory factor regarding variations of the basal area by about 62% (EDIRIWEERA *et al.*, 2008).

The above-mentioned factors can be considered stable over time. They can be understood as an envelope of environmental conditions in which a given ecosystem exists. However, there is a group of factors that can cause a rapid change in forest morphology. They include prolonged drought, forest fires, logging, silvicultural operations (thinning practices), insect infestations and global warming.

In studies of electromagnetic waves of microwave regions, biomass structure is considered because it influences the propagation of waves. The intensity of the influence depends on the size of the biomass components and the length of waves. Table 3 summarises the interaction of biomass structural elements versus the wavelength.

Table 1: Biomass structural elements influencing propagation of EM waves. *Source:* LE TOAN *et al.*, 2002.

| EM Band | X | C | L | P | VHF |
|------------------------------------|--------------------|---------------------------|---------------------|-----------------------------|----------------------|
| Frequency /Length (m) | ~9.6GHz/ ~0.031 | ~5.3GHz/ ~0.056 | ~1.3GHz/ ~0.235m | ~350MHz/ 0.85m | 20-90MHz/ 15-3.3m |
| Relevant structural elements | Leaves, Twigs | Leaves, Small branches | Branches | Major branches and stems | Stems |

This is, however, a commonly accepted understanding of the behaviour of radar waves within a forest canopy. In contrast, LE TOAN *et al.* (2002) showed that X-band radar does penetrate the canopy much more than was calculated and estimated under experimental conditions. Some experiments described in this report confirm that finding.

3.4 Biomass Density

Biomass density is considered to be the single most important parameter quantifying the *concentration* of matter to be observed using radar microwaves. In this section, estimates of the global average biomass density will be calculated.

This is intended to attempt to provide an idea of the quantities of biomass there must be to produce a radar disturbance. Using the data provided by the FAO (2005a), it can be found that the estimated total amount of carbon in the aboveground biomass is about 319 Pg. The same source quotes that the total area of forest, which is the biggest reservoirs of biomass, is just under 4.0×10^9 ha, which is about 30% of the land areas around the globe. Thus, the global average carbon density in the aboveground biomass is about 80 Mgha^{-1} or 8 kgm^{-2} . Taking into account the previously stated fact that carbon constitutes about 50% of biomass, the biomass density is about 164 Mgha^{-1} or 16.4 kgm^{-2} . These results obviously vary depending on location, measuring between 64.9 Mgha^{-1} and up to 222.9 Mgha^{-1} (FAO, 2005a).

Traditionally, the density of matter is expressed in kgm^{-3} . Expression of biomass in this way requires knowledge of the vertical extent of biomass or canopy height. Let h denote mean canopy height (m). Hence, the average density of the carbon stock stored in global forests is $8 \text{ kgm}^{-2}/h$, which is equivalent to 0.4 kgm^{-3} for an average canopy height of 20 m.

However, the biomass is distributed both vertically and horizontally in a heterogeneous fashion. A forest plot, even of the same species and the same age, can exhibit a great deal of horizontal variability due to a variety of environmental factors including topography (aspect, slope) and soil (nutrients, erosion, water). This single fact alone creates an important obstacle in any quantitative assessment of biomass of any ecosystem. Moreover, forests are distributed over the landscape in a random pattern that further complicates the issue. The vertical nature of the vegetation presents yet another complication in easily quantifying biomass. Figure 7 shows an example of the vertical distribution of biomass in a mixed species deciduous forest on the mid-Atlantic coast, USA (PARKER, 1995).

Temporal components both seasonal and systematic (depletion/enrichment) of the biomass variations warrant a mention as well. However, because of global warming, systematic changes or trends have become tremendously important. Rather than trying to produce absolute figures regarding how much biomass there is, the detection of relative changes should be the focus of our inquiries.

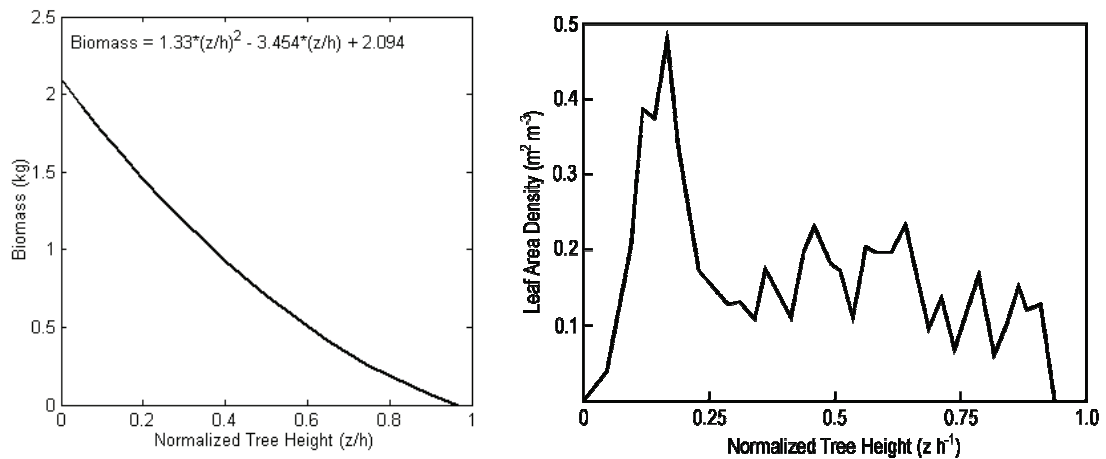


Figure 7: An example of vertical distribution of biomass of stems (left panel) and leaves (right panel). Source: Adapted from PARKER, 1995.

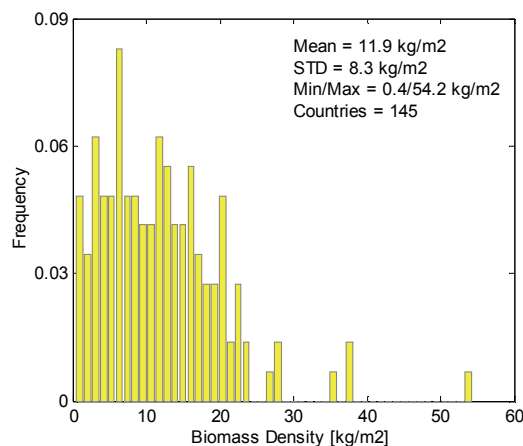


Figure 8: Histogram of the aboveground biomass density for country forest areas. (Data source: FAO, 2005a)

In the following, attention will be chiefly given to a detailed characterisation of the biomass, that is its constituent elements, forest and trees. The level of resolution of the study is the same as similar studies on the subject found in the appropriate literature.

3.5 Chemical Composition of Biomass

The major organic compounds of green plants are the following substances: cellulose, hemicellulose and lignin. The cellulose content of wood is about 50%, and it is the most common organic substance on Earth. Lignin constitutes 25% to 33% of the dry mass of wood. It is the second most abundant organic compound on Earth after cellulose. It contains about 30% of all organic carbon found on Earth (except fossil carbon). The remainder of the dry mass of wood is hemicellulose (BOERJAN *et al.*, 2003).

Chlorophyll, a green pigment found in leaves, is the most familiar compound to the remote sensing community because of its predominant presence in passive multispectral remotely sensed data. It is commonly used as an indicator of life processes occurring in vegetation. However, chlorophyll is less important for biomass estimation although its measurements, along with nitrogen, lignin and cellulose in the canopy, using imaging spectroscopy, can help to assess carbon absorption by forests (CURRAN *et al.*, 1997).

3.6 Microwave Dielectric Spectrum of Biomass

The propagation of microwave radiation in the presence of biomass is influenced by many factors including the dielectric properties of biomass and water. The nature of the variations of the dielectric constant of biomass, ϵ , and which physical and electromagnetic properties are relevant for the variations, was a subject of intense experimentation and subsequent phenomenological and theoretical modelling (EL-RAYES & ULABY, 1987, ULABY & EL-RAYES, 1987). For an oven-dried sample of various types of vegetation material, the dielectric constant was $1.5 \leq \epsilon' \leq 2.0$, $\epsilon'' \leq 0.1$ (imagery component), and the microwave frequency was from $0.5 \leq f \leq 20$ GHz, at 22° C, but it is believed that ϵ is not temperature dependent. However, the value of ϵ increases with the increase of 'free' water and water bound to vegetation molecules. Also, the salinity of the water influences the dielectric content of vegetation. A dual-dispersion dielectric model was extensively tested on the corn leaves. The results showed the model to be in excellent accordance with the measurements. However, for other types of plants, the relative prediction error was within +/- 20%. Due to salinity variations, the error is also within +/-20%, but only for frequencies ≥ 5 GHz.

The above findings are helpful in understanding the scattering phenomena of radar microwaves at various frequencies in the presence of moist vegetation. Moisture is becoming a factor for lower frequencies including the L-band, but is particularly important for P-band systems.

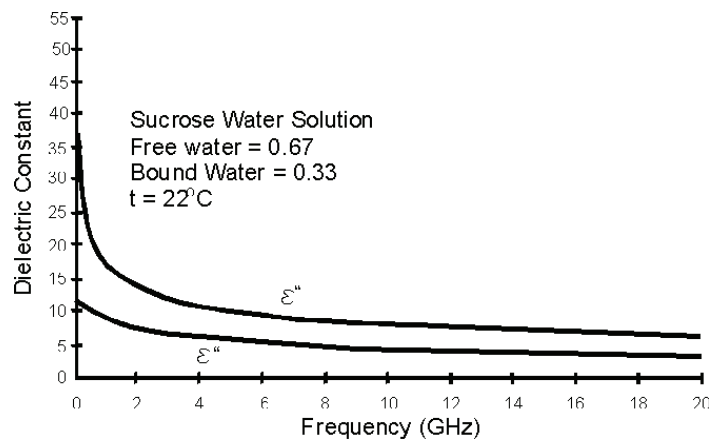


Figure 9: Dielectric spectrum of biomass. ϵ' , ϵ'' denote the real and imaginary part of the dielectric constant. The sucrose water solution was selected to model the composition of water in corn leaves. Depicted are fitting curves only. Source: Adapted from ULABY & EL-RAYES (1987).

3.7 Spatial Variability of Biomass

The spatial variability of biomass is a local to landscape feature of biomass that is profoundly influenced by local or landscape environmental conditions. They include soil and water conditions, topography, aspect, elevation above sea level, meteorological and climate factors such as precipitation, daytime temperature and wind direction (BOTKIN, 1993). They may also include certain anthropogenic factors like air/water pollution and the proximity to human-activity

areas. The spatial variability of biomass differs from the spatial distribution or spatial pattern of biomass, which is mainly controlled by climatic zone (the tropics, boreal zone, temperate, etc) and human activities (biomass depletion). Investigation of the interplaying factors on biomass density can be performed using what is known as the environmental gradient analysis (GREENBERG *et al.*, 2009). Such an analysis clearly shows great variability of biomass density even within a small size biome.

The spatial variability of biomass was investigated in several research studies done in different biomes over a long period of time. The most recent results indicate that spatial variability of undisturbed tropical lowland dipterocarp forest of Sabah, East Malaysia, can vary by as much as 60% between sampling sites within the same forest stand (TANGKI & CHAPPELL, 2008). It appears that in this case, the most important factor is the aspect and slope of the terrain.

The above-mentioned results on biomass modelling (NOGUEIRA *et al.*, 2008) indicate that the average spatial variability of the Brazilian Amazon forest is about 30%. This figure is significantly better than 60%, probably due primarily to differences in the topography of test sites.

3.8 Tree Morphology

The changing perception of a forest from a commercial resource to an ecological element is gradually occurring and bringing with it increased interest in other ecological elements, not only boles but also in other morphological components, including twigs, leaves, branches and roots. One topic under investigation by many researchers is the distribution of dry matter in trees among their morphological components. A general pattern emerging from these investigations is shown in Table 1.

Table 2: The distribution of biomass among components of a tree. Source: (PHILIP, 2002).

| Part of a tree | Forest trees (%) | Savannah/Woodland trees (%) |
|--------------------------|------------------|-----------------------------|
| Twigs and Leaves | 10 | 10 |
| Branches | 15 | 30 |
| Bole | 30 | 30 |
| Roots > 5 cm in diameter | 45 | 30 |

It is important to remember that distribution is variable from species to species, and from site to site. The distribution also varies between individuals. Those *in situ* results should be compared with the results achieved using remote sensing.

According to the results of a large study of the boreal forest, the aboveground biomass can be estimated within about 16 Mg/ha and up to about 150 Mg/ha across the SIR-C image under evaluation (RANSON *et al.*, 1997). The study applied the traditional remote sensing approach called a principal component analysis, which was aimed at reducing the number of channels used for forest classification. The first eight channels accounted for over 90% of the image variance. The highest contributor to the radar data was given by the SIR-C channel in HV polarimetric mode, and the SIR-L channel in HH mode. In this study, the following estimates of the contribution of tree components to the total biomass were used (see Table 2).

Table 3: Contribution of tree components to total biomass for selected boreal forest trees. Source: Modified Table 7, (RANSON *et al.*, 1997)

| Forest Type | Component | Contribution [%] |
|-------------|------------------|------------------|
| Pine | Bole | 82.0 |
| | Branches | 13.7 |
| | Twigs and Leaves | 4.3 |
| Spruce | Bole | 75 |
| | Branches | 12.6 |
| | Twigs and Leaves | 12.4 |
| Aspen | Bole | 90.0 |
| | Branches | 8.5 |
| | Twigs and Leaves | 1.5 |

The overall classification accuracy was greater than 90% for both forest and nonforest classes. The drawback of the models developed is the failure to consider mixed types of forests. The method appears to be of limited applicability for the aboveground biomass estimation of temperate and tropical forests that frequently have a much higher biomass than 150 Mg/ha.

3.9 Stochastic Properties of Vegetation

A natural question considering the interaction of microwaves with vegetation (M-V) is the dependence of the results of the reflection of microwaves from the vegetation on the incidence angle of the waves. In other words, is the vegetation cover a spatially homogeneous medium? If not, are there differences between the species and individuals that would be more or less homogeneous? Characterisations of the vegetation cover seem to be relevant because certain theoretical models of the stated M-V interaction assume such homogeneity. Also, a more promising method of radar tomography relies on the assumption of M-V unhomogeneity (LOMBARDINI, 2005).

3.10 Characterisation of Forest Structure

A description of a forest requires measurement of the parameters that might include (FRANKLIN, 2001):

- Type of species,
- Composition of forest (percentage of given type of species),
- Crown closure,
- Diameter at breast height (DBH),
- [Timber] volume,
- [Average tree] height,
- Stem density,
- [Forest stand] age, and
- Stage of development.
- Basal area.

The definition of some of the characterisations is straightforward, for instance type of species, composition of forest or stem density; some of them are calculated from others. For example, timber volume can be calculated from DBH (1.3m) and tree height, and, conversely, tree height can be calculated from DBH. For the latter, there are roughly 36 calculation formulas (FANG, Z. & BAILEY, 1998).

The crown closure is one of the forest parameters which are determined by the photointerpretation method. But multispectral data sets were also investigated in an effort to extract the crown closure characteristics of a forest (GONG *et al.*, 1994).

A missing parameter of a forest on the above list is the area of forest. Definitions of the above parameters can be found in FRANKLIN (2001). The collected parameters of forest structure vary from country to country. In Finland, for example, a forest's main characteristics include (HYYPPÄ *et al.*, 1993, 1997):

- Stem volume per hectare ($\text{m}^3 \text{ha}^{-1}$)
- Basal area per hectare ($\text{m}^2 \text{ha}^{-1}$)
- Mean height (m)
- Dominant height (m)

The above parameters are measured directly during forest inventories, or estimated using indirect methods. In the following paragraphs, the issue of deriving forest parameters, hence biomass estimation, will be addressed.

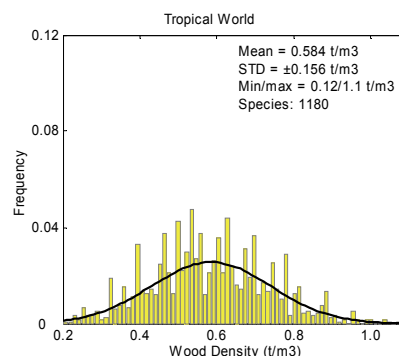


Figure 10: Histograms of wood density of tree species for tropical Africa, Asia, North/South America and the tropical part of the world. (Data source: FAO, 1997)

3.11 Methods of Quantitative Biomass Assessments

In the following section, an overview of methods of quantitative biomass assessment is presented. Two factors are emphasised here, the accuracy and spatial range for which a given method is practicable. Both factors are not completely independent. A general rule is that smaller scale studies (large area) require less accuracy in determining the biomass estimation, and *vice versa* for larger scale studies. Deciding factors for which the biomass inventory method should be used are the costs and time allowed for the biomass survey.

Another factor influencing the accuracy of biomass estimates in forests is its spatio-temporal variability. Also, in dense tropical forests, an additional limitation of the accuracy is related to the penetrability of the forest by humans.

Biomass can be assessed using: 1) ground-based methods, 2) photo-interpretation of aerial photography, and 3) remote sensing methods.

All biomass assessment methods rely on experimentally developed allometric equations that relate easily measurable tree and forest parameters with biomass. Depending on the scale of the survey (stand, forest, landscape, region, etc.), the measurable parameters may include DBH, tree height, basal area, type of species, area of forest and age. A commonly accepted model relating the tree diameter (DBH) to aboveground forest biomass is described by the following allometric Equation (1) (ZIANIS, 2008):

$$M = aD^b \quad (1)$$

where M is biomass,
 D is DBH, and
 a is the allometric intercept and b is the allometric exponent.

The average values for a and b are 0.1464 and 2.3322, respectively. These values are the best for a ‘global’ biomass equation. The reported relative biomass error for specific forest stands may reach up to 41% (ZIANIS, 2008). A regression equation for the biomass (M) versus DBH is shown in Figure 11. A regression equation relating DBH and tree height is shown in Figure 12.

Interesting new results regarding modelling of the biomass using allometric equations were recently developed for the Brazilian Amazon forests (NOGUEIRA *et al.*, 2008). The relative error of estimates of the biomass made using the new equations is about 30%.

A critical fact that determines the accuracy of the predictions made using the allometric equations is species and site specificity. This is especially valid in areas of high biodiversity such as tropical forests. A recent development in the area of allometry is a method of Bayesian Hierarchical Allometries (DIETZE *et al.*, 2008).

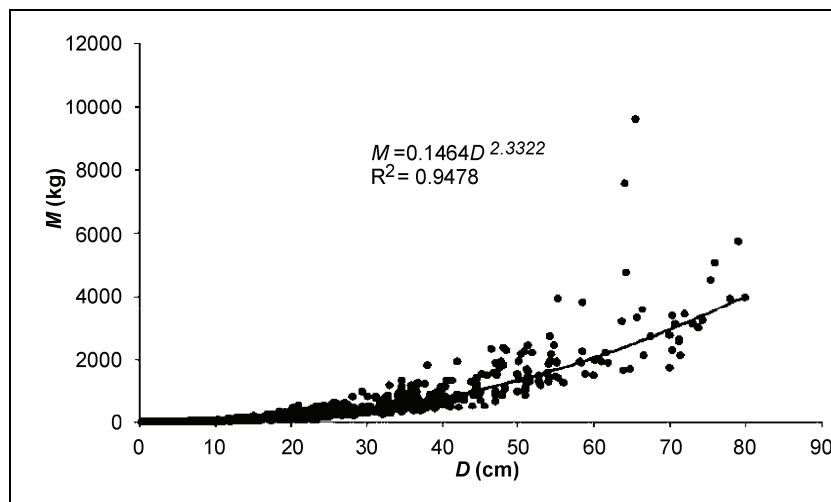


Figure 11: Biomass (M) as a function of tree diameter (DBH) based on 1211 tree species compiled from 34 biomass studies. Source: ZIANIS, 2008.

The latest development in allometry was reported by BASUKI *et al.* (2009). An intensive field study which was conducted in lowland mixed Dipterocarp forest located in Kalimantan, Indonesia, has found that the best equation

describing the relationship between the total aboveground biomass (TAGB) and a single predictor of DBH (Diameter at Breast Height) is:

$$\ln(\text{TAGB}) = c + a \ln(\text{DBH}), \quad (2)$$

where a and c are parameters.

It was found that for Dipterocarp trees $\alpha = 2.178$ and $c = 1.232$. It is worth noting that Equation (2) is also used to describe the power-law probability density function (CLAUSET *et al.*, 2009). This issue will be discussed in Chapter 7.

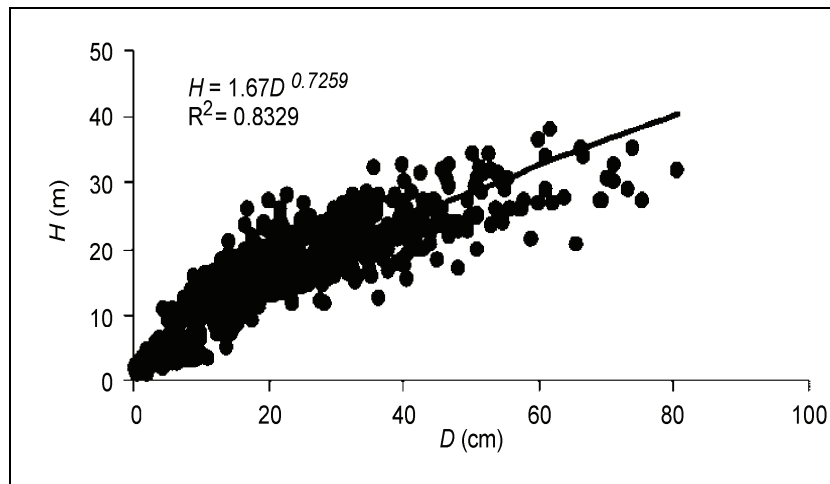


Figure 12. Tree height (H) as a function of tree diameter (DHB) based on 852 tree species compiled from 34 biomass studies. Source: (ZIANIS, 2008).

3.11.1 Ground-based methods

Ground-based forest inventory appears to be the most accurate because direct measurements and enumeration of the trees are carried out. Obviously, this is done in small sample plots of about 0.2 ha, spaced roughly every 800 m, along a transect line of variable length (ANDERSON and MARSDEN, 1984). However, despite various sophisticated sampling strategies (PHILIP, 2002), due to the variability of soil, water and slope conditions, differences between sample plots and the rest of the forest can be very significant. For example, results of forest inventories conducted in the Badas Peatland Swamp forest in 1954 by Anderson (ANDERSON and MARSDEN, 1984) clearly show that the variation in stem volume between samples can reach up to 23% (see Table 2.21, ANDERSON and MARSDEN, 1984). Noting that the Badas Peatland Swamp forest is a rather homogeneous ecosystem, it must be considered that the variations between samples are significant.

Taking into account both accuracy factors, for example natural variations within forest ecosystems (composition of tree species, etc), and variations due to change in environmental conditions (soil, water and slope), one can calculate the relative error of on-the-ground biomass inventories to be in the range of 20-30%. Note, however, that this estimate is valid primarily for a highly diversified tropical forest. Higher accuracy levels (10-15%) are achievable in boreal homogenous forests (HYYPÄ *et al.*, 1997; HYYPÄ, 2000). Chave *et al.* (2003) reported the highest accuracy of biomass assessment employing non-destructive methods. The 50 ha wet tropical forest in Panama was measured over a period of 15 years, every five years. For all trees with DBH ≥ 1 cm, the trunk diameter and height were observed. Lianas were also included. Using one of four tested allometric equations, it was found that the forest contained $281 \pm 20 \text{ Mg ha}^{-1}$ of biomass (about 7% error). The 15-year average annual increment of biomass was $+0.20 \text{ Mg ha}^{-1} \text{ year}^{-1}$ with a standard deviation of about -0.68 to $0.63 \text{ Mg ha}^{-1} \text{ year}^{-1}$ (CHAVE *et al.*, 2003).

The ground-based forest inventory method has been used to develop the Global Forestry Resource Assessment (GFRA) report (FAOa, 2005). This study has been prepared every five years since the 1940s based on national reports. Despite evidence of obvious errors in the national data sets, the GFRA is considered to be the most accurate and comprehensive assessment of the biomass on a global scale (BROWN, 1997). Undersampling and insufficiently validated allometric equations are among the major problems with some national reports (HESE *et al.*, 2005). Various long-term projects are in progress aiming at the improvement of national forest resources monitoring and reporting. Another problem with the GFRA is an incompatible definition of forest with what remote sensing methods are able to detect as forests

(DONG *et al.*, 2003). Moreover, the GFRA 2005 data have not been verified using remote sensing methods because of lack of financial resources.

3.11.2 Photo-interpretation of aerial or satellite imagery

Determining biomass estimates using aerial or satellite imagery through photo-interpretation involves a human operator. For the best results, he should be an experienced field forester trained as a photo-interpreter (HUSCH, 1971). After assuming a constant for human error, the accuracy of estimated forest parameters are mainly related to the scale/resolution and grey scale/colour of imagery used. Typically, for forest stand inventory, imagery at the scale 1:15,000 – 1:20,000 is recommended (*ibid*). Aerial and high-resolution satellite imagery (Quickbird or similar) can be used for delineating forest stands, tree species and their composition. Forest stand parameters like the crown diameter and crown closure can be relatively easily and accurately assessed (HOWARD, 1991). For the best results in assessing tree heights and average stand height, a stereopair is useful. For estimating the diameter at breast height (DBH), a relationship with the crown diameter can be used (*ibid*). However, this is only possible in the case of large-scale imagery (about 1:10,000). Otherwise, there is insufficient precision to satisfy the normal objectives of most forest inventories. In addition, the relationship between DBH and tree height can be used (Figure 12). Studies indicate that tree diameter can be estimated based on tree height and crown diameter with an accuracy of about ± 5 cm (HUSCH, 1971).

The stocking or bole area per hectare, which is the sum of the stem cross-section at the breast height of all trees per investigated area, can be estimated by counting trees, which is a tiring and time-consuming process. A simple formula does exist to estimate the number of trees, using measurements of the average crown diameter and crown closure (HOWARD, 1991). Results of photo-interpretation of forest parameters must be field checked (*ibid*), which obviously increases the costs of inventory. However, the quality of the photo-interpretation results is closely connected with the level of field check investments. Thus, this method of forest inventory is performed only every 10 years or so, especially for large areas. For example, the costs of a photo-interpretation-based forest inventory in Brunei Darussalam conducted in 1982-84 by external consultants (ANDERSON & MARSDEN, 1984) reached about \$750,000. Considering that the surveyed area was about 5765 km², one can calculate that the unit cost was about \$1.30 per hectare.

3.11.3 Remote sensing

The utilization of remote sensing data for forest inventory and monitoring is hindered by the spatial heterogeneity of forest by differences in tree species, age, density and canopy closure which affects the spectral signatures of forest (FRANKLIN, 2001; MASELLI and CHIESI, 2006). Situation is even more complicated by other environmental factors including topography, soils and ground water conditions (*ibid*).

Nevertheless, deriving the quantity of biomass using remote sensing methods has been attempted using 1) optical sensors, 2) LiDAR and 3) radar techniques. Optical remote sensing techniques are used to delineate and characterise forests. Although many vegetation models have been developed over the years, all aiming at estimating biophysical parameters of vegetation from multispectral data sets, typically the normalized difference vegetation index (NDVI) is used (WULDER, 1998). The NDVI can also be used for identifying the type (including canopy closure) and age of a forest stand. The quantity of biomass is estimated as a product of the area of forest and average biomass per hectare. For reasons already mentioned, for example spatial and temporal variation of biomass in a forest, but also variations in wood density (NOGUEIRA *et al.*, 2008), the accuracy of the results is limited. Note that the latter is applicable to every biomass calculating method. Limitations in using the NDVI are due to its saturation for biomass levels of about 100 Mgha⁻¹ (COHEN and SPIES, 1998). Somewhat confounding results were achieved in that respect for secondary forests in Brazil and Bolivia. STEININGER (2000) reports a saturation level at about 150 Mgha⁻¹ for Brazilian test sites, and no correlation between the NDVI and the biomass level for Bolivian test sites.

The accuracy of this approach depends on the level of misclassification (forest/non forest), but also as the result of mistakes in identifying forest type, canopy closure and age. One of the serious limitations of the optical remote sensing techniques for biomass estimation is that vegetation cover is considered to be a two-dimensional (flat) entity.

The Light Detection and Ranging (LiDAR) technique possesses the ability to quantitatively describe parameters of the vertical structure of vegetation in terms of tree height, crown density and crown layers (LI *et al.*, 2008). This technique was intensely investigated by HYYPPÄ (2000), who reported that, thanks to the three-dimensional tree height model, the following standard errors were obtained for mean height, basal area and stem volume at stand level (Table 4).

Main accuracy indicators obtained from 41 forest stands. Source: HYYPPÄ, 2000.

Table 4: Main accuracy indicators obtained from 41 forest stands. Source: HYYPPÄ, 2000.

| Error | Mean height | Basal Area | Volume |
|------------------|-------------|--------------------------|-------------------------|
| SE | 2.3 m | 1.9 m ² /ha | 16.5 m ³ /ha |
| SE (%) | 13.6 % | 9.6 % | 9.5 % |
| Systematic Error | + 2.5 m | - 9.7 m ² /ha | - 65 m ³ /ha |

These results are remarkable. However, there are a few factors limiting the application of LiDAR technology for biomass estimation. First of all, it has to be noted that the above results were obtained in the boreal forest zone in Finland for relatively uniform forest stands, with low biomass density (120m³ ha⁻¹). Under such circumstances, more than 30% of the LiDAR first returns originate from the ground (HYYPPÄ, 2000). This indicator may be much smaller for tropical forests (about 3% or less). Obviously, this fact can significantly influence the accuracy in a negative way. Another disadvantage of the LiDAR method is the inability to identify any bio-morphological characteristics of forests, like composition of species. The last prohibitive factor in using LiDAR methods is the costs involved. It is estimated that they can be as high as \$150 to \$250 ha⁻¹ but may cost as much as \$772 ha⁻¹ (INTERMAP, 2008). This single factor alone means that the LiDAR method is suitable only for small projects where the highest accuracy is required (timber industry, etc.).

The third remote sensing method for biomass estimation makes use of synthetic aperture radar (SAR) technology. One of the approaches in utilizing the technology may be described as ‘traditional’ because it is concentrated on analysing characteristics of the back-scattered radiation for describing vegetation (DOBSON *et al.*, 1995a, 1995b).

Another approach is to utilise SAR-derived methods including SAR Interferometry (InSAR) (ASKNE & SMITH, 1996; BALZTER, 2001), Polarimetric Interferometry SAR (PolInSAR) (CLOUDE & PAPATHANASSIOU, 1998; DURDEN *et al.*, 1994; POLATIN *et al.*, 1994; FERRAZZOLI *et al.*, 1997; SAATCHI & MOGHADDAM, 2000; METTE *et al.*, 2005, 2006; QUINONES & HOEKMAN, 2005; GUTJAHR & SCHARDT, 2006), and differential polarimetric interferometry SAR (dPolInSAR). The datasets produced using these techniques remain somehow dependent on the presence of, and biophysical and chemical properties of, vegetation. The magnitude of the relationship is mainly a complicated function of wavelength, but mutual geometrical and temporal orientation between incoming radiation and biomass components also plays a role. This may include incidence angle, volume (ASKNE & SMITH, 1996; ALBERGA, 2004) and temporal decorrelation, as well as the dielectric properties of vegetation and soil, etc. All these parameters of the SAR survey were investigated by a number of research studies and reported in a number of papers.

Implemented SAR technology includes systems installed on aircraft or on spaceborne platforms. All systems use microwaves ranging from the P-band (~0.85m) up to X-band (~0.031m). Simulation studies show that it is possible to distinguish three classes of boreal forest using the P-band SAR system assuming moderate ionospheric distortions. However, using a P-band satellite for biomass estimates can be difficult because of potential interference with defence early-warning systems, backscatter-to-biomass inversion techniques and the already mentioned ionospheric distortions (HALLBERG *et al.*, 2004).

Potentially the biggest advantages of the active remote sensing system are its independence from the position of the sun over the horizon and its all-weather operation capabilities. Moreover, the spaceborne systems allow for the development of homogeneity in terms of the methodology, uniformity in terms of accuracy, and within a very short period of time (~10 days), datasets that can be potentially used to estimate biomass or its changes on a global scale. A good example is the SRTM dataset (SLATER *et al.*, 2006), which implicitly (through vegetation-induced elevation bias) contains characteristics of biomass (BECEK, 2008a; CARABAJAL & HARDING, 2006; SIMARD *et al.*, 2008).

An important obstacle in characterising the biomass using radar technology is an effect known as saturation. Similar to optical sensors, there are certain limits beyond which increasing biomass density does not cause recognisable changes in the backscattered signal from the biomass. The effect, however, is not visible in the case of very low radar frequency – VHR (20 - 90 MHz) (FRANSSON *et al.*, 2000; MANNINEN & ULANDER, 2001).

Despite advances in satellite remote sensing techniques for quantifying biomass on a global scale (LI *et al.*, 2008), their applications are related to the level of humid tropical deforestation, and not yet to the amount of forest biomass (MOLLICONE *et al.*, 2003). Two distinct factors are responsible for the situation, which are the unacceptably low level of accuracy of results and the prohibitive level of costs for a global dataset. For example, remote sensing was too expensive to verify the data used for the Global Forest Resource Assessment, 2005 (FAO, 2005a).

3.12 Conclusion

The aim of this chapter was to identify morphological and biophysical benchmarks or extreme values of parameters of the object of interest of this work – the biomass. This is the first step in designing a device, procedure or technology for measuring the object of interest. One of the steps is the assessment of the expected/required accuracy of the results. Also important are estimates of costs for implementing such measurement technology and its operational, logistical and technical feasibility. In the following chapters, the identified benchmark values of biomass parameters will be used in assessing methods, procedures or technologies regarding their abilities to provide reliable datasets in relation to the biomass. As has been previously and frequently stated, the main slant accepted in this work is a focus on a global scale approach.

The findings and observations made clearly show that the issue of quantitative biomass estimates remains unresolved in terms of accuracy (desirable level of relative error less than 10%) and feasibility in terms of time and costs involved. What this means is that despite the advances made in SAR-based techniques for vegetation studies, the applicability of the methods on the ‘production’ scale still remains to be seen. Consequently, the vegetation cover is still considered as layer of paint on the surface of the Earth. Hence, it is investigated as a damage to that paint in different forms and shapes (deforestation).

Significant commercialisation of spaceborne remote sensing sensors is also a deterrent.

4. FUNDAMENTALS OF SYNTHETIC APERTURE RADAR INTERFEROMETRY

This chapter provides a review of the most important physical and technical facts plus the computing techniques that lead to development of synthetic aperture radar interferometry datasets. Most of the techniques were implemented through functional observation systems; some were designed through applicability tests and are now used in commercial settings. However, there are some techniques that are still under development. Nevertheless, these are also presented here as a contribution to their progression.

4.1 The Electromagnetic Waves

One way of introducing and explaining electromagnetic waves is to use a derivative of Maxwell's equations for a vacuum. These can be written as follows (SIGNELL, 2001):

$$\vec{\nabla} \cdot \vec{E} = 0, \quad (3)$$

$$\vec{\nabla} \times \vec{E} = -\frac{\partial \vec{B}}{\partial t}, \quad (4)$$

$$\vec{\nabla} \cdot \vec{B} = 0, \quad (5)$$

$$\vec{\nabla} \times \vec{B} = \epsilon_0 \mu_0 \frac{\partial \vec{E}}{\partial t}, \quad (6)$$

where ϵ_0, μ_0 is the permittivity and the permeability of the vacuum, respectively.

The above Equations (3) – (6) use the gradient ($\vec{\nabla}$), divergence ($\vec{\nabla} \cdot \vec{E}$) and curl ($\vec{\nabla} \times \vec{E}$) operators which are defined in APPENDIX 3.

Closer investigations of Maxwell's equations have commonly assumed the absence of magnetic charge or electric current at a given point in space. Despite this, it can be shown that the electromagnetic waves can still exist at that selected point. The differential equations for the electric and magnetic fields can be written as follows (BORN & WOLF, 1999):

$$\vec{\nabla}^2 \vec{E} = \epsilon_0 \mu_0 \frac{\partial^2 \vec{E}}{\partial t^2}, \quad (7)$$

$$\vec{\nabla}^2 \vec{B} = \epsilon_0 \mu_0 \frac{\partial^2 \vec{B}}{\partial t^2}, \quad (8)$$

It can be shown that Equations (7) and (8) are coincidental with the one dimensional wave equation:

$$\vec{\nabla}^2 f = \frac{1}{c_0^2} \frac{\partial^2 f}{\partial t^2}, \quad (9)$$

where c_0 is the speed of light in a vacuum, and f is displacement.

From Equations (8) and (9) one may conclude that:

$$\frac{1}{c_0^2} = \epsilon_0 \mu_0, \text{ or} \quad (10)$$

$$c_0 = \frac{1}{\sqrt{\epsilon_0 \mu_0}}, \quad (11)$$

with the symbols defined as per Equations 6 and 9.

Note, however, the surprising result that this closely relates the speed of light c_0 with the permittivity and permeability that represent electricity and magnetism.

Using Equations (5), (6) and an expression for the electric field in the form:

$$\vec{E} = E_0 f(\vec{k} x - c_0 t), \quad (12)$$

where E_0 is amplitude, f is a cosine or sine function, \vec{k} is a unit vector of the wave's propagation and x is a distance vector, it can be shown that:

$$\vec{E} \cdot \vec{k} = 0, \text{ and} \quad (13)$$

$$\vec{B} = \frac{1}{c_0} \vec{k} \times \vec{E}. \quad (14)$$

Equation (13) means that the electric field oscillates orthogonally to the direction of propagation. Equation (14) shows that the magnetic field is orthogonal to both the electric field and the direction of wave propagation. This also yields a relationship between the amplitudes of electric and magnetic fields, which is $E_0 = c_0 B_0$.

Figure 13 shows a representation of a self-supporting system for propagating electromagnetic waves, predicted and derived from Maxwell's equations. Strictly speaking the situation presented here concerns electric and magnetic waves that lie precisely in planes and are of constant wave length. This ideal model of electromagnetic waves represents plane-polarized waves. In nature, however, much more complicated situations occur (BORN & WOLF, 1999).

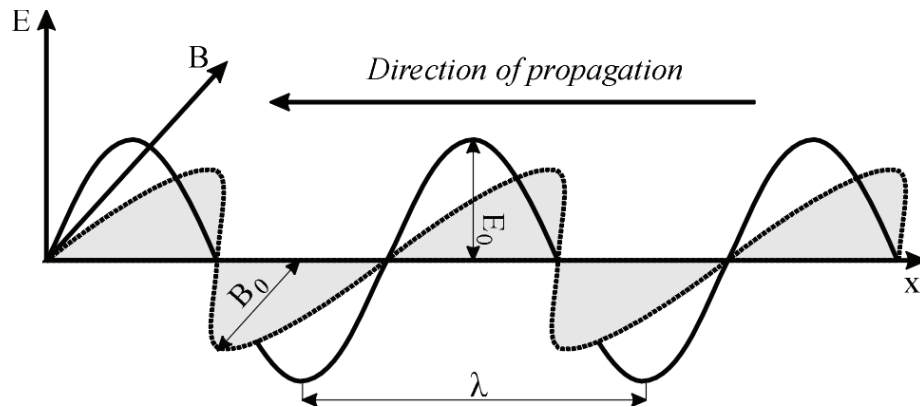


Figure 13: Relationship between electric and magnetic waves propagating from right to left. E_0 and B_0 indicate amplitudes of electric and magnetic waves, respectively. The wave length is indicated by λ .

Polarization plays an important role in radar technology. Frequently, in the literature the term ‘full polarization mode’ is used: this refers to all possible combinations of sent/received polarized waves, not to a fully polarized wave. Commonly, polarization is described by the orientation of the plane in which the wave is sent/received. Hence, H-polarization refers to a horizontal and V-polarization refers to a vertical plane of propagation. Thus, the possible combinations of radar backscattered waves are HH, HV, VH and VV. The first letter indicates the polarization of the sending antenna; the second letter indicates the polarization of the receiving antenna.

In addition to the above terms and equations, the following will also be referred to in this work:

Wave number k is the magnitude of the direction of propagation of the electromagnetic waves: it can be calculated as follows:

$$k = \frac{2\pi}{\lambda}, \quad (15)$$

where λ is the wavelength.

The wave's angular frequency ω is given by:

$$\omega = 2\pi f, \quad (16)$$

where f is the wave's frequency.

And finally, the basic relationship between wave frequency and wavelength is given by:

$$f\lambda = c, f = \frac{1}{T}, \quad (17)$$

where T is the period of the electric wave.

4.2 The Radar

The following section deals with some theoretical and technical aspects of radar technology, based primarily on information from the work of KINGSLEY & QUEGAN, (1993) and SKOLNIK, (1990). Please refer back to the introduction for a brief history of radar technology.

Radar systems use relatively few solutions to the technical problems involved in their operation. Radars emit and receive signals in and from precisely determined directions and also accurately measure the time delay between the sent and received electromagnetic pulse. Some radar systems are also able to scan an area of interest using a precisely oriented beam of electromagnetic energy.

The following simple formula calculates the distance or range R between the emitter and the target recipient assuming that they are located in a vacuum:

$$R = 0.5c t_d, \quad (18)$$

where t_d is the time delay and c is the average speed of the wave's propagation in a vacuum.

The radar's antenna is used for emitting and/or receiving radar waves and for identifying the direction from which backscattered waves have arrived. The dimensions of the antenna depend on the designated frequency of the radar. For example, for a 1MHz frequency radar, the antenna would be about 75m long (about a quarter of the wavelength). The performance of the antenna is characterized by its gain, which in an ideal case (i.e. one with no power loss) is found by the ratio between the number of steradians of a sphere and the width of the beam in two perpendicular directions (azimuth and elevation):

$$G(\Theta, \Phi) \cong \frac{4\pi}{\Delta\Theta \Delta\Phi}, \quad (19)$$

where $\Delta\Theta, \Delta\Phi$ is the width of the beam in azimuth and elevation directions, respectively.

For approximate calculations, Equation (17) can be estimated using the following formula:

$$G(\Theta, \Phi) \cong \frac{4\pi A}{\lambda^2}, \quad (20)$$

where λ is the wavelength (m), and
 A is its aperture (m^2).

The most important characteristic of a radar system is its sensitivity to the power of arriving backscattered signals. This sensitivity depends partly on the level of noise, which is always present in every practical system. The radar equation used to measure sensitivity is the ratio between the backscattered energy received by the radar and the noise. This equation, known as the signal-to-noise ratio, is usually expressed as follows:

$$SNR = \frac{P}{N} = \frac{P_t G_t G_R \sigma \lambda^2 L_s}{(4\pi)^3 R^4 N}, \quad (21)$$

where P is the power available to the system for calculating the results of the radar sensing (W),
 P_t is radar output power (W),
 R is the distance to the target (m),
 G_t represents the degree of concentration of output power towards the target,
 G_R represents the power gain of the receiving antenna,
 σ is the radar cross-section (m^2),
 λ is the wavelength (m),
 L_s is a radar system power loss coefficient,
 N is noise (W).

The term $4\pi R^2$ represents the area of a sphere with radius R .

Equation (21) is frequently written in a logarithmic form following the definition of decibels (dB):

$$SNR = 10 \log_{10}(P/N), \quad (22)$$

For example, if $SNR = 20\text{dB}$, which implies that the ratio $P/N = 10^2$, (because of multiplication by 10 and power 2). Another definition of decibel, which uses a multiplier of 20 rather than 10 (as in Equation (22)) and is used in image processing, will be introduced in due course.

Other radar system characteristics include bandwidth, range resolution and range accuracy. The bandwidth B of a radar system is the width of the frequency range for which the Fourier transform is above a certain threshold, usually -3dB, which is half the maximum value of power. In practical terms this means that a radar system with a certain bandwidth can process signals at that bandwidth. The bandwidth is reverse proportional to the duration of radar pulse τ . Hence, the following applies:

$$B \cong 1/\tau, \quad (23)$$

where the bandwidth B (Hz), and
 τ is the duration of radar pulse (s).

The range resolution of a radar is defined by its ability to distinguish two objects. The deciding factor is the pulse duration τ . The range resolution is given by the following expression:

$$\Delta D = 0.5c\tau, \quad (24)$$

where ΔD is the range resolution

For example, for $\tau = 10^{-6}\text{s}$ (pulse duration) the theoretical range resolution of the radar is about 150m, which means that the radial distance between the two objects to be recognized must be more than 150m.

The range accuracy σ_D depends on the duration and shape of the radar pulse (*ibid*), which is associated with the bandwidth through Equation (23). A shorter pulse (larger bandwidth) yields more precise range readings. This is similar to the calibration of a measurement device. For example, an old-fashioned survey tape has fixed marks every 10cm: this is its calibration. However, measurement results are estimated to 1 cm, leading to imprecise measurement and therefore error. In the same way errors are caused by the calibration set of (bandwidth B) and the noise generated by the radar physically (SNR). It can be shown (*ibid*) that range accuracy can be estimated using the following formula:

$$\sigma_D \cong \frac{c}{2B\sqrt{2SNR}}. \quad (25)$$

For example, assuming $SNR = 13\text{dB}$ and bandwidth $B = 1\text{MHz}$, the range accuracy σ_D would be about 24m.

Radar systems are used for many purposes. Frequencies are carefully selected, depending on the application and/or intensity of interaction between waves and the atmosphere. Table 5 below summarizes major frequency bands commonly used by radars.

Table 5: Radar frequency bands and their applications. Source: <http://en.wikipedia.org/wiki/Radar> (Edited). (Accessed November, 2008).

| Band | Frequencies (GHz) | Wavelengths (m) | Notes |
|------|----------------------------|------------------------------|--|
| HF | 3–30x10 ⁻³ | 10 – 100 | Over-the-horizon radar; 'high frequency' |
| P | < 300x10 ⁻³ | >1 | 'P' for 'previous', applied retrospectively to early radar systems |
| VHF | 50 – 330 x10 ⁻³ | 0.9 – 6 | Very long range, ground penetrating; 'very high frequency' |
| UHF | 0.3 – 1 | 0.3 – 1 | Very long range (e.g. ballistic missile early warning), ground penetrating, foliage penetrating; 'ultra high frequency' |
| L | 1 – 2 | 15–30x10 ⁻² | Long range air traffic control and surveillance; 'L' for 'long' |
| S | 2 – 4 | 7.5 – 15x10 ⁻² | Terminal air traffic control, long-range weather, marine radar; 'S' for 'short' |
| C | 4 – 8 | 3.75 – 7.5x10 ⁻² | Satellite transponders; a compromise (hence 'C') between X and S bands; weather |
| X | 8 – 12 | 2.5 – 3.75x10 ⁻² | Missile guidance, marine radar, weather, medium-resolution mapping and ground surveillance; X because the frequency was a secret during World War II. |
| Ku | 12 – 18 | 1.67 – 2.5x10 ⁻² | High-resolution mapping, satellite altimetry; frequency just under K band (hence 'U') |
| K | 18 – 24 | 1.11 – 1.67x10 ⁻² | 'Short' (Germ. Kurz); absorbed by water vapour; Ku and Ka are used instead for surveillance. K-band is used for detecting clouds |
| Ka | 24 – 40 | 0.75 – 1.11x10 ⁻² | Mapping, short range, airport surveillance; frequency just above K band, hence 'a' |
| mm | 40 – 300 | 7.5 – 1x10 ⁻³ | Millimetre band, subdivided as below. The frequency ranges depend on waveguide size. Multiple letters are assigned to these bands by different groups. |
| Q | 40 – 60 | 7.5 – 5x10 ⁻³ | Used for Military communication. |
| V | 50 – 75 | 6.0 – 4x10 ⁻³ | Very strongly absorbed by the atmosphere. |
| E | 60 – 90 | 6.0 – 3.33x10 ⁻³ | |
| W | 75 – 110 | 2.7 – 4.0x10 ⁻³ | Used as a visual sensor for experimental autonomous vehicles, high-resolution meteorological observation, and imaging. |

4.3 Synthetic Aperture Radar

The ideal remote sensing application of radar requires an RS system that provides high resolution (say 10m by 10m) and precise, geo-referenced data about a portion of the Earth's surface. However, a classic radar system scans the earth from a distance of 785 and km (ERS-1 orbit height) using a narrow cone of electromagnetic pulse, $\sim 0.5^\circ$, covers a ground area of only about 6.8 km in diameter.

This limitation was significantly reduced by the development of the synthetic aperture radar (SAR) technique in the mid 50's by Cutrona and his team (CUTRONA *et al.*, 1966; CURLANDER & McDONOUGH, 1991; HANSEN, 2001).

SAR requires that the radar and its target must be in motion, in relation to each other. The motion causes a small Doppler shift in signals reflected from the target, which allows an imaging resolution of about 3 arc-seconds ($\sim 90\text{m}$). SAR also requires the precise positioning and velocity of the radar, and the observation of the returning signal must be performed for a long time in terms of the length of pulse. For example, the duration of the ERS-1 signal is about $37.1\mu\text{s}$, but the scanning of the returning signal is about 0.6s (OLMSTED, 1993). Different methods are used for the range and azimuth processing.

In the following approach, formulas and terminology essential for SAR are introduced. Our starting point is the pulse of electromagnetic energy emitted and received by the antenna. As a consequence (see Paragraph 4.1) a pulse of energy of a uniformly distributed current is passed to the antenna. Assuming a rectangular antenna, it can be shown that the pulse produced is also rectangular, specifically of a sinc^2 (the *sinus cardinalis*(x)) $:= \frac{\sin(\pi x)}{\pi x}$) function. The energy of the pulse (E) can be expressed using the following formula:

$$E = \frac{\sin^2\left(\pi \frac{D}{\lambda} \phi\right)}{\left(\pi \frac{D}{\lambda} \phi\right)^2}, \quad (26)$$

where ϕ is the off-centre beam angle,
 λ is the wavelength, and
 D is the width of the antenna.

The shape of the emitted energy pulse is presented in Figure 14. The shape of the backscattered pulse is the same as that of the emitted pulse. A standard deployment of an SAR system is shown in Figure 15.

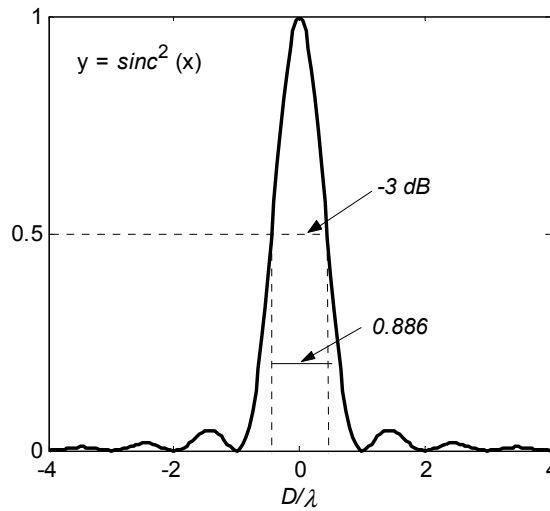


Figure 14: Graph of sinc^2 with argument in units of D/λ , where D is the width of the antenna and λ is the wavelength. Half power or $> -3\text{ dB}$ is emitted within the elevation or beam width angle range (see Figure 15) which is equal λ/D .

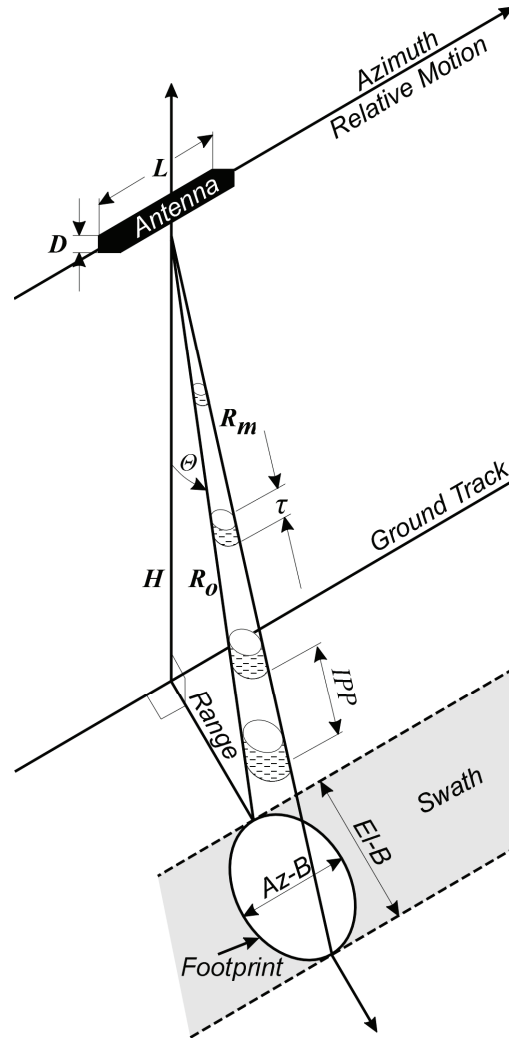


Figure 15: Right-hand SAR scanning configuration. $Az-B$ – Azimuth beam width = λ/L (rad), $El-B$ – Elevation beam width = λ/D (rad), IPP = Inter-pulse period, τ = Pulse duration, H = Nadir range, R_o = Minimum slant range, R_m = Maximum slant range, $L \times D$ = Dimensions of a rectangular antenna, λ = Wavelength, θ = Look angle. Source: Modified Figure 2 from (OLMSTEAD, 1993).

Range resolution in SAR can be controlled in two ways. The first method requires a very short pulse of very high energy to attain enough energy in the backscattered signal. Hence, the sampling process of the returned signal is performed for no longer than the duration of the emitted signal. The second method aims to achieve the same goal by hitting the target for longer but using much less power. For space borne radar systems the second method is preferred because of power budget considerations. The trade-off, however, is that the signal duration (τ) must be longer than the inter-pulse period (IPP). This means that received signals are overlapping. A signal processing method is available to digitally reconstruct individual returning pulses. This method is called Matched Filtering (*ibid*) and is based on the idea of comparing shapes of the returned and the emitted signal. The Matching Filter can be implemented as a cross-correlation function (CCF) of the emitted and received signals. The maximum value of CCF is attained for the time delay or lag between emitted and received signals. Once returned the pulse is associated with its origin and another signal processing step is performed. This is the integration of all the energy which ‘belongs’ to the returning signal. The final step in processing the range data is a windowing operation which is designed to ‘clean-up’ the shape of final signal. Most often Hamming windowing is performed.

A similar procedure must be performed to achieve high resolution in the azimuth direction. The azimuth beam width is a ratio between wavelengths versus antenna length - λ/L (Figure 15). For $\lambda = 0.056\text{m}$ and $L = 10\text{m}$ and range of 850km (ERS-1) the azimuth beam width is about 0.0056 radians or 0.3° , which translates to 4.7km on the ground. The motion of the radar sensor along the azimuth direction causes the illuminated area to continually change by just a tiny fraction of the illuminated area. In the case of ERS-1 it was just about 4m versus 4.7km of the azimuth beam width (illuminated area). At the same time, however, new pulses are emitted with a repetition frequency (PRF) of 1680Hz. Consequently,

thousands of samples of backscattered signals regarding any given point (within the azimuth beam width) are available for processing. The aim of the signal processing must also include attaining spatial association of the signal or associating a signal with a particular target point. The time for which the integration of samples is performed is called the coherent integration time.

The key role of the azimuth range data processing is due to the frequency change of the received signal, which is a consequence of the relative motion of the radar. This is the well known Doppler Effect. The frequency of the received signal can be calculated from:

$$f = f_0 - \frac{2v^2}{\lambda R} t, \quad (27)$$

where f_0 is the frequency of the emitted signal,
 v is the relative velocity of the radar versus the target, and
 t is the time delay.

4.4 Synthetic Aperture Radar Interferometry (InSAR)

Modelling the backscattered radar waves from the target was one of the most important research methods aiming to interpret the SAR data. The models developed were based on radiative transfer theory (RTT) (PICARD *et al.*, 2004) or distorted Born approximation (SARABANDI *et al.*, 2000; Picard *et al.*, 2004). However, the identification and application power of active remote sensing was greatly increased through SAR interferometry (BORGEAUD & WEGMÜLLER, 1996; WEGMÜLLER & WERNER, 1996).

The interference phenomenon, which involves a reference electromagnetic wave and a wave currently being investigated, has been known to physics since the nineteenth century. The qualitative explanation of the interference of optical waves is attributed to Thomas Young (BORN & WOLF, 1999). This interference became involved with active remote sensing through the invention known as the synthetic aperture radar interferometry or InSAR (GRAHAM, 1974). The theory of InSAR was already described in great detail by a few other authors (MADSEN *et al.*, 1993; RODRIGUEZ *et al.*, 1994; ROSEN *et al.*, 2000). In this section a brief overview of the fundamental elements of the InSAR technique is presented to introduce the terminology and notation. Some InSAR-based techniques are also briefly introduced.

4.4.1 Theoretical background

As with other instruments that use the interference phenomenon, each InSAR system is equipped with two receiving antennas, located at some distance (B) from each other, and a single transmitting antenna. The distance between the receiving antennas is referred to as the interferometric baseline (or just the baseline). Figure 16 shows the geometry of an InSAR system.

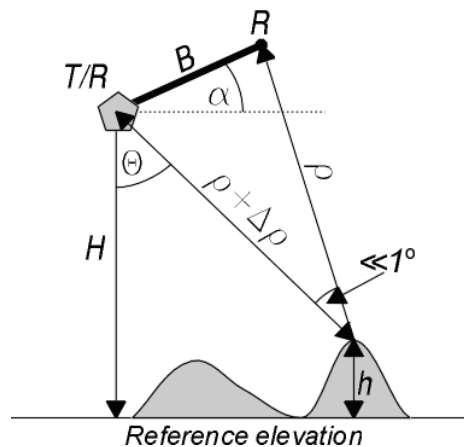


Figure 16: Principle of SAR interferometry. T/R and R are the Transmitting/Receiving and Receiving radar antenna. $\Delta\rho$ is the range difference between target and T/R or R antennas. α and Θ – are the roll and the look angle, respectively.

A single reading taken by InSAR produces two images of the same section of terrain, but different because taken from different antenna. An interferometric image is the average Hermitian of two complex signals from the same object. The following two quantities can be obtained from the complex correlation between two images. They are the coherence (γ) and the phase difference ($\Delta\rho$). Let us assume that g_1 and g_2 are the complex signals contained in images 1 and 2. Then the coherence can be expressed as follows (HEIN, 2004):

$$\gamma = \frac{E[g_1 g_2^*]}{\sqrt{E[|g_1|^2] E[|g_2|^2]}}, \quad (28)$$

where $E[\]$ indicates the ensemble averaging, but here it is understood as a spatial averaging, and $*$ denotes the conjugate complex.

In numerical solutions the coherence is estimated using an n -pixel by n -pixel window. The following formula can be used to calculate a topography-corrected estimate of the coherence (MARLIANI *et al.*, 2002):

$$\tilde{\gamma} = \frac{\left| \sum_{k=1}^n g_{1,k} g_{2,k} e^{-jv_k} \right|}{\sqrt{\sum_{k=1}^N |g_1|^2 \sum_{k=1}^N |g_2|^2}}, \quad (29)$$

where v_k is the phase shift between the k -th pixel and the corresponding pixel in the slave images caused by the local topography.

Coherence is influenced by many factors, including thermal noise, image mis-registration and wrong focusing parameters to name but a few, but the affects of these are relatively weak and may be neglected (FERRETTI *et al.*, 2001). The major factors creating distortion between the two coherent images (coherence = 1) are the spatial and temporal factors. The spatial factors include change due to different acquisition points in space, surface and volumetric scattering. The temporal factors include changes in dielectric and geometrical properties of the target, as a function of the time lapse between the acquisition of the two images. It is clear that instantaneous acquisition of both images prevents distortion from temporal factors.

The range difference ($\Delta\rho$) (see Figure 16) causes a phase difference (Φ) between the same signal received at the different antennas (T/R and R). The relationship between the range difference $\Delta\rho$ and phase difference (Φ) can be expressed in a simplified form as (MARLIANI *et al.*, 2002):

$$\Phi = k\Delta\rho, \quad (30)$$

where k is the wave number, see Equation (15).

In the case of the repeat-pass system, the right-hand side of Equation (28) must be multiplied by 2.

Using the InSAR system construction parameters, i.e. the roll angle - α and the baseline - B , one can calculate the look angle:

$$\Theta = \alpha + \arcsin\left(\frac{\rho^2 + B^2 - (\rho + \Delta\rho)^2}{2\rho B}\right), \quad (31)$$

The elevation of a target can be calculated from:

$$h = H - \rho \cos \Theta, \quad (32)$$

Equation (32) may also be written in the more elaborate form as follows (NI *et al.*, 2008):

$$z(y) = h - \rho \cos(\alpha - \arcsin(\sin(\alpha - \arccos(h/\rho))) + \frac{\lambda}{2\pi B}(\Delta\Phi_s - \Delta\Phi'_s)), \quad (32a)$$

Where h is the satellite height,
 ρ is the slant range from scatter to satellite,
 α is baseline angle,
 λ is wave-length,
 B is baseline length,
 $\Delta\Phi_s$ is the phase difference between the master and slave radar images of scatters, and
 $\Delta\Phi'_s$ is that of ground.

In summary, the following data processing steps are required to generate a DEM using the InSAR technique:

- The slave image must be co-registered with the master image. This procedure will produce the parameters of the best bilinear transformation, to be used for processing the slave image;
- The slave image must be re-sampled to match the pixels of the master image to produce the interferogram;
- The interferogram is unwrapped, that is, the 2π ambiguities in the phase measurements are removed;
- The elevation is calculated from the unwrapped phase using Equations (30) – (32) (DERAUW & MOXHET, 1996).

4.4.2 Limitations of InSAR method

The InSAR technique is very much a field of active research at the moment. Despite that it has already been successfully deployed in many areas of geoscience. The biggest advantage of the InSAR technique is its unprecedented accuracy combined with the ability to survey large areas. Its sensitivity is, however, also a source of limitations, since natural instabilities in the environment can trigger de-correlation (ZEBKER, 1992; ALBERGA, 2004). For example, in the case of the repeat-pass InSAR, vegetation moved by the wind (ASKNE *et al.*, 1997), moisture changes (RUDANT *et al.*, 1996), or even growing crops, can cause strong deterioration in coherence between the master and slave images, making it impossible to process the interferogram to extract a DEM. As experiments have many times proved, where the coherence drops below 0.4 – 0.5 an interferogram (or part of one) is usually useless for elevation extraction, because of the problem with unwrapping the interferogram. However, they may still be used as a data source for land cover classification (ASKNE & SMITH, 1996).

The InSAR technique is inherently associated with effects such as layover and shadows. A strategy to mitigate these, such as multi-look acquisition of data, must be implemented to minimize data voids. Despite this, the accuracy of the InSAR-derived elevations continues to be limited by the resolution cell dimensions or pixel size, and the slope of the terrain. This issue will be discussed later in this work.

A significant source of phase errors is our poor knowledge of the variable parameters of the ionosphere and troposphere, and their variability. This issue applies to repeat-pass InSAR systems, especially those using high orbits. But, even the tandem single-pass system, where the baseline is much longer than those of the SRTM mission (~60m), are affected by the atmospheric variability.

Depending on the wavelength of the InSAR system, the elevations obtained over vegetated terrain are, to various degrees, subject to elevation bias; see ROSEN *et al.*, (2000), for example. A P-band system produces a near bare earth elevation, while L- C- and X-band systems provide elevations that are burdened with a random but systematic bias. For those interested in DTM this is certainly a matter of concern. However, there are ways to tackle the issue, including dual frequency systems (P-band and X-band), which are described later. A space borne L-band InSAR coupled with LiDAR has also recently been proposed (DONNELLAN *et al.*, 2008).

Certain limitations of the InSAR technique are due specifically to the type of system (space borne vs. airborne). Table 6 summarizes characteristics of both systems.

Table 6: Comparison of space borne vs. airborne InSAR systems. Source: (ROSEN *et al.*, 2000)

| Characteristic | Space borne | Airborne |
|--------------------|------------------|------------------|
| Coverage | Global | Regional |
| Fine Resolution | Costly | Affordable |
| Repeat flexibility | Difficult | Natural |
| Track reparability | Difficult/Costly | Difficult/Costly |

| | | |
|----------------------------------|-----------------------|-------------|
| Motion compensation | Benign | Necessary |
| Atmospheric Propagation Effects: | | |
| - Two-Aperture | Benign | Benign |
| - Repeat Track | Problematic | Problematic |
| Ionospheric propagation effects | | |
| - Two-Aperture | Benign | N/A |
| - Repeat Track | Problematic | N/A |
| - Multi Frequency | Helpful | N/A |
| Frequency selection | Application dependent | |

One may conclude that both types of InSAR system have advantages and disadvantages. But both systems have a role to play in extending coverage, flexibility, availability, reparability and accuracy. There is no doubt that important environmental data acquisition needs will be served by airborne InSAR systems for years to come (ROSEN *et al.*, 2000).

4.5 Polarimetric SAR Interferometry (PolInSAR)

A solid theoretical introduction to polarimetric SAR interferometry can be found, for example in BOERNER, (2008). The identification power of the polarimetric approach is founded on the fact that objects on the ground possess different polarimetric signatures. Hence, the interferometric calculations based on a full polarimetric scattering matrix (HH, HV, VH, VV) may provide a much more comprehensive knowledge about the vertical structure of vegetation than single polarisation InSAR data would (CLOUDE & PAPATHANASSIOU, 1998).

The PolInSAR technique requires that the frequency used must penetrate the vegetation cover. This is because the scattering for HH polarisation tends to take place close to the ground as an effect of ground-trunk interaction. In contrast, the scattering for HV polarisation takes place within the crown cover (SRABANDI *et al.*, 1999). The difference between both heights (HH and HV) may give an estimate of tree height. Hence, the L-band is preferred. The lower frequency systems will create problems due to moisture in the soil. In turn, the higher frequency systems do not penetrate the vegetation cover as well as the L-band. Therefore, the information from all polarisation channels concerns vegetation at properties at the same height above the ground. Consequently, no estimate of the vegetation height can be produced.

A first experiment with the proposed PolInSAR technique was conducted using the L-band airborne repeat-pass system (PAPATHANASSIOU & CLOUDE, 2001). The results have demonstrated that in all four polarisation modes the backscattering contribution from the ground was present. This simply means that a straightforward inversion of the backscattered signal into vegetation height is not possible. A more advanced model-based approach is necessary (*ibid*). The random volume over ground scattering model was proposed in the reference (*ibid*). However, to solve the model for the forest height, estimation of additional parameters must be performed. This can be achieved by deployment of the multibaseline systems, but not via a multifrequency approach (*ibid*).

Another disadvantage of the PolInSAR technique is that it requires collection of full polarimetric data (PAPATHANASSIOU & CLOUDE, 2001).

The PolInSAR technique is an active research area. Current progress in applications of the L-band PolInSAR for forest biomass retrieval was presented in (METTE *et al.*, 2005; METTE 2008). PAPATHANASSION *et al.*, (2001) attempted to use the multibaseline PolInSAR approach to estimate the vegetation parameters including forest height. Still more research and development in this field are necessary and might be expected.

4.6 Differential SAR Interferometry (DInSAR)

This InSAR technique was first described by GABRIEL *et al.*, (1989). DInSAR is used to detect changes in the elevation of terrain to within a millimetre. The method is well suited to detecting changes of topography caused by tectonic movements, rapid erosion processes, mining operations and associated land deformation (GE *et al.*, 2004), and similar. Obviously, a repeat-pass with a sufficiently large time-lag between data acquisitions is required to capture the changes. It must be noted that, these changes may also be due to variations in the optical path. (DERAUW & MOXHET, 1996).

A repeat-pass interferogram contains fringes, due to the topography and the investigated small changes in topography. The DInSAR provides a way to separate the topography fringes from those caused by small topographical changes. The

topography fringes can be produced from an additional slave image, acquired soon after the reference image. A minimum of three images are therefore required: a master image; a slave image captured before the change; and another slave image taken after the change event. Two interferograms are generated, i.e. first-second image and second-third image. The first interferogram will contain the topography only information, and the second will contain the topography and the change information.

An existing DEM can be used to generate topography fringes. However, a proper quality DEM may not be available.

A strategy to use four radar images to separate the small change fringes was presented by DERAUW & MOXHET, (1996). The authors noted that “*it is easier to find two coherent pairs than one coherent triplet*”.

4.7 Permanent Scatterers SAR Interferometry (PSInSAR)

The permanent scatterers InSAR (PSInSAR™) method uses objects as a source of strong and temporarily stable backscattered radar signals. PSInSAR is therefore suitable for repeat-pass interferometry because there must be a sufficient time lapse between the master and slave images.

Permanent scatterers are almost always present in radar imagery. They form a natural discrete representation of the scene. This InSAR application is suitable for production of a sub-metre accuracy of DEM and sub-centimetre displacement of natural or man-made structures (FERRETTI *et al.*, 2001). The PSInSAR method is not suitable for vegetated areas, where there is generally a lack of permanent scatterers. It may be speculated, however, that this situation will gradually change with the introduction of much higher spatial resolution space borne radar systems, such as the X-band TerraSAR, which offers up to 1m by 1m pixel definition in SpotLight mode. This is because the probability of encountering small permanent scatterers in a high resolution image is much higher than finding large ones. Also, the L-band systems, such as the Japanese PALSAR, which penetrates vegetation cover well, can “produce” many more permanent scatterers than the lower frequency band systems.

The method was patented in 1999 by the authors of the paper (*ibid*). The patent is registered with the European Patent Office as “Process for Radar Measurements of the Movement of City Area and Landsliding Zones”, Patent number: EP 1183 551 B1 (<http://www.treuropa.com/>).

4.8 Other InSAR solutions

The InSAR technique possesses certain limitations, as discussed in the previous section. A few strategies have been proposed to tackle these restrictions and eliminate or reduce the degree of error. One such technique, discussed above, is PolInSAR. Other methods are based on: 1) Performing multitemporal InSAR observations, 2) Using the multibaseline technique (LI & GOLDSTEIN, 1990), and 3) Performing multi-frequency InSAR observations. The general idea is to get as much independent data as possible, allowing for redundant determination of the elevation of the target, within a single data acquisition act concerning a given target.

5. InSAR DATASETS

Chapter 4 introduced synthetic aperture radar interferometry and provided the basic concepts and terms used in InSAR technology. Chapter 5 offers an overview of InSAR products.

An InSAR dataset or elevation data product is the final outcome of the interferometry SAR data processing procedure. An InSAR dataset can take a few different forms. One generic example is a 3-tuple or triple (X, Y, Z). The components of a triple are sets of coordinates representing an *object*. A datum for the components will usually be somehow related to the earth. An object represented with an InSAR dataset must have a set of properties in order to be able to interact with radar signals. These properties include a) geometric properties (size and orientation); b) dielectric properties, and c) an appropriate level of stability of both its geometric and dielectric properties during the period of InSAR data acquisition. Radar wavelength is a deciding factor for the representation of the required range of these properties.

InSAR datasets are referred to as digital terrain models (DTM), digital elevation models (DEM), or digital surface models (DSM). However, in some cases the Shuttle Radar Topography Mission (SRTM) dataset is referred to as an “data product” (<http://www2.jpl.nasa.gov/srtm/dataprod.htm>). This may be because the InSAR-derived elevation of vegetated areas does not represent the elevation of any fixed point on any physical surface, but instead represents an integrated elevation product of many scatterers located within a volume of vegetation. Hence, InSAR elevation data products can describe the hypothetical surface as a “distributed surface” or a “very rough” surface.

5.1 Classification of InSAR datasets

Since there are several methods for developing InSAR elevation data products, a classification system of InSAR elevation data products is useful. The first classification criterion of InSAR elevation data products is the location of the radar system used to acquire the data. Possible options include:

- a. Airborne: when the radar system is installed on board of an aircraft.
- b. Spaceborne: when the radar system is located beyond the earth’s atmosphere.
- c. Terrestrial systems: when the radar is located on a ground station. Such systems have limited topographic applications. They can be used for capture of displacement of engineering or other type of objects (LEVA *et al.*, 2003; NICO *et al.*, 2005; and PIERACCINI *et al.*, 2001).

The second criterion for classification of InSAR elevation data products is the method by which and the time when the slave image is acquired. Possible options are:

- a. Fixed base systems with both master and slave images are recorded at the same time through antennas located at the separate ends of a physical base.
- b. Images are recorded at different times. An interferometric base is constituted by the difference in position of the same antenna. Those systems are referred to as repeat-pass systems.
- c. Images are recorded at the same time by two systems separated in space. A base is the distance between antennas on both systems. This solution is referred to as a tandem configuration or tandem flight. For this method to work, the interferometric base must be known with a very high precision and only spaceborne solutions are possible because of lack of high frequency disturbing factors (wind, control of an aircraft, etc.).
- d. Other options, such as multiple image InSAR (DERAUW & MOXHET, 1996).

The third criterion is the wavelength of the radar system. Possible options include:

- a. VHF (~7.86m wavelength): These systems penetrate vegetation cover and are used to detect military hardware (HYDE *et al.*, 2007).
- b. UHF (~0.88m wavelength): These ultra-high frequency systems are able to penetrate vegetation cover and are used in conjunction with VHF in SAR configuration mainly in military applications (HYDE *et al.*, 2007).
- c. P-band (~0.86m wavelength): These systems are able to penetrate the vegetation cover and, depending on the moisture levels, the uppermost layers of soil.
- d. L-band (~0.2m wavelength): These systems are able to penetrate vegetation cover and expose “bare” earth.
- e. C-band (~0.05m wavelength): These systems are able to partially penetrate vegetation cover and are sensitive to the type of vegetation.

- f. X-band ($\sim 0.03\text{m}$ wavelength): These systems are not thought to penetrate vegetation cover; however there is some evidence that they do so (REINARTZ *et al.*, 2005).
- g. Multiband systems: These systems consist of two or more radars operating at different frequencies. They may, in addition to the radar system, include a non-imagery device such as a laser ranging device.

The fourth criterion is the polarization mode utilized by the system:

- a. HH: The transmitting antenna has horizontal polarization and the receiving antenna has horizontal polarization.
- b. VV: The transmitting antenna has vertical polarization and the receiving antenna has vertical polarization.
- c. HV: The transmitting antenna has horizontal polarization and the receiving antenna has vertical polarization.
- d. VH: The transmitting antenna has vertical polarization and the receiving antenna has horizontal polarization.

The fifth criterion is the number of data takes used to derive the elevation for a given pixel:

- a. Single-look systems: when the elevation is derived from a single pair of images.
- b. Multi-look systems: when the elevation is a mean value of more than one pair of images.
- c. Other systems: when the elevation is adjusted by applying various error mitigation strategies, such as vegetation bias removal, etc.

The classification of all categories of InSAR data will be discussed in the remainder of the chapter.

5.2 Error Budget of InSAR Datasets

The accuracy of InSAR is affected by several sources of error. These errors distort the phase shift, which is a fundamental piece of data for elevation extraction. They include thermal noise, image mis-registration and erroneous focusing parameters (BAMLER & JUST, 1993). Another error source is the atmospheric inhomogeneity referred to as an atmospheric phase screen (APS) and depending on the random distribution of water vapour in the atmosphere, which can only be roughly estimated.

Assessment of the level of expected errors is a critical step in designing an InSAR system. A proper error analysis is carried out by careful study of all error sources which potentially contribute to the total error budget of a dataset. Typically, a ‘worst case’ scenario is assumed. Geometrical considerations of the InSAR method lead to the following expression of the standard deviation of the height error σ_h (LI & GOLDSTEIN, 1990):

$$\sigma_h = \frac{\lambda \rho}{2\pi B} \frac{\sin \Theta_s}{\cos(\alpha - \Theta_s)} \sigma_\phi \quad (33)$$

where λ denotes the wavelength (C-band - 5.6cm, X-band – 3.1cm),
 ρ is the path length difference between ground and emitting and receiving antennas,
 Θ_s is the incidence angle,
 α is the angle between horizon and the baseline (45°),
 σ_ϕ is the standard deviation of the phase noise, and
 B is the baseline length (60m).

This standard deviation of height error is accompanied by instrumentation errors. An overview of error sources of the SRTM elevation data product is presented in Table 7. The Random Phase Error (13m height error) and the Baseline Angle Error (9m height error) are by far the highest contributors to the SRTM system error.

The error sources discussed in Table 2 are associated with radar systems only and they can be collectively described as “instrumental errors.” In addition to instrumental errors, there are errors caused by other factors including radiometric inhomogeneity of target, variability of the refractive index along the propagation path of radar signals in the troposphere, and more. Some of these errors can be mitigated using a dual frequency instrument, e.g. scene contrast (GATELLI *et al.*, 1994), and modelling of index of refraction of the troposphere. A comprehensive analysis of the error budget of

airborne interferometric SAR's datasets is presented by RODRÍGUEZ and colleagues (1994). To some extent, all errors which are external to the instrument can be mitigated during the data processing stage.

Table 7: SRTM Height Error Budget. The first column (Level 0) contains the maximum allowable height error and subsequent columns contain contributing errors shown as a hierarchy from left to right. Expected errors are in parentheses. Estimated height error from non-metric terms (arc-seconds) are in braces {}. The Absolute Descending Pass Error has symmetrical components to the Absolute Ascending Pass Error and therefore is not presented here for clarity. Source: Modified Figure 4 (DUREN *et al.*, 1998).

| Level 0 | Level 1 | Level 2 | Level 3 | Level 4 |
|--|--|-------------------------------------|---|---|
| Absolute Height Error (1.6σ) 16m (12.6m) | Misregistration Error 2m (2m) | | | |
| | Absolute Descending Pass Error 22.6m (17.7m) | | | |
| | Absolute Ascending Pass Error 22.6m (17.7m) | Absolute Bias Error 3.4m (2.7m) | Reference Height Uncertainty 1m | Random Component of Bias Measurements Number of independent Bias Measurements |
| | | | 22.3m/√(50) (17.5m) | |
| | | 10 day Relative Error 22.3m (17.5m) | Baseline Length 3mm (1.9mm) ... {2.5m height error} | Baseline length/Angle Errors are contributed by the following factors: System margin 1mm, Range Finder Error 2mm (1.3mm), Mech Centroid Y Error 0.7mm (0.7mm), Phase Centre Y Error 1mm (1mm), Mech Centroid Z Axis Error 0.4mm (0.4mm), Phase Centre Z Axis Error 1mm (1mm), ATT Pitch Error 120" (82"), ATT Yaw Error 120" (54") |
| | | | Caltone Phase 8° (6.9°) ... {7m height error} | |
| | | | Radar Range Error 1.6m (0.8m) | |
| | | | Platform Position 1m (0.9m) | |
| | | | Random Phase Error 13.6° ... {13m height error} | |
| | | | Baseline Angle 9" (5.2") ... {9m height error} | |
| | | | Other Misc. Error Sources 0.8m (0.8m) | |

One of the error sources which are intrinsic to the InSAR method is the vegetation bias and volume decorrelation error (DAMMERT, 1996, HAGBERG & ULANDER, 1993, HAGBERG *et al.*, 1995).

This error source is a fundamental phenomenon on which this report is based and the vegetation bias of InSAR datasets is comprehensively discussed in forthcoming sections of this work. Another intrinsic error source not only in InSAR datasets, but also in all discrete-types of topography models, is the target- induced error source (BECEK, 2008b).

Discrete representation of a surface is associated with an error. The magnitude of the error depends on the 'roughness' of the surface and the number of discrete elevations used to represent that surface. Target-induced error is an error caused by rounding-off or quantization of elevation. These operations correspond to modelling of the terrain using contour lines with a given interval, e.g. 1m, 5m, 10m, etc., and obviously higher intervals cause larger errors. The error can be estimated using the following equation (SMITH, 2007; GRAY & DAVISSON, 2003):

$$\sigma^2 = \int_{-q/2}^{q/2} x^2 p(x) dx, \quad (34)$$

where x is an error caused by quantization ($x = \text{true elevation} - \text{round-off elevation}$),
 σ^2 is the variance of error x ,
 q is the level of quantization, and
 $p(x)$ the probability density function of the error x .

Assuming uniform distribution of the error on $[-q/2, q/2]$, i.e., $p(x) = 1/q$, the solution of the integral (34) is:

$$\sigma_q^2 = q^2 / 12, \quad (35)$$

For example, assuming a quantization level (contour line interval) of 1m, the variance of the error is $\sigma_q^2 = 0.083 \text{ m}^2$, which corresponds to an RMS error of $\pm 0.29 \text{ m}$, and that is about 30% of the contour interval.

This ‘vertical’ round-off is related to ‘horizontal’ sampling of a surface by the slope of that surface. Hence, the target-induced error caused by horizontal spacing can be calculated using the following expression (BECEK, 2008b):

$$\sigma_T^2 = q^2 \tan^2(s) / 12, \quad (36)$$

where σ_d^2 is an error caused by the horizontal spacing of spot elevations or pixel size,
 s is the slope of terrain, and
 q is the distance between samples or pixel size.

Figure 17 shows a graphical representation of Equation (36). From Figure 17, one can conclude that target-induced error is an important component of any DTM. The amount of error is dependent on pixel size and slope of terrain.

In summary, the total elevation error of an InSAR dataset can be expressed as a sum of at least three terms (BECEK, 2008b):

$$\sigma_e^2 = \sigma_I^2 + \sigma_T^2 + \sigma_V^2 + \sigma_R^2, \quad (37)$$

where σ_*^2 is a square of the InSAR elevation error; and
 (*) is one of the following: (*I*) instrumental, (*T*) target-induced, (*V*) vegetation, or (*R*) residual component.

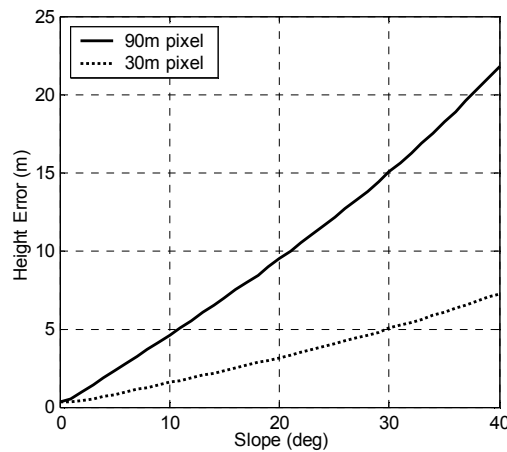


Figure 17: An RMS error caused by discrete representation of a surface. The magnitude of the error depends on the magnitude of slope within a DTM pixel. 30m and 90m pixel sizes were chosen because an SRTM elevation data product is available in those two versions. Source: (BECEK, 2008b).

The residual error component, σ_R^2 , can be any other error source, such as misregistration or other sources which have not yet been identified (VAN NIEL *et al.*, 2007; BECEK, 2008b).

5.3 Accuracy Assessment of InSAR Datasets

In addition to theoretical modelling of error sources, a series of practical experiments with a dataset are necessary and carried out to verify theoretical findings. In the case of an InSAR dataset a reference dataset of higher accuracy is required. The task may be much more difficult and expensive if a global InSAR dataset is to be verified. Reference

datasets used for the verification of SRTM are presented below. Also, an ultimate method for the accuracy assessment developed by BECEK, (2008b) is presented.

Considering the almost global coverage, the SRTM dataset had to be verified at many different locations around the world. Because of the lack of suitable quality datasets to be used as a reference, JPL used a very extensive ground-truthing program (RODRÍGUEZ *et al.*, 2003). Verification datasets include:

Kinematic Global Positioning System (KGPS) transects: The KGPS data were collected while driving vehicles equipped with GPS receivers. Estimated accuracy of elevation was about 0.5m. Nearly 9.4 million samples were taken on six continents. During the data validation process, all sample points within forested areas or where other large discrepancies were present were removed. Then the GPS elevations within a SRTM pixel were averaged and the difference of SRTM minus GPS elevation was calculated.

The Digital Terrain Elevation Data (DTED) Level 2 cells: A set of 42 one-degree cells with similar (or better) accuracy and with a similar resolution as SRTM were especially produced for the purpose of verification. Their locations were randomly selected around the world. The level of DTED indicates spatial resolution of a DEM. Level 0 refers to 30 arc-seconds, level 1 refers to three arc-seconds, and level 2 refers to one arc-second pixel (latitude).

Height patches: Similar to the DTED Level 2 cells, but with less restrictive quality requirements. A set of 141 patches were randomly selected and prepared for verification. Some of them were located in some extremely rough terrain.

Ocean Control Points (CPs): The sea surface up to 90km from the coast was used as a reference dataset because the model of elevation of the sea surface is known to a very high accuracy (due to tidal predictions plus a model of a geoid).

GeoSAR DEM data: An experimental airborne GeoSAR X-band DEM over US territory was also available for verification. The dataset was developed by averaging several datatakes and upsampled to the resolution of SRTM (30m). These operations reduced the high frequency noise of DEM. The absolute accuracy of DEM was about 2.5m. The size of the test area was about 42km by 36km.

Other GCPs: These points were located on land. The total number of GCPs was about 87,000. The use of this dataset for verification was biased by the fact that the points were mostly located in geographic areas with dense cloud cover.

While it was difficult to estimate the costs involved in the verification of SRTM elevation data product, it is not hard to estimate the costs involved in this huge and challenging operation in terms of logistic and man/hours. See the Acknowledgements section of the report for more information (*ibid*).

The report (*ibid*) provides a model for the total error of SRTM which is:

$$\delta h(x) = L(x) + \sigma(x)n(x), \quad (38)$$

where $L(x)$ is a low frequency error being a residual of the uncompensated roll of the shuttle,
 $n(x)$ is a white noise error with expected value = 0, and variance = 1, and
 $\sigma(x)$ is a high frequency spatially dependant error.

A much cheaper solution with a simple method to assess the accuracy of digital elevation data products was proposed by BECEK (2008b). This proposed approach assumes that the variation of the total random error of elevation for a pixel is a sum of three statistically independent components which can be written in the form of Equation (37), except that the systematic ‘vegetation’ term is excluded.

In order to estimate the instrumental error which represents a total contribution of all the platform-related error sources and data processing procedures, runways of airports around the world will be used as a test bed. The runways appear to fulfil all the requirements of a good test bed because:

- a) they are randomly distributed around the world,
- b) they are almost horizontal (slope <1°),
- c) the surface is homogeneous (usually concrete or asphalt),
- d) length of runway varies from 1km to 4km, and

- e) runway elevation data and other parameters are in the public domain.

A project aimed at establishing a Global Elevation Data Testing Facility (GEDTF) is currently underway at the University of Brunei Darussalam. It is funded by the Ministry of Education of Brunei Darussalam. The GEDTF will permit assessment of the accuracy of elevation data products such as SRTM or ASTER G-DEM (HAYAKAWA *et al.*, 2008) or similar global experiments.

The second error term in Equation (37) can be estimated using Equation (36). Estimates of the necessary slope data can be calculated from the DEM being investigated.

The fourth term in Equation (37), residual errors, does not presently have any quantitative model. There are some qualitative observations, however, which make it likely that this error is caused by proximity of large metallic objects. Further investigations of this error term are underway. Obviously, this error term is valid for the InSAR derived elevations. Some other characteristics of the term can be expected if elevations were derived using photogrammetric methods.

In summary, it should be noted that Equation (37) exposes a very important fact about the accuracy of digital elevation data products: the slope of the surface and the instrumental errors control the accuracy of the elevation model. This is valid in situations when a surface is represented using a regular grid (the same pixel size). Although not well suited for raster surface representation systems, a variable density cloud of points would solve this surface inhomogeneity problem.

In many respects, SRTM holds a unique position among Earth remote sensing datasets and is a central data source for the investigations reported in this work. Hence, a summary of accuracy investigations provided by JPL and conducted by the author is shown in detail in Table 8.

Table 8: Results of the accuracy assessments of SRTM datasets using various reference elevation datasets (average difference \pm one standard deviation expressed in metres). Sources: RODRÍGUEZ *et al.*, 2003; the last entry, “Runways,” is taken from BECEK, 2008b.

| Method | Africa | Australia | Eurasia | N. America | S.America |
|--------------|---------------|---------------|----------------|----------------|----------------|
| KGPS | 1.3 ± 3.8 | 1.8 ± 3.5 | -0.7 ± 3.7 | 0.1 ± 4.0 | 1.7 ± 4.1 |
| DTED Level 2 | 2.4 ± 4.7 | N/A | -0.1 ± 4.5 | 1.4 ± 4.0 | 11.4 ± 4.6 |
| Height Patch | 4.1 ± 4.3 | 2.1 ± 3.4 | -1.8 ± 6.0 | -0.6 ± 4.9 | N/A |
| Ocean CPs | 0.4 ± 4.8 | 0.1 ± 4.4 | 0.2 ± 5.0 | -0.2 ± 4.6 | 0.0 ± 5.1 |
| Land GCPs | 1.0 ± 5.4 | 0.7 ± 6.3 | 0.5 ± 6.1 | -0.8 ± 8.3 | -0.5 ± 9.6 |
| Runways | 0.5 ± 1.5 | 0.4 ± 1.4 | 0.8 ± 1.7 | 0.4 ± 1.9 | 1.1 ± 1.4 |

Results achieved by BECEK (2008b) are based on the investigations of 302 randomly selected runways on six continents.

The dramatic difference in the standard deviation between the last entry (Runways) and all the other entries is due to differences in the data models used, Equation (37) versus Equation (38). The problem with the model proposed by JPL [Equation (38)] is that it wrongly assumes an equal standard deviation for each pixel without considering the variability of slope across the landscape. Although the report mentioned that higher slopes cause bigger calculation errors, no attempt was made to model that factor (RODRÍGUEZ *et al.*, 2003). Consequently, the values of the standard deviations shown in Table 3 are much too high. This conclusion could have far reaching consequences for construction of the shuttle data acquisition system. For example, the extendable arm could be 50% shorter to obtain results within the limits of the SRTM mission.

Currently, the author and a team of collaborators are compiling a database of about 20,000 runways around the world. The data can be used by everyone for reference purposes for verification of the elevation datasets, for example. The project is known as the Global Elevation Data Testing Facility (GEDTF). It is funded by the Ministry of Development of the Brunei government.

Investigations on the accuracy of the SRTM data for various terrain forms and/or land cover were also conducted by several authors including BECEK (2006); BROWN *et al.* (2005); EINEDER (2003, 2005a, 2005b), and SMITH *et al.* (2003).

5.4 InSAR Data Acquisition Systems

There are few systems able to produce a digital elevation product using SAR Interferometry in the world today. A classification system for these is provided in Section 5.1. Some of the systems are commercial grade systems and others were/are experimental constructions or one-off programmes. An overview of what is currently available on the market is provided in this section. Also, some historical solutions and future projects are mentioned.

AeS-1 is an airborne InSAR system operating in the X- and P-bands. It was developed in 1996 by a German company, Aerosensing Radarsysteme GmbH. A single-pass X-band data acquisition is performed using a fixed baseline between 0.6m and 2.4m, which is selectable depending on the requirements of a particular project (low/high resolution projects). The repeat-pass P-band acquisition is performed using a baseline of about 25m. The absolute position of the system is determined using differential GPS (D-GPS) and the aircraft's inertial navigation system (INS) with an accuracy of about $\pm 3\text{cm}$. The accuracy tests of the X-band InSAR were conducted over various terrain types. The reported one- σ error was between $\pm 17\text{cm}$ and $\pm 25\text{cm}$. However, the accuracy assessments conducted over flat areas of the Wadden Sea showed results of about $\pm 4.3\text{cm}$ to $\pm 7.7\text{cm}$ (WIMMER *et al.*, 2000). Table 9 summarizes the main parameters of the AeS-1 system.

Table 9: Selected parameters of the AeS-1 InSAR airborne system. Source: MOREIRA *et al.* (2001).

| Parameter | X-band | P-band |
|-----------------------------|---------------------|--------------------|
| Frequency | 9.55GHz | 415MHz |
| Bandwidth | 400MHz | 70MHz |
| Polarization | VV | HH, VV, VH, HV |
| PRF | <16kHz | <7kHz |
| Antenna Beamwidth (azimuth) | 8° | 50° |
| Antenna Depression Angle | 48° | 50° |
| Operational Altitude | 500m – 11,000m | |
| Baseline length | 0.6m and 2.4m | 25m |
| Range/Azimuth Resolution | 0.5m/0.2m | 2.5m/0.7m |
| Elevation Resolution | $\geq 0.05\text{m}$ | $\geq 1.0\text{m}$ |

DOSAR - the multipolarimetric/interferometric and multifrequency airborne SAR was developed in the late 1980's as an experimental military system (HOFFMANN & FISCHER, 2002). The basic technical characteristics of the original DOSAR system are shown in Table 10.

Table 10: Basic technical parameters of the DOSAR system (HOFFMANN & FISCHER, 2002).

| Parameter | Range |
|----------------------------|---|
| Frequency and polarisation | S-band : 3.04 GHz (VV, VH, HH, HV) C-band : 5.30 GHz (VV, VH, HH, HV) X-band : 9.50 GHz (VV, VH, HH, HV) Ka-band : 35.0 GHz (VV) |
| Bandwidth | 50 MHz, 100 MHz, 200 MHz, 400 MHz |
| Pulse repetition frequency | 750 Hz, 1.5 kHz, 3.0 kHz, 6.0 kHz |
| Pulse duration | 1 μs – 12.8 μs |
| Swath width (Ground) | 300 m ... 9 km |
| Flight level | 100 m AGL ... 4000 m MSL |
| Incidence angle | 17 ° ... 89° (S-, X-band) 45 ° ... 89° (C-, Ka-band) |
| Beam width | Elevation : 20° (all bands) Azimuth : 18° (S), 10° (C), 5° (X), 3° (Ka) |
| Operational modes | Polarimetric (S-, C-, X- and Ka-band) Interferometric across-track (C- and X-band) Interferometric along-track (C-band on DO228) |
| Motion compensation | integrated INS combined with DGPS |

Since that time DOSAR has been upgraded several times. The new features include along- and cross-track single-pass interferometry capability, scan and spot mode, new frequency bands (X- and S-band), higher resolutions ($< 0.5\text{ m}$) and full polarimetry in all bands except the Ka-band. Also, the bandwidth has been increased to 600MHz, while the ground swath width now reaches up to 20km depending on the flight geometry.

The system was installed on a small Dornier DO228 aircraft, but it can also be installed on any other aircraft.

Since 1989 DOSAR has been flown on many missions in different configurations, for different tasks such as agriculture and forestry classification, DEM generation, in several countries around the world including Thailand, Switzerland, Indonesia and Germany. An interferometric configuration of the system includes the X-band, single (HH) polarisation mode with a fixed incidence angle of 23°. The range, swath width and pixel size is 10 km, 2 km and 1.5 m by 1.5 m, respectively (*ibid*).

A test flight which was carried out in low turbulence conditions has identified problems with the motion stability of the system. The precision obtained with a DTM derived using the DOSAR system for large and homogeneous areas was better than $\pm 2\text{m}$ (GOBLIRSCH *et al.*, 1995).

GeoSAR is an airborne dual-frequency (X- and P-Band), multi-polarization SAR, and single-pass system designed to collect data for interferometry processing towards extraction topography. It is referred to as the IFSAR system. It is made of four antennas located on both sides of a Gulfstream- II aircraft near the fuselage (X-Band) and at the tips of the wings (P-Band). Figure 18 shows the original configuration of the GeoSAR system. This configuration allows simultaneous collection of both data frequencies in two 10 km swaths on both sides of the aircraft, which eliminates non-volumetric de-correlation, image co-registration, etc. (HAARBRINK, 2003). The system can also be operated on a circular collect mode, which allows data acquisition from all aspects and increases the resolution of the radar imagery. In addition, the mosaicing of the imagery means every pixel of the DEM is viewed up to eight times. This redundancy is exploited during data processing. The system was developed in the late 1990s with the participation of the California Department of Conservation, Calgis Inc., and NASA's Jet Propulsion Laboratory (<http://southport.jpl.nasa.gov/html/projects/geosar/geosar.html>). The original design was later enhanced by a co-mounted LIDAR (1064nm) system to increase the performance of GeoSAR. During data acquisition, a nadir profile (LIDAR) is captured consisting of three returns. This allows the vertical structure of vegetation to be studied and supplies valuable high precision ground control data.

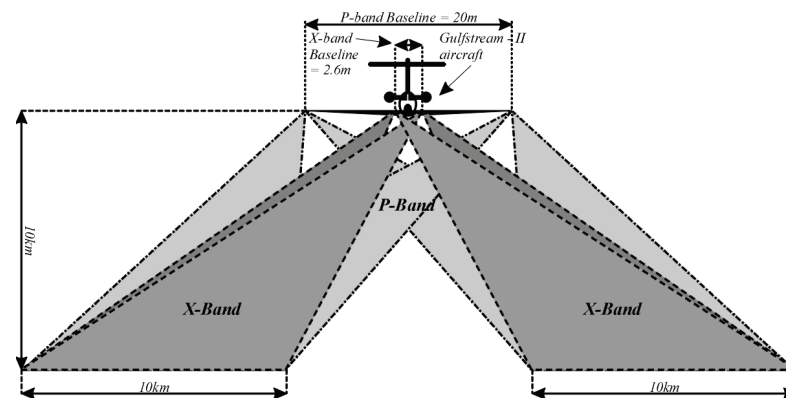


Figure 18: GeoSAR system configuration. Source: Modified Figure 1 (HAARBRINK, 2003).

Tests have shown that the vertical accuracy of LIDAR at a 10–12km altitude is about $\pm 0.26\text{m}$. Cloud cover presents a potential problem in deploying LIDAR at this altitude because LIDAR ($\lambda = 1064\text{nm}$) does not penetrate the cloud cover (HAARBRINK, 2003).

The X-Band delivers the “near the tops of trees” elevations, whereas P-Band elevations are “a near bare-earth” (*ibid*). GeoSAR covers about 288 km^2 per minute. Potential applications of the system include mapping topography, land cover, watershed delineation, DTM, DSM, and DEM along with contours and spot height production at a scale of 1:25,000–1:50,000. Extensive accuracy tests of X/P-band InSAR are reported (NORHEIM *et al.*, 2002). An example of deployment of the GeoSAR system is the mapping of oil pipes in Columbia (ALLEN & REIS, 2006). Currently GeoSAR is operated by Furgo EarthData, Inc (www.earthdata.com). Some basic parameters of the GeoSAR systems are shown in Table 4.

The author attempted to acquire test data from Furgo EarthData to verify their claim that the X-Band data represent near the tops of trees. Unfortunately, these requests remained unanswered.

Table 11: Basic technical parameters of the GeoSAR system. Source: Furgo Earthdata, Inc. (www.earthdata.com) and <http://southport.jpl.nasa.gov/html/projects/geosar/geosar.html>

| Parameter | X-Band | P-Band |
|----------------------|------------------|-------------------|
| DEM height accuracy/ | 2 m – 5 m (RMSE) | 5 m - 10 m (RMSE) |

| spatial resolution | 2.5 m - 3 m spatial resolution | 5 m spatial resolution |
|--------------------------------|--------------------------------|------------------------|
| Ground swath width | 20 km | 20 km |
| Wavelength at center frequency | 0.03 m | 0.86 m |
| Bandwidth | 80/160 MHz | 80/160 MHz |
| Polarization | VV | HH & HV or VV & VH |
| Baseline length | 2.6 m | 20 m |

Table 12: Technical parameters of IFSAR system operated by Intermap Technologies. Source: IFSAR Mapping Technology (a brochure); www.intermap.com

| Parameter | Value |
|----------------------------|-----------------------------------|
| Typical Flight Altitude | 6 km – 9 km |
| Maximum Coverage Rate | ~ 4000km ² /hr |
| DEM Vertical Precision | ±1 m (RMSE) |
| DEM Horizontal Precision | ±2 m |
| Swath Width | 5 km – 9 km |
| Highest Spatial Resolution | 5 m |
| Costs | ~US\$25 – US\$30/ km ² |

Intermap Technologies Inc., a USA-based company, operates a single-frequency X-Band IFSAR system. Its basic technical parameters are shown in Table 5. The company offers several 3-D products, including contours (2m and 5m), DSM, and DTM. DTM is achieved by an interactive process involving an operator who estimates the thickness of vegetation from DSM (John H. Michael, Senior Project Manager, personal communication). The thickness of the vegetation is estimated by comparing elevation of vegetation-free area with elevation of vegetation near the edges of vegetation. Also, some sophisticated filtering techniques are used to remove the anthropogenic components located on the surface of the earth. The company's marketing strategy is to contrast the costs of a LiDAR survey (US\$150–250/km²) (www.earthdata.com) with the costs of their survey, which is approximately five to ten times cheaper. Sample data are available from the company's web site (www.intermap.com).

TOPSAR. TOPSAR was one of the data acquisition modes within the Airborne Synthetic Aperture Radar (AIRSAR) program. AIRSAR commenced its operations in 1988 as a NASA/JPL mission. DC-8 aircraft were used as a vehicle accommodating a “fighting laboratory” (LOU *et al.*, 1996). TOPSAR collected single-pass interferometric data using the C- and L-bands. Interferometric data were collected in “ping-pong” mode, which means that each antenna was used for transmitting and receiving and this meant the baseline length was increased two-fold. Also, a “common-transmitter” mode was available, where antennas are used for transmitting or receiving radar pulses. The interferometric mode was available in the cross-track configuration (topographic applications) and in the along-track configuration (sensitivity to ocean waves monitoring). Data acquisition was done over areas requested by principal operators. Hence TOPSAR dataset coverage of the world is sparse. AIRSAR ceased to operate in 2004. A reach database of the digital elevation data products (C- and L-Band DEM) are available free of charge from <http://airsar.jpl.nasa.gov/>. Selected technical parameters of TOPSAT are shown in Table 6.

Table 13: Selected parameters of TOPSAR acquisition system. Source: <http://airsar.jpl.nasa.gov/>.

| | | |
|-------------------------|--|-----------|
| Frequencies | C- (5.31GHz, 5.7cm), L- (1.26GHz, 23cm), P- Band (0.45GHz, 0.67cm); Full polarization. | |
| Bandwidth | 20 MHz | 40/80 MHz |
| Operating Altitude | 8,000 m | |
| Data Swath Width | 15 km | 10 km |
| Baseline Length | 19.8 m at L-Band, 1.93 m at C-Band | |
| Slant Range Resolution | 6.7 m | 3.3 m |
| Spatial Resolution | 10 m | 5 m |
| DEM Vertical Precision: | | |
| C-Band, | 1m – 5m | 1m – 5m |
| L-Band | 2m – 10m | 2m – 10m |

E-SAR. The Experimental airborne SAR System of DLR (Deutsches Zentrum für Luft–und Raumfahrt) operates a Dornier DO 228 aircraft as a carrier for the SAR systems. The equipment includes the X-, C-, L-, and P-Bands. The systems are fully polarimetric. Single-pass interferometric mode is possible in the X-Band only. L- and P-Band interferometry is possible in repeat-pass situations. Due to the latest positional, flight control, and navigation equipment, the data is of very high positional precision. It is also possible to maintain the baseline in repeat-pass

situations shorter than 10m. Table 7 contains some basic parameters of the E-SAR system. Among many applications, E-SAR was deployed for marsh land and dyke measurements and analysis in Germany (MÜLLENHOFF, 2003).

Table 14: Selected parameters of E-SAR system. Source: www.dlr.de

| | |
|--------------------------------|--|
| Frequencies | X- (9.6GHz, 3.1 cm), C- (5.3GHz, 5.7cm), L- (1.3GHz, 23cm), P- Band (0.36GHz, 0.83cm); |
| Polarization | H and V |
| Bandwidth | 120 MHz(X,C), 100MHz(L), 60 or 25MHz(P) |
| Operating Altitude | 6,000 m |
| Data Swath Width | 3 or 5 km |
| Baseline Length | 19.8 m at L-Band, 1.93 m at C-Band |
| Slant Range Resolution | 2.3 m (HR), 4.5 m (MR) |
| Spatial Resolution | 5 m by 5m |
| DEM Vertical Precision: X-Band | $\pm 4m$ |

SAR 580. SAR 580 is a SAR system operated by Environment Canada since 1996 (HAWKINS *et al.*, 2002). The system is installed on board a Convair-580 aircraft. Operational altitude of the aircraft is typically 6500m. The SAR 580 operates in C- (5.3GHz, 5.66cm) and X-band (9.25GHz, 3.24cm) frequencies in a dual- or full-polarization mode. The cross-track and along-track interferometry is available in C-band only. The aircraft is equipped with a sophisticated SAR system integrated with both the navigation and flight control systems. The SAR 580 operates in three modes: nadir, narrow swath and wide swath. The width of the swath varies depending on the mode and can be 22km, 18km or 63km. The range/azimuth resolution for the nadir and narrow swath modes is 6m by 6m, and for the wide swath mode 20m by 10m.

EmiSAR. EmiSAR is a fully polarimetric C- (5.3GHz, 5.6cm) and L-band (1.25GHz, 24cm) SAR system operated by the Electromagnetics Institute of Denmark. EmiSAR is an experimental system and its main mission is to acquire data for the Danish Center for Remote Sensing (CHRISTENSEN *et al.*, 1998). The EmiSAR operates from a Gulfstream G-3 aircraft. The typical operational altitude is 12,000m. The system consists of a set of antennas allowing for cross-track and repeat track interferometric data takes. The radar is a 100MHz bandwidth system. It is equipped with an internal electronic loop that allows for absolute calibration of the instruments and this calibration is performed just before and just after the survey. The resolution in azimuth and slant range is 2.4m or 8m. The swath width is 12km or 24km. The positional data of the SAR system are supplied by the P-code GPS receiver. The data are then used by the SAR computer to emulate the output of an aircraft's Instrument Landing System (ILS). ILS then instructs the flight director computer to control the position of the aircraft to within a few meters of the selected path. Some test data for EmiSAR are available free of charge from <http://www.space.dtu.dk/>

Repeat-Pass InSAR systems. Repeat-Pass InSAR systems are generally less suitable for the production of digital elevation data products because of the difference between the master and slave images as a result of changes in the geometry of the scene. This effect is termed temporal decorrelation. Vegetation cover is particular prone to geometry change because of wind, for example (ASKNE *et al.*, 1997, ASKNE & SMITH, 1996). However, in the absence of vegetation cover or by masking low coherence area, temporal changes in the geometry of the slave image might provide the necessary information. For example, repeat-pass C-band InSAR is successfully used in detecting earth crust displacement after earthquakes, volcano activities, mining operations, movement of ice plates or movement of a glacier.

There are some situations, however, when repeat-pass InSAR datasets were successfully acquired. For example, an airborne X- and P-band system AeS-1 was deployed to produce DSM and DTM for the Brazilian Amazon rainforest area (MOREIRA *et al.*, 2001). The project may have been successfully completed because of the favourable calm weather typical of the tropics (no wind or very light wind). Another successful example of a repeat-pass project is VHF-band InSAR, also known as CARABAS (FRÖLIND & ULANDER, 2002). In this case, good results were attained because the longer waves are less sensitive to small changes caused by wind. Consequently, a coherent image pair can still be attained. A significant drawback of the CARABAS or VHF-band system may be the need to use a long baseline because of the usage of lower frequencies (*ibid*). Almost all the Repeat-Pass InSAR digital elevation data products were developed from SAR data including RADARSAT (GEUDTNER *et al.*, 1998), ERS-1, ERS-2 (BORGEAUD & WEGMUELLER, 1996), TerraSAR-X (KRAWCZYK *et al.*, 2008), and ENVISAT (MONTI GUARNIERI *et al.*, 2004).

InSAR-suitable radar images can also be acquired in a tandem configuration (RUFINO *et al.*, 1998). In tandem configuration, the baseline is the distance between the emitting and receiving antennas which are installed on separate platforms flying in a formation. This solution eliminates the temporal decorrelation and also increases the baseline length, which is a fundamental factor in controlling geometric error sources of InSAR-derived datasets (SOLAAS & GATELLI, 1996; TRINDER *et al.*, 2003; and WEGMÜLLER & WERNER, 1996). Though these examples of InSAR datasets extracted with tandem acquisition should be considered experimental, the future should soon bring a production-grade tandem mission involving a satellite already in orbit, TerraSAR-X, and a satellite to be launched in 2009. Both satellites will be orbiting in a constellation, hence the name TanDEM-X (FIEDLER *et al.*, 2006).

The existing InSAR data acquisition systems were designed for local, not global applications. They are mostly used for refining radar systems and/or for preparation of radar space missions. Current repeat-pass and tandem satellite solutions are also not suitable for global- or regional-scale InSAR projects. In addition to the technical complexity of such a project, one of the biggest obstacles to developing even a continental-scale InSAR dataset is the prohibitive high costs. This situation may improve significantly when the TanDEM-X mission commences operation.

The ASTER Global Digital Elevation Model (ASTER G-DEM), which is due to be released in mid 2009 (<http://www.ersdac.or.jp/GDEM/E/index.html>), should help make global- or regional-scale digital elevation datasets more easily available. ASTER G-DEM is a collaborative project between Japan's Ministry of Economy, Trade and Industry (METI) and NASA. The ASTER G-DEM will be produced from optical remote sensing data. For now, however, SRTM is the sole global elevation product available.

5.5 SRTM Digital Elevation Data Product

At the time this report was written, SRTM was a one-of-a-kind digital data elevation product and therefore deserves special attention. Some basic characteristics, perhaps in some cases less known, but still relevant to this research are presented in this section.

The eleven-day mission of the Space Shuttle Endeavour, which flew in February 2000, carried two separate sets of SAR instruments. They were the C-band (5.6cm) frequency instrument which was developed by NASA/JPL (RABUS *et al.*, 2003) and the X-band (3.1cm) instrument which was developed by the Italian Space Agency (ASI) and the Gerama Space Agency (DLR) (WERNER, 2001). These two elevation data products were developed by independent teams. In addition to the frequency, other major differences included the swath width (the C-band swath was 225km wide while the X-band swath was 50km wide) and the availability and resolution of the elevation data product.

Thanks to deployment of a ScanSAR mode, the C-band instrument allowed collection of sufficient data for the development of a continuous product (no gaps in the coverage). However, without the scan-mode facility, the data collected by the X-band instrument had gaps in coverage. Figure 19 shows SRTM.X coverage over the island of Borneo.

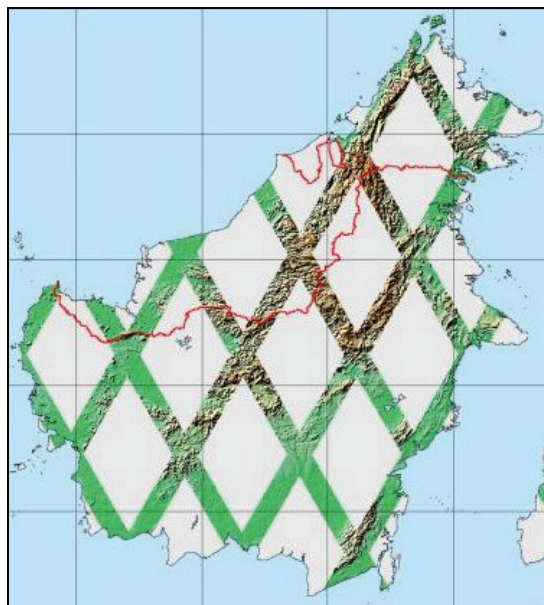


Figure 19: SRTM.X coverage over Borneo. Source: DLR

At the full resolution of the one arc-second or DTED 2 product, the C-band product is available over the contiguous US only. The remaining territories are only available at the three arc-second or DTED 1 resolution. The X-band product, however, is available at the one arc-second resolution only. A restrictive circumstance for the X-band product is available for purchase for 15 by 15 arc-minutes tiles (€1 per 1km²) (WERNER, 2001). There are some signs that the policy of distributing the C-band product in the DTED 2 version over the rest of the world may be relaxed at some point. Recently American authorities have made available the DTED 2 data over Australian test sites to Australian researchers (READ, 2008).

It is not widely known that the C-band product is available in two versions. These versions differ in the method used to arrive at the DTED 1. As far as the author knows, the JPL ftp site (<ftp://e0srp01u.ecs.nasa.gov/srtm>) is the only site where the averaged version of the C-band product is available. The less accurate product, which was achieved by subsampling or decimation, is available from any other server, including the USGS. In these investigations, the averaged version of the C-band product was exclusively used. Comparisons of averaged versus decimated products were studied by BECEK (2007). For the remainder of this document, SRTM.C/.X will be used when referring to the SRTM C-/X-band product.

6. BIOMASS REPRESENTATION IN InSAR DATASETS

The biomass that appears in many forms in the environment is a scattering medium for radar radiation. The propagation of signals and scattering from this medium can be described using two indicators: a) the extinction coefficient κ_e (Np/m – Neper/m), and b) the backscattering cross section σ_v (m²/m³) – often also called the volume backscattering coefficient (ULABY *et al.*, 1982). Traditional active remote sensing is actually based on identifying properties of land cover by observing the properties of the backscattered or returned “testing” signal from the land cover. Next, an assumption is made that a relationship between land cover and returning signal exists, which is then modelled using an empirically developed mathematical equation. A major drawback of this approach is that there is a certain level of biomass density above which no change in the backscatter coefficient is observed. This situation is referred to as saturation.

Another possibility to relate the backscattered radar waves from the biomass would be to utilise the InSAR interferometric phase which was linked to the tree height (BEAUDOIN *et al.*, 1996). Considering this relationship one can state that biomass is represented in InSAR datasets as an elevation bias. This suggests a relationship between the bias, some of the characteristics of the biomass, and properties of electromagnetic radiation used in the SAR survey. Hence, a general model of that dependency can be written as:

$$v = f(\text{Biomass}, EMW), \quad (39)$$

where v is the elevation bias,

Biomass and EMW denotes a set of parameters which characterise the biomass and electromagnetic waves, respectively.

Some of the parameters of the biomass and electromagnetic waves believed to be relevant to the magnitude of v will be studied. For biomass characterisation, these include:

- a) Biomass density;
- b) Vertical and horizontal biomass distribution;
- c) Biomass morphology;
- d) Biomass composition;

Parameters of electromagnetic waves will include:

- e) Frequency of electromagnetic waves;
- f) Incidence angle.

In this chapter, a review of the contribution of the above parameters to the elevation bias is presented. Also included is a description of several attempts at modelling the elevation bias that have been published to date. A term “biomass impenetrability” is introduced here, meaning the elevation bias caused by the presence of the biomass between ‘bald’ terrain and the antennas of an InSAR system. It is introduced to emphasize the origin of that elevation bias.

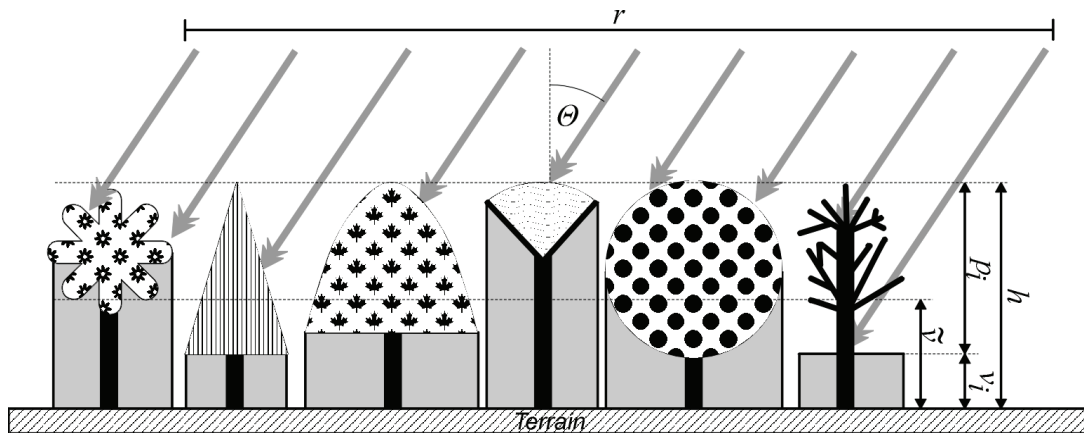


Figure 20: A model of an “impenetrable” forest. Here, h denotes the height of a line connecting top of the trees; r symbolises waves of an InSAR system illuminating the forest under an incidence angle of Θ . The vertical component of the path of the radar ray travelled within the forest is p_i . $v_i = h - p_i$ is the forest impenetrability. i indicates a resolution cell (pixel). \tilde{v} represents the mean impenetrability for a given number of resolution cells. The grey spaces underneath

the crowns indicate space which is not detectable by the InSAR system. In fact, the grey space extends into the crown to a certain distance which is not shown in the picture.

A cross-section of a forest illuminated by an InSAR system is shown in Figure 20. The impenetrability for an arbitrary selected resolution cell i , which is usually a pixel, is denoted as v_i . The mean impenetrability \tilde{v} is calculated from a selected number of resolution cells.

The term “impenetrability” was borrowed from the nineteenth-century description of Borneo forest: “*Where the ground was rising and dry, the forest could be easily crossed; but in the hollows the water accumulates, and the vegetation is so dense as to be quite impenetrable.*” (BECCARI, 1989, p.8.).

The chapter concludes with the presentation of the biomass model that will subsequently be investigated in the ensuing sections of the work.

6.1 Biomass Impenetrability

Biomass impenetrability has seldom been investigated as a distinct phenomenon. Reports found in the literature are generally aimed at determining the magnitude of this impenetrability. Attempts to correlate attributes of biomass with the impenetrability are restricted to a few reports that tend to characterise the biomass in qualitative terms. However, this is largely understandable because of the limited availability of reliable and quantitative reference data on biomass. Most available reports estimate the impenetrability by comparing an InSAR dataset with a reference DTM.

Simard and his team (SIMARD *et al.*, 2006) have used high resolution DTM and SRTM.C to produce a “landscape scale” map of mean tree height in mangrove forests in Everglades National Park. In order to estimate the corrections to tree heights, a LiDAR survey of a number of transects was performed. Developed regression equations were then used to estimate the ‘true’ tree heights from the SRTM.C readings. The regression equation is:

$$h_{SRTM.C} = 3.02 + 0.79 h_{LiDAR}, \quad (40)$$

where $h_{SRTM.C}$ and h_{LiDAR} are the SRTM.C and LiDAR elevation, respectively.

The RMSE calculated from the tests is on the order of ± 2.0 m. This finding allows calculation of the biomass impenetrability of SRTM.C for the mangrove forest at about 79%. This number is probably slightly too high because of the underestimation of tree heights by the LiDAR survey. According to several reports, the bias is between 0.5m (HYYPÄ & ENGDAHL, 2000). In this case, the impenetrability would be about 65 - 70%. However, for short mangroves, the relative impenetrability was about 47%. For similar reasons as above (the LiDAR bias), this number has to be reduced to about 30 - 35%. The average biomass density within the AOI was about 38.8Mg/ha and the area was 144,447ha.

A mangrove forest is composed of evergreen trees. The underlying water surface was most likely a factor that influenced the SRTM.C data. The average mangrove height was about 12.5m.

Hofton and his colleagues (HOFTON *et al.*, 2006) have used a medium-footprint (>10m diameter) laser altimeter system known as the NASA Laser Vegetation Imaging Sensor (LVIS) to validate behaviour of the SRTM.C over vegetated areas. LVIS-derived ground elevation, canopy top and vertical extent of vegetation were compared with the SRTM.C elevations. Experiments were performed over diverse test sites: Four test sites were located in the USA, and one in Costa Rica. The test sites were overflown by a LVIS system during leaf-on period. The data for the SRTM were collected during February (leaf-off period), except in Costa Rica, where vegetation is evergreen.

The average biomass impenetrability v for all test sites can be expressed using the following formula:

$$v = -1.718 + 0.422 h_L, \quad (41)$$

where h_L is the LVIS-derived tree height.

This means that the average relative impenetrability is 42%, which is the lowest value reported when compared to other authors’ results (>50%). The most probable justification for this situation is that the LVIS-derived tree height is underestimated. This is actually a well known effect that has been reported before (HARDING, 2005). Another contributing factor is the difference in the absence of leaves during the SRTM data acquisition (leaf-off period) versus LVIS data acquisition (leaf-on period). Results over the Costa Rica test site (~77% impenetrability) strengthen the former statement.

Carabajal and associates (CARABAJAL *et al.*, 2006) have used the ICESat Laser Altimetry and MODIS 500m resolution Vegetation Continuous Fields (VCF)–percentage tree cover layer (HANSEN *et al.*, 2003) to compare and correlate these with the SRTM.C dataset. The investigations were conducted over five regions in the Western US, the Amazon, Africa, Asia and Australia. The biomass impenetrability of SRTM.C was slightly more than 50% of the vegetation height for all of the tree cover classes. They have also pointed out that “*vegetation canopy height is a principle influence on the distance SRTM is biased above the ground surface*”. In other words, they did not provide any other factor that could be influencing the biomass impenetrability. It should be noted that the diameter of the ICESat laser altimeter footprint is around 65m.

WERNER, *et al.*, (2005) has calculated the biomass impenetrability for SRTM C- and X-band by comparing them with DTED 1 and 2, over a test site 720km by 720km in size located in California, USA. The site is only partially covered by forests. Hence, the biomass impenetrability, calculated as an average difference between SRTM data minus a reference dataset, is biased by areas free of vegetation. The average biomass impenetrability was 2.4 m and 3.2 m for the X- and C-bands, respectively.

Heipke and his team (HEIPKE *et al.*, 2002) carried out a comparative study of SRTM.X data over a 50 km by 50km test area located the south of Hanover. Three reference data sources including 700 benchmarks, a high resolution DTM (12.5m pixel) and also photogrammetrically derived DSM, were used. The test area was only partially covered by a deciduous forest (leaf-off conditions). The SRTM.X elevations over forests were below DSM by 4.12m. At the same time, they were 13.19m above the DTM. Hence, the approximate tree height was 17.31m (=4.12m + 13.19m). Therefore, the average biomass impenetrability for SRTM.X was around 76%.

Kellendorfer and his team (KELLENDORFER, *et al.*, 2004) have developed a linear relationship between averaged forest stand height and corresponding average biomass impenetrability, based on measurements performed over two test sites located in the Sierra Nevada near Quincy, California. The California site was heterogeneous mixed coniferous forests on highly variable terrain. The second site was located in southeastern Georgia near Jesup. It was made up of large homogeneous forest stands of slash pine (*Pinus elliotii*) plantations. The average biomass impenetrability for the California site was 88% and 57% for the Georgia site. The average forest height in the California site was 18.8m ±8.1m and 16.2m ±3.2m for the Georgia site.

An attempt to extract the height of the forest using ERS-1 repeat-pass interferometry was reported by (FLOURY, *et al.*, 1996). Utilizing the radiative transfer theory, the penetration depth was estimated by $1/e$. Hence, the biomass impenetrability was equal to $1 - 1/e = 0.63$ or 63% of the tree heights. Tests conducted in both coniferous and deciduous forests sites located in Landes, France, and tropical forests in South Sumatra, respectively, showed that the estimated tree height from interferometry *plus* the penetration depth underestimated the actual tree height. In other words, the biomass impenetrability was underestimated. (For more on penetration see DIDASCALOU *et al.*, 2000)

A comparative study of the relationship between SRTM.C and LiDAR DSM/DTM was conducted for a vegetated landscape located in the USA (HARDING, 2005). The DTED2 SRTM.C (30m pixel) was compared against a high resolution LIDAR-derived DSM/DTM. The reference dataset was observed during the leaf-off period in January/March, 2000. The SRTM.C elevation was 7.6 ± 14.3 m below the canopy top. The high value of the standard deviation is partially correlated with “canopy openness and roughness” (*ibid*). Although not directly stated, based on the results provided (*ibid*), the biomass impenetrability was 60-70%.

A study of the accuracy of the SRTM.C over test sites in Australia and Brunei Darussalam demonstrated that the biomass impenetrability varied according to land cover type (BECEK, 2006b). Tables 10 and 11 contain the biomass impenetrability for various types/densities of vegetation cover over the two test sites. These experiments did not provide an assessment of the relative biomass impenetrability, due to the lack of reliable tree canopy elevation data. However, based on the author’s knowledge of the test sites, including approximate tree heights, it can be confirmed that indeed the relative biomass impenetrability is about 60% of the tree heights.

Table 15: The Australian test site results. Source: (BECEK, 2006b), Table 1.

| Land Cover Type | Diff. & STD (m) |
|---|-----------------|
| Clear land (no trees or bush present) | 2.9 ± 2.6 |
| Scattered (individual trees or group of trees were present) | 14.6 ± 5.7 |
| Heavy (mainly tall trees with shrubs on lower levels) | 13.2 ± 7.9 |
| Dense (mostly dense bush, shrubs, young trees) | 18.1 ± 5.7 |
| Mixed (mixture of more than one of previous class) | 10.0 ± 10.0 |

Table 16: The Brunei test site results. Source: (BECEK, 2006b), Table 2.

| Land Cover Type | Diff. & STD (m) |
|--|-----------------|
| 1. Tropical healthy forest | 7.4 ± 13.4 |
| 2. Dense even, or semi-open, canopy of mainly small-crowned trees | 4.7 ± 10.6 |
| 3. Canopy uneven, or moderately open, some medium or large emergents | 10.8 ± 10.8 |
| 4. Dense even canopy of medium crowns | 16.0 ± 11.8 |
| 5. Dense uneven canopy, of medium-sized and large crowns | 11.5 ± 14.9 |
| 6. Dense uneven canopy, mainly large crowns | 23.5 ± 21.1 |
| 7. Generally over 25 years old | 4.7 ± 10.6 |

During the most recent study (SEXTON *et al.*, 2009), four methods of forest height estimates, i.e., SRTM.C, GeoSAR, LiDAR and field measurements were compared. The experiments were conducted on two test sites located in the Duke Forest of the Southern Appalachian Piedmont Section of the South-Eastern Mixed Forest Province, central North Carolina, USA. Two distinct forest types, pine and hardwood forests, were considered. The LiDAR survey was carried out during winter months, while GeoSAR was flown in October. Field data were collected in summer using a hand-held Haga altimeter. The pine forest and the hardwood forest (note leaf-off period) impenetrabilities for SRTM.C were 47% and 32%, respectively. Both values are significantly lower than those reported by other researchers. In the case of the pine forest, the conical shape of the pine tree is most likely the cause of this discrepancy (large gaps between trees at the top of the canopy level are gradually reduced towards the tree base). In the case of a deciduous forest during the leaf-off period, the discrepancy is rather self-explanatory.

Availability of both DSM and DTM over a mountainous and forested area located in the Western USA permitted another test to be carried out. The datasets were obtained using the IFSAR system owned and operated by Intermap Technology Inc. (see Section 5.4 for IFSAR (InSAR X-band system) description, and APPENDIX 1 and 2 for the test site and data characteristics respectively). The datasets are available free of charge from the Intermap Technology Inc. website. A summary of relevant properties of the test site and test results are explained below. Figure 21 shows a histogram of differences in DSM *minus* DTM. The histogram is a bi-modal type with two distinct local maxima. The first pick (a) in Figure 21 corresponds to vegetation-free areas of the test site (the vegetation-induced elevation bias is zero).

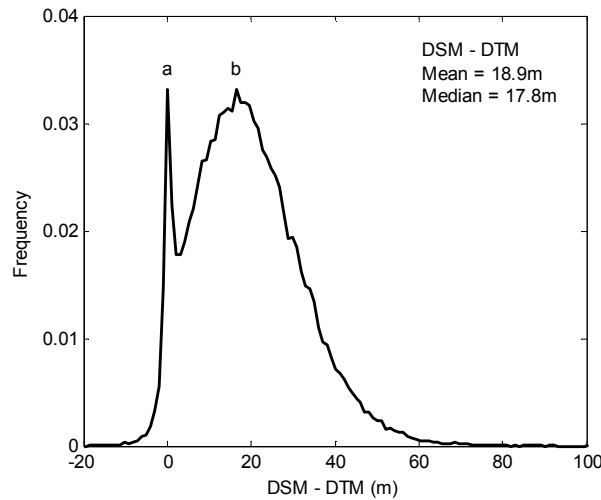


Figure 21: Histogram of differences in DSM *minus* DTM for the Western USA test site. The overall mean difference is 18.9m and median difference of 17.8m. Local maximum (a) corresponds to zero difference, while (b) corresponds to 16.4m.

The shape of the left-hand side part of the histogram resembles the shape of the Laplace probability density function, which can be expressed using the following formula (NORTON, 1984):

$$f(x|\mu, c) = \frac{1}{2c} e^{\left(-\frac{|x-\mu|}{c}\right)}, \quad (42)$$

where μ = location parameter,
 c = scale parameter.

The above two parameters, μ and b , can be estimated as follows:

For N independent and identically distributed differences d_1, d_2, \dots, d_N , estimator of μ - $\tilde{\mu}$ is the median of differences, and the estimator of c - \tilde{c} can be calculated using the maximal likelihood estimator from the following:

$$\tilde{c} = \frac{1}{N} \sum_{i=1}^N |d_i - \tilde{\mu}|, \quad (43)$$

The second local maximum (b) in Figure 22 corresponds to vegetated areas. It falls at about 16.4m, which is equivalent to the height of trees, according to the widely accepted position that the X-band does not penetrate the vegetation cover.

The shape of the right-hand side of the histogram resembles the shape of the Poisson density distribution function. Histograms of experiments involving counting the number of times a random event (the difference – for example) occurs in a given area follow the Poisson distribution.

A second test included comparison of the SRTM.C data with the IFSAR-derived DTM. Figure 22 shows a histogram of the differences in SRTM.C minus DTM.

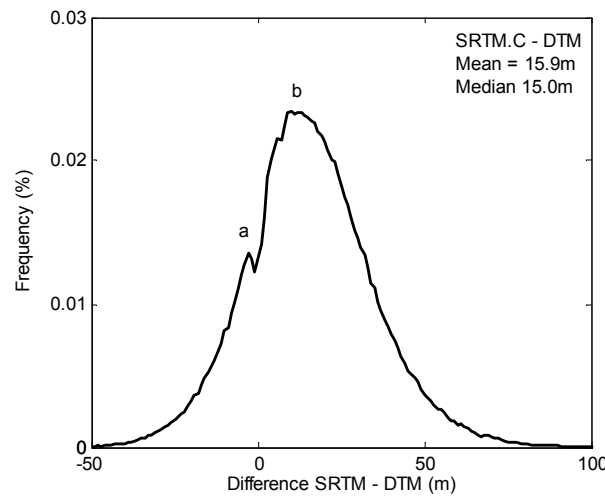


Figure 22: Histogram of differences in SRTM.C minus DTM. The overall average difference is 15.9m. The local maxima (a) and (b) are present for about -3m (SRTM.C is too low) and 12m, respectively.

In general, similar properties to those evident in Figure 22 are seen, e.g. it is a bimodal with two local maxima. However, due to the much higher standard error of the SRTM.C data, which depend on the slope of the terrain and the pixel size (three arc-second in this case) (Equation 28), the separation of the two local maxima is not that clear. Another observation is that the local maxima (a), which corresponds to vegetation-free terrain, is -3m. Such a large discrepancy must be considered as a systematic error either in IFSAR or SRTM.C. A possible explanation of this error may be related to conversion between various vertical data (NAVD88 for IFSAR versus EGM96 for SRTM) (NORHEIM *et al.*, 2002). Another possibility is a problem with the technology of attaining DTMs deployed by Intermap Technologies Inc. According to the product manual (INTERMAP, 2008) “the DTMs are created by digitally removing the cultural features contained in a DSM”. Whatever that means, it definitely constitutes a subjective step that may be a cause of the observed systematic error.

With regard to the second local maximum, which corresponds to vegetated areas and is about 12m, one can calculate that the biomass impenetrability is about 15m. This would also indicate that the biomass impenetrability in this case would approach 100%, contrary to all of the above reports. The only possible explanation of this conclusion is that the IFSAR-derived DSM does not represent the top of the vegetation canopy; rather, it appears that the X-band has penetrated the vegetation canopy to a depth similar to that of the C-band. In other words, the biomass impenetrability for the X- and C-band are very similar. This frequency-dependence of the impenetrability will be further investigated in Section 6.2.

The biomass impenetrability for SRTM.C was also performed over the Australian test site comprising the Nerang State Forest. The forest is a dry eucalyptus forest with variable tree height that is probably controlled by the moisture availability. The height of a few trees was estimated using photographs. The height was calculated by comparing the

length of a tree in the photograph with the known length of an object in the plane of that tree. The height varied from about 20m up to 30m. The average tree height can be estimated at about 25m.

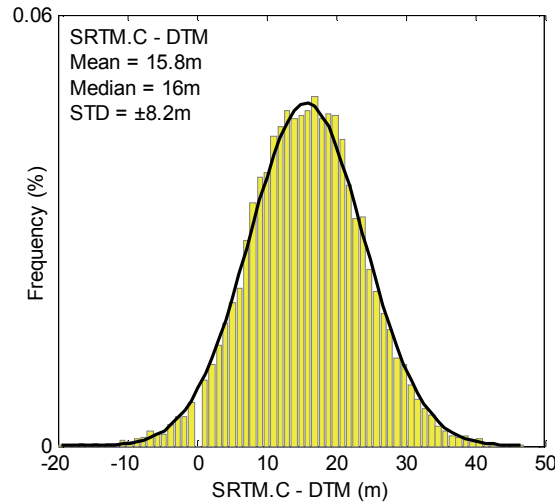


Figure 23: Histogram of differences in SRTM.C *minus* reference DTM for the Nerang State Forest, Queensland, Australia. The Gaussian fitting curve was plotted for $\mu = 15.8\text{m}$ and $\sigma = \pm 8.2\text{ m}$.

Figure 23 shows a histogram of the differences in SRTM.C *minus* DTM. Hence, the Nerang State Forest impenetrability for the SRTM.C is about 63% ($=15.8\text{m}/25\text{m}$).

The histogram follows the Gaussian density distribution function. This type of “normal” situation creates a chance to estimate stochastic properties of the vegetation cover or biomass. This will be discussed in detail in Section 6.5.

Any report on biomass impenetrability must not omit attempts to use repeat-pass SAR interferometry. One such attempt was carried out using the ERS-1 C-band system (ASKNE *et al.*, 1997). Five interferograms were analysed that were prepared from data acquired during winter. The longest time-lapse between the acquisitions of the pairing datasets was approximately four days. A very dense pine forest and a mixture of Norway spruce, pine and birch forest were selected for the test sites. The impenetrability of the pine forest varied between 21.6% up to 47.1%. The average tree height was 15.7m. The impenetrability for the second forest varied between 0% and up to 60%. The most likely explanation of these variations is the time-induced decorrelation effect. Nevertheless, the results are of the same order as those of other reports.

The temporal decorrelation was also noticed by Santoro and his team. They used the C-Band SAR data acquired with a one-day time interval. One of their conclusions was: “*that the tree height estimation from repeat-pass InSAR datasets is highly inaccurate, hence has limited forestry applications*” (SANTORO, *et al.*, 2005).

A standard strategy for estimation of biomass impenetrability involves comparison of the InSAR dataset with a reference “bare earth” DTM. There are some situations, however, when the reference DTM is not available; for example, in a dense tropical forest where the ground is barely visible or where human operators’ assistance would be impractical (large areas). Instead, a digital surface model (DSM) representing the tops of canopy trees is available. As an example, SPOT DEM and SPOT DEM Precision, which are produced by automatic correlation of SPOT 5 high resolution stereo pairs, can be used. Similar DSMs will be available on the market in the coming years, including a global DSM called ASTER DEM (FUJISADA *et al.*, 2005). Caution is advisable in assuming that these elevation products will represent the most outer reflective surface. In fact this is not the case, because of the uncontrollable process of selection of the interest points for autocorrelation. Consequently, elevation points in a forested area can be found both on top and at the bottom of the trees.

In order to test this approach, the SPOT DEM was purchased for an area of about 4,722km² over Brunei Darussalam (APPENDIX 2). The dataset contained some 6000 small areas of missing data due to production problems (lack of matching points or too low autocorrelation level). The DSM was compared with SRTM.C spot elevations over the Badas forest site. The comparison was carried out over homogeneous areas of forest, which were identified using orthorectified aerial photography. Circular buffers (90 m in diameter) centred on SRTM.C elevation points (located within the homogenous areas) were generated. An average elevation for each buffer was calculated from SPOT DEM points found within each buffer. The average tree canopy height was calculated using elevations of bare ground close to the edge of the forest. The average canopy height was 44m with standard deviation of $\pm 10.8\text{m}$. The large standard deviation was due to the fact that not all the elevation points represent the top of the canopy. Consequently, the average

tree height is, to a certain degree, underestimated. This issue of the large standard deviation of the average tree height will be discussed in Chapter 7. Nonetheless, comparing that result against SRTM.C, it can be easily calculated that the impenetrability for the Badas forest is at least 70%, and possibly close to 85%, because of the effect of the tree height underestimation.

Table 17: Biomass impenetrability as found by various authors for various types of biomass representations.

| Impenetrability | Biomass | Reference |
|-----------------------|---|-----------------------------------|
| 22% - 47%; 0 - 60% | Norway spruce, pine; birch (Northern Europe) | ASKNE <i>et al.</i> , 1997 |
| 63% | Gold Coast, Australia. | BECEK 2006b |
| >50% | Sites on five continents. | CARABAJAL <i>et al.</i> , 2006 |
| 63% | Lades Forest, France | FLOURY <i>et al.</i> , 1996 |
| 60-70% | Vegetated landscape, USA | HARDING, 2005 |
| 42% | Sites in USA and Costa Rica | HOFTON <i>et al.</i> , 2006 |
| 88% & 57% | California & Georgia (USA) | KELLENDORFER <i>et al.</i> , 2004 |
| 47% & 32% | Pine & hardwood forest, North Carolina, USA | SEXTON <i>et al.</i> , 2009 |
| ~65 - 70% | Evergreen National Park, Mangroves (USA) | SIMARD <i>et al.</i> , 2006 |
| 2.4 m (X) – 3.2 m (C) | California (USA) | WERNER <i>et al.</i> , 2005 |
| ~70% | Coniferous forest, western USA | This research |
| 63% | Dry Eucalyptus forest (Queensland, Australia) | This research |
| ~85% | Badas Forest (Brunei Darussalam) | This research |

Biomass impenetrability, mostly for C-band, was investigated by a number of authors at various test sites, using various reference data such as DTMs, LiDAR, laser altimeter data and field measurements, across the globe. The majority of the results point to an impenetrability of about 60% of tree height. This result is in an agreement with KARJALAINEN & HYYPPÄ, (2009), who claim a value from 0 – 60%. However, in the case of coniferous forest (spruce and pine), the impenetrability is significantly lower – about 35%. It is suspected that this is caused by the morphology of the biomass and spatial arrangement of the crown of coniferous trees. Modelling of the vertical structure of the forest will be discussed in the forthcoming section of this work.

One of the latest results confirming the significant magnitude of biomass impenetrability for the X-band is shown in Figure 24. The small crosses indicate the X-band InSAR acquired profile.

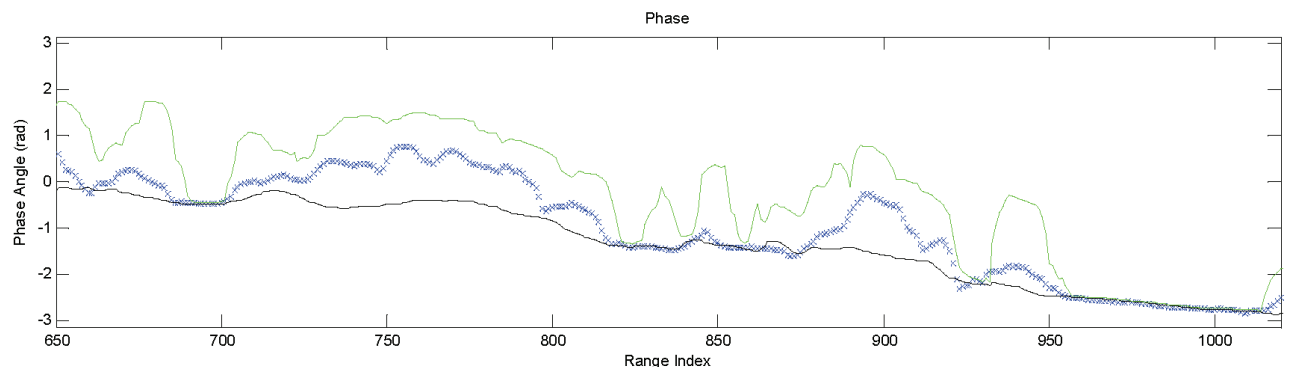


Figure 24: A cross-section of a forest stand and surrounding open space. Upper and lower lines indicate the tree canopy and bald earth elevations, respectively. The elevations were acquired using LiDAR. Blue crosses indicate the X-band elevation profile. Source: Figure 1 (PRAKS *et al.*, 2008).

The estimated elevation of the X-band profile is about 60% of the tree height (<the upper line> minus <lower line>).

6.2 The Frequency Factor

As already noted, the biomass is represented in InSAR datasets by the elevation bias, which is referred to as biomass impenetrability. The magnitude of the impenetrability depends on the radar frequency used. In the previous section, an overview of results of experimental investigations for the C-band was presented. Another radar frequency band which is commonly used for InSAR data acquisition is band X (~3.1cm, or ~9.3GHz). The biomass impenetrability for the X-band InSAR data product has been much less intensively investigated than has the C-Band impenetrability. The cost of data (X-band InSAR including SRTM.X) is the restricting factor. After reporting other authors' results, a comprehensive study of the X-band impenetrability conducted by the current author will be presented.

The average biomass impenetrability over the Amazon Rainforest for C-band and X-band were 13.95 m and 14.91 m, respectively (WERNER, *et al.*, 2005). The standard deviation was less than ± 4.7 m. No tree height data were available; hence, it is not possible to calculate the relative impenetrability in terms of tree heights. In conclusion, the impenetrability for SRTM.C/X is very similar, at least over the Amazon Rainforest.

Valuable conclusions on the biomass impenetrability can be drawn from the global comparison of SRTM.X/C data, grouped by the arbitral areas used in SRTM.C reporting. Table 10 contains the difference SRTM.X minus SRTM.C, including its standard deviation.

Table 18: Difference SRTM.X *minus* SRTM.C by continent. Source: Modified Table, p. 15, (WERNER *et al.*, 2005)

| Continent | Average difference (m) | Standard Deviation (m) |
|---------------|------------------------|------------------------|
| Europe | -0.89 | 18.25 |
| Africa | 1.04 | 48.74 |
| North America | -1.02 | 12.36 |
| South America | 1.66 | 16.01 |
| Asia | 0.24 | 20.15 |
| Australia | 1.45 | 12.85 |

It is interesting to note a potential correlation of the leaf-off state prevailing in Europe and North America and the negative value of the average difference for these areas. The negative difference means that the impenetrability for SRTM.X during winter is smaller than the impenetrability for SRTM.C. This observation is in a direct contradiction to the “official” assumption that the X-band waves are reflected from the top layer of vegetation.

The study on estimation of forest height by SEXTON *et al.*, (2009) also included a GeoSAR dataset (See Section 5.4). Forest height was estimated by subtracting the P-band InSAR elevation from the corresponding X-band height. The calculated impenetrability for the pine and hardwood forests was 45% and 41.6%, respectively. The results are quite similar to those obtained for the SRTM.C impenetrability (45% v. 47.1% - pine forest, and 41.6% v. 32.2% for hardwood forest). They are significantly lower than those reported by other authors. This is an effect caused by the shape of the tree canopy. This canopy-shape factor will be fully dealt with in the forthcoming sections of this work. It can also be noted that the lower value of the pine forest impenetrability for the X-band than for the C-band (45% v. 47.1%) suggests that the X-band radar penetrates the vegetation cover slightly more deeply than the C-band.

A comparative study of the biomass impenetrability for SRTM.X versus STRM.C has been reported (BECEK, 2008a). The impenetrability for SRTM.C was larger than for SRTM.X, which means that the X-band penetrates deeper into vegetation cover than does the C-band. These observations were confirmed by Lorraine Tighe of Intermap Technologies (Tighe, 2008, Private communication). However, a conditional acceptance of the conclusion was advised (BECEK, 2008a), because of suspected systematic error in the SRTM.X elevation of about 3m (the SRTM.X appears to be below reflective surfaces). Further investigations of the SRTM.X data product were suggested.

Let us now consider results of the original investigations, which were performed over test sites located in the Nerang State Forest, Queensland, Australia, East Kalimantan (Indonesia), Southern Germany and a site in Western USA, in order to throw some more light on the controversial issue that is the level of impenetrability for the C- and X bands. The question remains whether impenetrability is smaller/larger, or is it the same. Comprehensive characteristics of the test sites and datasets used can be found in APPENDIX 1 and 2, respectively.

Figure 25 shows a histogram of the differences SRTM.X *minus* SRTM.C. It follows the Gaussian distribution. The mean difference in the X- and C-band impenetrability is -2.6 m (X- is lower then C-band one) with a standard deviation of ± 5.35 m.

As was previously mentioned, some doubt was expressed regarding a possible systematic error in the SRTM.X dataset in the area of interest (BECEK, 2008a). In order to identify the potential error, the SRTM.X dataset was compared against a reference DTM. At this time, the area of interest was extended by including a certain amount of vegetation-free areas to identify the systematic error.

The reference DTM was developed from a set of photogrammetrically retrieved spot heights. It is estimated that the vertical accuracy of spot heights is about ± 0.3 m. Figure 25 shows a histogram of differences in SRTM.X – DTM. Although, less obvious then the histograms in Figure 21 or 22, it also possess a bimodal character marked by two local maxima (a) representing vegetation-free areas, and (b) – an area covered by forest. Estimated impenetrability for (a) is about zero, which indicates that the SRTM.X dataset in this area does not contain any systematic error.

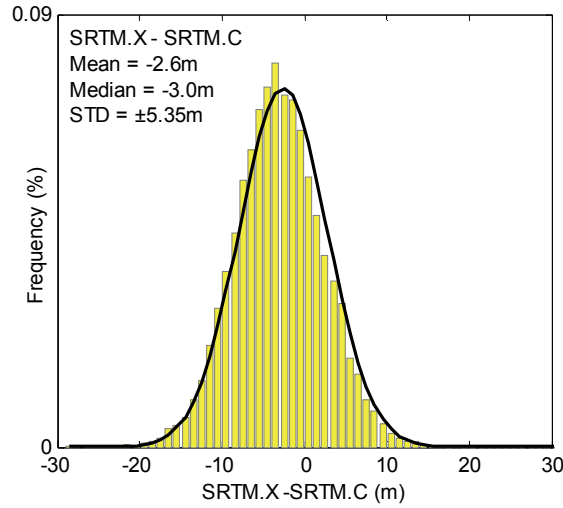


Figure 25: Histogram of differences SRTM.X *minus* SRTM.C over the Australian test site. The Gaussian fitting curve was drawn for $\mu = -2.6$ m and $\sigma = \pm 5.35$ m.

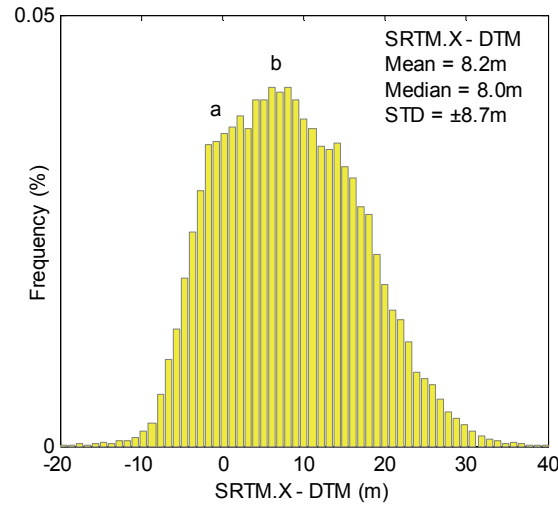


Figure 26: Histogram of differences in SRTM.X *minus* reference DTM over the Australian test site. The histogram has a bimodal character with two local maxima (a) and (b). Maximum (a) represents the differences for vegetation-free areas, while (b) is for the vegetated areas. Detailed inspection yields readings of 0 m for (a) and 8m for (b).

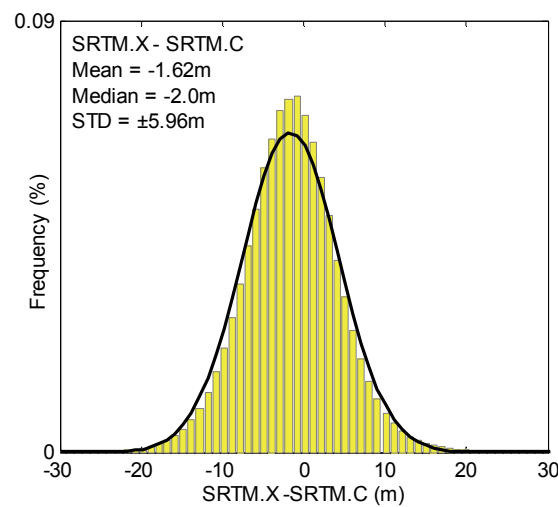


Figure 27: Histogram of differences in SRTM.X *minus* SRTM.C over the Kalimantan site. The Gaussian fitting curve was drawn for $\mu = -1.62$ m and $\sigma = \pm 5.96$ m.

A comparison of SRTM.X with SRTM.C was conducted over a test site located in the tropics over an aerial region referred to as the Kalimantan site (see APPENDIX 1 for the site characteristics). This setting is in a sharp contrast to the Australian test site, but quite similar in all aspects to the environment of Brunei Darussalam, where important experiments – still to be described – were carried out. A tile of the SRTM.X was purchased from DLR, which was compared to SRTM.C. No other elevation data are available for the site. Available high resolution satellite imagery over the area is also of poor quality (~75% cloud cover), despite establishing that the area is almost entirely covered by the mixed dipterocarp type of forest. Figure 27 shows a histogram of differences in SRTM.X *minus* SRTM.C. In this case also, it appears that the impenetrability of the SRTM.X is lower than that of the C-band by 1.62m. The standard deviation of the difference is ± 5.96 m, which is very similar to that of the Australian site.

Another test was performed over an area located in southern Germany (see APPENDIX 1 for detailed description of the site). The site is only partially (~15%) covered by deciduous forest, which was in a leaf-off state during the February 2000 SRTM mission. Figure 28 shows a histogram of differences in SRTM.X *minus* SRTM.C. The mean difference is about 0.5 m, which, considering the one-meter quantization level for both datasets, is significantly close to zero. The standard deviation is ± 5.3 m, which is relatively low and which indicates that the area is relatively flat. An attempt to fit the Gaussian curve fails, as is clearly visible in Figure 28. Instead, it was found that the Laplace fitting curve approximates the histogram much better. The lack of “bio-scatterers” (leaves) is the most likely cause for the different shape of the histogram. The Laplace fitting curve was also found to be the best approximation for a histogram of SRTM.X *minus* SRTM.C differences over the partially vegetated area in Australia during leaf-on state (BECEK, 2008a).

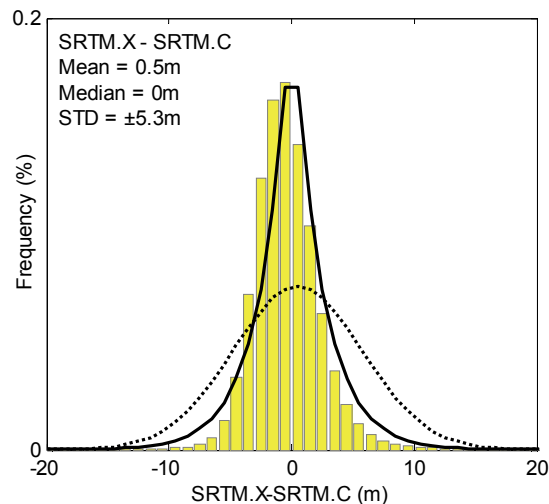


Figure 28: Histogram of differences in SRTM.X *minus* SRTM.C over the South Germany test site. The Gaussian fitting curve (dotted line) does not fit the histogram. Instead, the Laplace curve is more suitable.

An experiment over the western USA site was carried out using a free tile of data provided by Intermap Technology Inc. (See APPENDIX 1 for the site description and APPENDIX 2 for the dataset characteristics). The data consist of a high resolution (5m posting) DSM and DTM produced using the IFSAR system described in Section 5.4. In addition, both the one- and three arc-second versions of SRTM.C were used. Figure 29 shows a histogram of the differences in DSM *minus* SRTM.C (the three arc-second version). The mean difference is 2.6 m and the standard deviation is ± 22.7 m. This indicates that the impenetrability for the X-band is higher than for the C-band. However, considering the remarks made in Section 6.1 regarding the 3m systematic error in the IFSAR DSM/DTM datasets (the elevations are too high by 3m), one can calculate an adjusted mean difference as -0.4m (2.6m – 3m). In other words, the impenetrability for the X-band of the IFSAR is almost the same as that for SRTM.C.

The Gaussian fitting curve is suited to approximate the histogram. The histogram appears to be also of the bimodal type, although not so distinct (note a shift in the culminations of both the histogram and the fitting curve), which indicates the presence of some signal from the vegetation-free and vegetated areas.

In order to verify the validity of the relatively high standard deviation of the difference ± 22.7 m, an additional set of calculations was conducted. This time, the one arc-second SRTM.C dataset was subtracted from the DSM (DSM *minus* SRTM.C). Figure 30 shows a histogram of the differences. The mean difference is 2.7m which, after suspected data corrections of 3m (see previous paragraph), yields -0.3m. The standard deviation dropped to the level of ± 17.1 m. This

experiment illustrates how significant the pixel size is in situations when the terrain has very rough topography (average slope for the site is 32°; See APPENDIX 1 for the site characteristics).

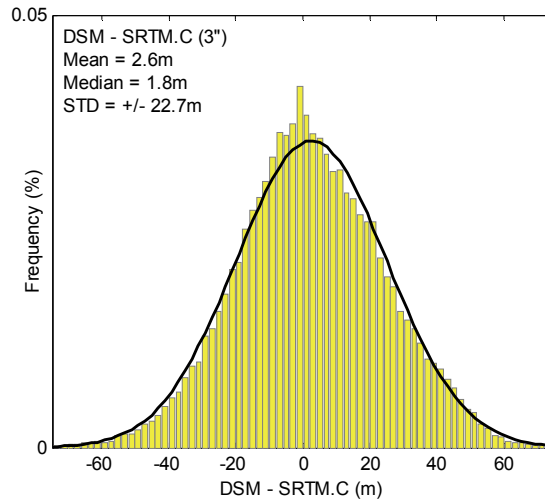


Figure 29: Histogram of the elevation differences in IFSAR X-band DSM *minus* SRTM.C (three arc-second pixel) over the USA site using data provided by Intermap Technology Inc.

A significant penetration depth of the X-band was also revealed in the study of the IFSAR dataset carried out by Andersen (ANDERSEN, *et al.*, 2006) for the USA site. LiDAR first return data were compared against IFSAR X-band DSM. The mean difference was -7.5 m (IFSAR is below LiDAR DSM). Adding also the LiDAR DSM bias of about 2m, one can estimate the X-band penetration depth as about -10 m. Assuming that the trees in the area of interest are about 35m tall, the impenetrability for the X-band would be about 71%, which is of the same order as the impenetrability for the C-band.

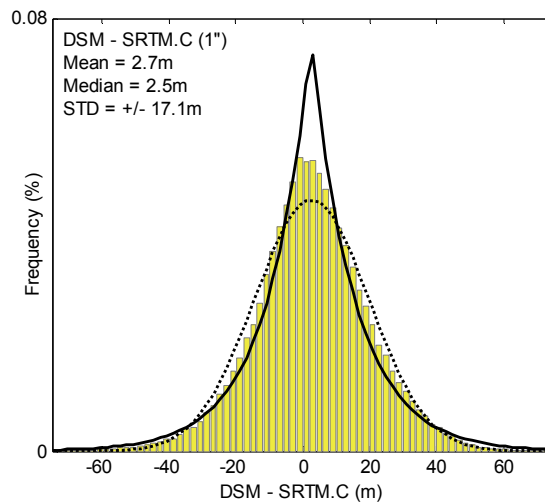


Figure 30: Histogram of differences in DSM *minus* SRTM.C (the one arc-second) over the USA site. Mean difference is 2.7m, median difference is 2.5m and the standard deviation is ± 17.1 m. The Gaussian (dotted line) and Laplace (solid line) curves have been included.

Both the Gaussian and Laplace fitting curves are shown in Figure 30. As can be seen, neither of the curves fit the histogram in a satisfactory way. A possible explanation could be that the white noise becomes dominated by a noise having an abnormal colour distribution. The question of stochastic properties of the biomass will be investigated in Section 6.5 of this chapter.

A penetration of the canopy trees by the X-band was suspected during analysis of the GeoSAR tree elevation data (X-band *minus* P-band) (HYDE, *et al.*, 2007). The team initially assumed that “*The X-band records the height and amplitude of the first intercepted surface, typically at or near the top of a forest canopy*”, but, in conclusion, they

expressed a caution by saying “*It is possible that given the relative openness of the canopy and the size of the individual trees, the X-band is penetrating into the canopy*” (*ibid*).

A concise summary of the frequency factors considered in this report is shown in Table 19. A first general conclusion is that both impenetrabilities are very similar. Some results indicate that the X-band penetrates slightly deeper than the vegetation covers, while others indicate something quite opposite. By averaging the results, one would probably get a value for the X-band *minus* C-band impenetrability close to zero. This conclusion seems to be also confirmed by M. Simard (MARC SIMARD of JPL, private communication, 17.10.2007).

Table 19: Comparison of the biomass impenetrability for X- *minus* C-band for various forest types.

| X <i>minus</i> C impenetrability | Biomass | Reference |
|----------------------------------|---|-----------------------------|
| < -1 m | Amazon Rainforest (Brazil) | WERNER <i>et al.</i> , 2005 |
| -1.02 m – 1.45 m | Impenetrability by continent (Global) | WERNER <i>et al.</i> , 2005 |
| 45% v. 47.1% | Pine /hardwood forest (USA) | SEXTON <i>et al.</i> , 2009 |
| -2.6 m | Dry Eucalyptus forest (Queensland, Australia) | BECEK, 2008a |
| -1.62 m | Tropical rainforest (Kalimantan, Indonesia) | This research |
| 0.5 m | Leaves-off forest (Germany) | This research |
| 2.7 m | Mainly coniferous forest (USA) | This research |

These small variations of the order of ± 2 m are most likely caused by measurement noise. Hence, true difference in impenetrability, which is probably less than 1m, is buried in that noise.

At this point, some comments on the biomass impenetrability for bands other than C/X-bands are necessary, because a number of disagreements between results obtained by various researchers seem to be present in the literature. In particular, the P- and L-band impenetrability is of interest, especially the strong sensitivity of the P-band SAR backscattering coefficient to the tree height, trunk biomass dbh and basal area (LE TOAN, *et al.*, 1992). This strong dependency should also have a visible effect on InSAR results in the form of impenetrability or elevation bias. Yet, the P-band InSAR systems, such as GeoSAR, are considered as acquiring bald earth elevations, which means that they are considered to be bias-free. Similar results/conclusions were also reported for the L-Band SAR backscattering coefficient (*ibid*).

6.3 Biomass Density

Biomass density, or more precisely, the density of scatterers representing the biomass, is a “natural” factor influencing biomass impenetrability. In the extreme case, when there is no biomass in an area of interest, the biomass impenetrability is zero. In the opposite extreme and hypothetical case, when the biomass is extremely dense, and no radar (at least C- and X-band) is able to penetrate the top vegetation layer, the biomass impenetrability will be equal to the elevation of the top layer. In reality, however, the top layer of vegetation is a discontinuous medium consisting of enough openings for the radiation to “travel” for some distance into the vegetation. The openings consist of distances between scatterers (leaves, branches and stems) of a tree, and also openings between trees. Holes in the vegetation cover are controlled by a few natural and anthropogenic processes, such as climate or air pollution, for example. Hence, biomass impenetrability is a dynamic entity, varying according to seasons (leaf-off/on status), long term factors such as forest growth and random events including insect infestation or instabilities in the environment (pollution and global warming).

Interaction between the radar and vegetation has been intensively investigated by various research studies. A standard passive remote sensing approach has been employed, which uses characteristics of the backscattered signal to identify the properties of the land cover. As was soon realised, the major obstacle of this type of approach was the so-called level of saturation. The level of radar saturation refers to the level of biomass density above which the properties of the backscattered signal remains unchanged. The level of saturation, as a function of the biomass density in terms of the oven-dry aboveground organic matter, versus radar frequency, are summarised in Table 11.

Table 20: Radar saturation levels of biomass for various frequencies.

| Frequency (GHz) | λ (cm) | Band | Biomass Level (Mgha ⁻¹) | Remarks | Reference |
|-----------------|----------------|------|-------------------------------------|----------------------|---|
| 0.02 – 0.09 | 330 – 1500 | VHF | 625 | Norway spruce forest | FRANSSON <i>et al.</i> , 2000, MANNINEN & ULANDER, 2001 |
| 0.44 | 68 | P | ~100-150 | | Lower values by IMHOFF, |

| | | | | | |
|-------|-----|---------------------------------|--------------|-------------------------------|---|
| | | | ~200 | Plantations of maritime pines | 1995 DOBSON <i>et al.</i> , 1992 |
| 1.225 | 21 | L | ~100 | Plantations of maritime pines | DOBSON <i>et al.</i> , 1992 |
| 5.3 | 5.7 | C | ~20 ~5-15 | Loblolly pine stands | IMHOFF, 1995 WANG <i>et al.</i> , 1994 |
| 9.5 | 3.1 | X | | No reference found | |
| N/A | N/A | Combination of C-, L-, & P-band | ~350-400 | Loblolly pine forest | KASISCHKE <i>et al.</i> , 1995 |

Careful study of the results in Table 11 leads to the conclusion that, for example, in the case of the C-band, all SAR measurements made over more than 20Mg ha^{-1} forest look very much the same. At the same time, however, increasing biomass density causes the biomass impenetrability to increase value. Moreover, as already mentioned, the process of increasing the biomass impenetrability has its culmination only when the top layer of vegetation reflects the entire radar radiation. This is just a hypothetical situation, but we can easily apply it to real situations. This remarkable observation clearly positions biomass impenetrability as a superior indicator of biomass density than are the traditional SAR-derived parameters.

A study was undertaken to investigate the relationship between biomass density and biomass impenetrability (BECEK, 2008a). A “classic” approach for investigating the dependency of a certain SAR parameter (say the backscatter amplitude) versus the biomass density is to use a test site for which a biomass inventory has been performed. However, remarks on forest inventories made in Chapter 3 indicate that this is usually a very costly proposal. Instead, a parcel based inventory was proposed for the present research. In this approach, parcels of land, defined by cadastral boundaries for example, are used as classification units. By means of photointerpretation of high resolution aerial



Figure 31: A parcel-based land cover classification. H, M, W (not shown) stand for “House”, “Mixture” and “Water”, respectively, and are members of an arbitral classification scheme. Another class denoted as T – “Trees” with an associated number indicates percent of parcel area covered by trees. Source: (BECEK, 2008a).

photography, each parcel was assigned one of four arbitrary classes: H – house, M – mixture (houses, transportation, water, and vegetation), W – water, and T – trees. For parcels covered by trees – the T class – the percentage of an area covered by trees was also produced. For example, T10 indicates a parcel covered 10% by trees. Some 71,500 parcels

were semi-automatically classified with about 50% of the work done by operators. The semi-automatic classification was performed by assuming that all parcels smaller than 1000m² were classified as H – house.

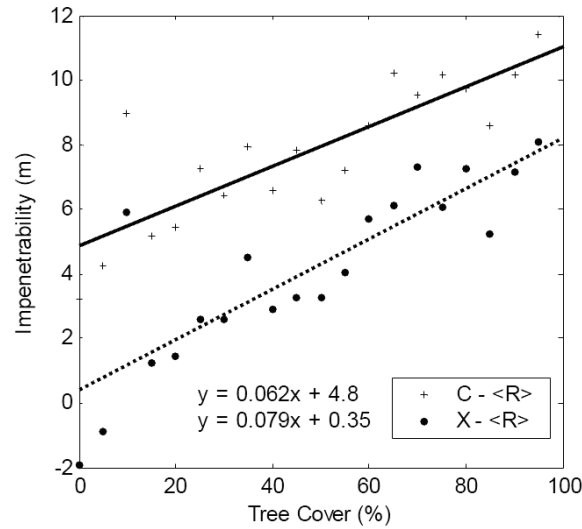


Figure 32: Biomass impenetrability versus percentage of tree cover for the site as described in (BECEK, 2008a). (solid line) and SRTM.X (dotted line). Source: (*ibid*).

Figure 32 shows a linear dependency of the impenetrability on the percentage of tree cover for both SRT.C and SRTM.X.

In addition to the linear dependency of the impenetrability on the percentage of tree cover, there is also a clearly visible difference in the penetration depth between the C- and X-band, i.e. the X-band penetrates deeper than the C-band, at least over the test site.

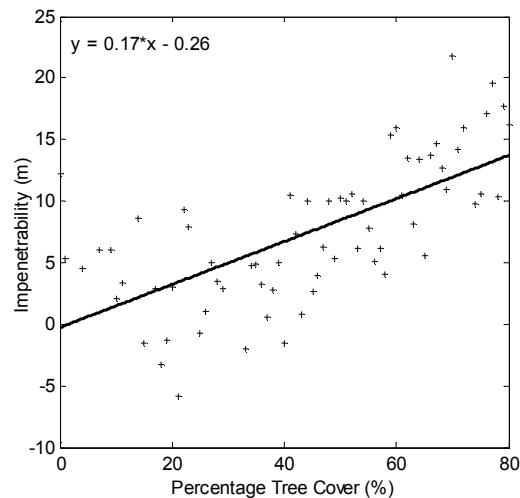


Figure 33: Percentage of tree cover versus biomass impenetrability for the Brunei Darussalam test site. A linear regression line along with the equation is also shown.

A verification of these results was carried out on different datasets and test sites. For a test site, the territory of Brunei Darussalam was selected. See APPENDIX 1 for a description of this test site. The biomass impenetrability was calculated by subtracting a DTM (APPENDIX 2) from SRTM.C. Note, however, that SRTM.X is not available over the test site. As tree density data, the MODIS Vegetation Continuous Fields dataset was used (HANSEN *et al.*, 2003). These data can be downloaded from the ftp server at ftp://ftp.glcf.umd.edu/modis/VCF/Collection_4_version_3. The spatial resolution of the data is 500m by 500m. Pixel values between 0 – 100 represent a percentage of the pixel area covered by trees. Value 251 represents water, while 245 represents ‘no data’. The data are aggregated to an annual level, and are available for the years 2000 to 2005. Figure 33 shows a scattergram of the percentage of tree cover versus the biomass impenetrability.

These results are consistent with the results attained for the Australian test site, and especially for the linear character of the relationship between the horizontal biomass density and biomass impenetrability.

The significant difference should be noted in the gradients of the equations (Figure 32 and 33), which read 0.062 and 0.17 for the Australian and Brunei test sites respectively. This occurs because impenetrability also depends on the height of the trees. Tree crowns located higher above the ground cause higher values of impenetrability. In the case of the Australian test site, the estimated average tree height was about 20m, while the corresponding value for the Brunei test site was about 40m (APPENDIX 1). This inconvenient effect justifies the necessity of a normalisation of the impenetrability. One way of introducing this would be to relate the impenetrability to the tree height.

6.4 Incidence Angle

The side-looking configuration of the SAR instruments causes variation in incidence angle (IA), which is responsible for geometric distortion variations in the backscattering intensities. Incidence angle is one of the parameters of side-looking SAR systems including InSAR systems.

IA is an angle between the radar beam and a line orthogonal to the surface at a point of intersection of beam and illuminated surface. This is shown in Figure 34. There are two factors controlling the magnitude of IA. First is the InSAR configuration. Typically, for optimal results, IA varies between 20° and 50°. The second factor is the slope and aspect of terrain at the intersection point A. In order to eliminate or reduce the shadowing effect and other IA-induced errors, the data acquisition procedure is typically repeated a few times for the area of interest. The final result is an average of these few sessions. In this way, the variance of the IA-induced errors is reduced and residuals are scrambled with other errors and cannot be identified. However, careful studies of InSAR data may reveal some minor residuals of the IA-induced errors to still be present (BECEK, 2008b).

The IA in relation to SAR observations has been investigated by a few authors. The leading idea behind these investigations was to somehow correct the SAR data to compensate for the variations in the incidence angle caused by the technical parameters of the airborne SAR and topography of the terrain. This is because the traditional image classification techniques cannot be applied directly to SAR data because the intensity of the backscatter depends on incident angle as well as on ground cover (MENGES, *et al.*, 2001). These researchers also noted that the characteristics of these effects depend both on topography and on vegetation type.

Warner and his team (WARNER, *et al.*, 1996) investigated the effect of the IA on X- (9.25GHz) and C- (5.3GHz) Band radar backscatter of a boreal forest. The variability of the IA was achieved as a combination of rugged topography and radar depression angle, which varied between 16° and 90°. The SAR data were collected in the HH polarisation mode only. Both the X- and C- Band data are very similar. However, for small IAs, multispectral X- and C-Band data provide optimal identification conditions of forest composition. The IA was also investigated by Ahmed, who investigated the nature of forest backscattering and how it depended on the IA. The SIR-B L-band HH polarization observations were used in the study (AHMED & RICHARDS, 1989).

In case of the SRTM.C, the final product was averaged from at least two acquisitions. According to JPL (<http://www2.jpl.nasa.gov/srtm/datacoverage.html>), the following are the data coverage statistics for SRTM.C:

Targeted land was 80% of Earth landmass ($119.56 \times 10^6 \text{ km}^2$)
99.968% targeted land mapped at least once ($119.51 \times 10^6 \text{ km}^2$)
94.59% targeted land mapped at least twice ($113.10 \times 10^6 \text{ km}^2$)
49.25% targeted land mapped at least 3 times ($58.59 \times 10^6 \text{ km}^2$)
24.10% targeted land mapped at least 4 times ($28.81 \times 10^6 \text{ km}^2$).

In contrast, the SRTM.X product was primarily developed from one acquisition. The second acquisition was performed in places where ascending and descending orbit swaths were intersecting. Figure 19 shows this arrangement.

A scanning mode available only for the SRTM.C data acquisition is the cause of the coverage differences between SRTM.C and SRTM.X.

In order to assess the magnitude of the IA-induced error, an experiment was carried out on the Australian site using both SRTM.C/X data products. The assessment was made by comparing SRTM.C and SRTM.X data with reference DTM for a few set values of IA and for pixels with similar slope and aspect. A working hypothesis was built upon the fact that SRTM.X was developed based on a single acquisition, while SRTM.C was developed based on averaging of three data takes. Therefore, some presence of IA-induced error can be expected in the SRTM.X data.

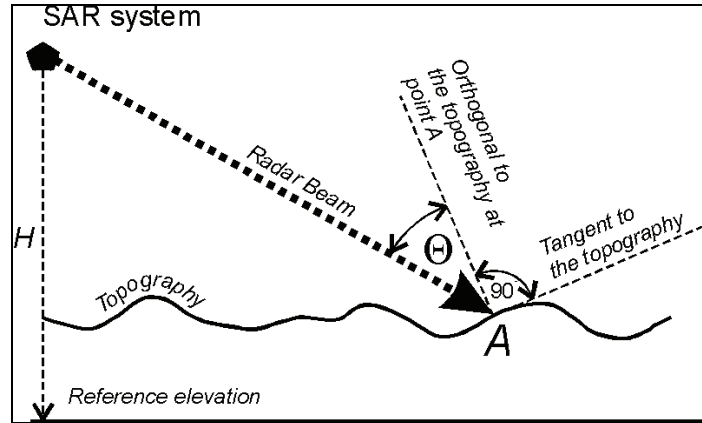


Figure 34: An illustration of the SAR incidence angle Θ .

A verification of this hypothesis was carried out using data over the Australian test site (APPENDIX 1). A 4-km long cross-section was drawn parallel to illumination direction of the SRTM during the X-band data take over the site. The azimuth of the illumination direction was about 306° (APPENDIX 2). The transect was located within the Nerang State Forest. Figure 35 shows a map of the differences in SRTM.X minus reference DTM and the location of the transect.

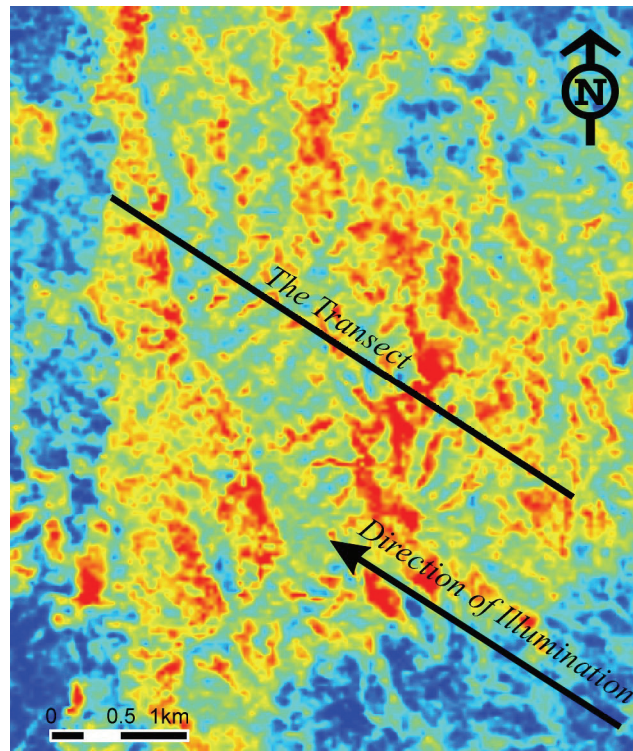


Figure 35: Location and orientation of the transect in NSF. As a background, a map of differences in SRTM.X minus DTM was used.

The following data were extracted along the transect:

1. Differences in SRTM.X minus DTM;
2. Differences in SRTM.C minus DTM;
3. Slopes derived from SRTM.X;
4. Slopes derived from SRTM.C;
5. Aspects derived from SRTM.X
6. Aspects derived from SRTM.C.

An index was assigned to every pixel along the transect. This index was calculated as the *sine* function of an angle constructed from the aspect of slope for a given pixel and the azimuth of the direction of the radar illumination. The index p was designed in such a way as to express, in relative terms, the fraction of the radar illumination that each pixel

receives, depending on the aspect of terrain on that pixel. For example, pixels perpendicular to the direction of the incoming radar radiation will get the highest radiation compared with pixels with different aspects. Hence, the index was calculated from:

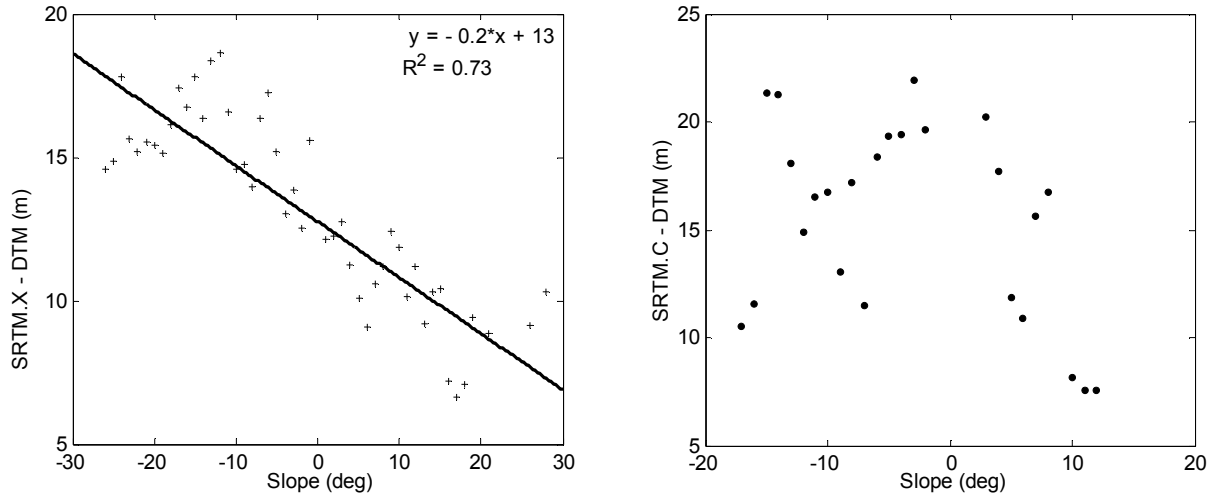


Figure 36: Differences in SRTM.X *minus* DTM (left pane) and SRTM.C *minus* DTM (right pane) as functions of slope. A positive slope indicates that it faces radar illumination, while negative indicates otherwise. The SRTM.X data were created from one data take, while SRTM.C is a product of three data takes. Note that there are significantly fewer data points visible in the right pane, which is due to the differences in the resolution of SRTM.X (more pixels) and SRTM.C (fewer pixels) data.

$$p = \sin(A - D - 270^\circ), \quad (43)$$

where A – aspect,
 D – azimuth of radar illumination.

The expression $D - 270^\circ$ (or $D - 90^\circ$) is an azimuth of the direction perpendicular to the azimuth D .

The index p takes values from < -1 to 1 , where $p = -1$ indicates a pixel having aspect the same as the radar illumination, while $p = 1$ indicates a pixel having an aspect opposite to the direction of the radar illumination. This convention was used to assign a sign to slopes: a negative slope indicates pixels facing away from the illumination, while a positive slope indicates pixels facing the illumination. Figure 37 explains this convention.

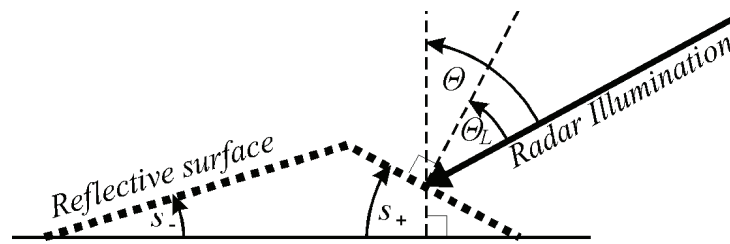


Figure 37: Illustration of the geometric relationship between slope and radar beam. S_+ , S_- indicates the positive (facing radar illumination), and negative slope (facing away radar illumination), respectively. Θ and Θ_L indicates the flat earth and local incidence angle, respectively.

In the next step, the weighted average of the differences in SRTM.C *minus* DTM and SRTM.C *minus* DTM were calculated for each slope value presented in the dataset, using Equation (11):

$$\bar{d}^s = \frac{\sum_{i=1}^{n(s)} d_i^s p_i^s}{\sum_{i=1}^{n(s)} p_i^s}, \quad \forall s \in \{\text{slope value present}\}, \quad (44)$$

where d_i^s - difference either SRTM.C or SRTM.X *minus* DTM for the i th pixels with slope s ;
 $n(s)$ – number of pixels with slope s ;
 p_i^s - the weight of the i^{th} pixel within all pixels with slope s .

As a weight, the index assigned to each pixel was used (ss above). Figure 36 (left-hand pane) shows a dependency $\bar{d} = f(s)$, e.g. both average SRTM.X *minus* DTM (left-hand pane), and average SRTM.C *minus* DTM (right-hand pane) versus slope.

As expected, a single data take, from which the SRTM.X dataset was created over the test site, is responsible for a strong linear dependency of the biomass impenetrability on the slope of the terrain. Increasing the value of the positive slope causes the impenetrability to become lower, and vice-versa. Contrary to the above, the right-hand plot in Figure 36 shows no signs of dependency of the impenetrability of SRTM.C on the slope. This is understandable because of the averaging of the three data takes used to create the SRTM.C for this site.

The above result provides an important caution for planning of future InSAR missions. Clearly, more than one data take is necessary to achieve an elevation data product that would be independent of the incidence angle.

Another important conclusion from the above is the proof that gaps between components of the biomass (leaves, branches and trunks) and between trees are the major players in controlling the magnitude of the biomass impenetrability. Of course, this is true only if trees can be considered as isotropic objects; i.e., they have stochastic properties independent of the direction of observation. This seems to hold, at least within a range of variations of the incidence angle.

6.5 Stochastic Properties of the Biomass

The biomass, in almost all known modelling attempts, has been considered to be a layer or layers of randomly distributed components that are large enough to interact with electromagnetic waves of a certain frequency. A stochastic model of biomass is used to invert the backscattered signal for estimation of a number of basic physical characteristics of biomass including biomass density, tree height or bole area. A classic example of this approach is offered by the radiative transfer theory (RTT) (JIN & LIANG, 2004, PICARD *et al.*, 2004, WEN *et al.*, 1990, WEST *et al.*, 1993). Some assumptions or simplifications regarding basic properties of biomass are made. These assumptions include: 1) the backscattered signal has a Gaussian distribution; 2) the biomass is an isotropic medium, and 3) the biomass is an isomorphic medium.

Obviously, in case of studies on biomass impenetrability, stochastic parameters of that impenetrability are of interest. Stochastic properties of biomass impenetrability describe, in a synthetic and simplified form, the otherwise complex interactions of radar radiation with biomass. The issue is even more complex in the case where two radar images are required for the interferometric procedure. Investigation of biomass impenetrability is much easier in terms of the quality of results, and the simplicity and the costs of experiments, among others. This is because these experiments can be carried out using real world data, which is not very difficult to obtain, rather than costly instrumentation such as the Helsinki University of Technology Scatterometer (HUTSCAT) profiling scatterometer (HALLIKAINEN *et al.*, 1993, HYYPPÄ, J. & HALLIKAINEN, 1993). These may include DTM, DSM, aerial/satellite imagery and *in situ* observations of a test site.

Some basic stochastic properties of biomass are now reported. The objective of this experiment was: 1) to investigate the biomass impenetrability in terms of its spatial variability, and 2) to describe the influence of gaps in the canopy on biomass impenetrability. The experiment was carried out on the Australian and Brunei Darussalam (Badas Forest) tests sites (APPENDIX 1). A wide range of morphological properties of the biomass (different tree species) and diverse topographic and other environmental conditions provided a proper setting for an experiment that allowed for inference of general conclusions. The framework of the error propagation law was the basic mathematical model for the experiment. The SRTM.C datasets and associated reference DTM or DSM were used to calculate the biomass impenetrability.

The Badas Forest is a larger undisturbed pristine peatland swamp forest (APPENDIX 1). A typical feature of this forest is its closed canopy. However, there are numerous holes present due to fallen trees. The average tree height is 44m, and the underlying terrain – mainly peat – is basically flat or extremely gently rising towards the centre of the forest. In the first experiments, the SRTM.C spatial variation over the homogenous forest canopy was estimated. To facilitate this, a set of 200 SRTM.C elevations over homogeneous (gap-free) canopy cover was manually selected. The process of

selection was guided by an ortorectified aerial photography. Figure 38 shows a north-eastern part of the Badas Forest with some elevations selected for further calculation. The image is one of 1:20,000 aerial photographs which were flown in 2002 (APPENDIX 2). The variance was calculated after removing a linear trend. Figure 39 shows a histogram of disparities in tree height for about 200 SRTM.C elevations.

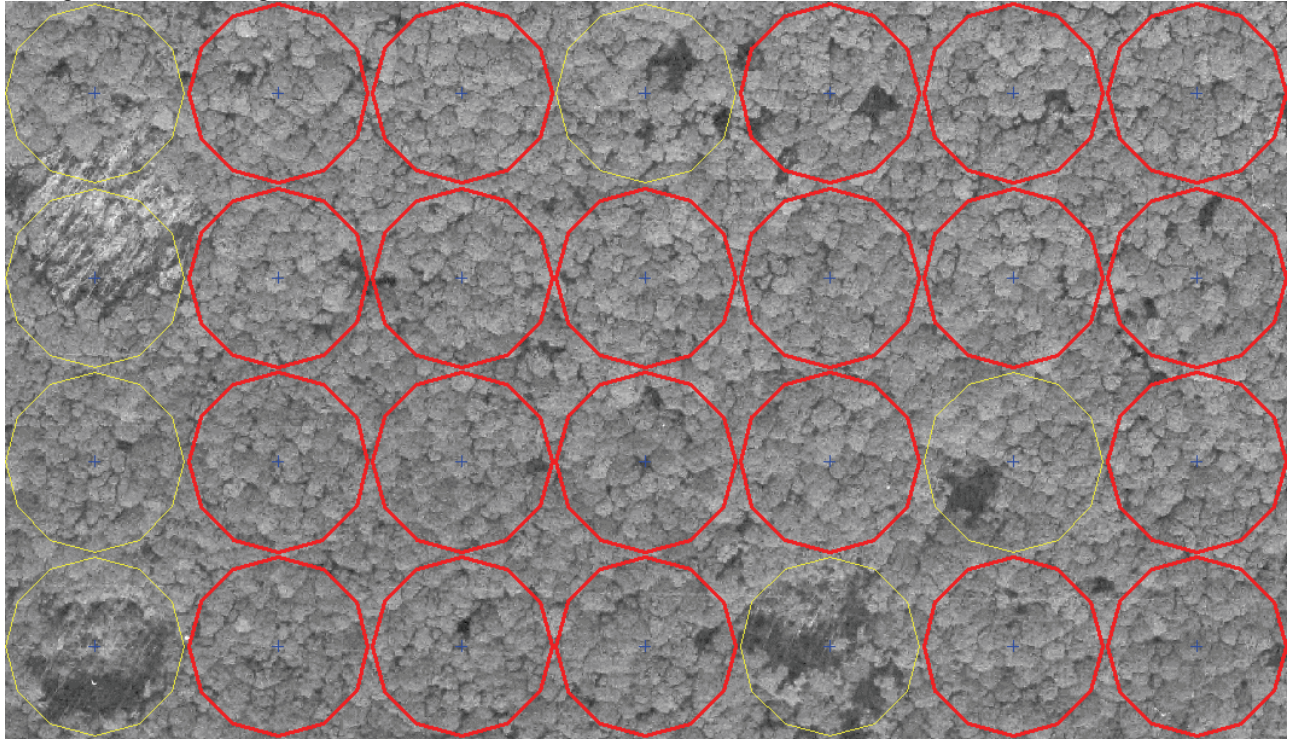


Figure 38: Aerial view of the tree canopy of the Badas Forest. The red circles indicate SRTM.C spot elevations selected for further calculations. The dark spots are gaps – discontinuities in the canopy cover. Spot elevations were selected avoiding large gaps in the canopy. The WGS84 coordinates of the lower left corner are: 4.568785°N, 114.357922°E. The diameter of a buffer is 90m (about three arc-seconds). The aerial photography was flown in 2002.

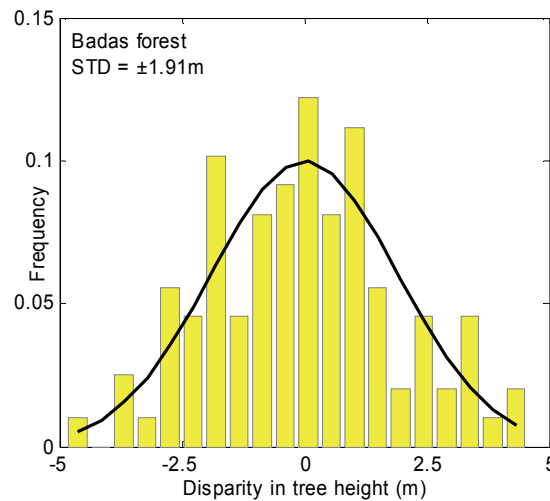


Figure 39: Histogram of disparities in tree height as observed by SRTM.C. A Gaussian fitting curve was drawn for the mean = 0 and standard deviation $\pm 1.91\text{m}$. Calculations were performed after removing a linear trend due to minor variations in topography. Three outliers were removed from the set of 200 elevations selected.

The result, in terms of standard deviation, was $\pm 1.91\text{m}$. It follows the Gaussian density distribution function. For reference proposes, the set of SRTM.C elevations selected (including the outliers) for analysis are readily available in Table 21.

Table 21: SRTM.C elevations including their coordinates (WGS84) selected for ananlysis

| ID | Lat (°) | Long (°) | Z |
|----|----------|----------|----|
| 1 | 4.575 | 114.3525 | 52 |
| 2 | 4.575 | 114.3533 | 54 |
| 3 | 4.575 | 114.3542 | 60 |
| 4 | 4.575 | 114.355 | 59 |
| 5 | 4.575 | 114.3558 | 59 |
| 6 | 4.575 | 114.3567 | 58 |
| 7 | 4.575 | 114.3575 | 59 |
| 8 | 4.575 | 114.3583 | 59 |
| 9 | 4.575 | 114.3592 | 56 |
| 10 | 4.575 | 114.36 | 56 |
| 11 | 4.575 | 114.3608 | 53 |
| 12 | 4.575 | 114.3617 | 52 |
| 13 | 4.575 | 114.3625 | 53 |
| 14 | 4.575 | 114.3633 | 55 |
| 15 | 4.575 | 114.3642 | 55 |
| 16 | 4.575 | 114.365 | 56 |
| 17 | 4.575 | 114.3658 | 56 |
| 18 | 4.575 | 114.3667 | 56 |
| 19 | 4.575 | 114.3675 | 53 |
| 20 | 4.575833 | 114.36 | 55 |
| 21 | 4.575833 | 114.3608 | 54 |
| 22 | 4.575833 | 114.3617 | 57 |
| 23 | 4.575833 | 114.3633 | 56 |
| 24 | 4.575833 | 114.3642 | 55 |
| 25 | 4.575833 | 114.365 | 53 |
| 26 | 4.575833 | 114.3658 | 56 |
| 27 | 4.574167 | 114.3625 | 56 |
| 28 | 4.574167 | 114.3633 | 55 |
| 29 | 4.574167 | 114.3642 | 54 |
| 30 | 4.574167 | 114.365 | 56 |
| 31 | 4.574167 | 114.3658 | 57 |
| 32 | 4.574167 | 114.3667 | 56 |
| 33 | 4.573333 | 114.3608 | 53 |
| 34 | 4.573333 | 114.3617 | 55 |
| 35 | 4.573333 | 114.3625 | 56 |
| 36 | 4.573333 | 114.3633 | 56 |
| 37 | 4.573333 | 114.3642 | 56 |
| 38 | 4.573333 | 114.365 | 56 |
| 39 | 4.573333 | 114.3658 | 56 |
| 40 | 4.5725 | 114.3583 | 53 |
| 41 | 4.5725 | 114.3592 | 52 |
| 42 | 4.5725 | 114.36 | 53 |
| 43 | 4.5725 | 114.3608 | 53 |
| 44 | 4.5725 | 114.3617 | 52 |
| 45 | 4.5725 | 114.3625 | 53 |
| 46 | 4.571667 | 114.3592 | 54 |
| 47 | 4.571667 | 114.36 | 54 |
| 48 | 4.570833 | 114.3592 | 55 |
| 49 | 4.570833 | 114.36 | 54 |
| 50 | 4.57 | 114.3592 | 56 |
| 51 | 4.57 | 114.36 | 54 |

| | | | |
|-----|----------|----------|----|
| 52 | 4.569167 | 114.3592 | 53 |
| 53 | 4.569167 | 114.36 | 54 |
| 54 | 4.568333 | 114.3592 | 55 |
| 55 | 4.568333 | 114.36 | 54 |
| 56 | 4.5675 | 114.3592 | 53 |
| 57 | 4.5725 | 114.3642 | 57 |
| 58 | 4.571667 | 114.3642 | 57 |
| 59 | 4.570833 | 114.3642 | 54 |
| 60 | 4.57 | 114.3642 | 51 |
| 61 | 4.569167 | 114.3642 | 54 |
| 62 | 4.5675 | 114.3642 | 48 |
| 63 | 4.5725 | 114.3633 | 52 |
| 64 | 4.5725 | 114.365 | 55 |
| 65 | 4.571667 | 114.3617 | 55 |
| 66 | 4.571667 | 114.3625 | 53 |
| 67 | 4.571667 | 114.3633 | 54 |
| 68 | 4.571667 | 114.365 | 54 |
| 69 | 4.570833 | 114.3575 | 54 |
| 70 | 4.570833 | 114.3608 | 54 |
| 71 | 4.570833 | 114.3617 | 53 |
| 72 | 4.570833 | 114.3625 | 54 |
| 73 | 4.570833 | 114.3633 | 55 |
| 74 | 4.570833 | 114.365 | 54 |
| 75 | 4.57 | 114.3575 | 54 |
| 76 | 4.57 | 114.3608 | 52 |
| 77 | 4.57 | 114.3617 | 53 |
| 78 | 4.57 | 114.3633 | 54 |
| 79 | 4.569167 | 114.3575 | 51 |
| 80 | 4.569167 | 114.3608 | 51 |
| 81 | 4.569167 | 114.3625 | 51 |
| 82 | 4.569167 | 114.3633 | 54 |
| 83 | 4.569167 | 114.365 | 50 |
| 84 | 4.568333 | 114.3575 | 56 |
| 85 | 4.568333 | 114.3583 | 55 |
| 86 | 4.568333 | 114.3608 | 54 |
| 87 | 4.568333 | 114.3617 | 54 |
| 88 | 4.568333 | 114.3625 | 53 |
| 89 | 4.568333 | 114.365 | 51 |
| 90 | 4.5675 | 114.355 | 51 |
| 91 | 4.5675 | 114.3558 | 53 |
| 92 | 4.5675 | 114.3567 | 54 |
| 93 | 4.5675 | 114.3575 | 53 |
| 94 | 4.5675 | 114.3583 | 54 |
| 95 | 4.5675 | 114.3617 | 52 |
| 96 | 4.5675 | 114.3625 | 53 |
| 97 | 4.5675 | 114.3633 | 51 |
| 98 | 4.5675 | 114.365 | 52 |
| 99 | 4.570833 | 114.3567 | 53 |
| 100 | 4.57 | 114.3567 | 51 |
| 101 | 4.569167 | 114.3567 | 53 |
| 102 | 4.568333 | 114.355 | 52 |
| 103 | 4.568333 | 114.3558 | 56 |

| | | | |
|-----|----------|----------|----|
| 104 | 4.568333 | 114.3567 | 57 |
| 105 | 4.574167 | 114.3533 | 52 |
| 106 | 4.574167 | 114.3542 | 55 |
| 107 | 4.574167 | 114.355 | 58 |
| 108 | 4.574167 | 114.3558 | 57 |
| 109 | 4.574167 | 114.3567 | 55 |
| 110 | 4.574167 | 114.3575 | 56 |
| 111 | 4.578333 | 114.3608 | 54 |
| 112 | 4.578333 | 114.3617 | 55 |
| 113 | 4.5775 | 114.36 | 58 |
| 114 | 4.5775 | 114.3608 | 54 |
| 115 | 4.5775 | 114.3617 | 54 |
| 116 | 4.5775 | 114.3658 | 53 |
| 117 | 4.576667 | 114.3642 | 55 |
| 118 | 4.576667 | 114.365 | 57 |
| 119 | 4.576667 | 114.3658 | 58 |
| 120 | 4.575833 | 114.3583 | 59 |
| 121 | 4.575833 | 114.3592 | 57 |
| 122 | 4.5725 | 114.3658 | 55 |
| 123 | 4.571667 | 114.3658 | 55 |
| 124 | 4.570833 | 114.3658 | 54 |
| 125 | 4.58 | 114.3608 | 55 |
| 126 | 4.58 | 114.3617 | 58 |
| 127 | 4.58 | 114.3625 | 55 |
| 128 | 4.58 | 114.3633 | 54 |
| 129 | 4.58 | 114.3642 | 50 |
| 130 | 4.58 | 114.365 | 58 |
| 131 | 4.58 | 114.3658 | 55 |
| 132 | 4.58 | 114.3667 | 50 |
| 133 | 4.58 | 114.3675 | 47 |
| 134 | 4.58 | 114.3683 | 52 |
| 135 | 4.58 | 114.3692 | 54 |
| 136 | 4.58 | 114.37 | 53 |
| 137 | 4.58 | 114.3708 | 56 |
| 138 | 4.58 | 114.3717 | 54 |
| 139 | 4.58 | 114.3725 | 56 |
| 140 | 4.578333 | 114.3683 | 53 |
| 141 | 4.578333 | 114.3692 | 57 |
| 142 | 4.5775 | 114.37 | 54 |
| 143 | 4.576667 | 114.3692 | 56 |
| 144 | 4.576667 | 114.37 | 54 |
| 145 | 4.575833 | 114.3683 | 56 |
| 146 | 4.575833 | 114.3692 | 53 |
| 147 | 4.573333 | 114.3667 | 56 |
| 148 | 4.571667 | 114.3667 | 54 |
| 149 | 4.570833 | 114.3667 | 56 |
| 150 | 4.569167 | 114.3667 | 52 |
| 151 | 4.5675 | 114.3658 | 53 |
| 152 | 4.5675 | 114.3667 | 54 |
| 153 | 4.580833 | 114.3675 | 55 |
| 154 | 4.580833 | 114.3683 | 56 |
| 155 | 4.580833 | 114.3692 | 56 |

| | | | |
|-----|----------|----------|----|
| 156 | 4.580833 | 114.37 | 54 |
| 157 | 4.579167 | 114.3608 | 54 |
| 158 | 4.579167 | 114.3617 | 56 |
| 159 | 4.579167 | 114.3642 | 55 |
| 160 | 4.579167 | 114.3692 | 52 |
| 161 | 4.579167 | 114.37 | 51 |
| 162 | 4.579167 | 114.3708 | 55 |
| 163 | 4.578333 | 114.365 | 55 |
| 164 | 4.575833 | 114.3675 | 57 |
| 165 | 4.580833 | 114.3725 | 53 |
| 166 | 4.580833 | 114.3733 | 51 |
| 167 | 4.580833 | 114.3742 | 55 |
| 168 | 4.579167 | 114.3742 | 52 |
| 169 | 4.578333 | 114.3708 | 52 |
| 170 | 4.578333 | 114.3725 | 55 |
| 171 | 4.578333 | 114.3733 | 58 |

| | | | |
|-----|----------|----------|----|
| 172 | 4.578333 | 114.3742 | 56 |
| 173 | 4.5775 | 114.3708 | 52 |
| 174 | 4.576667 | 114.3708 | 54 |
| 175 | 4.575833 | 114.3708 | 53 |
| 176 | 4.5775 | 114.3625 | 53 |
| 177 | 4.576667 | 114.36 | 56 |
| 178 | 4.576667 | 114.3608 | 53 |
| 179 | 4.576667 | 114.3617 | 56 |
| 180 | 4.574167 | 114.36 | 54 |
| 181 | 4.574167 | 114.3608 | 54 |
| 182 | 4.575 | 114.3683 | 53 |
| 183 | 4.574167 | 114.3683 | 52 |
| 184 | 4.573333 | 114.3675 | 54 |
| 185 | 4.5725 | 114.3675 | 53 |
| 186 | 4.5725 | 114.3683 | 54 |
| 187 | 4.571667 | 114.3683 | 53 |

| | | | |
|-----|----------|----------|----|
| 188 | 4.570833 | 114.3675 | 56 |
| 189 | 4.57 | 114.3675 | 53 |
| 190 | 4.569167 | 114.3675 | 53 |
| 191 | 4.568333 | 114.3667 | 51 |
| 192 | 4.568333 | 114.3675 | 54 |
| 193 | 4.5675 | 114.3675 | 55 |
| 194 | 4.578333 | 114.3575 | 57 |
| 195 | 4.578333 | 114.3583 | 57 |
| 196 | 4.578333 | 114.3592 | 58 |
| 197 | 4.5775 | 114.3592 | 57 |
| 198 | 4.576667 | 114.3575 | 59 |
| 199 | 4.576667 | 114.3583 | 59 |
| 200 | 4.575833 | 114.3558 | 57 |

The standard deviation of the disparity in tree height can be split into four components, e.g. the instrumental, target-induced, vegetation-induced and residuals of other sources, as was explained when introducing Equation (29). The target-induced component is a function of the slope of the terrain (Equation 28) and, in this case, can be neglected because of the flatness of the terrain underlying the Badas Forest. The instrumental error component can be estimated by analysing SRTM.C elevation with known elevation of a nearly flat and homogeneous object. A good candidate with these attributes is a runway (BECEK, 2008b). A runway is flat, hence the standard deviation of the disparities in SRTM.C and reference runway elevations are of instrumental origin. Using this technique, the instrumental component of standard deviation for the Badas Forest disparities in tree height was calculated using the closest runway, which is located some 50km southwest from the site in Miri, Malaysia. The standard deviation for the runway was $\pm 0.49\text{m}$. Figure 40 shows a transect over the SRTM.C model along runway 02-20 of the Miri airport. A continuous, piecewise linear trend (one break point was identified) was removed from the data prior calculating standard deviation of disparity in elevation of SRTM.C data from the trend line, which was designed to model the runway.

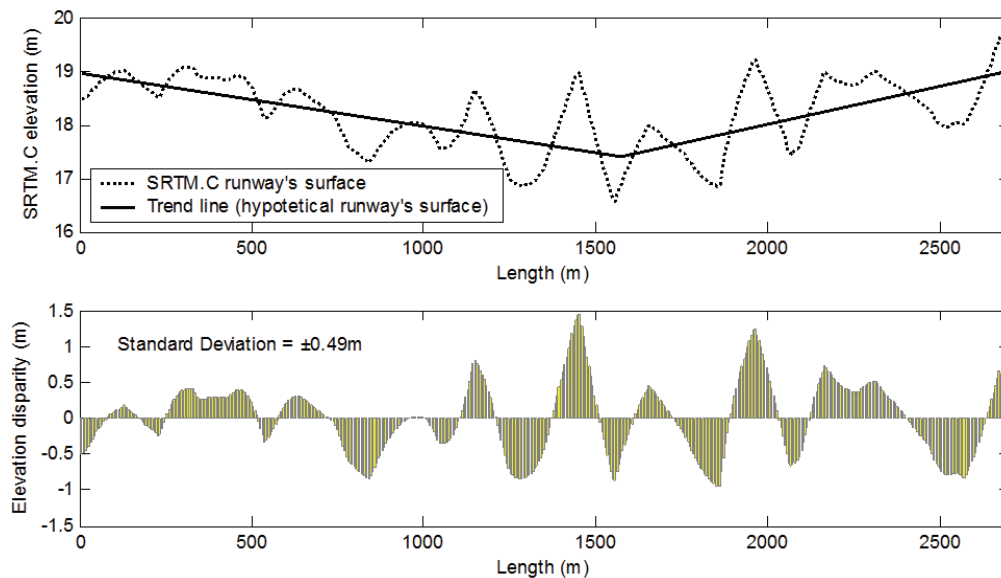


Figure 40: Transect of runway 02-20 at Miri airport, Malaysia. The upper pane shows the SRTM.C elevation along the runway (dotted line), and a trend line which represents a hypothetical surface of the runway. The lower pane shows the disparities in elevation between SRTM.C and the trend line.

The vegetation-induced component of the standard deviation can be calculated using low error propagation. Hence, the vegetation-induced error component is about $\pm 1.85\text{m}$. The standard deviation is remarkably small, considering that typically around five-fold results have been obtained by numerous researchers for various types of forest. Therefore, the value of the vegetation-induced component of standard deviation of the disparity in tree height could be considered as a lower limit for this stochastic characteristic of biomass impenetrability.

Similar tests were carried out using selected data from the Australian site. The selection process and all other steps were identical to those described above. The value of the standard deviation obtained was $\pm 10.3\text{m}$. This value is biased because of a well developed topography: the average slope was 18.2° . The target-induced component was estimated using Equation (28), and its value was $\pm 8.54\text{m}$. In addition, the localised value of the instrumental SRTM.C error was estimated using a runway at the Coolangatta airport, Queensland, which is located some 30km southeast of the site (28.16556°S , 153.5056°E). The localised instrumental error was $\pm 1.26\text{m}$. Therefore, the vegetation-induced standard deviation was estimated at $\pm 5.6\text{m}$.

Comparing results of both tests, it is clear that the standard deviation of the biomass impenetrability for the Australian site is significantly higher than that for the Badas Forest site. Since, visually, both canopies appear similarly dense, a most likely explanation for these disparities in the standard deviations are variations in the types of forests at both sites. The critical difference between the forests are most likely the gaps in the canopy (between individual trees and within each tree individually).

These observations are consistent with the following statement “*The standard deviation of the backscattering coefficient between compartments was shown to decrease as function of stem volume (...) due to the fact that at higher stem volume the canopy is a closed, relatively homogeneous layer*” (HYYPÄ *et al.*, 1994). Although, this observation was made while investigating the SAR backscattered radiation, the physical background of both SAR and InSAR observations remains the same.

It should also be noted that the target-induced error must be considered in similar calculations in order to “recover” the true picture of the situation.

A standard approach to investigate the biomass using radar assumes that a functional relationship exists between the biomass and certain characteristics of backscattered signal (QUINONES & HOEKMAN, 2004). Contrary to this view, the proposed approach investigates properties of radar signals and gaps in the biomass. The second experiment exploits the influence of inconsistency in canopy cover or gaps and biomass impenetrability. As a test field, a fragment of the Badas Forest was selected because, as proven in the previous experiment, the vegetation-induced component of the standard deviation was $\pm 1.85\text{m}$.

Careful study of Figure 38 allows the conclusion that the darker pixels indicate spatial separation between trees. This also applies to large dark areas that are due to missing individual tree(s) in the canopy cover. A typical histogram of grey-scale aerial photography of a small portion of the canopy cover, which is shown in Figure 41, clearly reveals the presence of two distinct pixel values in the canopy cover. The bi-modal shape of the histogram can be modelled using a sum of the two Gaussian density distribution functions, in the form of Equation (45):

$$y(x) = a_1 \exp(-((x - b_1)/c_1)^2) + a_2 \exp(-((x - b_2)/c_2)^2), \quad (45)$$

Using a generic form of the Gaussian density distribution function:

$$y = f(x | m, \sigma) = \frac{1}{\sigma\sqrt{2\pi}} e^{\frac{-(x-m)^2}{2\sigma^2}}, \quad (46)$$

with m and σ being the mean and standard deviation of x , respectively, one can find that $a_1 = k_1 / \sigma_1 \sqrt{2\pi}$, and $c_1 = \sigma_1 \sqrt{2}$, where k_1 can be described as a scaling factor. The same applies to a_2 and c_2 .

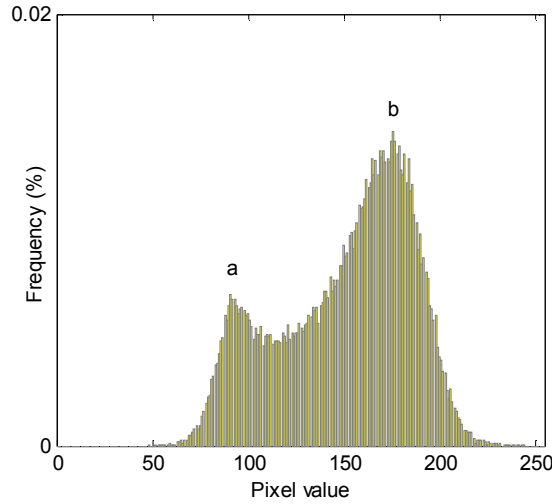


Figure 41: A typical bimodal histogram of the pixel density of grey aerial photography showing the canopy of the Badas Forest. The local maxima **a** and **b** represent gaps in the canopy and the canopy itself. The shape of the histogram depends on the pixel size. In this case, the pixel size was 0.32m.

Experimenting with the pixel size at which the aerial photography of the canopy cover was scanned (0.32m) indicated that the histogram was losing its distinct bimodal shape as pixel size increased. This is understandable because larger pixels also include some canopy fragments. Consequently, only large enough gaps are able to manifest themselves in the histogram. However, increasing the size of the study area for which the histogram is calculated should reveal larger gaps, and the histogram should retain its shape. This scale-independent property of the histogram of the canopy cover or canopy cover itself will be discussed in the next chapter.

For the experiment, a block of 12 rows by 17 columns totalling 204 samples was selected. Each sample was 3 arc-seconds in size, and these were coincidental with SRTM.C pixels. For each sample, a histogram with 256 bins was calculated. For every histogram, a fitting curve, following Equation (45), was calculated in the least squares sense. The first term of Equation (45) was considered as a histogram representing the darkest pixels (holes). A ratio between the number of pixels representing holes to the number of all pixels of the 3 by 3 arc-second area was calculated, which is considered as a measure of the “gapness” of the canopy cover.

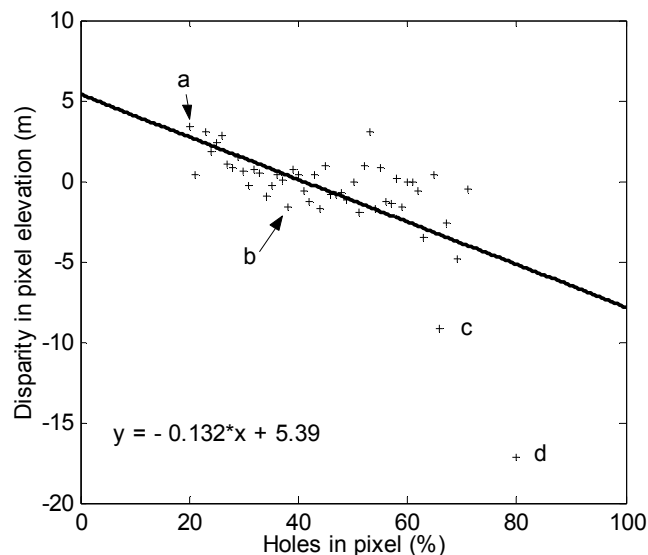


Figure 42: Average disparity in elevation of the 204 SRTM.C pixels as a function of the percentage of holes in the canopy. The marks ‘**a**’ through ‘**d**’ refer to Figure 43 showing pictures of the selected samples of the canopy.

In the next step, after subtraction of a trend line from SRTM.C elevation of selected samples, the average disparity in the SRTM.C elevations was calculated. The residuals were averaged for a given percentage of holes in the canopy. Figure 42 shows a scattergram of the disparity in the SRTM.C elevation versus percentage of holes in the canopy. A fitting line was also included.

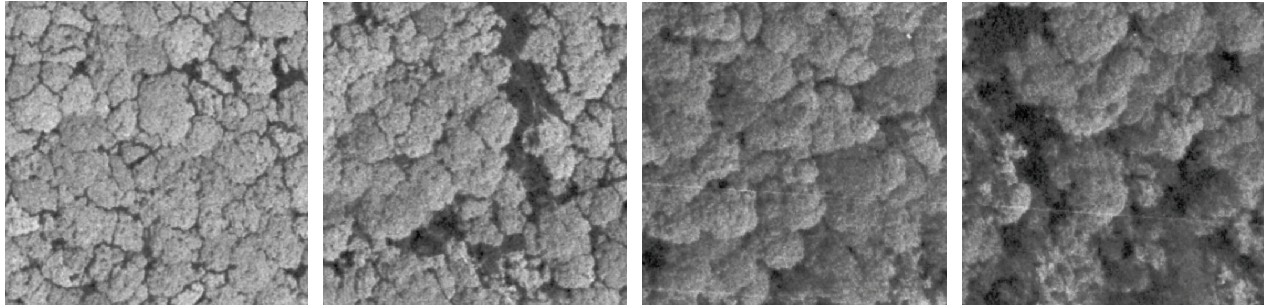


Figure 43: Picture of selected 3 by 3 arc-second samples of the canopy. The percentage of holes in the samples from left to right is 20%, 38%, 66% and 80%, respectively. Orthorectified aerial photography taken in 2002 was scanned with a 0.32m pixel for the calculations.

Figure 43 illustrates four SRTM.C pixels (3 by 3 arc-second) with various hole levels. Samples ‘c’ and ‘d’ (the last two on the right-hand side) represent pixels being considered as outliers (Figure 42). Outstanding results for these pixels are most likely due to different type of trees. It is believed that this part of the forest is a secondary forest, because it was infested by caterpillars or similar insects in the 1950’s. Hence, this is the most likely source of the inconsistency in the two outstanding samples.

A closer study of the scattergram in Figure 42 reveals that a 100% hole sample (no trees) would produce about -8m average disparity in three heights. Knowing that the tree heights in the area are about 60m tall, this would indicate an obvious error. However, this discrepancy can be explained by a very likely possibility that holes are not reaching to the bottom of the forest. This is the case when a forest is a complex multi-storey structure that is almost impossible to penetrate even by a narrow laser beam. In fact, the chance of reaching the bottom of this type of forest using LiDAR instrument are about 1-3%.

The linear character of the relationship between the average disparities in tree heights versus percentage of holes in canopy is notably consistent with the level of biomass impenetrability versus percentage of tree cover, as shown in Figure 32.

7. STUDIES ON BIOMASS IMPENETRABILITY

In view of the studies presented in Chapter 6, and based on the opinion of a number of other research studies, it is clear that gaps in the canopy are more important in the collective responses of biomass to radar radiation than was previously thought. This opinion was expressed, for example, by Rodríguez and his team, who wrote (ROSEN *et al.*, 2000, p. 370): “*the dominant mechanism is due to penetration through gaps in the canopy, although other mechanisms, such as ground-trunk interactions, may also play a significant role.*” This opinion was corroborated by the results of investigations reported by ASKNE *et al.*, (1997), TREUHAFT (ROSEN *et al.*, 2000), or more recently by KARJALAINEN and HYYPPÄ, (2009).

The aboveground biomass is living matter; consequently, it is continuously changing its properties in response to life cycles, phenology and environmental factors. Gaps or holes in biomass are one of the well known and easily recognisable effects of these types of changes. Hence, investigations of the “gapness” of the biomass (WEISHAMPEL *et al.*, 2000) can provide information on its status.

A study of this issue is presented in this chapter. The approach adopted is to create a model of the gaps in a canopy and then to subsequently investigate these using computer simulation. The biomass impenetrability is then an output of the simulation process. The simulation experiments allow investigation of the sensitivity of biomass impenetrability to various instrumental and environmental factors. This is a preferred investigation method because of the myriad of situations that can be found in the real world, but which are very often extremely difficult to identify within experimental data. The process of modelling of gaps in the biomass will commence with the establishment of some basic geometric properties and shapes of trees, which are ‘negatives’ or a plaster cast form of the gaps in the biomass. Some stochastic properties of spatial distribution of trees in a natural forest will also be investigated. These estimates are necessary for the simulation study to be conducted. It is assumed that the findings, although derived from measurements taken in the Badas Peat Swamp Forest, can be extrapolated over all types of natural forest.

7.1. Modelling a Tree and Forest

In the first step, the average tree crown dimensions were determined by two methods. The manual approach was based on 72 randomly selected samples of canopy cover. Every identified crown was manually delineated by a polygon within a GIS software package. This was performed using the already described orthorectified 2002 grey-scale aerial photography. Figure 44 shows a one hectare sample, including a vector overlay with the identified tree crowns.

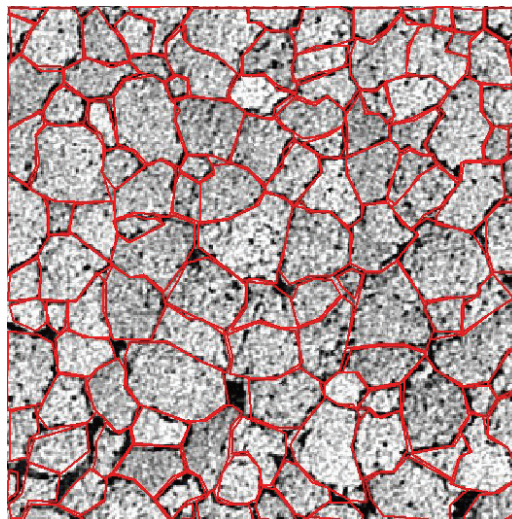


Figure 44: A one ha sample of manually delineated crowns. Coordinates of the bottom left corner are 207470E, 506972N (WGS84, UTM50N). Some 123 trees were enumerated. The average crown area was 75.4m², which is equivalent to the crown diameter of 9.8m (assuming that they are circular in shape). The area covered by crowns is 9275m², which translates to a 92.7% canopy cover.

Subsequent analysis of the polygons yielded the following facts:

1. The average area of a crown was 75.4m² ± 48.4m², ranging from 7m² to 226m²;
2. The tree density was 123 stems/ha;

3. The crown diameter was $9.8\text{m} \pm 7.8\text{m}$, ranging from 3m – 17m, and
4. The average crown cover was 92.7%.

A histogram of crown diameters is shown in Figure 45.

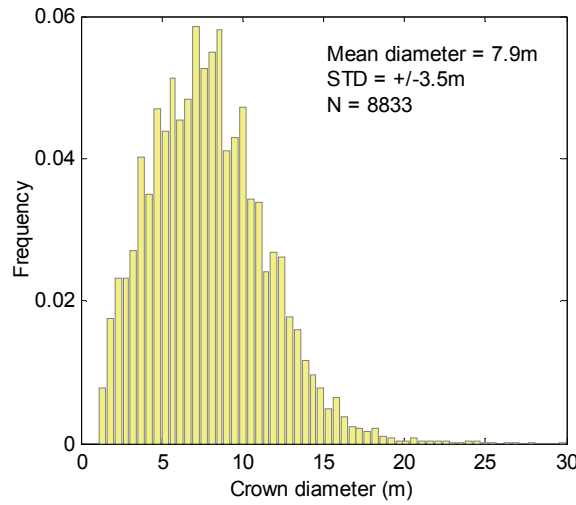


Figure 45: Histogram of diameters of manually extracted tree crowns in the Badas Forest. Mean crown diameter was 7.9m and standard deviation was $\pm 3.5\text{m}$. Some 8833 crowns were extracted.

The above described manual method is extremely time-consuming and requires a group of dedicated and well trained photo-interpreters. Therefore, a semi-automatic method was carried out to allow an independent verification of the above results. A starting point for this novel approach was the observation that an image of the crowns, as shown in Figure 44, reveals a pattern formed by the lighter crowns and the darker gaps. This actually was a justification for an attempt to determine an average diameter of a crown by performing a spectral analysis of pixel values. This method allowed the identification of the frequency or period of the most powerful periodic process within a stochastic process $y = f(x)$, where the domain of x could be any non-empty subset of real numbers; the domain of x being referred to as the time domain. This could be achieved by calculating a discrete Fourier transform of the stochastic process. An efficient algorithm needed for this is known as the Fast Fourier Transform (FFT), which can be defined as follows:

$$f(x) \xrightarrow{\Phi} \Phi_x(t), \quad (47)$$

where $\Phi_x(t)$ is the discrete Fourier transform of the stochastic process $f(x)$, and Φ is a discrete Fourier transform operator.

The discrete Fourier transform of a stochastic process is its spectral representation. A discrete Fourier transform of the probability density function of a stochastic process is called its characteristic function.

To estimate dimensions of the average tree crown and its standard deviation using this method, a set of grey-scale values of pixels located along a transect line was selected. In total, twenty randomly distributed transects, of a length of about 500m, were chosen for the calculation. The azimuth of transects was also random, which was necessary to ensure that the results were of an isotropic nature. For every set of selected pixels along each traverse, a discrete Fourier transform was calculated. The average crown diameter for each transect was identified by the maximal power spectrum, as shown in Figure 46. The average crown diameter was calculated by averaging the crown diameters for twenty transects. This allowed an estimation of the standard deviation of the mean crown diameter as well.

The average crown diameter calculated from all of the transects was $10.3\text{m} \pm 3.7\text{m}$. This method appears to be much more cost effective and convenient for performing crown diameter estimation and it produces similar results to those obtained with manual crown delineation. However, applicability of the method for other type of forests needs to be further investigated, as Figure 46 reveals significant presence of high frequency noise, which may be due, for example, to shadow and the internal structure of the tree canopy. Alternative methods for delineation of individual trees have been presented by WARNER *et al.*, (1998), whose approach was based on utilising a search window. The size of that window must be about three times larger than the average crown diameter. These assumptions are not necessary when utilising the power spectra analysis of the grey-scale value of pixels transformed into a frequency domain.

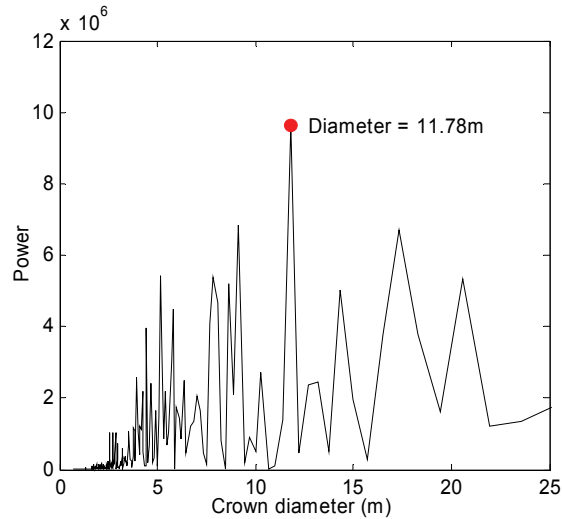


Figure 46: A typical power spectrum of pixels taken along one of the transects of the grey-scale aerial photography of the canopy cover in Badas Forest. In this case, the maximum power was for the diameter of 11.78m.

In summary, both methods produce similar results in terms of the average tree crown diameter and its standard deviation. These results will be utilised during simulation study for producing a “realistic” model of a forest.

Modelling of a forest requires statistical characteristics of the tree distribution. This applies to natural or pristine forest, where tree distribution is a result of complex ecological factors including the access to solar energy. Obviously, distribution of trees in forest plantations before commencing selective logging or other forest management operations is a deterministic one, since trees are planted in equidistant rows with equal separation between individuals within rows.

There are significant numbers of publications dealing with the spatial patterns of tree distribution; e.g., CONDIT *et al.*, (2000) and the references therein. Major findings of this extensive research are that most tree species tend to be distributed in an aggregated fashion rather than a random one. This is apparently true of all forest types.

In this research, a different modelling approach than the above has been utilised for determining spatial distribution of tree species. In this approach, the following two assumptions are made in simulating a forest. 1) Crowns of neighbouring trees do not intercept, and 2) All tree species tend to cover every piece of land. In other words, any neighbouring tree must not be closer to a given tree than the sum of the crown radiuses of both trees. A third tree to be placed in proximity of two trees must fulfil two conditions; i.e., it must not be closer than the sum of its own crown and the crowns of its neighbours. This can be expressed as:

$$\begin{aligned} R1 + R2 &= a \\ R2 + R3 &= b \\ R3 + R1 &= c \end{aligned} \tag{48}$$

where $R1$, $R2$ and $R3$ are crown radiuses of individual trees.

Equation (48) expresses the condition that must be fulfilled by a triangle with a , b and c sides. This means that a basic spatial structure is built based upon a triangle. Therefore, in order to simulate distribution of tree species in a forest, it is sufficient to randomly generate three numbers representing the radiuses of three trees. In the next step, using Equation (48), the sides of a triangle can be calculated. It is clear that the proposed approach does not allow for building any spatial relations between individual triangles, but this is not necessary in this particular study.

7.2 Modelling Gaps in the Canopy Cover

Gaps in the canopy cover can be modelled in several different ways. One of the options would be to consider the canopy as a fractal. Fractals are mathematical abstracts that hold a property referred to as self-similarity, meaning that certain properties of a fractal are scale-independent. This property of fractals is the most attractive one for practical applications, considering that many fractal-like structures have been identified among natural objects. These include trees, forests and gaps in the canopy cover (WEISHAMPEL *et al.*, 2000). A useful methodology for investigating the pattern of gaps in the canopy is the lucunarity method. Lucunarity is a fractal geometry-related method which has

already been successfully used to quantify textural patterns in single trees (USTIN *et al.*, 1991, MARTENS *et al.*, 1993), and to monitor changes in forests at various scales (WEISHAMPEL *et al.*, 2000).

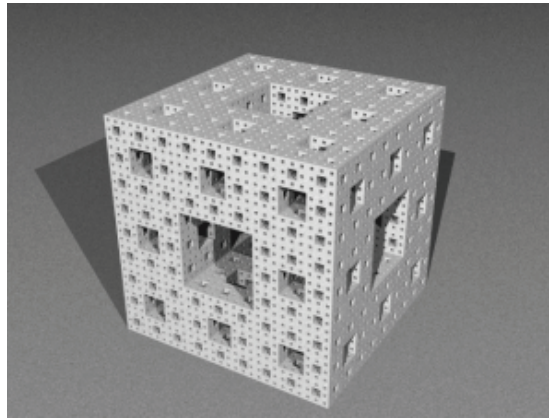


Figure 47: The Menger sponge – 3D fractal. Source: http://en.wikipedia.org/wiki/Menger_sponge.

Figure 47 shows an example of a 3D fractal known as the Menger sponge. This structure is considered here as an intellectual stimulus or potential outcome of the modelling of the tree canopy. The most important property of the Menger sponge is the fact that it has an infinite surface area and encloses zero volume. In other words, the fractal is an extremely complicated 3D structure, and yet it is empty. That ‘emptiness’ appears to be the most attractive feature of the fractal because of its similarity to the ‘gapness’ found in the forest.

The term gap or hole in the biomass refers to a fragment of 3D space of any size located within boundaries of the biomass (say, the forest stand). It is also assumed that a gap is free of any particles suitable for interacting with radar radiation of a certain frequency, and that a gap allows propagation of a beam of radiation for a distance larger than zero.

Modelling of gaps in a forest is built upon a few commonly observed facts. Here, we assume that the three following types of gaps are found in the forest:

1. Gaps in the canopy of the size of at least one tree, (Type 1).
2. Gaps that occur between neighbouring individual trees (Type 2), and
3. Gaps that are found within tree crown.

The above classification of gaps implies that they are of various sizes, which means that they are present at all scales of biomass representation, e.g. micro scale – individual tree, mezoscale – forest stand, and macro scale – regional to global forest ecosystems.

Another important property of gaps in the biomass is the fact that they are the same everywhere and are independent of the forest ecosystem. The differences are in their stochastic properties. It is this single fact that makes the gaps such an attractive and powerful a device for investigation of biomass.

Modelling Type 1 gaps.

This type of gap in the forest canopy is a sign of a random event such as a lightning strike, forest fire, insect infestation, or logging, among others, and is referred to as a scar. These can be of the size of a single fallen tree. Therefore, all gaps of the size of the crown of a single tree and larger are classified as Type 1 gaps. The only possibility to include gaps larger than one tree in the modelling would be to determine their stochastic properties. A useful starting point for the statistical modelling of gaps is the assumption that a relationship between the size of gaps and their number follows a power-law distribution function. A justification can be built upon similarity of decaying or wearing processes of natural and man-made objects, which follows a power-law function, and a process of forest degradation or decay. In addition, a power-law possesses the property of scale invariance. In other words, the same function is valid for both small and large areas. In the case of a forest, this translates to the fact that the distribution of gaps of a given size in a one-hectare plot is the same as in a one-hundred hectare plot. However, this is a logical consequence of the observable fact that the same natural mechanisms are at work, independently of the size of the object. Discussions on properties of power law can be found, for example, in MITZENMACHER, (2003), and references therein.

A measurable variable x follows a power law if it can be shown that its probability distribution function is proportional to a power function of x , which can be expressed using Equation (49) (CLAUSET *et al.*, 2009):

$$p(x) \propto x^{-\alpha}, \quad (49)$$

where α is the scaling parameter.

In the case of discrete values of x representing the area (m^2) of the Type 1 gaps, the probability distribution takes the following form:

$$p(x) = \Pr(X = x) = Lx^{-\alpha}, \quad (50)$$

where L is the normalisation constant.

The density function in that form diverges for $x = 0$. Hence, a lower bound $x_{\min} > 0$ must be found. This means that the so called “long tile” or just a part of the dataset $x > x_{\min}$ follows the power law probability distribution. It is a well known fact that a complimentary way of presenting a probability distribution function is its cumulative probability density function (CDF).

Estimation of the constant parameters in Equation (50) can be done by maximizing the likelihood estimator (CLAUSET *et al.*, 2009). However, the task is somewhat easier when Equation (50) is rewritten as follows:

$$\ln p(x) = -\alpha \ln x + \ln L, \quad (51)$$

Necessary data for the estimation were acquired by extracting gaps from the Badas site. Figure 48 shows a part of the test site used in the experiment. The site was about 2350m by 2470m, within which some 2360 gaps were delineated. Extracted polygons were used to calculate the size of each gap. The smallest and largest gaps were 46m^2 and $342,556\text{m}^2$, respectively.

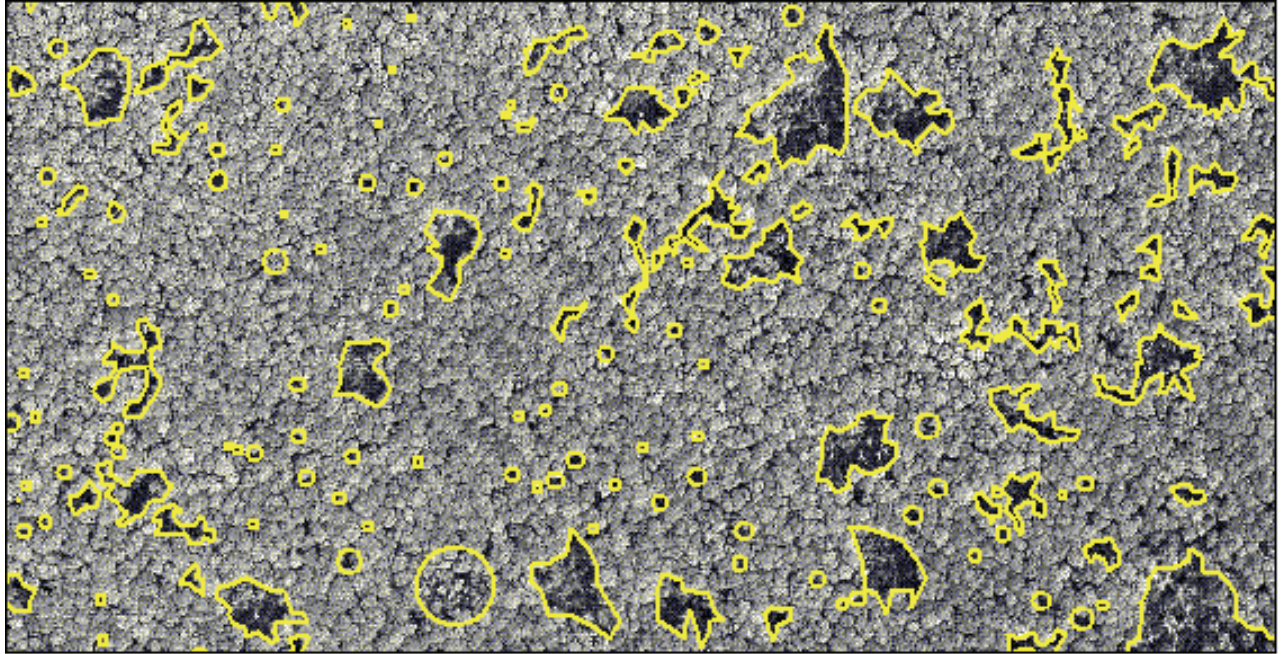


Figure 48: Identified gaps in the canopy cover of the Badas test site. The area shown in the picture is about 1km by 0.5km. The coordinates of the bottom left-hand corner are 207817E, 505990N (WGS84, 50N).

A software package attached to the article (CLAUSET *et al.*, 2009) was utilised for computations. The software automatically identified the lower limit for the gap size, which was $x_{\min} = 146\text{m}^2$. This means that all gaps larger than x_{\min} follow the power-law distribution. Figure 49 shows the cumulative density function calculated from the data ($x \geq x_{\min}$). Circles indicate the calculated values of CDF, whereas the solid line indicates the regression line fitted in the CDF. The slope of the fit is an estimate α' for the scaling parameter α .

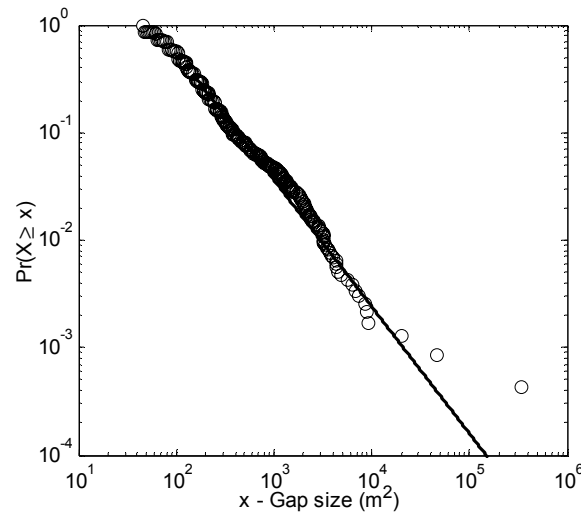


Figure 49: Cumulative probability density function – CDF of the Type 1 gap sizes in the Badas Forest.

The scaling parameter was $\alpha = 2.18$ and the normalisation constant was $\ln L = -25.448$. A *p-value* test of statistical significance indicated that the hypothesis about the power-law probability distribution of the size of gaps in a forest canopy cannot be ruled out.

The few outliers visible in the right hand corner of the plot are due to the single occurrence of very large gaps in the forest canopy.

The power-law distributed random number generator was used to simulate gaps in a modelled forest (CLAUSET *et al.*, 2009).

Modelling Type 2 gaps

Modelling of Type 2 gaps – free space between trees – is the most relevant for the studies of the biomass impenetrability. This is because the gaps are a ‘natural’ part of the forest ecosystem, not like Type 1 gaps which may be products of some kind of “accidents” caused by both natural and anthropogenic forces. In addition, Type 2 gaps are stable in terms of their dimensions. They can be described by the shape of the tree crown and its diameter, tree height and distance between trees. Therefore, the approach to modelling these gaps will involve modelling the trees themselves. It is assumed that the gaps are open from the top, and that they may be open from the bottom, because it is rather uncommon to see a 100% closed forest. The basic shapes of trees and dimensions used to describe them are shown in Figure 51. These generic tree shapes are utilised in the simulation studies. Obviously, many more shapes of trees exist; some references to the classification of the tree vegetation can be found in (QUINONES & HOEKMAN, 2004). However, it is believed that investigation of these basic shapes is sufficient to draw universal conclusions from the simulation results. A more detailed mathematical model of tree crowns has been provided in the recent report by CRECENTE-CAMPO *et al.*, (2009) and the reference list therein. Advanced mathematical tree models such as the AMAP model which are able to produce a realistic and flexible tree model suitable for studies of trees crowns using, for example, a radiative transfer theory do exist (CASTEL *et al.*, 1997), and may probably be applied for studies on the biomass impenetrability. More work in this area is required. Some prominent attempts to mathematically model trees and forest growth were presented in numerous papers including reports by Ranson *et al.*, (1997), Sun & Ranson (1995) and Picard *et al.*, (2004a) to mention a few.

A model of Type 2 gaps will be built upon trees located in vertices of a triangle. Figure 50 shows horizontal and vertical cross-sections of a fragment of forest. The crowns are of conical shape in this case. The gap in the centre of the dark triangle is free of trees and allows the radar waves to penetrate to the ground.

A concluding step in the modelling of Type 2 gaps is calculation of the impenetrability that is contributed by the three trees located in the vertices of the triangle. Because the shapes of tree crowns to be used in the simulation are mathematically-simple revolving solids, the impenetrability for a single triangle can be easily calculated.

The impenetrability for a collection of triangles will be an arithmetical mean of the impenetrabilities of all triangles in the collection. This approach implies that the trees are considered as impenetrable solids. However, the penetrability of trees will be allowed and modelled using Type 3 gaps in the forthcoming section.

It is worthwhile noting that the proposed model of the Type 2 gap implies that the crown closure or crown cover (HOWARD, 1991), in the extreme case when all crowns are touching each other, as in Figure 50, is always below 100%. Depending on the shape of the triangle, it is about 92%. By changing the diameter of tree crowns (once used to generate a triangle), it is possible to control the crown closure parameter for that triangle within the simulation software.

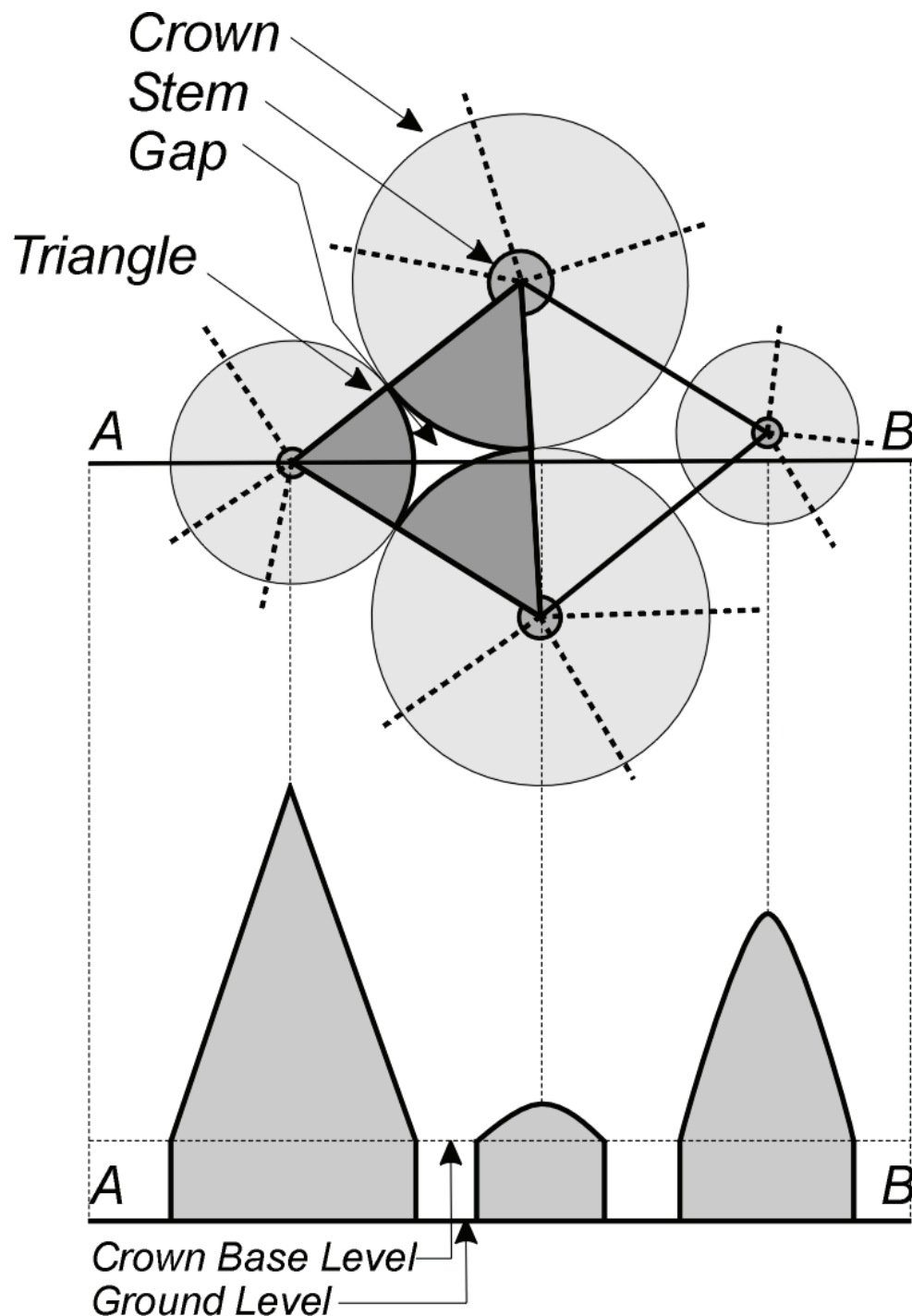


Figure 50: Horizontal cross-section at crown base level. (upper part of the graph). Triangles are built upon tree stems. Crowns may not overlap. White area within a dark triangle is an opening which is free of trees. The lower part of the graph shows a vertical cross-section along the AB line. Some lines between the upper and lower parts of the graph were provided for reference to indicate corresponding points in both cross-sections.

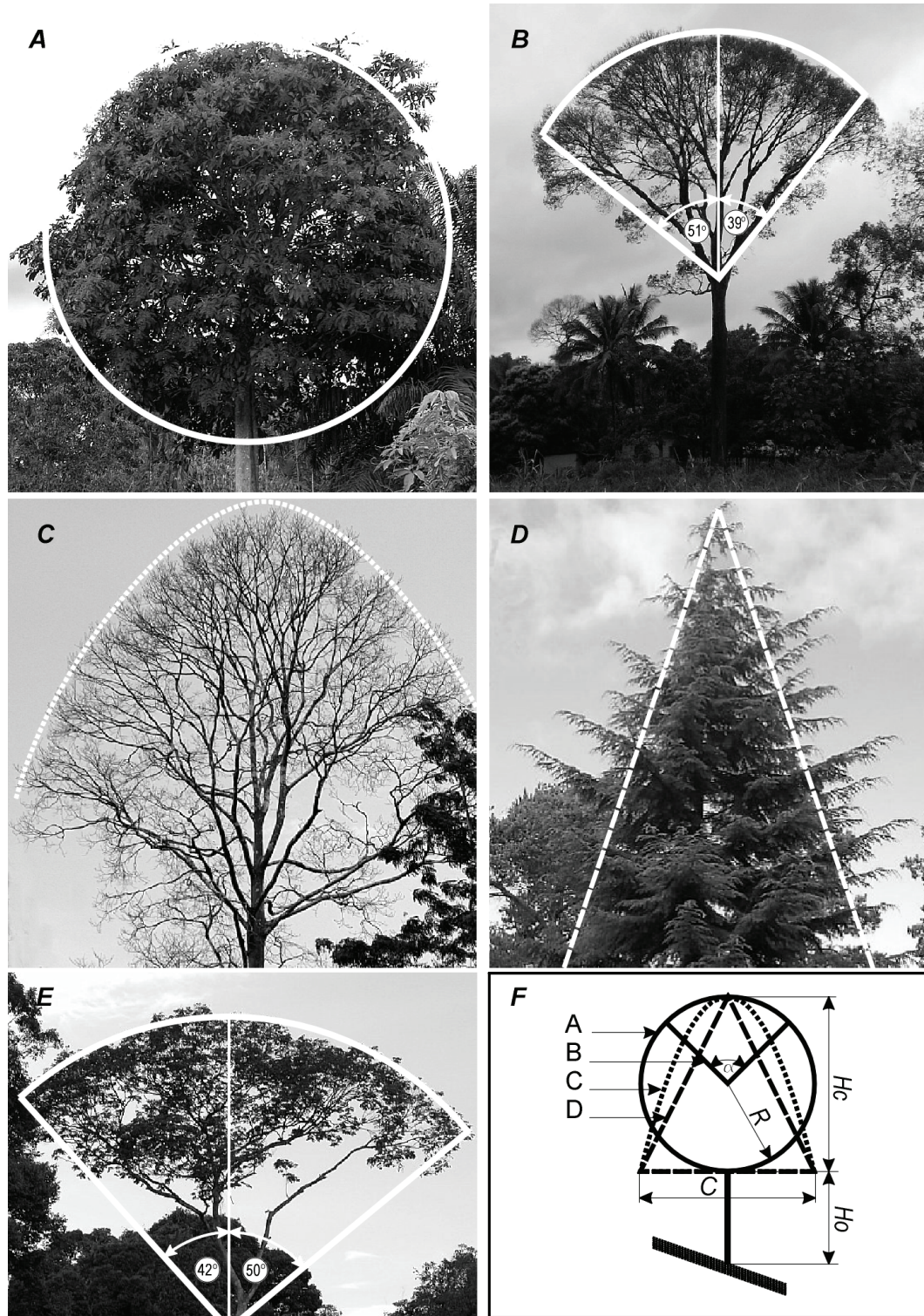


Figure 51: Selected shapes of trees crowns used in the simulation study. Panel A – sphere; Panel B and E – part of a sphere; Panel C-paraboloid; Panel D - cone. Pane F shows dimensions used to describe the shapes, where R (m) is the radius of the sphere (model A), H_o (m) is the stem height from the ground to the crown base (all models except models B and E), H_c (m) is the height of the crown (all models except models B and E), C (m) is the width of the crown at its base (all models except models B and E), α is a solid angle (deg or sr) describing the part of a sphere (models B and E). The stem height for models B and E is $H_o + R$. The crown base $C = 2R\sin(\alpha/2)$. Models B and E are essentially identical. The only difference is that both models exhibit an asymmetry (note the angles in the centre of the crown). The asymmetry is caused by the adaptation of the tree to the local conditions, i.e., the presence of neighbouring trees. The symmetry, i.e., both angles are equal, is assumed in the study.

The impenetrability caused by each tree depends on its shape dimensions. Panel F in Figure 51 explains the symbols adopted for the dimensions of a tree. The impenetrability of a triangle is a sum of volumes of parts of tree crowns found within the triangle over the area of the triangle. Therefore, it can be calculated from the following formula:

$$v_t = \frac{V_1^t + V_2^t + V_3^t}{A_t} \quad (52)$$

where V_1^t, V_2^t, V_3^t are the volumes of parts of crowns relevant for triangle t (Figure 50),
 A_t is the area of a triangle.

Formulas for calculation of volumes of crowns of various shapes are readily available from Table 22.

Table 22: Formulas for calculation of volume of crown of various shapes.

| Tree Shape | Impenetrability | Note |
|---------------|--------------------------------------|--|
| Cone | $V = \frac{\pi}{12} C^2 Hc$ | C – crown diameter, Hc – Crown height |
| Paraboloid | $V = \frac{\pi}{8} C^2 Hc$ | C – crown diameter, Hc – Crown height |
| Sphere | $V = \frac{\pi}{12} C^3$ | C – Crown diameter |
| Spherical cap | $V = \frac{\pi}{6} h (3C_B^2 + h^2)$ | $2C_B = C \sin(\alpha/2)$ - diameter of the crown cap; α – angle of spherical cap representing the crown (Figure 51, Panel F) $h = C/2 (1 - \cos(\alpha/2))$ |

In calculating the impenetrability of a tree, more than just the contribution of the crown must be considered. The volume between the ground and the base of the crown is the space shadowed by the crown, and therefore must be added to the total volume of the tree to be considered in the calculation of impenetrability. The volume of this space can be estimated as a volume of a cylinder with the diameter of the base equal to the diameter of the crown, with the height equal to stem height - H_o (Figure 51). For example, the volume considered in calculation of the impenetrability of a cone-shaped tree is $V_{total} = \pi/12(C^2 Hc) + \pi/4(C^2 H_o)$.

It is clear that each tree in a triangle contributes only a fraction of its volume to the impenetrability (Figure 50). That fraction is a function of the internal angle associated with the vertex in which the tree is located. The following formula can be used to calculate that fraction:

$$p_i = \frac{\varepsilon_i}{2\pi}, \quad \text{with} \quad \sum \varepsilon_i = \pi, i = 1, 2, 3. \quad (53)$$

where ε_i is the internal angle of the triangle.

The area of a triangle can be calculated using Heron's formula, which in numerically stable forms, can be written as follows (<http://www.eecs.berkeley.edu/~wkahan/Triangle.pdf>):

$$A = \frac{1}{4} \sqrt{(a + (b + c))(c - (a - b))(c + (a - b))(a + (b - c))}, \quad (54)$$

Symbols assigned for the sides must follow the order: $a \geq b \geq c$. Also, it is important to follow the calculations as indicated by the parentheses.

Finally, it is assumed that tree crowns do not intersect, and not all trees must be present in the triangle.

Modelling Type 3 gaps

Type 3 gaps are spaces within the tree crown. Borders of these gaps may be defined by leaves and other morphological parts of the tree. For the purpose of this study only gaps which are penetrable by the incoming radar waves are considered. Two parameters will be used to characterise these gaps:

1. The size (area) of the gap, and
2. The depth of the gap.

The penetrable gaps can be imagined as cylinders which are open at the top and may be closed within tree perimeters or by underlying land cover, if any. An illustration of the penetrable gaps is shown in Figure 52.

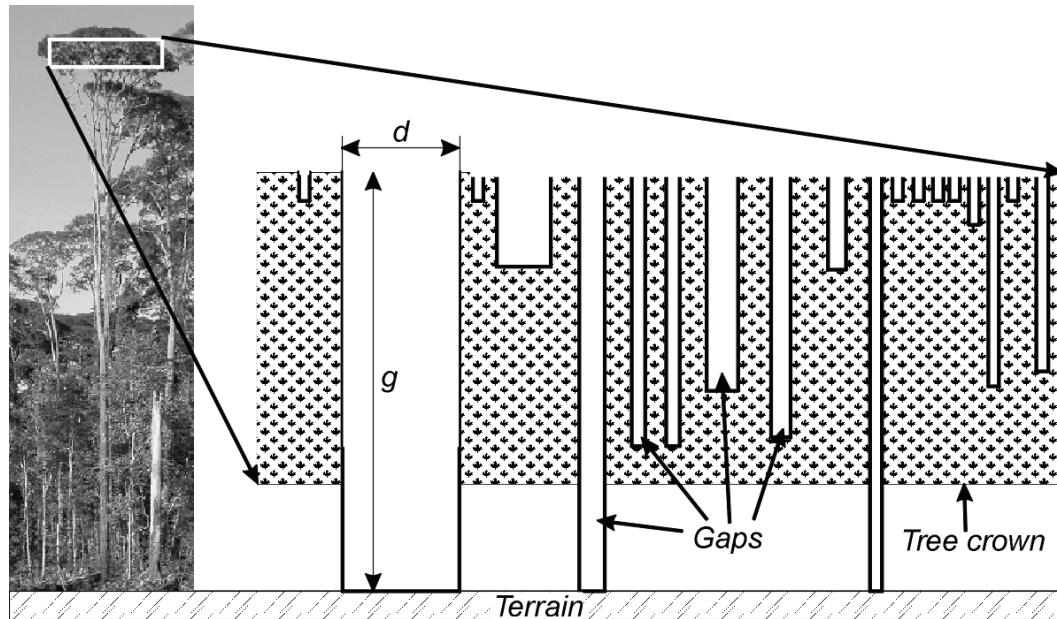


Figure 52: Illustration of the penetrable gaps within the tree canopy.

The size and the depth of the gaps are continuously changing in response to the environmental factors over very wide time scales. For example, wind alters boundaries of the gaps at a very high rate, while long-term climate variations alter the gaps at a much slower rate.

The majority of the literature sources relate foliage changes to the meteorological conditions (wind) and seasonal variations (leaf on/off periods) (ASKEN *et al.*, 1997). The long-term variations of gaps are considered in BECEK & ODIHI, (2008), and BECEK, (2008c), (2008d). The spectrum of the dimensions of gaps is also very wide, and includes small gaps (larger than the radar wavelength) within a single leaf, up to big gaps between branches and stem.

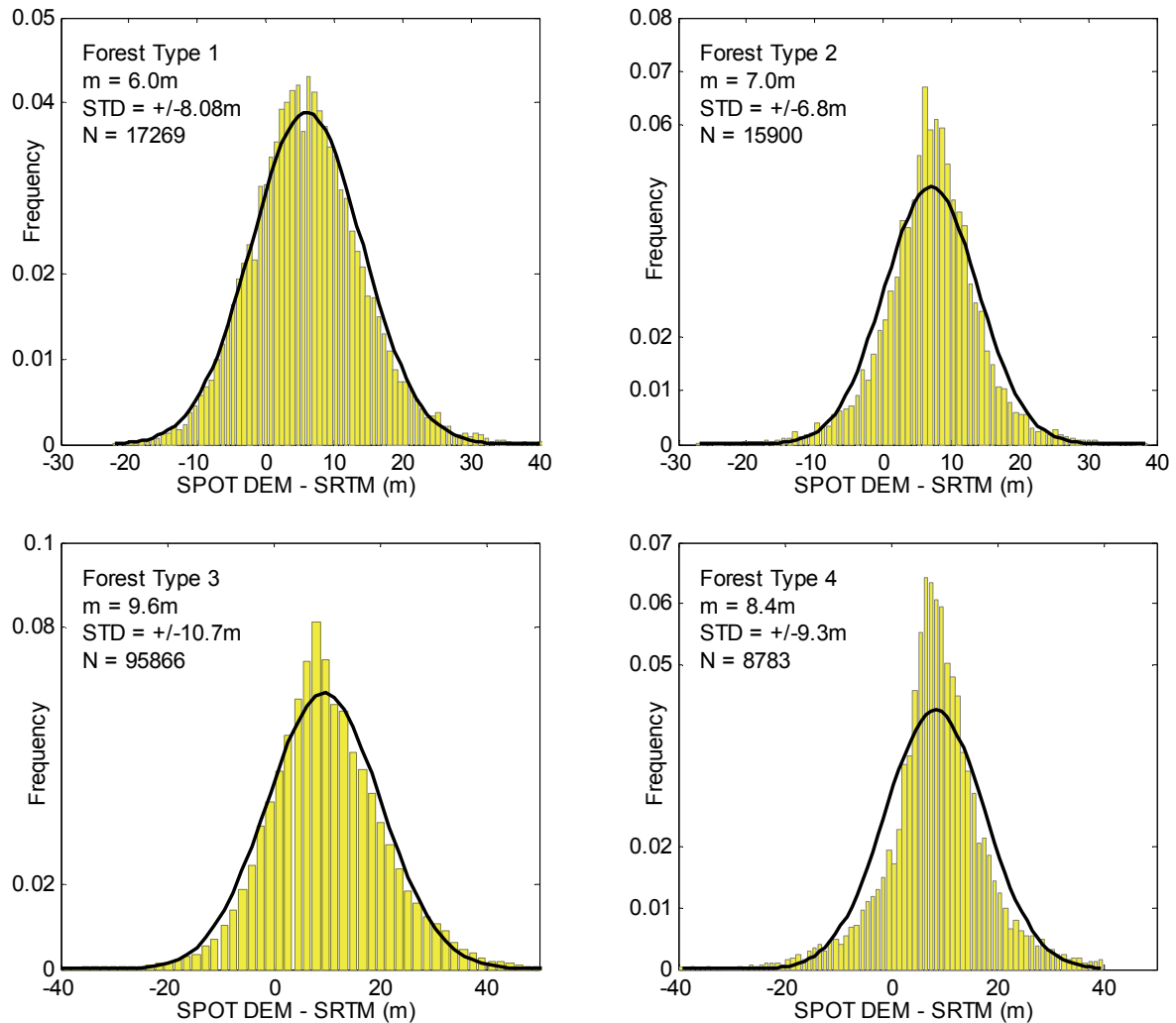
There are few literature sources in which the gaps have been explicitly studied (WEISHAMPEL *et al.*, 2000). This study was conducted using a LiDAR survey of a patch of a tropical forest in Costa Rica. An already mentioned method, known as the lucunarity method, indicated that the tree canopy exhibits fractal-like properties. The canopy could also be considered as an isotropic medium.

To model Type 3 gaps, a statistical model of Type 1, e.g., the power law distribution of the gaps, was adopted. This assumption was founded on the fundamental property of the power law distributed phenomenon, which implies that the properties of the phenomenon are scale-invariant. In particular, the following assumptions are made:

1. The size (area) of gaps in crown follows a power law density distribution,
2. The depth of gaps follows a power law density distribution.

The “gapness” of a tree crown can be investigated using a LiDAR survey of the crowns. This method was demonstrated by several researchers including Rodríguez and his colleagues (ROSEN *et al.*, 2000, WEISHAMPEL *et al.*, 2000, SOLBERG *et al.*, 2008). At this point, it is worth noting Rodríguez’s remarks that the gap penetration is frequency-independent, and this is valid at high frequencies (ROSEN *et al.*, 2000). This means that both the SRTM C- and X-band should provide similar results; i.e., they should have very similar impenetrability readings. However, what this also

means is that a DEM derived from the optical data such as SPOT DEM (APPENDIX 2) should also represent a surface within a canopy tree. Obviously, this is not the case, because SPOT DEM represents the elevation of the first reflective surfaces, e.g., the canopy tree. To the best knowledge of the author, this as yet unpublished source of disparities in both SRTM and SPOT DEM elevations most likely is a quantisation level of backscattered signal or level of the radiometric resolution. The 8 bit resolution of SPOT 5 HRS (High Resolution Spectroscopic) imagery that is used to produce the DEM is too low to extract any useful data from areas of weak signal such as shadows and including gaps. In the case of the SRTM, the amplitude or backscattered data were acquired at 16 bit resolution, which greatly increases the sensitivity in areas of weak signal. Therefore, the SRTM represents lower levels of the canopy than are the SPOT DEM, which represent the outermost elements of the canopy.



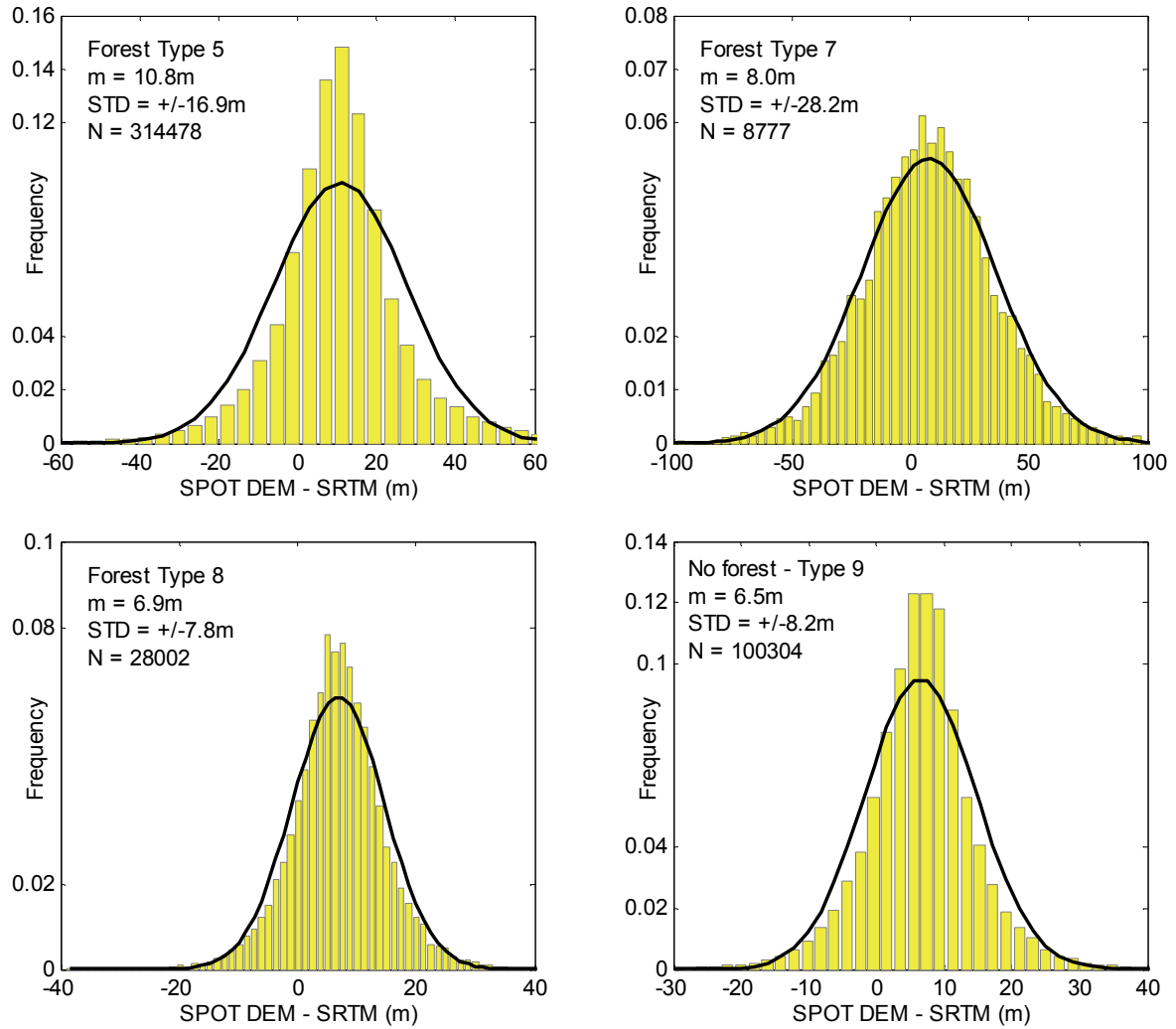


Figure 53: Histograms of differences SPOT DEM minus SRTM for each forest type and the Type 9 land cover for Brunei Darussalam. The Gaussian fitting curve was drawn for mean (m) and standard deviation (STD) as provided in each panel.

A useful conclusion from this observation is the possibility to characterise the “gapness” of tree crowns by comparing corresponding pixels of DEM, extracted using backscattered signals at various radiometric resolutions. This can be facilitated for the same forest parcel to ensure that the influence of both Type 1 and 2 gaps on the impenetrability will be cancelled by subtracting one DEM from the other.

In the following, results of this type of attempt are described. The SPOT DEM and SRTM.C are compared. The disparities in elevations over forested areas are attributed to the gaps in the canopy cover only. Naturally, the difference was subject to noise from various sources.

The SPOT DEM that was supplied at 20m resolution was down-sampled to match the resolution (3 arc-second) of the SRTM.C elevations. The coincidental location of both pixels was maintained. A difference SPOT DEM minus SRTM.C for all available pixels was calculated. The differences were tagged using the forest types and Type 9 land cover, as per the forest map of Brunei Darussalam (APPENDIX 2). Figure 53 shows eight histograms of the differences for all of the forest/land cover. A few conclusions may be drawn from these histograms.

The first conclusion is that the mean difference for all of the histograms is fairly similar (6.0m – 10.8m). The spread among the forest Types 2 – 7 is even smaller (7.0m – 10.8). The Type 1 forest appears to be a special case with the lowest difference – 6.0m. However, this figure appears to be consistent with the tightly arranged leaves, branches and stems of the mangrove forest. Type 8 forest and remaining land cover possess relatively low differences, which is probably due to the significant contribution of open spaces, in which the difference between both DEM is equal to zero. Hence, the average difference tends to be lower.

The standard deviation of the difference, SPOT DEM minus SRTM.C, is the highest for the Type 7 forest at $\pm 28.2\text{m}$. This is the type of forest that is located in rugged terrain. Therefore, the target-induced error is a significant component of the figure. The second largest standard deviation is for the mixed dipterocarp forest (Type 5). This is most likely caused by a contribution from areas which had been previously logged out. The presented findings are somehow biased because of the time lapse between reference years of both SRTM and SPOT DEM datasets (2000 vs. 2008). However, it is believed that the overall pattern holds. These data will be used, along with the assumption regarding the power-law distribution of the gaps, in the simulation study in order to generate the gaps within tree crowns.

7.3 Modelling the Incidence Angle

The approach to model the gaps presented in the preceding section is based on an assumption that the radar waves enter the vegetation cover from the zenith down perpendicular to the ground. In terms of the incidence angle Θ (see Section 5.2) this means that it is zero. In such a case, the impenetrability reaches the lowest possible value. For any not equal zero incidence angle the impenetrability will be larger than minimal and may theoretically reach 100% for a hypothetical incidence angle equal $\pi/2$.

It must be noted that this is only theoretical situation for an InSAR system. In order to fulfil the optimal geometric condition for InSAR, the look (incidence) angle must be between $20^\circ - 60^\circ$. For example, the SRTM.X system was operated at a constant incidence angle of 52° , while the SRTM.C system operated in a scan mode allowing variations of the incidence angle between 30° and 58° (KIEL *et al.*, 2006). See (BAYER *et al.*, 1991) for more details on incidence angle.

One can also note that the incidence angle of zero represents a vertical LiDAR survey. Hence, the presented here study, may be applicable for LiDAR analysis.

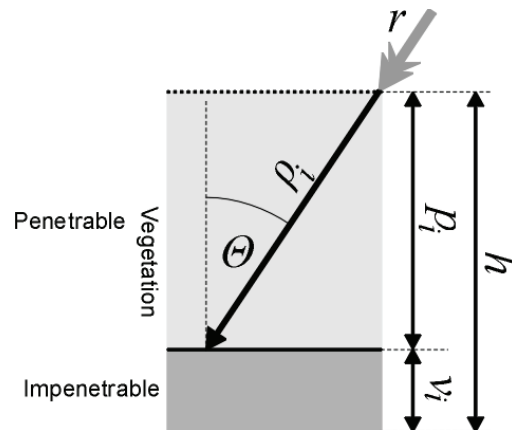


Figure 54: Model of vegetation medium. The vegetation of the thickness (h), is splitted into the penetrable and impenetrable layer. The thickness of the impenetrable layer corresponds the impenetrability – v_i , of a resolution cell (pixel). The thickness of the penetrable layer – p_i is obtained from the path length (ρ_i) of the radar waves (r) and the incidence angle Θ .

In this study, the incidence angle will be used to convert the “stright-down” impenetrability to its realistic values. Figure 54 shows a resolution cel – a pixel – including all necessary symbols and notations. Let, the radar waves (r) enters vegetation layer under the angle of Θ . Assuming that the path length is ρ_i , one can calculate the thickness of the penetrable layer of vegetation p_i . Hence,

$$p_i = \rho_i \cos \Theta, \quad (55)$$

As it was already mentioned, that in the case $\Theta = 0$ the tickness of the penetrable layer reaches its maximum (hence the impenetrability is minimum!) Therefore, the tickness of the penetrable layer for $\Theta > 0$ can expressed as follows:

$$p_\Theta = p_{\max} \cos \Theta, \quad (56)$$

Equation (56) can be expressed in terms of impenetrability as follows:

$$\frac{v_i}{h} = \frac{h - (h - v_{\min}) \cos \Theta}{h} \quad (57)$$

where $\frac{v_i}{h}$ is the impenetrability normalised by the forest height, for the incidence angle larger than zero.

The formula in Equation (57) can be used to convert the $\Theta = 0^\circ$ impenetrability which is the lowest possible into a “realistic” $0 < \Theta < 90^\circ$ impenetrability which might be theoretically equal to 100% for the incidence angle $\Theta = 90^\circ$. Because the relationship is a monotonic type of function for clarity reasons all calculations will be performed assuming the $\Theta = 0^\circ$.

7.4 Simulation study of the biomass impenetrability

In the previous section, a model of both horizontal and vertical structure forest was developed. This model will now be used to test how the various parameters of forest and the incidence angle influence the forest impenetrability. A computer program was developed to facilitate the simulation studies. The major data processing steps include:

1. For a given mean crown diameter and its standard deviation, three crowns are generated using a normally distributed random number generator. Crowns with diameter smaller than a certain threshold are rounded up to that threshold;
2. A triangle is constructed based on the generated crowns;
3. Stem height H_o , crown height H_c and type of crown shape are assigned to each tree individually;
4. By repeating steps 1 – 3, a required number of triangles is generated;
5. Type 1 and 3 gaps are generated, if required. The power-law distributed random numbers are generated.
6. These numbers are used to alter tree crowns (allowing for a degree of penetrability of the crown), and a group of trees by removing some of these from the set of generated triangles;
7. The impenetrability versus selected variable is simulated.

The input data structure includes the following records:

1. R1 – R3: Crown diameters;
2. R4 – R6: Internal angles of triangle;
3. R7: Area of triangle;
4. R8: Tree type (Cone, Paraboloid, Sphere and Spherical cap);
5. R9 – R12: Crown height;
6. R13 – R14: Stem height.

The canopy closure (HOWARD, 1991) will be modelled using a ratio between the area of tree crowns covering a triangle and the area of the triangle. Canopy closure (CC) will be expressed in (%). It must be noted that this definition of CC does not allow for $CC = 100\%$. This is because of the assumption that tree crowns do not intercept. Hence, there is always a gap in the centre of a triangle, which is shown in Figure 50. The area of the gap depends on the shape of the triangle. Due to this fact, a normalisation is necessary. This may be achieved by dividing the CC of a triangle by the maximum CC found among all simulated triangles. In this way, the normalised CC may be equal to 100%.

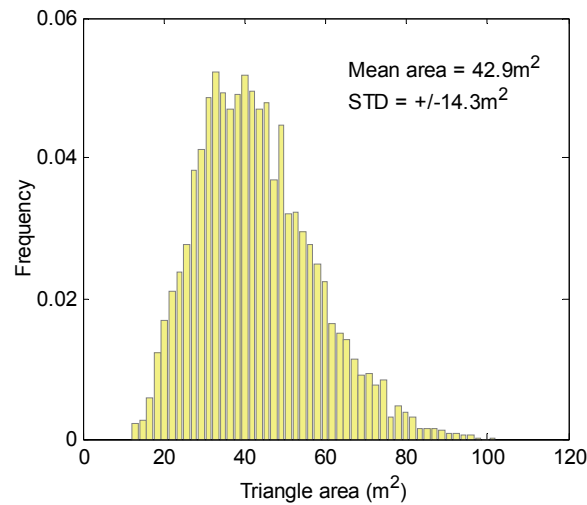
The use of the canopy closure to characterise a forest is a long-standing practice in forestry science. However, it is not adequate for describing a forest in 3D terms, including the impenetrability. One obvious reason for this is that the canopy closure does not depend either on the shape of the crown or on the height of the tree. However, for documentation purposes, a simulation experiment will be carried out to investigate the relationship between the impenetrability and the canopy closure.

Impenetrability vs. type of tree shape

The first experiment was designed to assess the influence of the type of tree shape on the impenetrability (Type 2 gaps). Table 17 shows the constants used in the simulation. The area of an average triangle was 43.1m^2 . This translates into a pixel size of $\sim 6.6\text{m}$. Incidence angle was $= 0$.

Table 22: Constants used in the first simulation experiment.

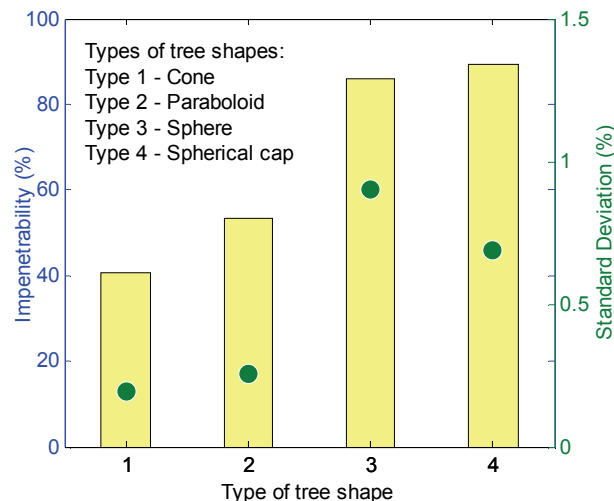
| Crown Diameter (m) | Min. Crown Diameter (m) | STD (m) | H_o (m) | H_c (m) | No of triangles | Forest Area (ha) |
|-----------------------|----------------------------|------------|--------------|--------------|-----------------|---------------------|
| 10 | 5 | 3 | 5 | 25 | 50000 | 215.5 |

**Figure 55:** Histogram of areas of simulated triangles.

The histogram in Figure 55 was produced based on 50,000 randomly generated triangles. The mean area of a triangle was 42.3m^2 with standard deviation $\pm 14.3\text{m}^2$. The triangles were calculated based on randomly generated tree crowns. As per Table 23, the mean crown diameter and its standard deviation were set to $10\text{m} \pm 3\text{m}$.

Due to the rounding up of the crown diameters less than the minimal crown diameter (5m), the histogram does not look like a “normal” histogram. However, it is very much similar to the histogram shown in Figure 45. This histogram was produced based on nine thousand crown diameters collected in the Badas Forest.

The bar graph in Figure 56 shows the impenetrability values caused by various tree shapes. The lowest and highest impenetrability is caused by the conical and spherical cone type of trees, at ~40% and ~89%, respectively. Considering the average tree height ($H_o + H_c = 30\text{m}$) the impenetrability translates to 12m and 26.7m. The adjusted canopy cover was 100%.

**Figure 56:** The impenetrability vs. type of tree shape (Type 2 gaps). The dots indicate standard deviation of the impenetrability.

The lowest impenetrability (40%) was exhibited in a forest composed of cone-shaped trees, such as spruce trees of the genus *Picea*. The highest impenetrability shows a forest with trees of spherical cap shape such as the Alan tree (*Shorea albidia*). Differences in impenetrability between types 1, 2 and 3 or 4 indicate an opportunity to identify the type of tree shape based on the impenetrability, in the case when the forest is fully stocked (CC approaching 100%).

The most important conclusion from this experiment is that Type 2 gaps explain the bulk of the impenetrability usually reported in the literature, e.g., between 50 to 60% of tree height (see also Chapter 6). This is a stunning result, which provides an important insight into the interaction between radar radiation and biomass. However, it is important to note that Type 3 gaps (the gaps within the crown) and the incidence angle must still be considered for a comprehensive assessment of the magnitude of the impenetrability in the real situation.

It was already mentioned that only the Type 2 gaps influence the SPOT DEM. This is because the eight-bit coding of the optical images is too low to register reflected light from the interior of the canopy. This hypothesis seems to be supported by investigations of the SPOT DEM over forested areas in Bavaria. It was found that the SPOT DEM exhibits an elevation bias of about 12 m, which is roughly 50% of the real mean tree height (REINARTZ *et al.*, 2006).

Impenetrability vs. crown closure

In this experiment, the relationship between crown closure and impenetrability was investigated. The crown closure is a forest parameter that can be easily estimated using the photo-interpretation technique (HOWARD, 1991). Therefore, a relationship between the crown closure and impenetrability can be used to calculate an estimate of the impenetrability. Figure 57 shows this relationship for the basic crown shapes. The calculations were performed for the input data as per Table 17, for example for trees of even height.

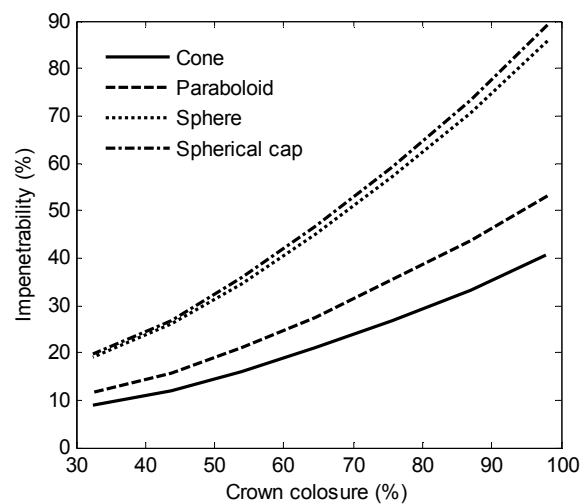


Figure 57: Impenetrability vs. crown closure for different crown shapes. The tree height was 30 m and the crown diameter was $10 \text{ m} \pm 3 \text{ m}$.

The impenetrability for the cone- and paraboloid-shaped tree crowns is increasingly and significantly slower than for the sphere and spherical cap, with an increase of the crown closure. Such a significant disparity in the impenetrability for the same crown closure but different crown shapes offers an opportunity to identify what type of crown is dominant in the forest investigated. For example, one can conclude that there is predominantly a component of a spherical or spherical cap type of crown, if the crown closure is 70% therefore making the impenetrability about 50%. Otherwise, impenetrability at a level of 20% would indicate conical or paraboloid-shaped trees.

It is interesting to note that the results are in general agreement with the graph in Figure 32, which was constructed from the Australian field data (BECEK, 2008a). On this graph, the impenetrability for crown cover of 70% is about 9 m, or about 40%. This clearly indicates dominance of the sphere-shaped crown, though there is some contribution from the paraboloid- or cone-shaped crowns.

Impenetrability vs. crown height

In this experiment, the rate of change of impenetrability as a function of the height of the crown was calculated. The calculations were carried out for various crown heights (H_c), but a constant stem height ($H_o = 5 \text{ m}$) was used. The curves in Figure 58 show that the impenetrability for the cone- and paraboloid-shaped crowns becomes lower for higher crowns, while for the sphere and spherical cap shaped trees the impenetrability increases. This unique behaviour of the impenetrability suggests an interesting problem of determining a shape of a crown such that the impenetrability (caused by the Type 2 gaps) is independent of the height of the crown. This question remains, however, beyond the focus of the investigations. Therefore, it will not be discussed here any further.

The impenetrability for the cone- and paraboloid-shaped crowns decreases much more rapidly than it increases for the sphere and spherical cap shaped trees.

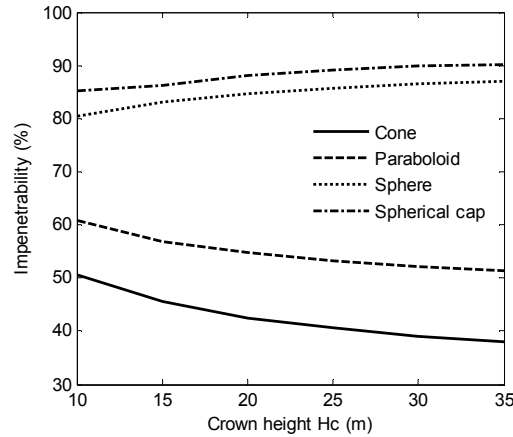


Figure 58: The Impenetrability vs. crown height (H_c) for the basic crown shapes and 100% crown closure. The stem height (H_o) was 5 m.

Impenetrability of a “free forest”

In the preceding experiments, impenetrability was calculated for a simulated forest with only one parameter as the independent variable. This approach is useful for investigating the type of relationship between the dependent and independent variables. The results of the simulation should provide a more realistic forest with the more forest parameters one allows to vary. In this case, not only the type of relationship between variables will be captured, but also its dynamics (in terms of probable ranges and standard deviation). The following are results obtained for a “free forest” in which the crown shape, crown diameter, crown height, and tree height are allowed to change randomly. A normally distributed random number generator was used to simulate the tree height ($H_c + H_o$) and crown closure.

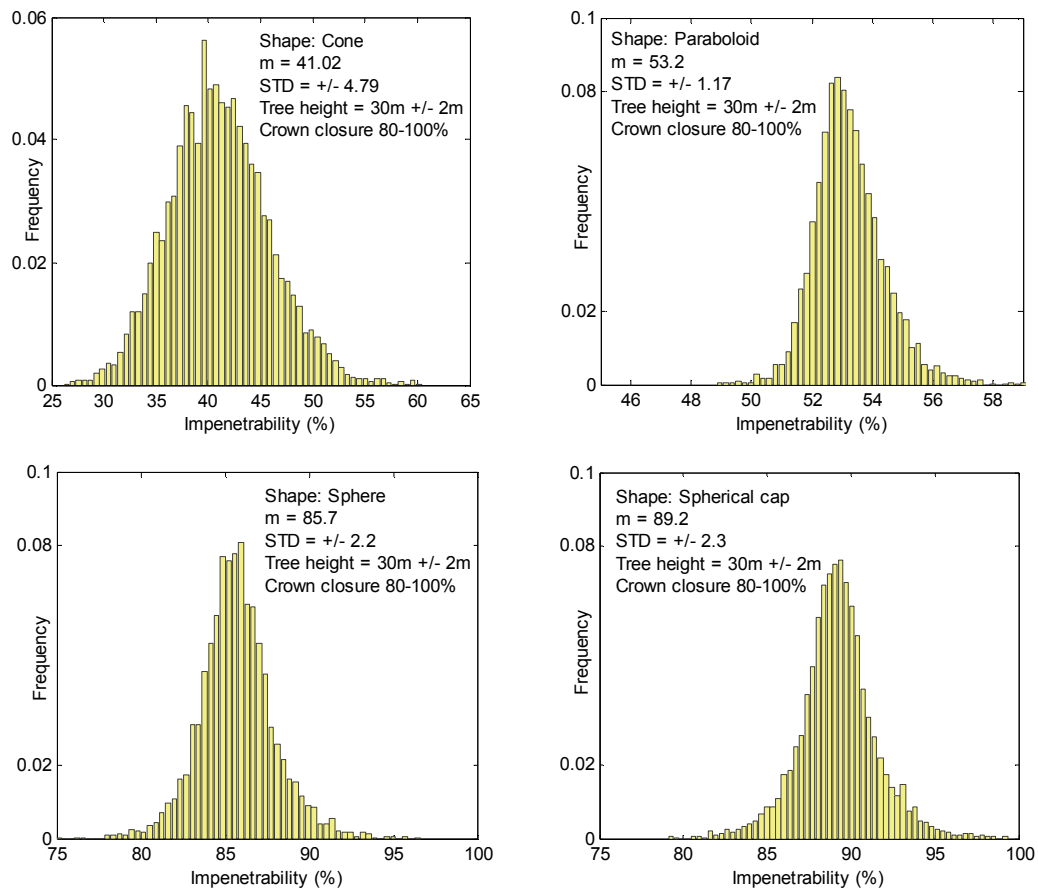


Figure 59: Histograms of the impenetrability of a “free forest”. Panes from top-left to bottom-right represent cone, paraboloid, sphere, and spherical-shaped, respectively. The Gaussian distribution of tree height was assumed to model

the variability of these parameters. The tree height was $30 \text{ m} \pm 2 \text{ m}$. The crown diameter was evenly distributed between 80 percent and 100 percent.

Figure 59 shows the results of the calculations of the impenetrability caused by type 2 gaps in a “free forest”. The highest sensitivity in terms of the standard deviation of the impenetrability is exhibited in the cone-tree forest. The type of tree shape also significantly differs in terms of mean impenetrability; it is much lower for the cone shaped tree (41%) than for the other type of tree crowns (53%, 86%, and 89%).

Impenetrability vs. Type 1 gaps

In the next simulation experiment, the influence of Type 1 gaps on impenetrability was investigated. The Type 1 gaps represent missing fragments of the forest cover due to natural and anthropogenic events. Unlike Type 2 gaps, which are of a deterministic character and change only as a result of forest growth, Type 1 gaps appear in the forest cover randomly. However, due to forest growth, Type 1 gaps can also disappear over a sufficiently long period of time. One can imagine that, for a given forest stand that is exposed to natural forces only, the total area of Type 1 gaps remains constant. Only then, when some external forces disturb the forest, the area of the gaps increases until the next level of stability of the forest system is reached. This behaviour of the forest makes it a dynamic system that can be assessed by observing the area of the Type 1 gaps. Commonly, forces such as deforestation, degradation or forest depletion, forest fires, insect infestation, lightning strikes, and fallen trees cause the forest to change and the area of the gaps to grow. Reporting on the extent of these changes is usually done in percentage terms of the gap area versus the forest area for a set period of time (year). It is rather obvious that a decrease of the total forest area by a given percentage will also cause the impenetrability to drop proportionally. Figure 60 shows the dependency of the impenetrability for a forest plot from the percentage of the area taken by the Type 1 gaps. As expected, the relationship appears to be linear.

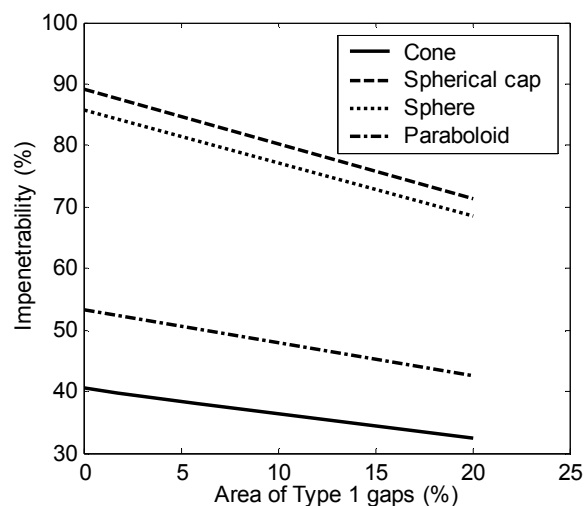


Figure 60: Impenetrability of a forest plot as a function of the percentage of the Type 1 gaps.

As it will be shown in the next chapter, this finding can be useful for measuring the forest depletion because it linearly maps a relationship between forest depletion (due to Type 1 gaps) and the impenetrability.

Impenetrability vs. Type 3 gaps

The interaction of radar waves with tree crowns used to be one of the most frequently investigated topics in synthetic aperture radar (SAR) research in the 1990s. One reason for this is the fact that radar waves, depending on their length, penetrate the interior of a tree crown to various degrees. Experiments were conducted with various datasets (RADARSAT; ERS-1 and 2; JERS-1; and others) on various types of vegetation cover, mostly forests (KASISCHKE *et al.*, 1995, LE TOAN *et al.*, 2002), but also some agricultural crops (MARLIANI *et al.*, 2002). Despite those efforts, at the present time there is no SAR system in place that could be used for biomass studies such as those required by the Global Forest Resource Assessment Programme (FAO, 2005a). The Japanese Global Rainforest Mapping Project—used JERS-1 satellite L-band SAR data to create a mosaic showing the forest cover of tropical regions (ROSENQVIST *et al.*, 2000, 2004) seems only to confirm the situation. Interferometric synthetic aperture radar (InSAR) technique is a more promising technology for studying the vertical structure of vegetation or biomasses than SAR. .

IZZAWATI *et al.* (2004, 2006) used the InSAR technique to investigate the vertical structure of vegetation. The authors attempted to calculate the elevation of a volumetric element (vexel) within a tree crown. The average elevation

was calculated from all the voxels of that tree. The procedure was carried out for a few basic tree shapes. This approach definitely has some merit; however, the results are of limited value mainly because of the likely bias in the data used to define the model parameters. This bias is due to the fact that the digital surface model (DSM) used in the calculations was produced using the InSAR technique. Therefore, the tree heights used were not accurate (tree heights were underestimated). This is discussed in Chapter 6 of this report. Another drawback of this method is the implicit assumption that voxels are homogenous.

The InSAR elevation for a resolution cell (pixel) is proportional to the backscatter phase delay, which is a coherent sum of contributions from all scatterers located in that pixel and their differential path delays (ROSEN *et al.*, 2000). This can be written in a shorter manner as follows:

$$h \propto A_b e^{-j\varphi_b} = \sum_i A_{ei} e^{-j\varphi_{ei}} e^{-j\frac{4\pi}{\lambda}\rho_{ei}}, \quad (58)$$

where h is the elevation,

A_b is the intensity of the backscattered signal from a pixel,

φ_b is the propagation phase delay for a pixel,

φ_{ei} is the propagation phase delay for an i^{th} scatterer within a pixel, and

ρ_{ei} is the differential range delay for an i^{th} scatterer within a pixel.

One may deduct from Equation (58) that the elevation of a pixel is a product of elevations of all scatterers contributing their backscattered energy to a given pixel. One may also assume that the scatterers are located at various distances from an arbitrary plane perpendicular to the radar view direction. Considering the case of tree crowns in the leaves-on state, one may note that apart from scatterers located at the perimeters of the crown, some scatterers may be found at various distances from the perimeters of the crown. These scatterers are located at the bottom of gaps within the crown.

Few remarks are needed regarding the “gapness” of tree crowns. The gaps can be permanent or not. Hence, two types of trees are distinguishable, evergreen and deciduous, the latter shedding their foliage at the end of the growing season. It may be assumed that the evergreen trees possess a species-specific and relatively constant over time percentage of gaps in their crowns. This measure of the gapness of tree crowns (G) can be defined as the total area of a cross-section of gaps over the total area of a cross-section of the crown. It is clear that for evergreen trees, the following is valid: $0 < G < 100\%$.

One may also note that in the case of deciduous species, G also has a temporal character. Figure 61 shows the difference in gapness between evergreen and deciduous trees over time. As may be seen from the graph, except for the beginning and after the end of the growing season, the level of gapness remains relatively constant (subject to temporal environmental conditions) on a level that is species- and environment-specific.

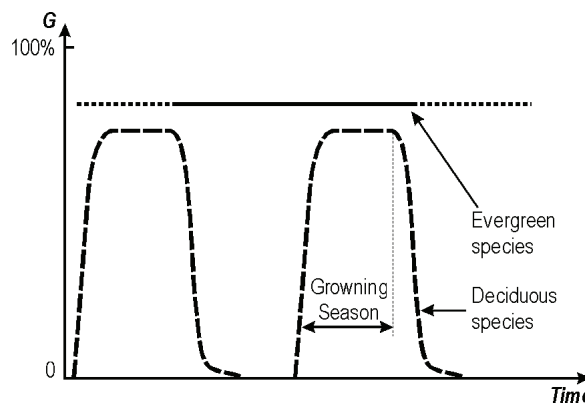


Figure 67: The tree crown gapness, G , of deciduous and evergreen tree species over time.

In relation to the gapness of the tree crown, the following may be assumed:

1. There is a species-specific minimal size (area) of the cross-section of a gap;
2. The gap size varies according to the power-law probability density function, which is not a species-specific property of tree crowns;
3. At least the outer part of the tree crown is homogeneous and isotropic, and

4. In the case of deciduous species, the minimum gap size decreases during the initial phase of the growing season and increases at the end of the growing season.

The above assumptions are based on common knowledge, and therefore no references are provided.

The next key step in the process of modelling the impenetrability of tree crowns using Type 3 gaps is to model the radiometric response of gaps to radar waves. It is clear that the intensity of the response, which is simply the backscattered energy from the bottom of a gap, will depend on the length of a gap. As one may imagine, the length of a gap can be very small or very large (up to the height of a tree). Yet, not all the gaps can provide enough strong backscattered signals that can be received by the radar system. Three factors control this effect. They are the diameter and the length of gap (as previously mentioned) and the sensitivity of the radar system. The sensitivity of a radar system is usually expressed as signal-to-noise ratio (SNR).

The intensity of signal (I_R) backscattered from the bottom of a gap is at the top of the gap a function of the length and diameter of the gap. This relationship can be derived from the *geometrical optics law* of intensity, which essentially follows the inverse square law (BORN & WOLF, 1999):

$$g^2 = a \frac{d^2}{I_R} \quad (59)$$

where g is the length of the gap,
 d is the diameter of the gap,
 I_R is the portion of the backscattered signal escaping the gap, and
 a is a coefficient.

In practical consideration, I_R cannot be smaller than the SNR in order to carry a useful signal. Therefore, Equation (59) must be modified by replacing I_R with the SNR of the InSAR system.

Equation (59) and the first assumption can be used to calculate the length of a gap, which can be detected for a given wavelength, and SNR from the following Equation (60):

$$g_\lambda = \sqrt{\frac{\lambda^2}{SNR}} \quad (60)$$

The signal-to-noise ratio is unitless, since $a = 1$.

In the case of the SRTM, SNR was about -20 dB (the weakest signal registered). Therefore, the detectable length of a gap (g_λ) for the smallest gaps was 0.56 m and 0.31 m for the C- and X bands, respectively.

It is worth nothing that g_λ represents the maximum detectable length of a gap only. Longer gaps are a common occurrence in nature, but they do not influence impenetrability because they do not produce a detectable backscattered signal. This lack of detectable signal restricts the definition of tree gapness (G). Only detectable gaps are taken into account.

Equation (60) can also be used for calculating the limiting length of a gap (g_{max}) of any diameter. In this case, the wavelength in Equation (60) must be replaced by the diameter of the gap.

The length of a gap represented by Equation (60) is related to the extinction or attenuation coefficient or the loss factor. Typically, the extinction coefficient is described using the exponential probability density function (MOUGIN *et al.*, 1990). However, other types of models are possible, including power-law distribution. In this study, the power-law model was implicitly adopted because the model is a consequence of the linear relationship between the length of the gap and its diameter, and the diameter is the power-law distributed.

The issue of tree-crown gapness has not been investigated much (CHEN & CIHLAR, 1995, NILSON, 1999). Hence, insufficient experimental data exists that could be used in the simulation study. Therefore, gapness will be one of the parameters used in this study. Figure 66 shows an example of tree crowns with various numbers of gaps (the sum of the

area of all gaps is divided by the area of the crown). The gaps follow the power-law probability density distribution, which is justified by the experimental findings of CHEN & CIHLAR, (1995).

The model of Type 3 gaps presented above was implemented in simulation software. The major objective of the simulation study was to investigate how significant the contribution of Type 3 gaps is to the overall impenetrability of forests.

In summary, the following processing steps were performed in order to assess the contribution of Type 3 gaps to the impenetrability of forests:

1. For assumed wavelength (λ), a large (20,000) set of random numbers Γ representing the squared diameter of gaps were generated. The numbers followed the power-law distribution and were generated using the software package provided with the article by CLAUSET *et al.*, (2009). The software requires two parameters: the scaling parameter (α) and the smallest value of a generated number (x_{min}). The scaling parameter (α) was 2.18. This value was found while analysing the stochastic properties of gaps in the forest canopy (see Chapter 6). The smallest gap was $x_{min} = \lambda^2$. The generated set of random numbers was verified by fitting a regression line, as per Equation (51), into the cumulative probability density function described in Chapter 6. Figure 62 shows the empirical log-log cumulative probability density function for two wavelengths, -5.6cm and 3.1cm (C- and X- bands). The graphs confirm that the gaps indeed follow the power-law density distribution. The gaps were randomly distributed within the tree crown, e.g., the easterly and northerly coordinates were uniformly distributed. Figure 66 shows examples of cross-sections of tree crowns with the various numbers of gaps. The bottom panes were generated for the X-band.
2. For the assumed percentage of gaps in the tree crown (gapness), a subset G was drawn from the set generated in step 1. Each such subset represented a tree crown:

$$G_j \in \Gamma = \{\gamma_i, i = 1, \dots, 20000, d = d_0, \lambda = \lambda_0\} \quad (61)$$

where d_0 and λ_0 are the percentage of gaps in the tree crown and the wavelength of the radar,
 γ_i is i^{th} gap and
 G_j is a subset representing gaps in a j^{th} tree canopy.

3. For each gap of a given diameter, the length was calculated according to Equation (60).
4. For each subset of gaps, G , the weighted mean length of gap g_G was calculated. The squared diameter of each gap was used as weight.

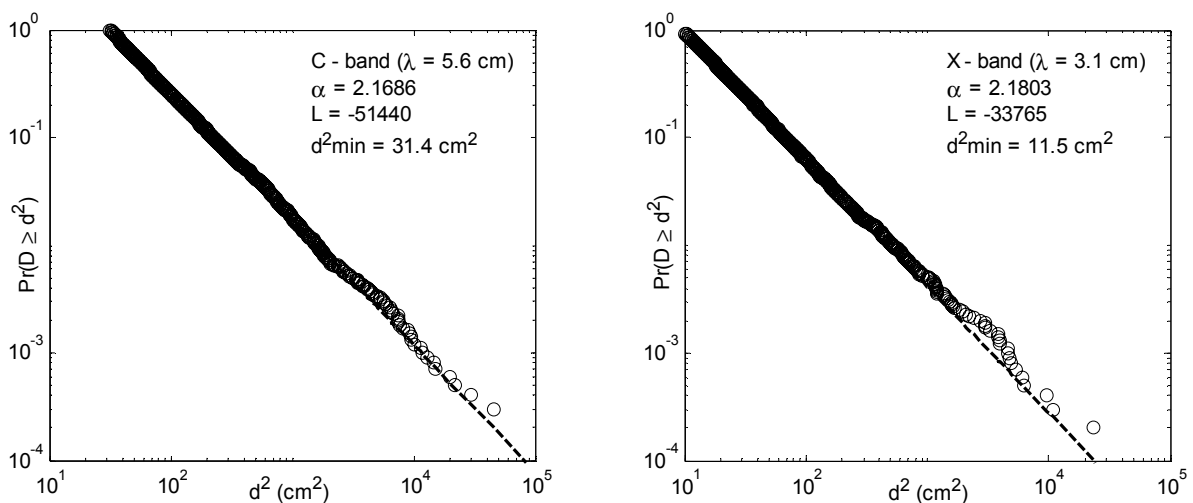


Figure 68: Empirical cumulative probability density function for the randomly generated diameter (d) of the tree gaps for the C- (left pane) and X-band (right pane). The smallest diameter assumed was $d^2_{\min} = 31.4$ cm^2 and $d^2_{\min} = 9.6$ cm^2 for C- and X-bands, respectively. In both cases, the scaling parameter was $\alpha = 2.18$.

5. Typically, 500 subsets of gaps, G , were generated. An average length and the standard deviation of the mean weighted length of gaps (g_G) were calculated. A typical histogram of the weighted mean length of gaps is shown in Figure 63. The histogram shows that the weighted mean length of gaps, which is equivalent to the penetration depth of the radar waves into the tree crown, appears to adhere to the power-law probability distribution. The histogram was generated for the $d_0 = 20\%$ gaps in the tree crown.

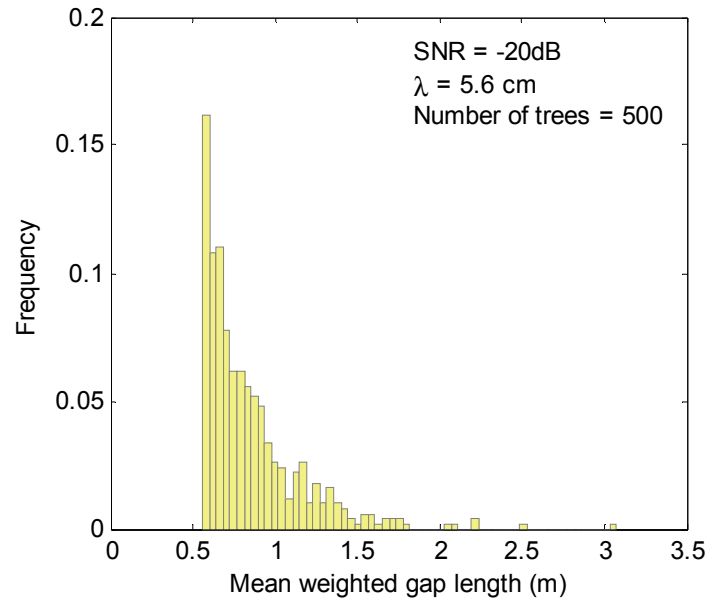


Figure 69: Typical histogram of the mean weighted length of gaps (m), which were generated assuming that their size follows the power-law probability density function. Gaps with diameters smaller than the radar wavelength were not considered and they are not shown in the graph.

In a series of experiments, the first step was to investigate the dependency of the penetration of the radar waves into the tree crown. For a given SNR = -20dB, a series of simulations were performed calculating the mean penetration depth or gap length as a function of the wavelength. Figure 64 (left pane) shows the obtained results. Considering just the two commonly used wavelengths, 3.1 cm (X-band) and 5.6 cm (C-band), one can conclude from the graph that the disparity in the penetration length between C- and X-bands is very small (about 0.20 m). This result leads to a few important conclusions:

1. The X-band radar waves are able to penetrate the tree crown. This is contradictory to the common assumption that this frequency wave does not penetrate the crown at all.
2. The mean penetration length does not depend on the size of scatterers (leaves, twigs, and small branches), but it rather depends on the wavelength and the InSAR radiometric resolution (SNR). Note, however, that the presence of scatterers is necessary to backscatter the radar waves. In this study, an ideal and very optimistic case of 100% reflection is assumed.
3. In the case of SRTM elevation data products, which are delivered at the vertical resolution level of 1 m (quantisation level), the disparity in elevation between SRTM.C and SRTM.X over vegetated areas is unidentifiable. This is because this disparity is well below the quantisation threshold of SRTM.

The error bars shown in Figure 64 (left pane) represent one standard deviation of the mean penetration length into the tree crown. They indicate that the inherent feature of the InSAR measurements is increasing level uncertainty with increasing wavelengths.

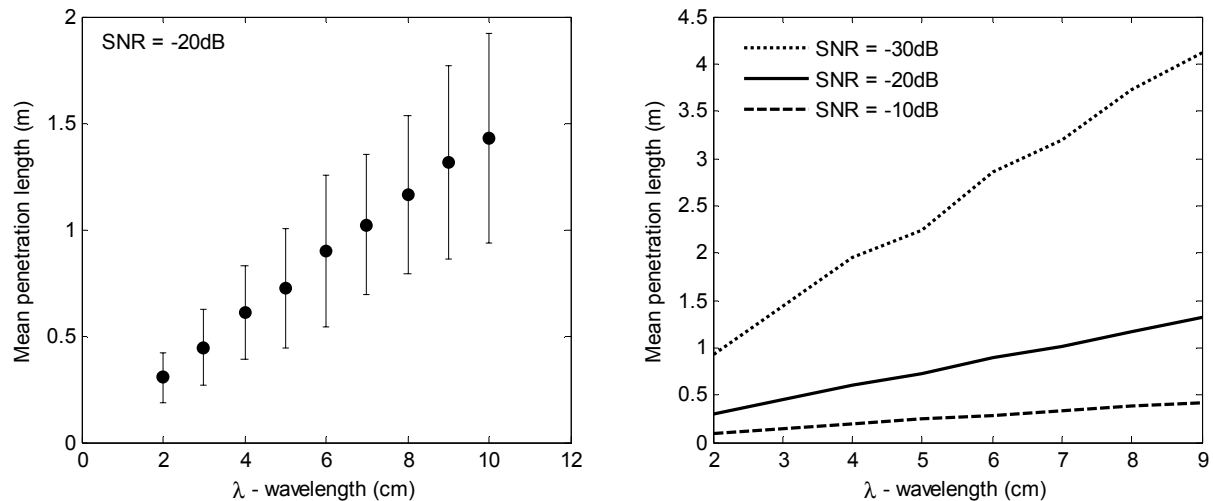


Figure 610. Mean penetration length versus wavelength, including standard deviation (left pane), and for various levels of the signal-to-noise-ratio (right pane).

Figure 64 (right pane) clearly shows how increasing levels of InSAR sensitivity dramatically increase the mean penetration length which is equivalent to lowering the impenetrability. This observation leads to the conclusion that an InSAR with higher sensitivity may lower the elevation bias over vegetated areas, thus increasing the precision of digital elevation models. Obviously, measurements carried out using even an extremely sensitive InSAR would always produce a certain level of impenetrability as a result of scatterers at the perimeters of the tree crown.

Radar penetration depth of the tree crown, which was explained using the Type 3 gap model, influences the magnitude of forest impenetrability. In order to calculate this magnitude, one may note that these gaps lower the volume of the tree crown by an amount equal to the volume of the gaps. Hence, a data processing procedure will involve:

1. Calculation of the volume of the tree crown considered as a solid object,
2. Generation of gaps,
3. Calculation of the volume of gaps, and
4. Calculation of impenetrability for various parameters of the experiment.

In the following experiment, only tree crowns were considered in the calculations. Also, only tree crowns in the form of a sphere were considered. This approach was confirmed experimentally to be sufficient to provide results for a quantitative assessment of the influence of Type 3 gaps on the impenetrability of forests.

Figure 65 shows the results of a simulation of the relationship between the percentage of gaps in a cross-section of the crown and its impenetrability for two frequencies (C- and X-bands). Clearly, the relationship appears linear and almost identical for both frequencies. It is worth noting that the regression line is shifted above the one-to-(minus)one line, i.e. 40% of gapness corresponds to about 70% impenetrability. In a perfect one-to-(minus)one case it should read 40% against 60%. This shift is caused by the level of the radar sensitivity. In this case SNR was -20dB. A higher SNR, e.g. 30dB, would cause a smaller shift. A physical justification of this effect is the much larger presence of and contribution by small gaps to the impenetrability of lower levels of gapness. The linear character of the investigated relationship seems to be confirmed by a simulation study of the twigs' density versus the attenuation of the radar waves (MOUGIN *et al.*, 1990).

As can be seen from Figure 65, the impenetrability of the tree crown is about 80% for a gapness level of about 30%, which is the best guess for the maximum stage of leaf development (leaves-on state). Hence, when comparing the impenetrability caused by Type 2 versus Type 3 gaps, one may note that the Type 3 gaps cause significantly lower impenetrability than the Type 2 gaps. Therefore, in the case of a forest in the leave-on state, the Type 2 gaps contribute the most to the forest impenetrability.

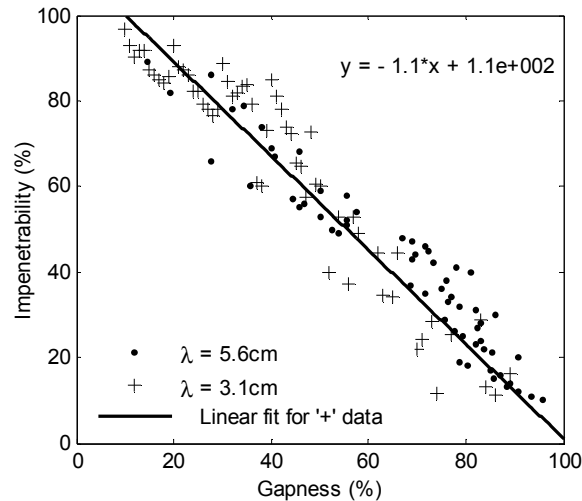


Figure 611. Simulation result of the impenetrability of tree crown versus percentage of gaps in the crown. A linear fit was drawn for the X-band ($\lambda=3.1\text{cm}$ data denoted as '+'). The C-band data are shown as dots '•'. The equation of the linear fit is also shown.

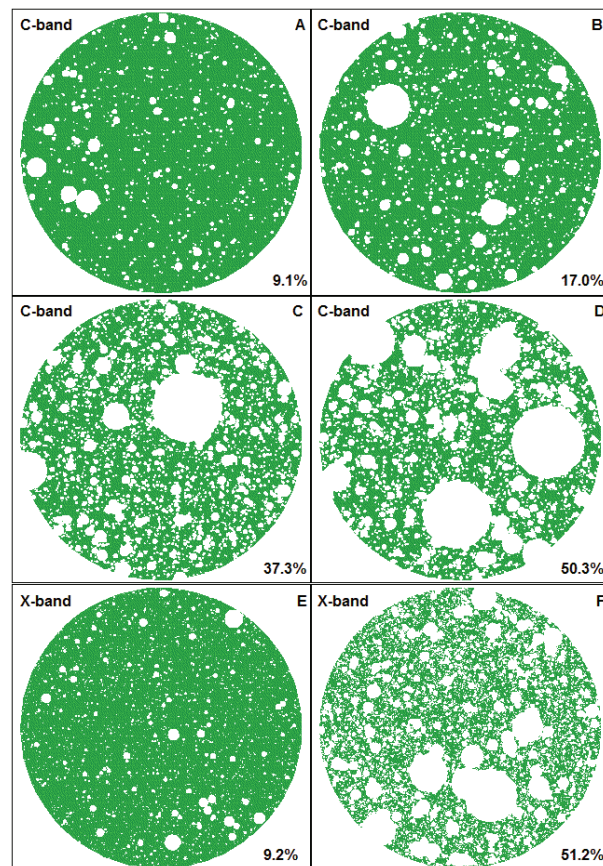


Figure 612. Examples of simulated horizontal cross-sections of a tree crown with various numbers of gaps and different radar bands. The gaps are uniformly distributed within the crown. However, the gap size follows the power-law density distribution. Some gaps overlap or partially overlap each other. This overlapping is responsible for the reduction of the initially assumed percentage of gaps in the canopy to the level shown in each panel. Panels A and E were generated for 10% gaps, panel B for 20%, panel C for 50%, and panels D and F for 75% gaps.

In the above considerations the tree gapness has been used as one of the critical parameters that control the impenetrability. In this context, the question of how to measure the gapness of trees arises. One possible way to do this would be to utilise the same techniques, methods, or instruments for measuring the leaf area index (LAI). This is because LAI may be estimated by inversion of the gapness of tree (NILSON, 1999).

7.5 The Biomass Equation

One of the conclusions from the above study is that the biomass impenetrability changes from point to point and also as a function of time. This can be expressed using Equation (62):

$$v_{i+1}(s) = v_i(s) + \frac{\partial v(s)}{\partial t}(t_{i+1} - t_i) + v_i(s)f(\omega t) + n, \quad (62)$$

where $v_{i+1}(s)$ is the impenetrability at a given point (s) in space and a moment in the future (t_{i+1});
 $v_i(s)$ is the impenetrability observed at a given point (s) in space and a moment in time (t_i);
 $\partial v(s)/\partial t$ is the time derivative of the impenetrability or the rate of change at a given point (s);
 $f(\omega t)$ is a function of time that describes periodic changes in the impenetrability, and
 n is noise due to random estimation errors of the parameters.

System theory considers similar equations that describe the dynamic properties of a system (EYKHOFF, 1974).

Equation (62) describes the temporal behaviour of the forest's impenetrability in response to natural and/or anthropogenic forces acting upon it. The forest's response changes from point to point depending on environmental variations, including the species composition of the forest, the soil and water conditions, and topography. Since the biomass impenetrability is regarded as a representation of the biomass, Equation (62) can be considered the "biomass equation".

Estimating the biomass equation's parameters involves two major steps: 1) finding the state of impenetrability for a given point (s) and moment (t_i), and 2) figuring the two time-dependent parameters, that is, a) the biomass impenetrability rate of change due to biomass depletion - $\partial v(s)/\partial t$, and b) the periodic change in impenetrability due to seasonal changes in vegetation (leaves-off/on) - $f(\omega t)$.

For evergreen trees, the periodic term - $f(\omega t)$ - in Equation (62) is obviously zero. To estimate the biomass depletion term, the power-law distribution (Type 1 gaps) may be used as a guide.

7.6 Conclusions

This chapter presented a novel approach to modelling biomass representation in the InSAR dataset; it also included preliminary testing using a computer simulation and an example of an application of the the biomass impenetrability. The idea behind this biomass impenetrability approach is that the "topography" of the biomass, or forest, controls the magnitude of the elevation bias of the InSAR-derived elevation data or the biomass impenetrability. Three scale-dependent features of forest topography were identified: large gaps in forest stands, gaps between trees forming a forest, and gaps within the tree crown. The theoretical modelling, the simulation experiments and the analysis of the field experiments, formulating the following major conclusions:

1. The deciding factor for the magnitude of forest impenetrability are Type 2 gaps, e.g., the natural "topography" of a forest formed by the shapes of tree crown, crown dimension, and the density of trees per area unit. These gaps reflect many environmental- and tree-species-dependent conditions such as soil, water, nutrients, and terrain aspect as well as the age and height of the trees. These gaps are relatively stable over time, changing with the growing forest. These gaps are natural organisational elements of a forest ecosystem.
2. Type 1 gaps result from small-scale, (to a large extent) natural and anthropogenic depleting forces acting upon forests, such as forest fires, logging, and others. These gaps are the subject of forest change reporting on the national and the global level. Hence, these gaps are of interest for remote sensing. Although it is impossible to predict when or where another gap will pop up in the forest, at least the statistical characteristics – the probability distribution of the gap size – may be identified. The power-law distribution appears to be a good candidate for modelling the Type 1 gaps in the Badas Peat Swamp Forest. It is suspected that the power-law distribution can also be used in other types of forests. More investigations are needed in this field.
3. Type 3 gaps play an extremely important role as part of the interface between the environment and the aboveground tree parts. An exchange of energy, carbon, water and sun radiation takes place through these gaps (BRUENIG, 1998). Interaction between the biomass scatterers and the InSAR radar waves is also possible because of porosity in the tree crown. Not only can radar waves penetrate the crown through the gaps, but the gaps also allow the back-scattered energy to escape the tree canopy to be detected by an InSAR system's antennas.

4. For the purpose of the InSAR investigations, it appears that a tree crown can be modelled using Type 3 gaps. In this approach, two gap characteristics control the radar waves' penetration length into the tree crown: the length of the gap measured along a parallel to the incoming radiation, and the diameter of the cross-section of the gap. The latter parameter must be at least as long as the wavelength of the radar.
5. The length of radar-wave penetration of the canopy is proportional to the diameter of the gaps' cross-section. Small gaps and long gaps are most likely to produce a back-scattered signal that is too weak to be noticeable above the InSAR noise level. More research in this field is certainly needed.
6. The incidence angle influences the magnitude of impenetrability significantly. However, applying a suitable correction built upon Equation (62) may reduce this. This operation would also significantly reduce the elevation bias of the InSAR elevation data products.
7. The biomass equation represents a proposed framework to describe the state of a biomass at any given point in time, as well as a probable status for some point in future. The equation relates the state of the biomass to its spatio-temporal properties. Estimation of the parameters of the state of the biomass is one of the major tasks needed for this model to work. In other words, one must know a biomass's initial state before attempting to predict its future state. In the second stage, one must find the estimate of the spatio-temporal parameters; that is, one must know the time and space derivatives of the biomass to make predictions (EYKHOFF, 1974). This approach follows the concept of the Global Earth Observation System of Systems or GEOSS (<http://www.earthobservations.org/geoss.shtml>).

8. BIOMASS IMPENETRABILITY FOR FOREST CHANGE DETECTION AND ASSESSMENT

The simulation studies documented in the preceding chapter have shown that the magnitude of the biomass impenetrability depends on three types of gaps in the forest. While Type 2 gaps (free space between trees) are stable (distances between stems remain unchanged), type 1 and 3 gaps can rapidly change within anywhere from a fraction of a second (wind) up to months (seasonal or life cycle changes). Some of the changes may have an irrevocable character (at least within a reasonable time frame – say seconds, minutes or a season), for example, deforestation and changes due to adverse environmental conditions.

A final result of the above changes can be termed “forest or biomass depletion”. The differences between the commonly used terms in this context - “forest degradation” and “forest depletion” - is that the latter is more inclusive because it encompasses all the adverse forces acting upon a forest while “forest degradation” usually means alternations made by humans. BEE (1987) probably used the term “forest depletion” for the first time.

In a report on reducing greenhouse gas emissions DeFRIES *et al.*, (2006) noted that one of the prohibitive factors for many developing countries in deploying remote sensing for their forest resource monitoring and assessment is the costs of high-resolution optical data and capacity building. The authors have also noted that there are emerging remote sensing technologies, including LiDAR and radar, which are not used operationally for tropical deforestation monitoring as yet. Besides the economic arguments, another problem is that the SAR results are still not mature enough for operational applications. The InSAR technology may change the situation because it is cheaper than LiDAR. In addition, the InSAR datasets can be acquired at all times and in all weather conditions.

In the following sections, an application of biomass impenetrability for forest change detection and monitoring is demonstrated. The superiority of an impenetrability-based change detection method versus SAR and passive remote sensing data for forest change detection is presented.



Figure 67: There is no factor clearly responsible for these diebacks in Brunei Muara district, Brunei Darussalam. Source: Author.

8.1 The Change Detection Method

Change detection is probably one of the most frequently performed tasks in the environmental sciences. Sophisticated methods and technologies are at researchers' disposal in order to achieve the ultimate goal of the identification of areas of an object that appear different than before. Change detection inherently requires a certain temporal separation between the reference and the assessed representation of the object being studied (LI *et al.*, 2008). A change is said to have occurred when the detected difference between two representations of an object is larger than a certain threshold value. A difference can be calculated between selected characteristics of objects. For example, the normalised difference vegetation index (NDVI) can be calculated for both the reference and evaluated multispectral representations of a forest area. Then the difference, $dn = NDVI_E - NDVI_R$ (the indexes E and R refer to evaluated and reference images, respectively), is calculated for each pixel. In the final step, an image thresholding, $|dn| > \varepsilon$, where ε is a threshold, may be performed. There are many literature sources documenting cases in which this method has limited applicability and should be used with caution (*ibid*, COPPIN & BAUER, 1992, 1994, de ANGELIS *et al.*, 2000). Another group of methods are described as object-oriented methods (DESCLÉE *et al.*, 2006). A change is identified by comparing corresponding objects, using both reference and evaluated images. These methods are considered to be much more robust possibilities and they are currently the subject of intense research efforts.

The change detection method presented below can be classified as an object-oriented one. It is similar to a method described by DESCLÉE *et al.* (2006). A fundamental assumption on which the method is built is the requirement that an object to be distinguished from the background must possess properties allowing this. In remote sensing, one of the most frequently investigated properties is the spectral signature. However, the spectral signature does not exhaust all inherent properties of an object; Many properties are hidden or "transparent" to the passive remote sensing method.

Let us endeavour to use a different way to characterise an object that may include biomass impenetrability (BECEK, 2008c).

The impenetrability-based forest change detecting method introduced requires a predefined set of objects that are believed to be homogeneous. An existing forest map should be developed using photo-interpretation and/or a field survey. This condition is necessary for maximum accuracy of the results.

The change detection is achieved by comparing the mean maximum impenetrability (MMI) with the impenetrability of an object being evaluated. MMI is established for each forest type, and it is based on the impenetrability of forest parcels believed to be pristine.

Traditional forest change detection methods do not allow for measuring the depth or severity of change. In contrast, the MMI-based method can provide a quantitative expression of the severity of change of an object or part of it, which can be as small as a pixel.

As will be demonstrated, the MMI-based forest change detection method possesses several unique properties. The most important is the fact that using this method also allows for the severity of change to be obtained. This allows for more accurate assessments of forest resources because, not only is the area of forest calculated, but also its real density is taken into account. For example, forest degradation in Nepal in the context of tree canopy density is discussed by PANTA *et al.* (2008).

8.2 Problem Formulation

The Forestry Department of Brunei Darussalam supports its operations with a comprehensive forest inventory that was carried out in the early 1980's (ANDERSON & MARSDEN, 1984). Since then, no updates of these reference data have been conducted. A simple linear regression model was used to produce a time-adjusted forest resource estimate. The regression was built upon the international estimates of deforestation, 0.7% per year (FAO, 2005a). Current estimate (2002-2005) of average deforestation for Borneo is 1.7% per year (LANGNER *et al.*, 2007). This approach was the only possible way to compensate for the lack of resources, both financial and human, but it also compensated for the insufficient level of collaboration in data sharing between government departments. This is not a result of the lack of any desire to collaborate, but rather a result of a lack of data required.

In what follows, an attempt has been made to detect, delineate and evaluate changes in the forest cover of Brunei, specifically what has taken place since the last comprehensive forest inventory.

8.3 Data

The following data sources were used in the forest change detection experiment.

1. An existing forest map of Brunei Darussalam. As a base map, the 1:50,000 topographic map was used. Although the map was published in 1984, the reference year of 1980 is adopted. This is because the forest inventory was essentially based on colour aerial photography from 1976, but also included, to a lesser degree, gray-scale aerial photographs acquired in 1982. The map contains eight types of forest from 1 to 8 (the number 6 was omitted as the result of a mistake). Type 9 areas include urban, cleared land and cultivated lands. There were also several subtypes of forests identified. However, they were included within the main forest types. A copy of the summary map at a scale of 1:200,000 and some statistics are presented in APPENDIX 2.
2. The SRTM C-band (the three-arc-second) digital elevation data product. The reference year is 2001.
3. A DTM was developed from the 1:50,000 topographic map. The maps were developed in the 1960's using analogue photogrammetry. Over forested areas, the ground elevation was obtained by subtracting an estimated tree height. The pixel size was matched to the SRTM.C size, and the pixels were coincidental with the SRTM pixels.

8.4 Data Processing Procedures

The data processing steps included the following:

1. The forest map was digitized and attributed using a GIS software package. The smallest/ and largest parcels were 6 ha and 32,255 ha, respectively. In total, 1074 parcels were identified, including 102 parcels of the non-forest type (Type 9).
2. Using the SRTM dataset, a slope for each pixel was calculated. This was done using one of the standard slope generating procedures as implemented by ERMMapper. The slope was used in the following steps to estimate the target-induced error.
1. The impenetrability, v , was calculated for each pixel by subtracting DTM from SRTM: $v_i = h_{SRTM}^i - h_{TOPO}^i$, for $i = 1, \dots, N$, where N is the number of pixels. The standard deviation of the impenetrability was calculated using $\sigma_v = \sqrt{\sigma_{TOPO}^2 + \sigma_{SRTM}^2}$, where σ_{SRTM} (σ_{TOPO}) are standard deviations of the SRTM and the DTM, respectively, which were estimated using Equation (36).
2. The weighted mean impenetrability, \hat{v}_i , $i = 1, \dots, n$, where n is the number of parcels, was calculated for each parcel from:

$$\hat{v}_i = \frac{1}{\sum w_j} \sum v_i^j w_j, \quad i = 1, \dots, n, \quad j = 1, \dots, k, \quad (63)$$

$$w = \begin{cases} 10, & \text{for } s = 0^\circ; \\ 1/q^2 \tan^2(s)/6, & \text{for } s \neq 0^\circ \end{cases}$$

where k is the number of pixels within a forest parcel,
 n is the number of parcels,
 s is slope at each pixel, and
 q is pixel size.

The weight is based on the target-induced error, which depends on the pixel size and the slope of terrain, see Equation (36). For flat terrain ($s = 0^\circ$), the weight was arbitrarily set to 10, while the weight for slope $s = 1^\circ$ is 2.43 and quickly drops for higher slopes.

The standard deviation of the weighted mean impenetrability \hat{v}_i $i = 1, \dots, n$, can be estimated using the following equation:

$$\sigma_{\hat{v}} = \sqrt{1 / \sum w}, \quad (64)$$

where the summation includes all the weights relevant for a given parcel. The statistical independence of all variables in all the calculations is assumed.

3. In this step, a mean maximum impenetrability (MMI) was calculated. MMI is defined as mean impenetrability of the 10% of forest parcels with the largest impenetrability. It can be expressed using the following equation:

$$MMI_t = E(\hat{v}_t)_{10\%}, \quad t = 1, 2, 3, 4, 5, 7, 8, 9. \quad (65)$$

where t is the forest type number,

E is the averaging operator, and

\hat{v}_t is the mean impenetrability of forest parcels belonging to the forest type t .

MMI was calculated for each forest type. Type 9 was also included for consistency.

4. Parcels with the highest impenetrability that were used for the calculation of MMI are considered as pristine among all within a given forest type, and within a given area of interest. The remaining parcels are said be depleted. For example, pristine parcels are 0% depleted; parcels that were converted to a non-forest are 100% depleted. Parcels with impenetrability below MMI but larger than 0 are partially depleted (between 0 and 100%).
5. To facilitate the conversion from impenetrability to depletion, a linear depletion equation is introduced. It is derived from two facts: MMI corresponds to 0% depletion, and 0 m impenetrability corresponds to 100% depletion.
6. The depletion equation is scale-independent. This means that it is applicable to any parcel size including that of a single pixel. Therefore, it can be used to calculate pixel-based depletion. An instant advantage of this approach is the option to identify location(s) that are depleted within a forest parcel.

It is worthwhile noting that the depletion does not always need to be associated with adverse forces acting upon a forest. A lower MMI for a forest parcel or pixel may well indicate the spatial variation of the forest in response to local environmental conditions.

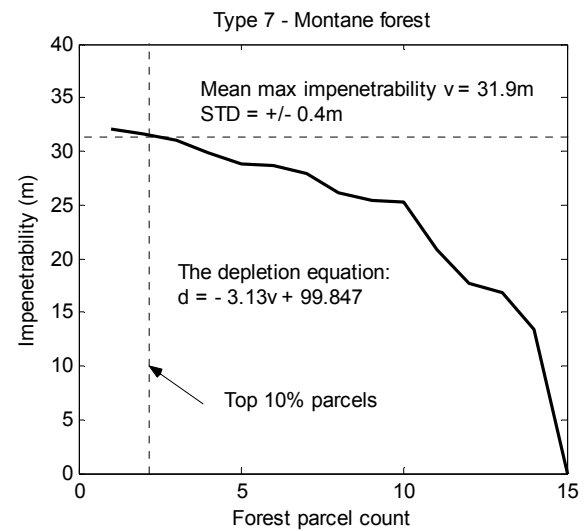
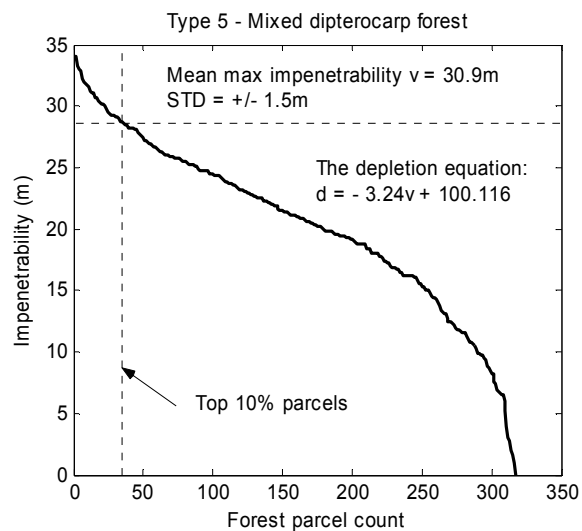
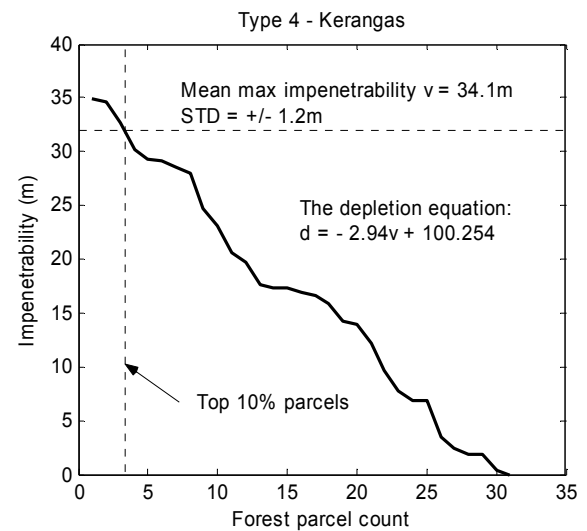
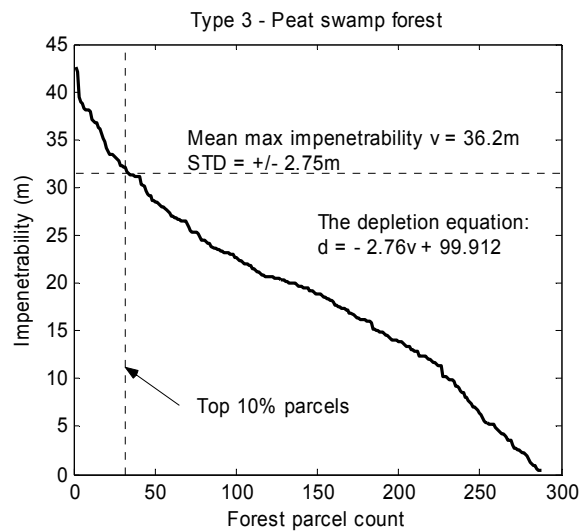
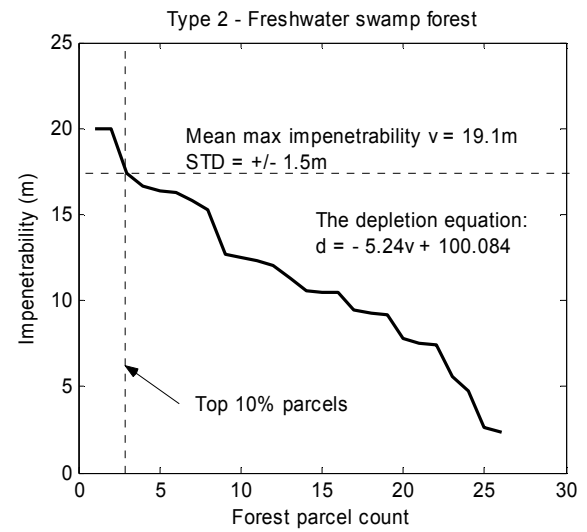
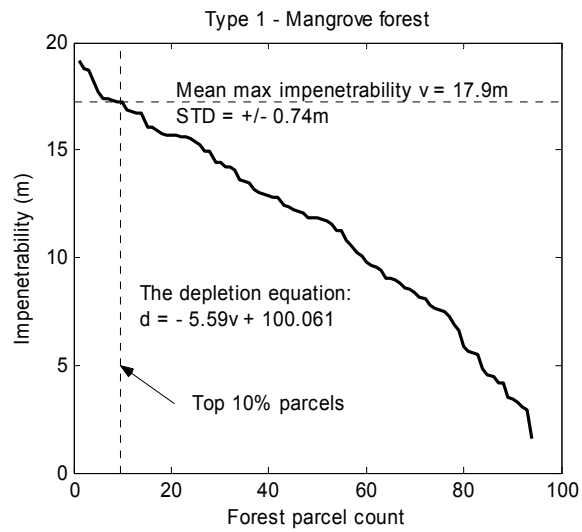
It may be noted that the depletion level of a forest parcel can be used to identify a change if the depletion of that forest parcel is referenced to the depletion of the sample parcel at some point in the past. Otherwise, the depletion describes the spatial variation of forest density, which, as will be demonstrated, can be a very handy and useful asset for any forestry department or forest scientists. It may also be noted that depletion as a relative measure of forest density allows for comparison of the densities of different forest types. This can be used to develop a forest or vegetation density map (BECEK, 2008d).

8.5 Results

The impenetrability was determined for every forest parcel as described in Section 8.4. The forest parcels were grouped by forest type and ordered by the descending value of impenetrability. The 10% of forest parcels with the highest impenetrability were considered to be pristine. Those parcels were used for calculating the mean maximum impenetrability (MMI) and its standard deviation. Figure 68 shows the results for each forest type. For consistency, a graph for Type 9 plots (urban, cleared land & cultivated lands) is also included. The corresponding depletion equation is also shown in Figure 68.

The graphs for forest Types 1, 2, 4 and 8 generally appear to be nearly linear. This indicates that that the number of parcels with similar depletion is equal. It may indicate that depleting forces or natural conditions for forest growth are equally distributed. In turn, Types 3, 5 and 7 forest plots follow a non-linear pattern, which means that there are a number of parcels that are more depleted than others. This may indicate that the parcels were exposed to an extraordinary depleting force in addition to those acting in a proportional manner on the forest. Examples of those

extraordinary forces are logging and forest fires. In the case of the Type 3 forest, the most likely extraordinary force was the 1997 forest fire in the Badas peat swamp forest and the Tutong Mid-Valley. But the Type 5 forest parcels are currently being commercially logged (ZAINAL, 2009).



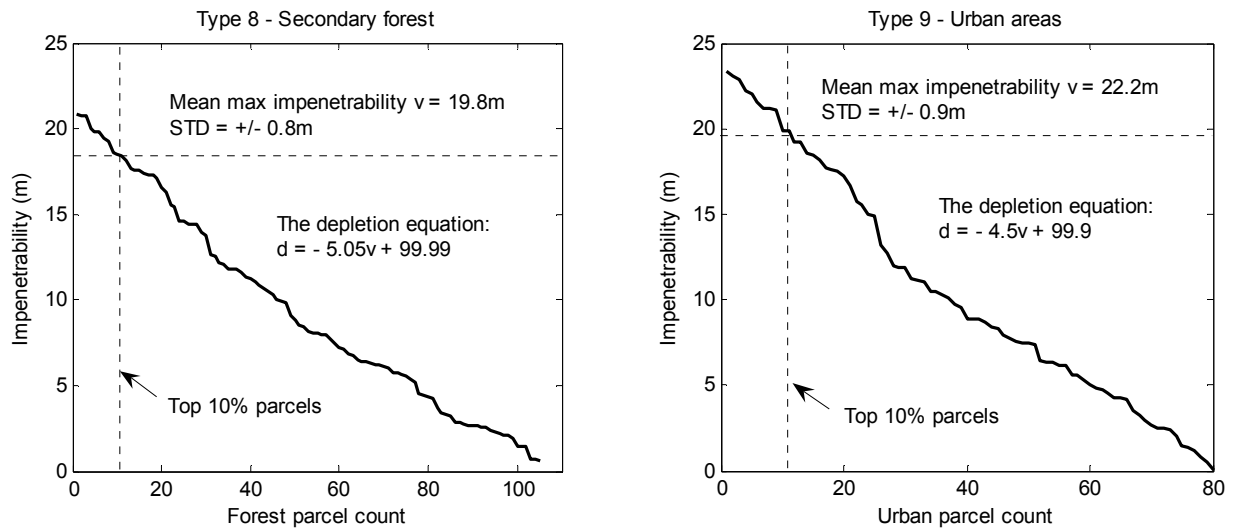


Figure 68: The impenetrability for various forest types including areas classified as Type 9 (Urban, cleared land & cultivated lands). The mean max impenetrability and standard deviation are calculated as an average value of the top 10% of forest parcels with the highest impenetrability. The outliers were removed before calculation.

Figure 69 shows a comparison of MMI and its standard deviation for all forest types and Type 9 areas.

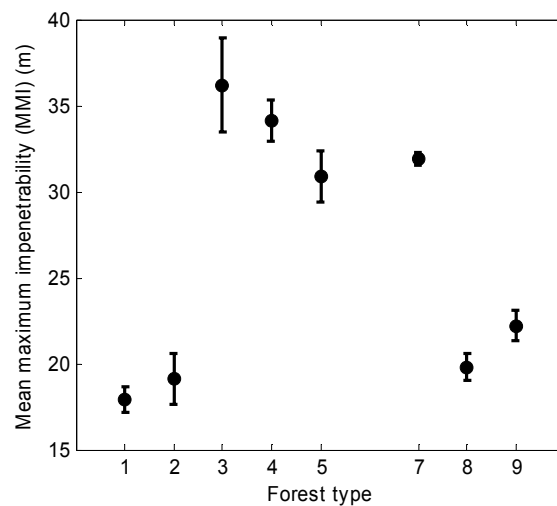


Figure 69: Mean maximum impenetrability and its standard deviation for various forest types and urban, cleared land and cultivated areas.

As expected, the lowest impenetrability is found in the mangrove and freshwater swamp forests. The highest values of impenetrability (between 30m and 36m) are typical of forest Types 3 – 5. The impenetrability of the Type 8 forest is relatively low. This is probably due to the lower density vegetation and young age of the trees (about 45 years).

8.6 Accuracy Assessment of Forest Depletion

Due to the lack of independent, high-quality reference elevation data, accuracy assessment of forest depletion using impenetrability was performed with the help of photo-interpretation. From each forest type, nine forest parcels were selected for the procedure: three from the highest, the middle and the lowest impenetrability. The extracted test parcels were overlayed on the GeoCover 2000[®]/GoogleEarth[®] image. Each parcel was investigated, and a polygon was drawn representing inconsistent regions within the given parcel. A ratio denoting the area of change versus the total area of parcel was adopted as a measure of the change. This ratio was compared with the depletion of a given parcel, calculated based on its impenetrability and the mean maximum impenetrability of the type of forest. Figure 70 shows a scattergram relating both depletions.

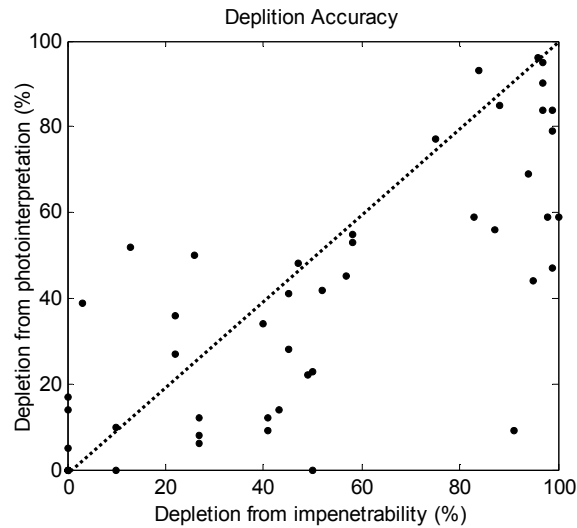


Figure 70: Accuracy assessment of depletion estimated from photo-interpretation versus depletion estimated from impenetrability for selected forest parcels. A 1-1 line was included indicating an ideal agreement between both estimated depletions.

Visual inspection did not provide any signs of depletion for many of the parcels; forest parcels looked pristine. Yet, the impenetrability of those parcels indicated a significant level of depletion. This phenomenon is most likely due to the spatial variability of properties (density) of forest, which was discussed in Chapter 3. Figure 71 shows an example of such a situation.



Figure 71: Forest parcel with depleted regions marked as 'a' (left pane). The dashed line indicates a modified boundary of a pristine section. Depletions estimated from photo-interpretation and impenetrability are 56% and 58%, respectively. The parcel shown on the right does not show any traces of depletion yet its depletion was estimated at 50% using the impenetrability method.

In light of the above, it must be concluded that the depletion estimated using impenetrability is much more sensitive to biomass variations than can be detected using photo-interpretation of the satellite imagery at that resolution (14.25m pixel size of the GeoCover 2000® imagery).

There were administrative and financial preparations taking place within the Forestry Department, at the Ministry of Development, at the time this report was written (April, 2009) to engage an international consulting company to conduct a comprehensive forest inventory in the country. It is expected that findings presented here will be compared against the latest forest inventory. This verification procedure will be further enhanced due to the planned acquisition of the LiDAR data over the entire country within the next six months, around October 2009.

8.7 Assessment of Forest Resources Using the Depletion Method

One of the most important applications of biomass impenetrability may be an option to develop a better method for assessment of forest resources. This can be done by defining the effective forest area (EFA) (BECEK & ODIHI, 2008). The EFA is calculated as a weighted sum of areas of forest plots. As weights, the depletion of forest plots can be used. This can be expressed as (BECEK & ODIHI, 2008):

$$EFA = \sum_{i=1}^N a_i \frac{(100 - d_i)}{100} \quad (66)$$

where N = number of forest plots in the area of interest

d_i = average depletion level of i^{th} forest plot varying between 0 and 100%, and

a_i = area of i^{th} forest plot.

With the help of Equation (66), the EFA was calculated for Brunei based on SRTM elevation data and a reference DTM. Table 24 shows the EFA for all types of forest.

Table 23: Effective forest areas in Brunei Darussalam. The reference year is 2000. Source for column titled “Extent of forest as per 1980 inventory”; ANDERSON & MARSDEN, (1984).

| Forest Type | Extent of forest as per 1980 inventory (ha) | Effective Forest Area (ha) in 2000 | Change (%) |
|-----------------------------------|---|------------------------------------|------------|
| Mangrove | 18,487 | 12,749 | -31.0 |
| Freshwater swamp | 13,656 | 9,793 | -28.3 |
| Peat Swamp | 105,994 | 59,352 | -44.0 |
| Kerangas | 9,506 | 4,807 | -49.4 |
| Mixed Dipterocarp | 266,159 | 188,096 | -29.3 |
| Montane | 7,160 | 6,166 | -13.9 |
| Secondary | 56,958 | 11,564 | -79.7 |
| Total Forest | 477,920 | 289,670 | -39.4 |
| Urban, cleared & cultivated lands | 104,277 | 292,527 | 180.5 |
| Grand Total | 582,197 | 582,197 | |

Overall, the forest cover of Brunei has shrunk over the past 20 years (1980-2000) by about 39%, which averages out to about 1.97% per annum. This figure is in good agreement with the average deforestation rate in Borneo, which was about 1.7% per annum between 2002 and 2005 (LANGNER *et al.*, 2007). However, according to ACHARD *et al.*, (2002) the average deforestation rate for Southeast Asia during the 1990 – 1997 period was 0.91% only.

Most of the changes appear to be due to urban expansion and construction of highways and other transportation facilities. However, other factors cannot be ruled out, including forest depletion caused by global warming (BECEK & ODIHI, 2008). Consequently the countries’ forest cover was about 50% in 2000.

It has to be noted that using the same approach, BECEK & ODIHI (2008) determined the forest cover for Brunei to be about 65%. The source of the disparities is the way the mean maximum impenetrability and the typical impenetrability (BECEK & ODIHI, 2008) were established. In the case of the typical impenetrability, the range of forest parcels considered to be pristine or unchanged was roughly the top 30% of all parcels of a given forest type, whereas in this report only the top 10% of forest parcels were taken into considerations. Consequently, the impenetrability determined for this report was almost twice as great. Both numbers can be obtained from Table 25.

Table 24: Mean maximum impenetrability versus corresponding typical impenetrability. Typical impenetrability was described by BECEK & ODIHI (2008).

| Forest Type | Mean maximum impenetrability (m) | Typical Impenetrability (m) |
|-------------------|----------------------------------|-----------------------------|
| Mangrove | 17.9 | 9.0 |
| Freshwater swamp | 19.1 | 9.6 |
| Peat Swamp | 36.2 | 18.5 |
| Kerangas | 34.1 | 7.1 |
| Mixed Dipterocarp | 30.9 | 13.3 |
| Montane | 31.9 | Not determined |
| Secondary | 19.8 | 4.2 |

It is somewhat likely that the mean maximum impenetrability (MMI) will need to be verified again when a more accurate DTM is available.

A possible deployment of the forest depletion method (FDM) is relatively easy and inexpensive provided that a good quality DTM exists. In that case, many countries are in position to conduct at least a benchmark inventory using the existing SRTM and a DTM. The results of the EFA obtained using the FDM are always lower than the total forest area calculated using the traditional methods. This is simply because no spatial variations of forest density are taken into consideration. A good example of this is the Global Forest Resource Assessment report (FAO, 2005). In addition, reporting for FRA allows for the inclusion of *in suite* forest areas.

However, the EFA is a much more realistic measure of forest resources. It can be used to revise the amount of aboveground biomass stored in forests of the world, for example.

8.8 Biomass Impenetrability versus other Remote Sensing Types of Data

Another aspect of the investigation was designed to correlate the impenetrability of the forest parcels with other types of remote sensing data, both active and passive. The aim was to initially investigate and document whether information about both vertical and horizontal vegetation structures, which are embedded in the biomass impenetrability, would improve the outcome of remote sensing investigations. The following remote sensing data types were investigated:

1. SPOT XS data set consisting of four scenes that covered almost the entire country. The reference year for the imagery is 1998.
2. JERS-1 SAR data in the form of the Global Rain Forest Mapping (GRFM) dataset. Only the 1998 dataset was used. The pixel size of the data is 100 m.
3. German TerraSAR-X, acquired in scan mode and in HH polarisation, data was used. The pixel size is 16 m. The reference data for this dataset is January 15, 2009.
4. Japanese PALSAR L-band data with HH polarity, which was acquired on January 1, 2007. The scene covers the northwestern part of Brunei Darussalam. The pixel size is 6.25 m by 6.25 m. A comprehensive description of the above datasets is presented in APPENDIX 2.

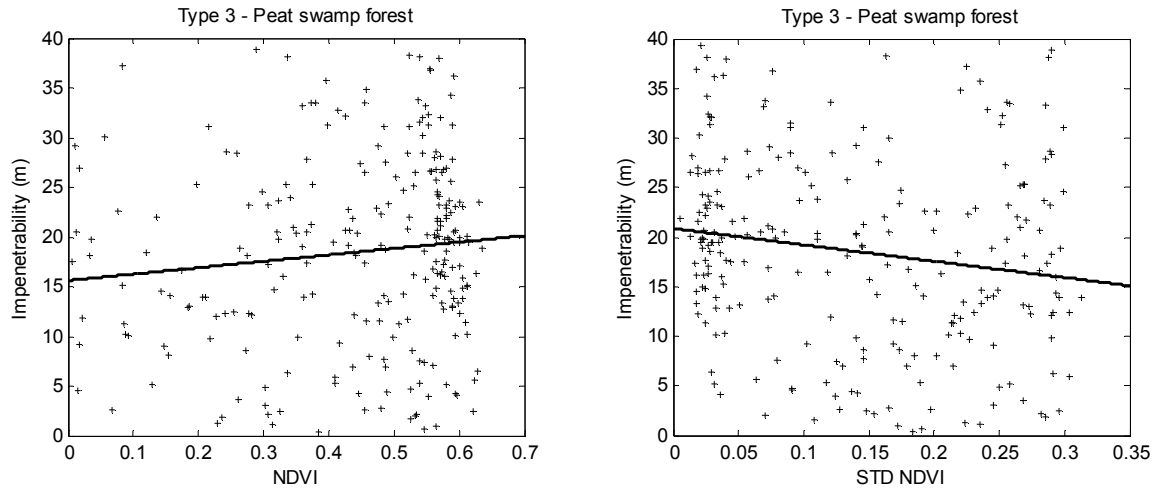


Figure 72: Scattergram of Impenetrability versus NDVI (left pane), and impenetrability versus standard deviation of NDVI (right pane) for Type 3 – Peat swamp forest. Fitting lines are also shown. Every data point (+) corresponds to impenetrability as a tool for investigations of the SAR.

8.8.1 Impenetrability vs. NDVI

SPOT multispectral datasets were radiometrically calibrated to the top-of-atmosphere reflectance using the published parameters (LILLESAND & KIFER, 2000). The normalised difference vegetation index (NDVI) was calculated from the calibrated pixel values using the following formula: $NDVI = (NIR - R)/(NIR + IR)$, where NIR , IR denotes the near infrared and infrared channels, respectively. For each forest parcel, the mean $NDVI_i$ and its standard deviation σ_{NDVI}^i , $i = 1, \dots, n$ (n is the number of forest parcels) were calculated.

Figure 72 shows scattergrams of impenetrability versus mean $NDVI$ and its standard deviation for Type 3 forest parcels. According to the forest change detection method proposed by DESCLÉE *et al.* (2006), as an indicator of change, an average of the NDVI and its standard deviation can be used. This means that a correlation between impenetrability and NDVI or standard deviation should be present. Indeed, Figure 72 reveals a linear relationship between the parcel impenetrability and its NDVI and standard deviation. However, the relationship is very noisy. A possible source of the noise may be the fact that the change detection method was tested over forests that had been logged (*ibid*). In such a situation, the changes in NDVI are much more distinct because of increased soil contributions. On the other hand, the changes in tropical forests might not be well reflected by NDVI because of fast revegetation of damaged areas of forest by shrubs and other low vegetation. This may well be the case as the reference years for impenetrability (2000) and NDVI (1998) are two years apart.

In summary, it can be stated that it appears a relationship between parcel-based mean $NDVI$ and impenetrability does exist, but it is too weak to be useful. Similar conclusions may be drawn regarding the standard deviation of NDVI and impenetrability. All other forest types proved to follow the same trend.

8.8.2 Impenetrability vs. GRFM data

The second dataset investigated was L-band (23.5cm) SAR obtained by the Japanese JERS-1 satellite during the 1990's. These data were used to develop the Global Rain Forest Mapping (GRFM) dataset (ROSENQVIST *et al.*, 2000). According to DOS SANTOS *et al.* (2000), the GRFM data utilised by the authors to develop the forest biomass maps are not well suited for the purpose because of the poor representation of the variability of the biomass. Quite different results were obtained by an Australian team (AUSTIN *et al.*, 2003). They identified a positive linear relation between backscattering coefficients versus biomass of dry eucalyptus forest.

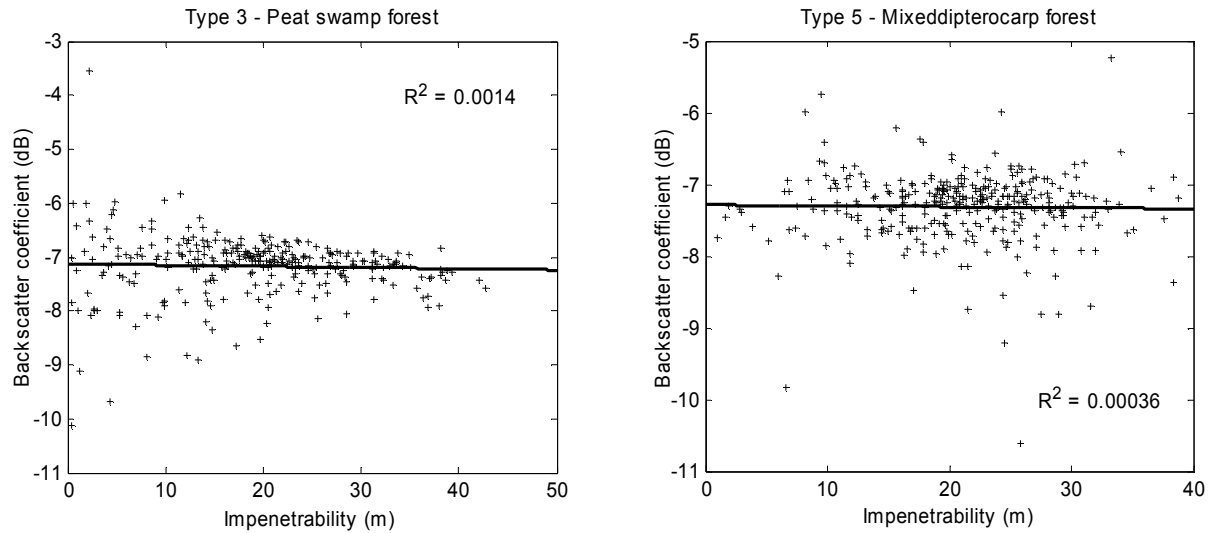


Figure 73: Scattergram showing values of the radar backscatter versus impenetrability for peat swamp (left pane), and mixed dipterocarp forests. A data point (+) represents one forest parcel.

The pixel size of the GRFM dataset is 3 arc-seconds by 3 arc-seconds (about 100 m by 100 m on the Equator). The pixel value is provided as an 8-bit integer. A mean of the pixel values was calculated for every forest parcel. The mean values were subsequently converted into L-band backscatter coefficients using the formula: $backscatter_coefficient = 20 * \log_{10}(50 * pixel_value + 1000) - 84.66$, which is provided as a part of the metadata to the GRFM datasets. It is good for the 100 m pixel size version of the GRFM data. The backscatter coefficient is expressed in decibel units (dB).

Figure 73 shows scattergrams of the backscatter coefficient versus impenetrability. In both cases, there is no significant correlation between impenetrability and the backscattering coefficient for impenetrability larger than ~12 - 15 m, indicating the saturation of the radar backscatter. For impenetrability values lower than that threshold, the backscatter is more variable (left pane in Figure 73), which is due to an increased contribution of non-biomass components. Other forest types in Brunei exhibit similar properties in relation to the L-band SAR GRFM dataset. The reference year for the investigated GRFM dataset was 1998. It is believed that the two-year acquisition disparity between the SRTM.C and GRFM (1998 vs. 2000) datasets is not a significant factor influencing the above results. This is because no dramatic change took place in Brunei forests in that time period.

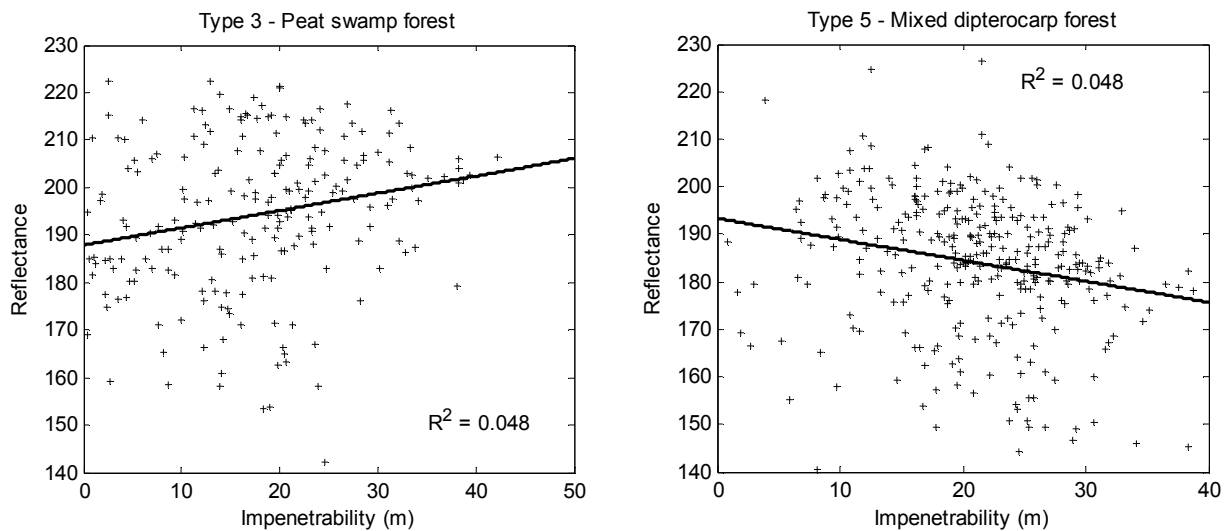


Figure 74: Scattergrams showing the X-band reflectance vs. impenetrability for peat swamp and mixed dipterocarp forest. Fitting lines are also shown. No significant correlation between variables is evident. A data point (+) represents one forest parcel.

8.8.3 Impenetrability vs. TerraSAR-X data

The third dataset investigated was the X-band SAR HH-polarised dataset, which was acquired by the German TerraSAR-X satellite on January 15, 2009. It covers about 90% of Brunei. The data were acquired in scan mode. A pixel value (the intensity of the backscatter) is stored as a 16-bit unsigned integer. The size of a pixel was 8.25 m by 8.25 m. The mean backscatter was calculated for every forest parcel. As scattergrams in Figure 74 document, again, there is no significant correlation between the impenetrability of a parcel and its mean X-band backscatter. This means that X-band SAR is not suitable to capture the biomass variations.

At this point, a comment regarding the correlation between the TerraSAR-X backscatter and heavy clouds/rain should be made. Figure 75 shows a part of the TerraSAR-X radar backscatter image in the left pane, while in the right pane the weather radar image is shown. The time lapse between both images is about 8 minutes. Clearly, the sudden drop indicated in the intensity of the backscatter in the left image corresponds with the thunderstorm cloud in the right image.

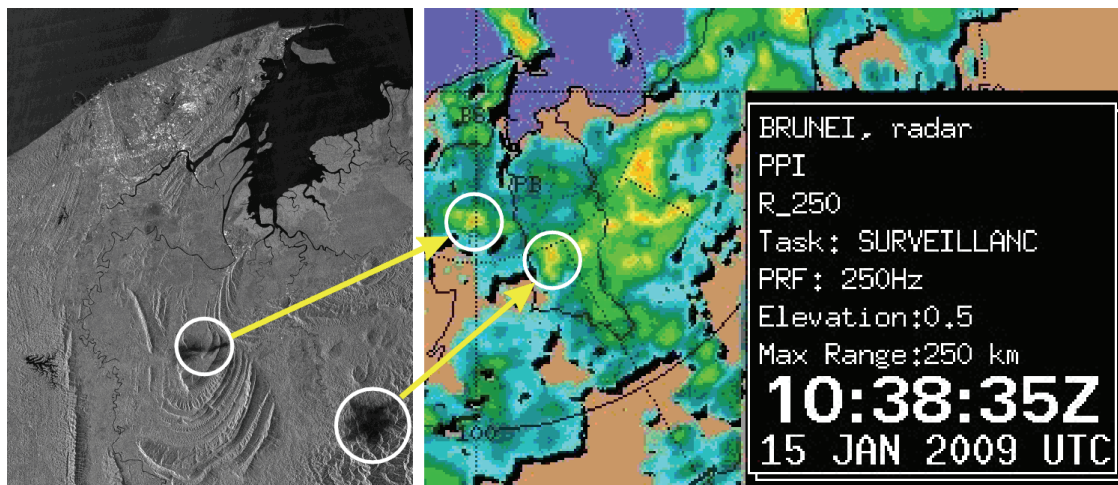


Figure 75: TerraSAR-X (left pane) and weather radar image (right pane). Indicated dark areas in the radar image correspond with the thunderstorms in the right image.

In this context, it is unknown to what extent rain during the acquisition time of the TerraSAR-X image influenced the conclusion regarding the correlation between the radar backscatter coefficient and the impenetrability. Certainly, the rain cells did not cause significant error in the interferometric phase during the SRTM acquisition (WERNER *et al.*, 2005).

8.8.4 Impenetrability vs. PALSAR data

The forth investigated dataset was the PALSAR, available at the L1.5 processing level. The image was downsampled to 25m by 25m pixel size, using the nearest neighbour algorithm.

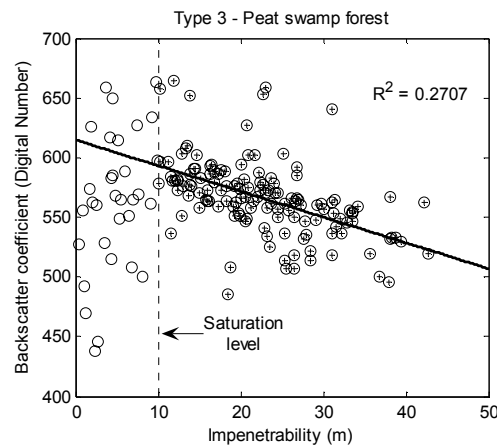


Figure 76: Scattergram showing a relationship between the impenetrability and the backscatter coefficient of the PALSAR L-band HH data. The dashed line indicates a hypothetical “saturation” level for the PALSAR data. Below the

10m impenetrability level it appears that there is no correlation with the PALSAR signal. The regression line was drawn for the impenetrability higher than 10m (only the dark circles were considered).

The pixel values of the image are available as 16 bit integers. They were not converted to sigma nought backscatter coefficient (dB), but rather used as provided digital numbers (DN). Figure 76 shows a scattergram of the impenetrability versus the backscatter coefficient for Type 3 forest. Circles indicate all data points available. Circles with a cross inside indicate data points used to draw the regression line. The split for subsets below and above saturation level was done visually. Clearly, the data points below 10 m of impenetrability show no signs of correlation. A possible reason for this is a much stronger influence of soil moisture than biomass. The data points above the saturation level do show a strong correlation indicating the PALSAR L-band data are sensitive to biomass at higher densities. This property of the PALSAR data allows for vegetation mapping. But for low density forests, e.g. Siberian Taiga, it can produce very noisy readings. In other words, the biomass impenetrability in C-band exhibits superior sensitivity to the biomass at all density levels.

9. OUTLOOK

Over the last three decades, air- and space-borne methods of acquiring data about our planet have been rapidly developed. However, active remote sensing techniques have not yet fully revealed their potential for these purposes. This uneven development in both active and passive remote sensing cannot be justified by the view that photography of the earth's surface is much more appealing to our visual perception system than a grey-scale radar image. Insufficient computation power to process high-resolution SAR and InSAR data, a lack of scientific knowledge for fully understanding and interpreting radar data, a lack of appropriate education and training in the radar techniques, and insufficient data and software infrastructure all contribute to the underdevelopment of SAR and InSAR techniques.

However, the last decade witnessed a very strong development of active air- and space-borne systems. This trend seems to have continued into this decade, considering several countries' advanced plans to develop space-borne radar systems. This major idea behind of these developments is to create radar data sources that could study the environment of our planet as a complement to already-existing passive data sources.

The production of the SRTM elevation data product is one of active remote sensing's brightest achievements in the past two decades. This unprecedented turn-of-the-millennium achievement has not only provided a 3D description of the planet's land surface, but also has made available an extremely valuable dataset for studying the biomass that covers some 30% of the earth's land area. This biomass is an extremely important player in global climate-control mechanisms. The SRTM dataset has also created an unprecedented opportunity to commence integration of the third dimension within the traditional 2D remote sensing framework. This can be considered the birth of 3D remote sensing (3DRS). The success of the SRTM program will most likely be an important stimulus for similar missions in the future (ROSEN *et al.*, 2000).

In fact, an InSAR mission, which should produce results comparable to the SRTM.X elevation datasets once it becomes fully operational, is already underway. This mission will probably launch in the early months of 2010. It is very likely that the data from the TanDEM program will also become a valuable source of information as far as the study of biomass is concerned. Another potential advantage of this mission is that it can achieve a high level of temporal resolution. This would allow study of the aboveground biomass at various stages of the vegetation cycle, including leaf-on/off states.

Without much speculation, it can be stated that the foreseeable future will bring hybrid space-borne systems equipped with passive sensors and also with InSAR capabilities. Currently, this trend is becoming more and more recognisable. Although the ALOS platform is still not InSAR enabled, it is a good example of a hybrid approach in the construction of space-borne remote-sensing systems. This trend will likely continue, considering that in 2007 the U.S. Committee on Earth Science and Applications from Space recommended undertaking studies of seventeen future space missions. One of them is the Deformation, Ecosystem Structure, and Dynamics of Ice, or DESDynI mission (DONNELLAN *et al.*, 2008). This mission would consist of an L-band SAR able to deliver repeat-pass InSAR data, and an infrared multiband LiDAR instrument. This unique combination is designed to collect data about small and localized movement of the ice cover of the earth's surface, but it will also allow investigation of the vertical vegetation structure and vegetation change. Confining these comprehensive capabilities within a single space-borne platform seems to be the right solution. However, some other solutions may also be available.

The correlation between biomass impenetrability and the actual amount of the biomass (g/m^2) remains an unresolved question in this report. It is believed that the conversion of impenetrability into biomass is necessary only in limited cases. One of our civilization's major concerns is not how much carbon is fixed in the aboveground biomass, but at what rate we are converting the biomass into CO_2 , or vice-versa.

Simulation studies were not considered to influence the topography of impenetrability. However, several leads were provided that pointed out a potentially fruitful research topic for future projects. One such lead is an exploration of the target-induced error formula introduced in Chapter 5. The limited size of the work is one reason for omitting these topics from exhaustive discussions.

The MMI method (mean maximum impenetrability) and its outcome – the effective forest area (EFA) – provide a new tool for forest, vegetation, or biomass studies carried out in many scientific disciplines. The method can also be used to prepare more accurate and reliable biomass density estimates in forms such as biomass density maps (BECEK, 2008d). These maps may become a primary tool to be used for more informed forest management decisions, forest fire management, and other related purposes.

10. CONCLUSIONS

The focus of the investigations was the systematic effect found in elevations derived by means of SAR interferometry. This effect is attributed to the vegetation cover, and is termed elevation bias or 'biomass impenetrability'. So biomass impenetrability is a form of representation of the biomass in the InSAR elevation datasets. Depending on the type of application, one may consider biomass impenetrability as an error, but for those studying vegetation the impenetrability may carry useful information for their subject of study. The investigations on biomass impenetrability from the latter vantage point have resulted in a number of observations and conclusions. The most important are presented below.

1. Biomass impenetrability appears to be a reliable and robust means for characterising biomass density, in both its vertical and horizontal extent or dimensions. It must be noted, however, that biomass density is not an absolute measure. Rather, it is referenced to the highest impenetrability found in an ecological unit of study. As an example of an ecological unit, forest stand, forest of certain types, forest resources in a country, region, climatic region, etc., can be provided.
2. Comprehensive economic analyses are required in order to assess cost and benefits associated with the potential deployment of the mean maximum impenetrability (MMI) method for regional and global forest resource monitoring and assessments.
3. The proposed effective forest area (EFA), which is based on biomass impenetrability, provides a framework and opportunity for much realistic global or regional re-evaluation of the aboveground biomass of our planet and its dynamics. But right away the "real-forest-only-counts" approach justifies the statement that the amount of aboveground biomass is significantly lower than currently thought.
4. The leading mechanism which controls the depth of penetration by radar radiation is the inter-trees space (Type 2 gaps). It must be noted at this point that the space is directly related to the fundamental characteristics of the forest, including the number of trees per hectare, tree type (shape of crown), crown diameter, crown and tree heights. Using conventional regression analyses and allometric equation, one can attempt to relate the impenetrability to a very important characteristics of the forest – the bole area. The bole area can then be reliably converted into biomass units of measure.
5. It is believed that biomass impenetrability should be considered as an addition to the conventional remote sensing methods, a powerful tool in the more accurate and comprehensive characterisation of biomass, vegetation and forest. This is because InSAR data are derived from signals backscattered by the structural elements of the vegetation, and not by the chemical composition as is the case in optical remote sensing (MANGES *et al.*, 2001). Much discussed in recent years, the data assimilation approach is one of the ways to "scramble" both multispectral and spatio-morphological characteristics of a forest to provide a much more comprehensive and quantitative description of the forest.
6. The United Nations through its Food and Agriculture Organisation should take a leading role in conducting a global forest inventory and monitoring independent of economic and political constraints. Countries, instead of providing national data for the Forest Resource Assessment five-year report, should financially support such a program.
7. The Type 3 gaps depend on the wavelength. The minimal cross-sectional area of a gap is proportional to the wavelength. For example, longer wavelengths require comparably large objects to be found in their path. This is why such radiation can travel within the canopy much longer than for shorter waves.
8. The conclusions regarding the role of gaps in the vegetation cover can be adapted to study vegetation by means of alternative measurement techniques, including LiDAR. This is in particular applicable to the modelling of the forest canopy.
9. The proposed modelling methodology of the "topography" of vegetation allows for significant reduction of the elevation bias of a DTM caused by the vegetation. For example, the vegetation bias for a forested area can be easily estimated based on just a few basic forest characteristics. A simple subtraction of the estimated bias from the DTM should provide a dramatic improvement in the accuracy of the DTM. It is worth noting that this strategy is in fact identical with the traditional photogrammetric technique of subtracting the mean tree height from the tree top elevation in order to estimate the bare earth elevation. Therefore, contours under a dense forest canopy must always be considered with caution.

11. REFERENCES

- ABDUL J. J., 1977: *The Shannon Sampling Theorem—Its Various Extensions and Applications: A Tutorial Review*. Proceedings of the IEEE, Vol. 65, pp. 1565–1595.
- ACHARD, F., EVA, H.D., STIBIG, H.-J., MAYAUX, P., GALLEG0, J., RICHARDS, T. & MALINGREAU, J.-P., 2002: *Determination of Deforestation Rates of the World's Humid Tropical Forests*. Science Magazine, Vol. 297, No. 9. Available online (March 2007): http://www-gem.jrc.it/tem/PDF_publicis/2002/Achard_Science_2002_deforestation.pdf.
- AHERN, F.J., LECKIE, D.J. & DRIEMAN, J.A., 1993: *Seasonal Changes in Relative C-band Backscatter of Northern Forest Cover Types*. IEEE Transactions on Geoscience and Remote Sensing, Vol. 31, No. 3, pp 668-680.
- AHMADZADEH, M.R. & PETROU, M., 2001: *Error Statistics for Slope and Aspect When Derived from Interpolated Data*. IEEE Trans. Geosci. Remote Sensing, Vol. 39, no. 9, pp.1823 – 1833.
- AHMED, Z. & RICHARDS, J.A., 1989: *Multiple Incidence Angle SIR-B Forest Observations*. IEEE Transactions on Geoscience and Remote Sensing, Vol. 27, No. 5, pp 586-591.
- ALBERGA, V., 2004: *Volume Decorrelation Effects in Polarimetric SAR Interferometry*. IEEE Transactions on Geoscience and Remote Sensing, Vol. 42, No. 11, pp 2467- 2478.
- ALLEN, J. & REIS, J., 2006: *Mapping an Oil Pipeline*. GIM International (The Global Magazine for Geomatics), July 2006.
- ANDERSEN, H.E., McGAUGHEY, R.J., & REUTEBUCH, S.E., 2006: *Assessing the Influence of Flight Parameters and Interferometric Processing on the Accuracy of X-band IFSAR-derived Forest Canopy Height Models*. Proceedings of Workshop on 3D Remote Sensing in Forestry, Vienna. Available online (Feb. 2007): http://www.rali.boku.ac.at/fileadmin/_/H85/H857/workshops/3drsforestry/Proceedings_3D_Remote_Sensing_2006_rev_20070129.pdf
- ANDERSEN, H.-E., McGAUGHEY, R.J., CARSON, W.W., REUTEBUCH, S.E., MERCER, B., & ALLAN, J., 2003: *A Comparison of Forest Canopy Models Derived From LiDAR and InSAR Data in a Pacific Northwest Conifer Forest*. Proceedings of the ISPRS Working Group III/3, Dresden, Germany. Available online (Feb. 2009) at www.isprs.org/commission3/wg3/workshop_laserscanning/papers/Andersen_ALSDD2003.pdf
- ANDERSON & MARSDEN (FORESTRY CONSULTANTS LTD), 1984: *Forest Map Brunei Darussalam*. The Government of Negara Brunei Darussalam.
- de ANGELIS, C.F., da COSTA FREITAS, C., de MORISSON VALERIANO, D., & DUTRA, L.V., 2000: *JERS-1 Backscatter Temporal Behavior of Land Use Types in The Tapajos National Forest, Brazilian Amazonia*. Geoscience and Remote Sensing Symposium, 2000. Proceedings. IGARSS 2000. IEEE 2000 International, Vol. 1, pp 7 – 9, DOI: 10.1109/IGARSS.2000.860403.
- ASHTON, P.S., 1964: *Manual of the Dipterocarp Trees of Brunei State*. Oxford University Press.
- ASKNE, J.I.H., DAMMERT, P.B.G., ULANDER, L.M.H. & SMITH, G., 1997: *C-band Repeat-Pass Interferometric SAR Observations of the Forest*. IEEE Transactions on Geoscience and Remote Sensing, Vol. 35, No. 1, pp 25 – 35, DOI: 10.1109/36.551931.
- ASKNE, J.I.H. & SMITH, G., 1996: *Forest InSAR Decorrelation and Classification Properties*. Proceedings of FRINGE 96. Available online (Feb, 2007): www.geo.unizh.ch/ysl/fringe96/papers/skne.
- AUSTIN, J.M., MACKEY, B.G. & VAN NIEL, K.P., 2003: *Estimating Forest Biomass Using Satellite Radar: An Exploratory Study In A Temperate Australian Eucalyptus Forest*. Forest Ecology and Management, Vol. 176, No. 1-3, pp. 575-583.

- BAILEY, R. G., 1996: *Ecosystem Geography*. Springer-Verlag. New York, New York. 216pp., ISBN 0-387-94586-5.
- BAILEY, J.E., SELF, S., WOOLLER, L.K. & MOUGINIS-MARK, P.J., 2007: *Discrimination of Fluvial and Eolian Features on Large Ignimbrite Sheets Around La Pacana Caldera, Chile, Using Landsat and SRTM-Derived DEM*. Remote Sens. Environ., Vol.108, No.1, pp 24-41.
- BALZTER, H., 2001: *Forest Mapping and Monitoring with Interferometric Synthetic Aperture Radar (InSAR)*. Progress in Physical Geography, Vol. 25(2), pp 159–177.
- BAMLER, R. & JUST, D., 1993: *Phase Statistics and Decorrelation in SAR Interferograms*. IEEE Geosci. Remote Sensing Symp., IGARSS'93, Tokyo, pp.980 – 984.
- BASUKI, T.M., VAN LAAKE, P.E., SKIDMORE, A.K. & HUSSIN, Y.A., 2009: *Allometric Equations For Estimating The Above-Ground Biomass In Tropical Lowland Dipterocarp Forests*. Forest Ecology and Management, Vol. 257, pp 1684–1694.
- BAUER, A.O., 2005: *Christian Hülsmeier and about The Early Days of Radar Inventions*. Available online (September, 2005): <http://www.xs4all.nl/~aobauer/Huelspart1def.pdf>
- BAYER, T., WINTER, R. & SCHREIER, G., 1991: *Terrain Influences in SAR Backscatter and Attempts to their Correction*. IEEE Transactions on Geoscience and Remote Sensing, Vol. 29, No. 3, pp 451-462.
- BEADLE, N.C.W., 1981: *The Vegetation of Australia*. Cambridge University Press, Cambridge.
- BEAUDOIN, A., CASTEL, T. & RABAUTE, T., 1996: *Forest Monitoring over Hilly Terrain Using ERS InSAR Data*. Proceedings of FRINGE 96. Available online (Feb, 2007): <http://www.geo.unizh.ch/rsl/fringe96/papers/beaudoin-et-al/>.
- BECCARI, O., 1989: *Wanderings in the Great Forests of Borneo*. Oxford University Press, Singapore.
- BECEK, K., 2008a. *Investigation of Elevation Bias of the SRTM C- and X-band Digital Elevation Models*. Proceedings of the XXI Congress of ISPRS, Beijing, China, Vol. XXXVII (B1-1), pp. 105-110.
- BECEK, K., 2008b: *Investigating Error Structure of Shuttle Radar Topography Mission Elevation Data Product*. Geophys. Res. Lett., 35, L15403, doi:10.1029/2008GL034592.
- BECEK, K., 2008c. *Detection of Tropical Forest Depletion by Exploring Second-Degree Moment of Its Spectral Profil*. Proceedings of the 14th Australasian Remote Sensing and Photogrammetry Conference, Darwin, Australia.
- BECEK, K., 2008d. *Development of a Vegetation Density Map of Brunei Darussalam*. Proceedings of the MapAsia 2008 Conference, 18th - 20th, August, 2008, Kuala Lumpur, Malaysia.
- BECEK, K., 2007: *Comparison of Decimation and Averaging Methods of DEM's Resampling*. Proceedings of the MapAsia 2007 Conference, Kuala Lumpur, Malaysia. Available online (December, 2008) at: <http://www.gisdevelopment.net/technology/ip/ma07267.htm>
- BECEK, K., 2006b: *Accuracy Evaluation of the SRTM Topographic Data Product over Selected Sites in Australia and Brunei Darussalam*. Proceedings of the 8th Bilateral Geodetic Meeting Poland-Italy, Wroclaw, Poland, 22-24 June 2006. In Reports on Geodesy, Vol. 77, no. 2, pp 283-289.
- BECEK, K. & MICHAEL, P., 2005: *Socio-Economic Development and Biomass Depletion: A Case Study of a Selected Site in Tutong District, Brunei Darussalam*. 8th South East Asian Survey Congress, Brunei Darussalam, 2005.
- BECEK, K. & MICHAEL, P., 2006: *Biomass Depletion as a Result of Socio-Economic Development in Brunei Darussalam*. ICORG 2006 Conference, Hyderabad, India, June 2006.

- BECEK, K., and ODIHI, O.J., 2008. *Identification and Assesment of Factors Affecting Forest Depletion in Brunei Darussalam*. Proceedings of the XXI Congress of ISPRS, Beijing, China, Vol. XXXVII (B2-1), pp. 209-213.
- BEE, O.J., 1987: *Depletion of the Forest Resources in the Philippines*. Field Report Series No. 18, Institute of Southeast Asian Studies, Singapore.
- BERTHIER, E., ARNAUD, Y., KUMAR, R., AHMAD, S., WAGNON, P. & CHEVALLIER, P., 2007: *Remote Sensing Estimates of Glacier Mass Balances in The Himachal Pradesh (Western Himalaya, India)*. Remote Sens. Environ., Vol. 108, No. 3, pp 327-338.
- BOERJAN, W., RALPH, J., & BAUCHER, M., 2003: *Lignin bios.* Ann. Rev. Plant Biol. Vol. 54, pp 519–549. doi:10.1146/annurev.arplant.54.031902.134938.
- BOERNER, W-M., 2008: *Introduction to Synthetic Aperture Radar (SAR) Polarimetry*. Wexford Press.
- BORGEAUD, M. & WEGMUELLER, U., 1996: *On the Use of ERS SAR Interferometry for the Retrieval of Geo- and Bio-Physical Information*. Proceedings of the Fringe '96 Workshop, 30 Sept - 2 Oct 1996, Zurich, Switzerland.
- BORN, M. & WOLF, E., 1999: *Principles of Optics*. 7th edition, Cambridge University, ISBN 0-521-64222-1.
- BOTKIN, D.B., 1993: *Forest Dynamics : An Ecological Model*. Cary, NC, USA: Oxford University Press, Incorporated.
- BOYD, D.S. & DANSON, F.M., 2005: *Satellite Remote Sensinf of Forest Reosurces: Three Decades of Research Development*. Progress in Physical Geography, Vol. 29, 1, pp 1-26.
- BROWN, C.G., JR., SARABANDI, K. & PIERCE, L.E., 2005: *Validation of the Shuttle Radar Topography Mission Height Data*. IEEE Transactions on Geoscience and Remote Sensing, Vol. 43, No. 8, pp 1707- 1715.
- BROWN, S., 1997: *Estimating Biomass and Biomass Change of Tropical Forests: a Primer*. (FAO Forestry Paper - 134). Available online (March 2007): www.fao.org/docrep/W4095E/W4095E00.htm.
- BRUENIG, E.F., 1998: *Conservation and Management of Tropical Rainforests. An Integrated Approach to Sustainability*. CABI, Oxon, UK.
- CANDEIAS, A.L.B., 1996: *Drainage Network Extraction from a SAREX'92 RADAR Image*. In proc. of SIBGRAPI, pp. 243 – 250. Available online: <http://mirror.impa.br/sibgrapi96/trabs/pdf/a07.pdf>.
- CARABAJAL C.C. & HARDING, D.J., 2006: *SRTM C-band and ICESat Laser Altimetry Elevation Comparisons as a Function of Tree Cover and Relief*. Photogrammetric Engineering & Remote Sensing (PE&RS), Vol. 72, No. 3, pp287-298.
- CASTEL, T., BEAUDOIN, A., FLOURY, N., LE TOAN, T., CARAGLIO, Y. AND BARCZI, J-F., 2001: *Deriving Forest Canopy Parameters for Backscatter Models Using the AMAP Architectural Plant Model*. IEEE Transactions On Geoscience and Remote Sensing, Vol. 39, No. 3, pp. 571-583.
- CHAPMAN, A.D., 2005: *Numbers of Living Species in Australia and the World*. Report for the Department of the Environment and Heritage, Canberra, Australia. Available online (March 2007): <http://www.environment.gov.au/biodiversity/abrs/publications/other/species-numbers/pubs/number-living-species-report.pdf>.
- CHAVE, J., CONDIT, R., LAO, S., CASPERSEN, J. P., ROBIN B. FOSTER, R. B. & HUBBELL, S. P. 2003: *Spatial and Temporal Variation of Biomass in a Tropical Forest: Results from a Large Census Plot in Panama*. Journal of Ecology, Vol. 91 pp 240 - 252.
- CHEN, J.M. & CIHLAR, J., 1995: *Quantifying the Effect of Canopy Architecture on Optical Measurements of Leaf Area Index Using Two Gap Size Analysis Methods*. IEEE Transactions on Geoscience and Remote Sensing, Vol. 33, No. 3, pp 777-787.

- CHRISTENSEN, E.L., DALL, J., SKOU, N., WOELDERS, K., GRANHOLM, J., & MADSEN, S.N., 1998: *EmiSAR: C- and L-band Polarimetric and Interferometric SAR*. IEEE Trans. on Geoscience and Remote Sensing, Vol. 36, No. 6, pp 1852-1865.
- CLAUSET, A., SHALIZI, C.R. & NEWMAN, M.E.J., 2009: *Power-Law Distributions In Empirical Data*. SIAM Review. arXiv:0706.1062. Available online (March, 2009):
- CLOUDE, S.R. & PAPATHANASSIOU, K.P., 1998: *Polarimetric SAR Interferometry*. IEEE Transactions on Geoscience and Remote Sensing, Vol. 36, No. 5, pp 1551 – 1565.
- COHEN, W.B., SPIES, T.A., 1992: *Estimating Structural Attributes of Douglas-Fir/Western Hemlock Forest Stands from Landsat and SPOT Imagery*. Rem. Sens. Environ. Vol. 41, pp 1–17.
- CONDIT, R., ASHTON, P.S., BAKER, P., BUNYAVEJCHEWIN, S., GUNATILLEKE, S., GUNATILLEKE, N., HUBBELL, S.P., FOSTER, R.B., ITOH, A., LaFRANKIE, J.V., LEE, S.H., LOSOS, E., MANOKARAN, N., SUKUMAR, R. & YAMAKURA, T., 2000: *Spatial Patterns in the Distribution of Tropical Tree Species*. Science, Vol. 288, No. 5470, pp 1414 – 1418.
- COPPIN, P.R. & BAUER, M.E., 1992: *Optimization of the Information Content of Multitemporal Landsat TM Data Sets for Monitoring Forest Cover Disturbance*. Geoscience and Remote Sensing Symposium, IGRASS'92, Vol. 2, pp 983-985.
- COPPIN, P.R. & BAUER, M.E., 1994: *Processing of Multitemporal Landsat TM Imagery to Optimize Extraction of Forest Cover Change Features*. IEEE Transactions On Geoscience and Remote Sensing, Vol. 32, pp 918-927.
- CORRIPIO J.G., 2003: *Vectorial Algebra Algorithms for Calculating Terrain Parameters from Dems and Solar Radiation Modelling in Mountainous Terrain*. International Journal of Geographical Information Science, Vol. 17, No 1, pp 1-23.
- CRECENTE-CAMPO, F., MARSHALL, P., LeMAY, V., & DIÉGUEZ-ARANDA, U., 2009: *A Crown Profile Model for Pinus Radiata D. Don in Northwestern Spain*. Forest Ecology and Management, Vol. 257, pp. 2370 – 2379.
- CURLANDER, J.C. & McDONOUGH, R.N., 1991: *Synthetic Aperture Radar Systems and Signals Processing*. – John Wiley and Sons, New York.
- CURRAN, P.J., KUPIEC, J.A. & SMITH, G.M., 1997: *Remote Sensing the Biochemical Composition of a Slash Pine Canopy*. IEEE Transaction on Geoscience and Remote Sensing, Vol. 35, No. 2, pp 415-420.
- CUTRONA, L.J., LEITH, E.N., PORCELLO, L.J. & VIVIAN, W.E., 1966: *On the Application of Coherent Optical Processing Techniques to Synthetic-Aperture Radar*. Proceedings of the IEEE, Vol. 54, No. 8, pp 1026 – 1032.
- DESCLÉE, B., BOGAERT, P. & DEFOURNY, P., 2006: *Forest Change Detection by Statistical Object-Based Method*. Remote Sensing of Environment, Vol. 102, pp 1–11.
- DAMMERT, P.B.G., 1996: *Accuracy of InSAR Measurements in Forested Areas*. Proceedings of the Fringe '96 Workshop, 30 Sept - 2 Oct 1996, Zurich, Switzerland.
- DeFRIES, R., ACHARD, F., BROWN, S., HEROLD, M., MURDIYARSO, D., SCHLAMADINGER, B. & DeSOUZA, C., 2006: *Reducing Greenhouse Gas Emissions from Deforestation in Developing Countries: Considerations for Monitoring and Measuring*. Report of the Global Terrestrial Observing System (GTOS) number 46, GOFC-GOLD report 26. Available online: (March 2007): www.fao.org/gtos/pubs.html.
- DERAUW, D. & MOXHET, J., 1996: *Multiple Images SAR Interferometry*. Proceedings of the Fringe '96 Workshop, 30 Sept - 2 Oct 1996, Zurich, Switzerland.
- DIDASCALOU, D., YOUNIS, M. & WERNERWIESBECK, W., 2000: *Millimeter-Wave Scattering and Penetration in Isolated Vegetation Structures*. . IEEE, Transaction on Geoscience and Remote Sensing, Vol. 38, No. 5, pp 2106-2113.

- DIETZE, M.C., WOLOSIN, M.S. & CLARK, J.S., 2008: *Capturing Diversity and Interspecific Variability in Allometries: a Hierarchical Approach*. Forest Ecology and Management, Vol. 256, pp. 1939–1948.
- DIXON, R. K., SOLOMON, A. M., BROWN, S., HOUGHTON, R. A., TREXIER, M. C. & WISNIEWSKI, J., 1994: *Carbon Pools and Flux of Global Forest Ecosystems*. Science, Vol. 263, no. 5144, pp. 185 – 190.
- DLR, 2003: *SRTM DTED Format Product Description, SRTM/PD-01/03. Version 1.2*. Document supplied by DLR along with the purchase of the SRTM.X dataset.
- DEPARTMENT OF NATURAL RESOURCES (DNR), 1998: *Old Growth Forest in South East Queensland, Technical Report: 1998/01*. DNRQ980145, Department of Natural Resources, December 1998, Brisbane.
- DOBSON, M.C., ULABY, F.T., LE TOAN, T., BEAUDOIN, A., KASISCHKE, E.S. & CHRISTENSEN, N., 1992: *Dependence of Radar Backscatter on Conifer Forest Biomass*. IEEE Trans. Geosci. Remote Sens., Vol. 30, pp. 412-415.
- DOBSON, M.C., ULABY, F.T., PIERCE, L.E., SHARIK, T.L., BERGEN, K.M., KELLNDORFER, J., KENDRA, J.R., LI, E., LIN, Y.C., NASHASHIBI, A., SARABANDI, K. & SIQUEIRA, P., 1995a: *Estimation of Forest Biophysical Characteristics in Northern Michigan with SIR-C/XSAR*. IEEE Trans. Geosci. Remote Sens., Vol. 33, pp 877-895.
- DOBSON, M.C., ULABY, F.T., PIERCE, L.E., 1995b: *Land Cover Classification and Estimation of Terrain Attributes Using Synthetic Aperture Radar*. Remote Sens. Environ., Vol. 51, No 1, pp. 199-214.
- DONNELLAN, A., ZEBKER, H. & RANSON, K.J., 2008: *Radar and LiDAR Measurement of Terrestrial Processes*. EOS, Transactions, American Geophysical Union, Vol. 89, No. 38
- DONG, J., KAUFMANNA, R.K., MYNENIA, R.B., TUCKERB, C.J., KAUPPIC, P.E., LISKID, J, BUERMANNNA, W., ALEXEYEV, V., & HUGHESG, M.K., 2003: *Remote Sensing Estimates of Boreal and Temperate Forest Woody Biomass: Carbon Pools, Sources, and Sinks*. Remote Sensing of Environment, Vol. 84, pp 393–410.
- dos SANTOS, J.R., de ARAUJO, L.S. & LACRUZ, M.S.P., 2000: *Potential use of JERS-1 data for biomass estimation of tropical forest environments in Brazilian Amazonia*. Proceedings. IGARSS 2000. IEEE 2000 International, Vol. 1 pp. 10 – 12.
- DUBOIS-FERNANDEZ, P., CHAMPION, I., GUYON, D., CANTALLOUBE, H., GARESTIER, F., DUPUIS, X. & BONIN, G., 2005: *Forest Biomass Estimation from P-band High Incidence Angle Data*. PolInSAR 2005 conference, European Space Agency. Available online (Feb. 2007): http://earth.esa.int/workshops/polinsar2005/participants/88/paper_biomass_estimation_from_pband.pdf.
- DUPÉRET, A., DEFFONTAINES, B., 2004: *Digital Analysis and Basic Shape Relief Extraction from DTM*. Proceedings of XXth ISPRS Congress, Comm. 2, 23/2004 Istanbul, Turkey, pp. 810-815. Available online: www.isprs.org/istanbul2004/comm2/papers/236.pdf.
- DURDEN L.S., KLEIN, J.D. & ZEBKER H.A., 1991: *Polarimetric Radar Measurements of a Forest Area Near Mt. Shasta*. IEEE, Transaction on Geoscience and Remote Sensing, Vol. 29, No. 3, pp 444-450.
- DUREN, R., WONG, E., BRECKENRIDGE, B., SHAFFER, S., DUNCAN, C., TUBBS, E. & SALOMON, P., 1998: *Metrology, Attitude, and Orbit Determination for Spaceborne Interferometric Synthetic Aperture Radar*. SPIE AeroSense Conference on Acquisition, Tracking and Pointing XII, April 1998.
- EARTHDATA 2007: Frequently Asked Questions. Available online: (November, 2007), www.earthdata.com/pdfs/GeoSar_FAQ.pdf
- EDIRIWEERA, S., SINGHAKUMARA, B.M.P., & ASHTON, M.S., 2008: *Variation in Canopy Structure, Light and Soil Nutrition across Elevation of a Sri Lankan Tropical Rain Forest*. Forest Ecology and Management, Vol 256, pp 1339–1349.

- EINER, M., 2003: *Problems and Solutions for InSAR Digital Elevation Model Generation of Mountainous Terrain*. Available online (Feb. 2007): http://earth.esa.int/fringe03/proceedings/papers/33_eineder.pdf.
- EINER, M., 2005a: *Interferometric DEM Reconstruction of Alpine Areas – Experiences with SRTM Data and Improved Strategies for Future Missions*. Available online (Feb. 2007): www.ipi.uni-hannover.de/html/aktivitaeten/EARSeL-Workshop2005_Paper/Eineder.pdf.
- EINER, M., 2005b: *Alpine Digital Elevation Models from Radar Interferometry - a Generic Approach to Exploit Multiple Imaging Geometries*. Available online (Feb. 2007): www.ipi.uni-hannover.de/html/publikationen/2005/workshop/125-eineder.pdf.
- EL-RAYES, M.A. & ULABY, F.T., 1987: *Microwave Dielectric Spectrum of Vegetation-Part I: Experimental Observations*. IEEE Transactions on Geoscience and Remote Sensing, Vol. GE25, No. 5, pp 541-549.
- EYKHOFF, P., 1974: *System Identification. Parameter and State Estimation*. John Wiley and Sons, London.
- FERRETTI, A., PRATI, C. & ROCCA, F., 2001: *Permanent Scatters in SAR Interferometry*. IEEE Transaction on Geoscience and Remote Sensing, Vol. 39, No. 1, pp 8-20.
- FANG, Z. & BAILEY, R.L., 1998: *Height-Diameter Models for Tropical Forests on Hainan Island in Southern China*. Forest Ecology and Management, Vol. 110, pp. 315-327.
- FAO, 2004: *Global Forest Resources Assessment Update 2005; Terms and Definitions (Final Version)*. FAO, United Nations, Rome, Paper - 83/E. Available online (March 2007): <http://www.fao.org/docrep/007/ae156e/ae156e00.htm>.
- FAO, 2005a: *Global Forest Resources Assessment 2005*. FAO Forestry Paper 147, United Nations, Rome. Available online (March 2007): <http://www.fao.org/forestry/fra2005>.
- FAO, 2005b: *Global Forest Resources Assessment 2005. Brunei Darussalam. Country Report*. FAO Forestry Paper 149, United Nations, Rome. Available online (March 2007): <http://www.fao.org/forestry/fra2005>.
- FERRAZZOLI, P. & GUERRIERO, L., 1995: *Radar Sensitivity to Tree Geometry and Woody Volume: a Model Analysis*. IEEE Transactions on Geoscience and Remote Sensing, Vol. 33, No. 2, pp 360-371.
- FERRAZZOLI, P., PALOSCIA, S., PAMPALONI, P., SCHIAVON, G., SIGISMONDI, S. & SOLIMINI, D., 1997: *The Potential of Multifrequency Polarimetric SAR in Assessing Agricultural and Arboreous Biomass*. IEEE Transactions on Geoscience and Remote Sensing, Vol. 35, No. 1, pp 5-17.
- FIEDLER, H., KRIEGER, G., ZINK, M., EINER, M. & MOREIRA, A. 2006: *TanDEM-X: A New Satellite Mission for Deriving a Global DEM with Unprecedented Height Accuracy*. (Abstract only). Available online (March 2007): <http://ifn.bauw.unibw-muenchen.de/gw06/fiedler.html>.
- FLOURY, N., LE TOAN, T., SOUYRIS, J-C., SINGH, K., STUSSI, N., HSU, C.C. & KONG, J. A., 1996: *Interferometry for Forest Studies*. Available online (March 2007): http://earth.esa.int/workshops/fringe_1996/floury/.
- FOSBERG, F.R., 1967: *A Classification of Vegetation for General Purpose*. In Guide to the checksheet for IBP handbook 4, Peterken, G.F. (editor), 73-120. Oxford - Blackwell.
- FRANKLIN, S.E. 2001: *Remote Sensing for Sustainable Forest Management*. Lewis Publishers.
- FRANKLIN, S.E. & LUTHER, J.E., 1995: *Satellite Remote Sensing of Balsam Fir Forest Structure, Growth, and Cumulative Defoliation*. Canadian Journal of Remote Sensing. Vol. 21, pp. 400-411.
- FRANSSON, J.E.S., WALTER, F. & ULANDER, L.M.H., 2000: *Estimation of Forest Parameters Using CARABAS-II VHF SAR Data*. IEEE Transactions on Geoscience and Remote Sensing, Vol. 38, No. 2, pp 720-727.

- FREEMAN, T., 1996: *What is Imaging Radar?* Available online (March 2007): <http://southport.jpl.nasa.gov/desc/imagingradarv3.html>.
- FRÖLIND, P.-O. & ULANDER, L.M.H., 2002: *Digital Elevation Map Generation Using VHF-band SAR Data in Forested Areas*. IEEE Transactions on Geoscience and Remote Sensing, Vol. 40, No. 8, pp 1769- 1776.
- FUJISADA, H., BAILEY, G.B., KELLY, G.G., HARA, S. & ABRAMS, M.J., 2005: *ASTER DEM performance*. Geoscience and Remote Sensing, IEEE Transactions on, Vol. 43, No. 12, pp 2707- 2714.
- GABRIEL, A.K., GOLDSTEIN, R.M. & ZEBKER, H.A., 1989: *Mapping Small Elevation Changes over Large Areas: Differential Radar Interferometry*. J. Geophys. Res., Vol. 94, No. B7, pp 9183-9191.
- GATELLI, F., GUAMIERI, A.M., PARIZZI, F., PASQUALI, P., PRATI, C. & ROCCA, F., 1994: *The Wavenumber Shift in SAR Interferometry*. . IEEE Transactions on Geoscience and Remote Sensing, Vol. 32, No. 4, pp 855-865.
- GE, L., CHANG, H.C., RIZOS, C. & TRINDER, J., 2004: *Multi-pass Differential Radar Interferometry with the Aid of GIS*. Available online (April 2007): <http://www.isprs.org/istanbul2004/comm2/papers/245.pdf>.
- GEOSCIENCE AUSTRALIA, 2007: *Datums and Coordinates*. Available online (Dec. 2007): www.ga.gov.au/geodesy/datums/aboutdatums.jsp
- GEUDTNER, D., VAEHON, P.W., MATTAR, K.E. & GRAY, A.L., 1998: *RADARSAT Repeat-pass SAR Interferometry*. Geoscience and Remote Sensing Symposium Proceedings. IGARSS, IEEE International, Vol. 3, pp 1635 – 1637.
- GOBLIRSCH, W., WERNER, C., NÜSCH, D. & FALLER, N., 1995: *Accuracy of interferometric elevation models generated from DOSAR airborne data*. Geoscience and Remote Sensing Symposium, IGARSS'95, Vol.1, pp 770 – 774.
- GONG, P., MILLER, J.R. & SPANNER, M., 1994: *Forest Canopy Closure from Classification and Spectral Unmixing of Scene Components-Multisensor Evaluation of an Open Canopy*. IEEE Transactions on Geoscience and Remote Sensing, Vol. 32, No. 5, pp 1067-1080.
- GRAHAM, L.C., 1974: *Synthetic Interferometer Radar for Topographic Mapping*. Proceedings of the IEEE, Vol. 62, No. 6, pp 763–768.
- GREENBERG, J.A., DOBROWSKI, S.Z. & VANDERBILT, V.C., 2009: *Limitations on Maximum Tree Density Using Hyperspatial Remote Sensing and Environmental Gradient Analysis*. Remote Sensing of Environment, Vol. 113, pp 94– 101.
- GEO, 2007: *The Full Picture*. Group on Earth Observations (GEO), Geneva, Switzerland, ISBN 978-92-990047-0-8.
- GRAY, R. M., & DAVISSON, L. D., 2003: *An Introduction to Statistical Signal Processing*. Cambridge Univ. Press, Cambridge, U. K.
- MONTI GUARNIERI, A., DARIA, D. CAFFORIO, C., GUCCIONE, P., PASQUALI, P., NÜETSCH, D. SMALL, D., MEIER, E. & DESNOS, Y.L., 2004: *ENVISAT Interferometry for Mapping and Monitoring: Preliminary Results*. Proceedings of the FRINGE 2003 Workshop (ESA SP-550). ESA/ESRIN, Frascati, Italy. p.33.1.
- GUTH, P. L. 2006: *Geomorphometry from SRTM: Comparition to NED*. Photogrammetric Engineering & Remote Sensing (PE&RS), Vol. 72, No. 3, March 2006, pp 269-277.
- GUTJAHR, K. & SCHARDT M., 2006: *Retrieval of Forest Parameters from Multi-Polarimetric, Multi-Frequency Interferometric SAR Data*. Proceedings of Workshop on 3D Remote Sensing in Forestry, 14th-15th Feb. 2006, Vienna – Session 4b. Available online (Feb. 2007): http://www.rali.boku.ac.at/fileadmin/_/H85/H857/workshops/3drsforestry/Proceedings_3D_Remote_Sensing_2006_rev_20070129.pdf.

- HAARBRINK, R.B., 2003: *High Altitude LiDAR to Enhance Geosar System Performance*. Proceedings of the ISPRS working group III/3 workshop, Deesden, Germany. Available online (December 2008): http://www.isprs.org/commission3/wg3/workshop_laserscanning/papers/Haarbrink_ALSDD2003.pdf.
- HAGBERG, J.O. & ULANDER, L.M.H., 1993: *On the Optimization of Interferometric SAR for Topographic Mapping*. IEEE Transactions on Geoscience and Remote Sensing, Vol. 31, No. 1, pp 303-306.
- HAGBERG, J.O., ULANDER, L.M.H. & ASKNE, J., 1995: *Repeat-pass SAR Interferometry over Forested Terrain*. IEEE Transactions on Geoscience and Remote Sensing, Vol. 33, No. 2, pp 331-340.
- HEIN, A., 2004: *Processing of SAR Data: Fundamentals, Signal Processing, Interferometry*. Springer-Verlag, Berlin, Heidelberg, New York.
- HALL, S.A., BURKE, I.C., BOX, D.O., KAUFMANN, M.R. & STOKER, J.M., 2005: *Estimating Stand Structure Using Discrete-Return LiDAR: an Example From Low Density, Fire Prone Ponderosa Pine Forests*. Forest Ecology and Management, Vol. 208, pp 189 - 209.
- HALLBERG, B., SMITH, G., OLOFSSON, A. & ULANDER, L.M.H., 2004: *Performance Simulation of Spaceborne P-band SAR for Global Biomass Retrieval*. Proceedings of Geoscience and Remote Sensing Symposium, IGARSS, IEEE International. Vol.1, No. 20-24, pp 503 – 506. D.O.I. 10.1109/IGARSS.2004.1369074.
- HALLIKAINEN, M., HYYPPÄ, J., HAAPANEN, J., TARES, T., AHOLA, P., PULLIAINEN, J. & M. TOIKKA, 1993: *A helicopter-borne eight-channel ranging scatterometer for remote sensing—Part I: System description*. IEEE Transactions on Geoscience and Remote Sensing, Vol. 31, No. 1, pp. 161–169.
- HANSEN, M., DeFRIES, R.S., TOWNSHEND, J.R.G., CARROLL, M., DIMICELI, C. & SOHLBERG, R.A., 2003: *Global Percent Tree Cover at a Spatial Resolution of 500 Meters: First Results of the MODIS Vegetation Continuous Fields Algorithm*. Earth Interactions, Vol 7, No. 10, pp 1-15.
- HANSEN, R.F., 2001: *Radar Interferometry. Data Interpretation and Error Analysis*. Hingham, MA, USA: Kluwer Academic Publishers.
- HARDING, D. 2005: *Comparison of Airborne LiDAR and SRTM C-band Elevations for a Vegetated Landscape*. Workshop: “The Shuttle Radar Topography Mission – Data Validation and Applications”, June 14-16, 2005, Reston, Virginia, USA. Available online (April 2007): http://edc.usgs.gov/conferences/SRTM/presentations/Slides23_Harding.pdf.
- HAWKINS, R.K., BROWN, C.E., MURNAGHAN, K.P., GIBSON, J.R., ALEXANDER, A. & MAROIS, R., 2002: *The SAR-580 Facility – System Update*. Geoscience and Remote Sensing Symposium, IGARSS. IEEE International Vol. 3, pp 1705 – 1707.
- HAYAKAWA, Y.S., OGUCHI, T., & LIN, Z., 2008: *Comparison of New and Existing Global Digital Elevation Models: ASTER G-DEM and SRTM-3*. Geophys. Res. Lett., 35, L17404, doi:10.1029/2008GL035036.
- HEIPKE, C., KOCH, A. & LOHMANN, P. 2002: *Analysis of SRTM DTM - Methodology and Practical Results*. Proceedings of ISPRS Commission IV Symposium in Ottawa, July 2002.
- HERLAND, E-A., 1996: *Operational Use of SAR Interferometry for DEM Generation and Land Use Mapping*. Proceedings of the Fringe '96 Workshop, 30 Sept - 2 Oct 1996, Zurich, Switzerland.
- HESEA, S., LUCHTB, W., SCHMULLIUSA, C., BARNSELYC, M., DUBAYAH, R., KNORRA, D., NEUMANNA, K., RIEDELA, T., & SCHRFTERE, K., 2005: *Global Biomass Mapping for an Improved Understanding of the CO₂ Balance—the Earth Observation Mission Carbon-3D*. Remote Sensing of Environment, Vol. 94, pp. 94–104.
- HOEKMAN, D.H. & QUIÑONES, M.J., 2002: *Biophysical Forest Type Characterization in the Colombian Amazon by Airborne Polarimetric SAR*. IEEE Transactions on Geoscience and Remote Sensing, Vol. 40, No. 6, pp 1288-1300.

- HOEKMAN, D.H. & QUIÑONES, M.J., 2000: *Land Cover Type and Biomass Classification Using AIRSAR Data for Evaluation of Monitoring Scenarios in the Colombian Amazon*. IEEE Transactions on Geoscience and Remote Sensing, Vol. 38, No. 2, pp 685-696.
- HOFFMANN, K. & FISCHER, P., 2002: *DOSAR : a multifrequency polarimetric and interferometric airborne SAR-system*. Geoscience and Remote Sensing Symposium, IGARSS '02. IEEE International, Vol. 3, pp. 1708- 1710.
- HOFTON, M., DUBAYAH, R., BLAIR, J.B. & RABINE, D., 2006: *Validation of SRTM Elevations over Vegetated and Non-vegetated Terrain Using Medium-Footprint LiDAR*. Photogrammetric Engineering & Remote Sensing (PE&RS), Vol. 72, No. 3, pp 279-285.
- HOLLING C S, 1973. *Resilience and Stability of Ecological Systems*. Annual Review of Ecology and Systematics Vol. 4, pp 1-23.
- HOUSER, P.R., 2001: *Land Data Assimilation Systems*. IGARSS, Vol. 1, pp 28 – 30, doi: 10.1109/IGARSS.2001.976047.
- HOWARD, J.A., 1991: *Remote Sensing of Forest Resources. Teory and Application*. Chapman & Hall, London.
- HUSCH, B., 1971: *Planning a Forest Inventory*. FAO Forestry Series, No. 4.
- HYDE, P., NELSON, R., KIMES, D. & LEVINE, E., 2007: *Exploring LiDAR-Radar Synergy – Predicting Aboveground Biomass in a Southwestern Ponderosa Pine Forest Using LiDAR, SAR and InSAR*. Remote Sensing of Environment, Vol. 106, pp 28-38.
- HYYPÄ, H.J., 2000: *Feasibility for Estimation of Single Tree Characteristics Using Laser Scanner*. Geoscience and Remote Sensing Symposium, 2000. Proceedings. IGARSS 2000. IEEE 2000 International, Vol.3, No. 2000, pp 981 – 983.
- HYYPÄ, J. & HALLIKAINEN, M., 1993: *A helicopter-borne eight-channel ranging scatterometer for remote sensing—Part II: Forest inventory*. IEEE Transactions on Geoscience and Remote Sensing, Vol. 31, No. 1, pp. 170–179.
- HYYPÄ, J. & PULLIAINEN, J., 1994: *Inventory by Compartments Using Radar-Derived Stand Profiles*. IEEE Transactions on Geoscience and Remote Sensing, Vol. 32, No. 1, pp 108 – 110.
- HYYPÄ, J., HALLIKAINEN, M. & PULLIAINEN, J., 1993: *Accuracy of Forest Inventory based on Radar-Derived Stand Profile*. IEEE Transactions on Geoscience and Remote Sensing, Vol. 31, No. 2, pp 391 – 393.
- HYYPÄ, J. & ENGDAHL, M., 2000: *Verification of the capability of repeat-pass SAR interferometry to provide tree height information in boreal forest zone*. Proceedings. IGARSS 2000. IEEE 2000 International, Vol, 1, pp. 402-404.
- HYYPÄ, J., PULLIAINEN, J., HALLIKAINEN, M. & SAATSI, A., 1997: *Radar-Derived Standwise Forest Inventory*. IEEE Transactions on Geoscience and Remote Sensing, Vol. 35, No. 2, pp 392 - 404.
- HYYPÄ, J., PULLIAINEN, J., HEISKA, K. & HALLIKAINEN, M., 1994: *Statistics of Backscattering Source Distribution of Boreal Coniferous Forests at C- And X-band*. Geoscience and Remote Sensing Symposium, IGARSS '94. Surface and Atmospheric Remote Sensing: Technologies, Data Analysis and Interpretation., Vol. 1, pp 241 – 242.
- HYYPÄ, J., HYYPÄ, H., INKINEN, M., ENGDAHL, M., LINKO, S. & ZHU, Y.H., 2000: *Accuracy Comparison of Various Remote Sensing Data Sources in the Retrieval of Forest Stand Attributes*. Forest Ecology and Management, Vol. 128 (1-2), pp 109-120.
- IMHOFF, M.L., 1995: *Radar Backscatter and Biomass Saturation: Ramifications for Global Biomass Inventory*. IEEE Transactions on Geoscience and Remote Sensing, Vol. 33, No. 2, pp 511 – 518.
- IPCC, 2003: *Good Practice Guidance for Land Use, Land-Use Change and Forestry*. Intergovernmental Panel on Climate Change (IPCC). Available online (March 2007): <http://www.ipcc-nggip.iges.or.jp/public/gpglulucf/gpglulucf.htm>.

- INTERMAP, 2008: *Product Handbook & Quick Start Guide*. Intermap Technologies, Standard Edition, v4.2. Available online (December, 2008): www.intermap.com.
- IZZAWATI, WALLINGTON, E.D. & WOODHOUSE, I.H., 2004 : *The Impact of Forest Heterogeneity on the Height Retrieval using X-band Interferometry*. Proceedings of IGRASS'2004, IEEE International, Vol. 3, pp 2042 – 2045.
- IZZAWATI, WALLINGTON, E.D. & WOODHOUSE, I.H., 2006: *Forest Height Retrieval from Commercial X-band SAR Products*. IEEE Trans. Geosci. Remote Sens., Vol. 44, No. 4, pp 863-870.
- JALI, D., 2003: *Cellulose Decomposition in Tropical Peat Swamp*. Wetland Science, Vol 1, pp 28 – 35.
- JIN, Y-Q. & LIANG, Z., 2004: *An Approach of Three-Dimensional Vector Radiative Transfer (3-D-VRT) Equation for Inhomogeneous Scatter Media*. IEEE Transactions on Geoscience and Remote Sensing, Vol. 42, No. 2, pp 355–360.
- JPL, 2008: *SEASAT 1978*. Available online (Sep. 2008): <http://southport.jpl.nasa.gov/scienceapps/seasat.html>.
- JUSTICE, C.O. & TOWNSHEND, J.R.G., 1981: *Integrating Ground Data with Remote Sensing*. In Terrain Analysis and Remote Sensing. Townshend, J.R.G. (editor), George Allen & Unwin, London.
- KARJALAINEN, M., & HYYPPÄ, J, 2009: *Obtaining Digital Elevation Models Using SAR Techniques*. Available online (Jan. 2009), http://www.fgi.fi/osastot/projektisivut/kk_www_portaali/rswww/vhrSAR_index.html
- KASISCHKE, E.S., CHRISTENSEN, N.L., JR. & BOURGEOU-CHAVEZ, L.L., 1995: *Correlating Radar Backscatter with Components of Biomass in Loblolly Pine Forests*. IEEE Transactions on Geoscience and Remote Sensing, Vol. 33, No. 3, pp 643-659.
- KELLNDORFER, J.M., WALKER, W.S., PIERCE, L.E., DOBSON, M.C., FITES, J. HUNSAKER, C., VONA, J., CLUTTER, M., 2004: *Vegetation Height Derivation from Height Derivation from Shuttle Radar Topography Mission and National Elevation Data Sets*. Remote Sensing of Environment, Vol. 93, No. 3, 339-358.
- KIEL, B., ALSDORF, D. & LEFAVOUR, G., 2006: *Capability of SRTM C and X Band DEM Data to Measure Water Elevations in Ohio and the Amazon*. Photogrammetric Engineering & Remote Sensing (PE&RS), Vol. 72, No. 3, pp 313-320.
- KINGSLEY, S. & QUEGAN, S., 1993: *Understanding Radar System*. McGraw-Hill Book Company, Singapore.
- KRAWCZYK, A., PERSKI, Z., MARINKOVIĆ, P. & HANSSEN, R., 2008: *Evaluation of TerraSAR-X InSAR for the Measurements of Mining Subsidence*. The 3rd TerraSAR-X Science Team Meeting, 25 – 26 November, 2008. Available online (December, 2008): http://sss.terrasar-x.dlr.de/papers_sci_meet_3/poster/MTH0246_perski.pdf.
- KROPATSCH, W.G. & STROBL, D., 1990: *The Generation of SAR Layover and Shadow Maps from Digital Elevation Models*. IEEE Transactions on Geoscience and Remote Sensing, Vol. 28, No. 1, pp 98-107.
- LANGNER, A., MIETTINEN, J. & SIEGERT, F., 2007: *Land Cover Change 2002-2005 in Borneo and the Role of Fire Derived from MODIS Imagery*. Global Change Biology, Vol. 13, No. 11, pp 2329-2340, doi: 10.1111/j.1365-2486.2007.01442.x
- LE TOAN, T.; BEAUDOIN, A.; RIOM, J.; GUYON, D., 1992: *Relating Forest Biomass to SAR Data*. IEEE Transactions on Geoscience and Remote Sensing, Vol. 30, No. 2, pp 403-411.
- LE TOAN, T., PICARD, G., MARTINEZ, J-M., MELON. P. & DAVIDSON. M., 2002: *On the Relationships between Radar Measurements and Forest Structure and Biomass*. Proceedings of the 3rd International Symposium 'Retrieval of Bio- and Geophysical Parameters from SAR Data for Land Applications', Sheffield, UK, 11-14 Sept. 2001, (ESA SP-475).

- LEVA, D., NICO, G., TARCHI, D., FORTUNY-GUASCH, J. & SIEBER, A.J., 2003: *Temporal Analysis of a Landslide by Means of a Ground-based SAR Interferometer*. IEEE Transactions on Geoscience and Remote Sensing, Vol. 41, No. 4, pp 745–752.
- LI, Z., CHEN, J., & BALTSAVIAS, E. (Eds), 2008: *Advances in Photogrammetry, Remote Sensing and Spatial Information Sciences: 2008 ISPRS Congress Book*. Taylor & Francis Group, London, UK.
- LI, F.K. & GOLDSTEIN, R.M., 1990: *Studies of Multibaseline Spaceborne Interferometric Synthetic Aperture Radars*. IEEE Transactions on Geoscience and Remote Sensing, Vol. 28, No. 1, pp 88 – 97.
- LIN, W., CHOU, W., LIN, C., HUANG, P. & TSAI, J., 2006: *Automated Suitable Drainage Network Extraction from Digital Elevation Models in Taiwan's Upstream Watersheds*. Hydrological Processes, Vol. 20, 2, pp 289-306.
- LILLESAND, T.M., & KIEFER, R.W., 2000: *Remote Sensing and Image Interpretation*. 4th edition, Wiley, New York.
- LLOYD, G.E.R., 1968: *Aristotle: The Growth and Structure of his Thought*. Cambridge: Cambridge University. Press.
- LOEW, A., ed, 2008: *Remote Sensing Data Assimilation Special Issue*. Remote Sensing of Environment, Vol. 112, No 4, pp 1257-1908.
- LOMBARDINI, F., 2005: *Differential Tomography: a New Framework for SAR Interferometry*. IEEE Transactions on Geoscience and Remote Sensing, Vol. 43, No. 1, pp 37- 44.
- LOU, Y., KIM, Y. & VAN ZYL, J., 1996: *The NASA/JPL Airborne Synthetic Aperture Radar System*. Available online (December, 2008): http://airsar.jpl.nasa.gov/documents/genairsar/airsar_paper1.pdf.
- LU, Z., WICKS, C., DZURISIN, D., THATCHER, W., FREYMUELLER, J., McNUTT, S. & MANN, D., 2000: *A Seismic Inflation of Westdahl Volcano, Alaska, Revealed by Satellite Radar Interferometry*. Geophys. Res. Lett. Vol. 27, pp 1567–1570.
- LU, Z., RYKHUS, R., MASTERLARK, T. & DEAN, K.G., 2004: *Mapping Recent Lava Flows at Westdahl Volcano, Alaska, Using Radar and Optical Satellite Imagery*. Remote Sens. Environ., Vol. 91, No. 3-4, pp 345-353.
- MALHI, Y., MEIR, P. & BROWN, S., 2002: *Forests, Carbon and Global Climate*. Phil. Trans. R. Soc. Lond. A, Vol. 360, pp. 1567-1591. Available online (March 2007): http://www.geog.ox.ac.uk/~ymalhi/publications/malhi_et_al_ptrs_forests_carbon_and_global_climate.pdf.
- MARECHAL, N., 1995: *Tomographic Formulation of Interferometric SAR for Terrain Elevation Mapping*. IEEE Transactions on Geoscience and Remote Sensing, Vol. 33, No. 3, pp 726-739.
- MADSEN, S.N., ZEBKER, H.A. & MARTIN, J., 1993: *Topographic Mapping Using Radar Interferometry: Processing Techniques*. IEEE Transactions on Geoscience and Remote Sensing, Vol. 31, No. 1, pp 246-256.
- MARLIANI, F., PALOSCIA, S., PAMPALONI, P. & KONG, J.A., 2002: *Simulating Coherent Backscattering from Crops during the Growing Cycle*. IEEE Transactions on Geoscience and Remote Sensing, Vol. 40, No. 1, pp 162-177.
- MARTENS, S.,N., BOREL, C.C. & GERLST, S.A.W., 1993: *High Fidelity Computer Reconstruction of Tree Canopy Architecture*. Bulletin of the Ecological Society of America, Vol. 74, No. 345.
- MARSCHALK, U., BAUER, M., PFEIFFER, B., ROTH, A., HOFFMANN, J. & RABUS, B., 2004: *Derivation of a Multi-Sensor Interferometric DEM of the Dead Sea Region*. Proc. of the 2004 ENVISAT & ERS Symposium, Salzburg, Austria, 6-10 Sep. 2004. Available online (Feb. 2007): http://earth.esa.int/workshops/salzburg04/papers_posters/3P05_22_marschal_217.pdf.
- MAY, R. M. 1988: *How Many Species are There on Earth?* Science Vol. 247, pp 1441-1449. Available online (March 2007): <http://www.ciesin.columbia.edu/docs/002-253/002-253.html>.

- MAYAUX, P., HOLMGREN, P., ACHARD, F., EVA, H., STIBIG, H.-J. & BRANTHOMME, A., 2005: *Tropical Forest Cover Change in the 1990s and Options for Future Monitoring*. Philosophical Transactions of the Royal Society B 360, pp 373–384.
- MENGES, C.H., HILL, G.J.E., AHMAD, W. & VAN ZYL, J.J., 2001: *Incidence Angle Correction of AirSAR Data to Facilitate Land-Cover Classification*. PE&RS, Vol. 67, No. 4, pp 479–489.
- METTE, T., *Potential of PolIn-SAR to Estimate Forest Biomass*. Available online (Sept. 2008): http://earth.esa.int/dragon/prog_pdfs/TM_polinsar.pdf
- METTE, T., KUGLER, F., PAPATHANASSIOU, K. & HAJNSEK, I., 2006: *Viewing Forest in Pol-InSAR*, Proceedings of Workshop on 3D Remote Sensing in Forestry, Available online (Feb. 2007): http://www.rali.boku.ac.at/fileadmin/_H85/H857/workshops/3drsforestry/Proceedings_3D_Remote_Sensing_2006_rev_20070129.pdf.
- METTE, T., PAPATHANASSIOU, K. & HAJNSEK, I., 2005: *Forest Biomass from Pol-InSAR L-band and Forest Allometry - What We Learnt from Temperate Forest*. Available online (Feb 2007): http://earth.esa.int/workshops/polinsar2005/participants/94/pres_mette_94.pdf.
- MITZENMACHER, M., 2003: *A Brief History of Generative Models for Power Law and Lognormal Distributions*. Internet Mathematics Vol. 1, pp 226 – 251. Available online (March, 2009): www.internetmathematics.org/volumes/1/2/pp226_251.pdf.
- MOLLICONE D., F. ACHARD, H.D. EVA, A.S. BELWARD, S. FEDERICI, A. LUMICISI, V.C. RIZZO, H.-J. STIBIG, R. VALENTINI, 2003: *Land Use Change Monitoring in the Framework of the UNFCCC and its Kyoto Protocol: Report on Current Capabilities of Satellite Remote Sensing Technology*. European Communities, Luxembourg. EUR 20867 EN. 48 p. Available online (March 2007): http://www-tem.jrc.it/PDF_publicis/2003/Mollicone_COP9_2003.pdf.
- MOREIRA, J., SCHWÄBISCH, M., WIMMER, C., MURA, J., 2001: *Surface and Ground Topography Determination in Tropical Rainforest Areas Using Airborne Interferometric SAR*. Photogrammetric Week 2001, Wichmann Verlag, Heidelberg, 2001.
- MOUGIN, E., LOPES, A. & LE TOAN, T., 1990: *Microwave Propagation at X band in Cylindrical-Shaped Forest Components: Attenuation Observations*. IEEE Transactions on Geoscience and Remote Sensing, Vol. 28, No. 1, pp 60–69.
- MÜLLENHOFF, O., 2003: *Evaluation of Multi-Frequency and Multi-Polarisation Airborne SAR Data for Marsh Land and River Dyke Analysis*. Photogrammetric Week '03, (D. Fritsch – Editor), Herbert Wichmann Verlag, Heidelberg.
- NADKARNI, N.M., McINTOSH, A.C.S. & CUSHING, J.B. 2008: *A Framework to Categorize Forest Structure Concepts*. Forest Ecology and Management, Vol. 256, pp 872–882.
- NASA, 2000: *SRTM As-Flown Mission Timeline*. Available online (December 2007): www2.jpl.nasa.gov/srtm/SRTM_TIM_AF.pdf
- NASA, 2005: *SRTM Topography*. Available online (March 2007): ftp://e0srp01u.ecs.nasa.gov/srtm/-version2/Documentation/SRTM_Topop.pdf.
- NI, W., SUN, G., GUO, Z. & QIN, W., 2008: *Effect of Forest Structure on Scattering Center Height From Model and SAR Data*. IEEE International, Geoscience and Remote Sensing Symposium, IGARSS 2008, Vol. 5, pp 421–424.
- NICO, G., LEVA, D., FORTUNY-GUASCH, J., ANTONELLO, G. & TARCHI, D., 2005: *Generation of Digital Terrain Models with a Ground-based SAR System*. IEEE Transactions on Geoscience and Remote Sensing, Vol. 43, No. 1, pp 45–49.
- NILSON, T., 1999: *Inversion of Gap Frequency Data in Forest Stands*. Agricultural and Forest Meteorology, Vol. 98–99, pp 437–448.

- NOGUEIRA, E.M., FEARNside, P.M. & NELSON, B.W., 2008: *Normalization of Wood Density in Biomass Estimates of Amazon Forests*. Forest Ecology and Management, Vol. 256, pp 990–996.
- NOGUEIRA, E.M., FEARNside, P.M., NELSON, B.W., BARBOSA, R.I. & KEIZER, E.W.H., 2008: *Estimates of Forest Biomass in the Brazilian Amazon: New Allometric Equations and Adjustments to Biomass from Wood-Volume Inventories*. Forest Ecology and Management, Vol. 256, pp 1853–1867
- NORHEIM, R.A., QUEIJA, V.R. & HAUGERUD, R.A., 2002: *Comparison of LIDAR and INSAR DEMs with Dense Ground Control*. Proceedings of the Environmental Systems Research Institute 2002 User Conference, July 2002, San Diego. Available online (March 2007): <http://gis.esri.com/library/-userconf/proc02/pap0442/p0442.htm>.
- NORTON, R.M., 1984: *Double Exponential Distribution: Using Calculus to Find a Maximum Likelihood Estimator*. The American Statistician, Vol. 38, No. 2, pp. 135-136.
- OLMSTED, C., 1993: *Scientific SAR User's Guide*. Alaska SAR Facility, July 1993. Available online (April 2007): <http://www.asf.alaska.edu/reference/general/SciSARUserGuide.pdf>.
- PANTA, M., KIM, K. & JOSHI, C., 2008: *Temporal Mapping of Deforestation and Forest Degradation in Nepal: Applications to Forest Conservation*. Forest Ecology and Management, Vol. 256, No. 9, pp 1587-1595, DOI: 10.1016/j.foreco.2008.07.023.
- PAPATHANASSION, K.P., CLOUDE, S.R., REIBER, A., & BOERNER, W.M., 2000: *Multi-baseline Polarimetric SAR Interferometry for Vegetation Parameters Estimation*. Geoscience and Remote Sensing Symposium, 2000. Proceedings. IGARSS 2000. IEEE 2000 International, Vol. 6, No. 2000, pp 2762 – 2764.
- PAPATHANASSIOU, K.P. & CLOUDE, S.R., 2001: *Single-baseline Polarimetric SAR Interferometry*. IEEE Transactions on Geoscience and Remote Sensing, Vol. 39, No. 11, pp 2352 – 2363.
- PARKER, G.G., 1995: *Structure and Microclimate of Forest Canopies*. In Forest Canopies (eds. Lowman, M. D. and Nadkarni, N. M.), pp. 73-106. Academic Press, San Diego, USA.
- PAUCHARD, A., UGARTE, E. & MILLÁN, J., 2000: *A Multiscale Method for Assessing Vegetation Baseline of Environmental Impact Assessment (EIA) in Protected Areas of Chile*. USDA Forest Service Proceedings, RMRS-P-15, Vol 3, pp 111-116.
- PHILIP, M.S., 2002: *Measuring Trees and Forests*. CABI Publishing, Oxon, UK.
- PICARD, G., LE TOAN, T. & QUEGAN, S., 2004a: *A three-dimensional radiative transfer model to interpret ranging scatterometer measurements from a pine forest*. Waves Random Media, Vol. 14, pp 317–331.
- PICARD, G., LE TOAN, T., QUEGAN, S., CARAGLIO, Y. & CASTEL, T., 2004: *Radiative Transfer Modeling of Cross-Polarized Backscatter from a Pine Forest Using the Discrete Ordinate and Eigenvalue Method*. IEEE Transactions on Geoscience and Remote Sensing, Vol. 42, No. 8, pp 1720- 1730.
- PIERACCINI, M., LUZI, G. & ATZENI, C., 2001: *Terrain Mapping by Ground-based Interferometric Radar*. IEEE Transactions on Geoscience and Remote Sensing, Vol. 39, No. 10, pp 2176 – 2181.
- POLATIN, P.F., SARABANDI, K. & ULABY, F.T., 1994: *An Iterative Inversion Algorithm with Application to the Polarimetric Radar Response of Vegetation Canopies*. IEEE Transactions on Geoscience and Remote Sensing, Vol. 32, No. 1, pp 62–71.
- PRAKS, J., HALLIKAINEN, M. & YU, X., 2008: *Tomographic Measurements of Boreal Forest with Synthetic Aperture Radar*. Available online (Feb. 2009): http://www.ursi.fi/2008/data/files/URSI2008_Praks.pdf.
- QUIÑONES, M.J. & HOEKMAN, D.H., 2004: *Exploration of Factors Limiting Biomass Estimation by Polarimetric Radar in Tropical Forests*. IEEE Transactions on Geoscience and Remote Sensing, Vol. 42, No. 1, pp 86- 104.

- RABUS, B., EINEDER, M., ROTH, A., & BAMLER, R., 2003: *The Shuttle Radar Topography Mission- a New Class of Digital Elevation Models Acquired by Spaceborne Radar*. Photogramm. Rem. Sens, Vol 57, pp 241-262.
- RANSON, K.J., SUN, G., LANG, R.H., CHAUHAN, N.S., CACCIOLA, R.J. & KILIC, O., 1997: *Mapping of Boreal Forest Biomass from Spaceborne Synthetic Aperture Radar*. Journal of Geophysical Research, Vol. 102, No. D24, pp 29,599 - 29,610.
- RANSON, K.J., SUN, G., WEISHAMPEL, J.F., & KNOW, B.G., 1997: *Forest Radar Biomass from Combined Backscatter Modeling*. Remote Sensing of Environment, Vol. 59, pp 118-133.
- READ, A.M., 2008: *Removal of Vegetation Height Offset in the SRTM DEM of Australia*. Proceedings of the 14th Australasia Remote Sensing and Photogrammetry Conference 14ARSPC, Darwin, Australia.
- REIGBER, A. & SCHEIBER, R., 2003: *Airborne Differential SAR Interferometry: First Results at L-band*. IEEE Transactions on Geoscience and Remote Sensing, Vol. 41, No. 6, pp 1516–1520.
- REINARTZ, P., MÜLLER, R., HOJA, D., LEHNER, M. & SCHROEDER, M., 2005: *Comparison and fusion of DEM derived from SPOT-5 HRS and SRTM data and estimation of forest heights*. Proc. EARSEL Workshop on 3D-Remote Sensing, Porto. Available online (May, 2009): http://testwww.ipi.uni-hannover.de/html/aktivitaeten/EARSEL-Workshop2005_Paper/Reinartz.pdf
- REINARTZ, P., MÜLLER, R., LEHNER, M. & SCHROEDER, M., 2006: *Generation of DEM and Orthoimages from SPOT HRS Stereo Data Without using GCP*. ISPRS Volume Number: XXXVI-1/W41, Ankara, Commision I, WG I/5. Available online (May, 2009): http://www.isprs.org/commission1/ankara06/makaleler/Reinartz_Generation_DEM.pdf.
- RENAUDIN, E., 2000: *Evaluation of DEMs from SAR Interferometry and SPOT Stereoscapy for Remote Sensing Applications*. Institute for Geodesy and Photogrammetry, Swiss Federal Institute of Technology, Zürich, Switzerland.
- RIGNOT, E.J.M. & VAN ZYL, J.J., 1995: *Spaceborne Applications of P Band Imaging Radars for Measuring forest Biomass*. IEEE Transactions on Geoscience and Remote Sensing, Vol. 33, NO. 5, pp 1162 – 1169.
- RODRÍGUEZ, E., IMEL, D.A., & MADSEN, S. N., 1994: *The Accuracy of Airborne Interferometric SAR'S*. Available online (March 2007): <http://ntrs.nasa.gov/search.jsp?R=116780&id=2&q=N%3D4294776381>
- RODRÍGUEZ, E., MORRIS, C.S., BELZ, J.E., CHAPIN, E.C., MARTIN, J.M., DAFFER, W., & HENSLEY, S. 2003: *An Assessment of the SRTM Topographic Products*. Technical Report JPL D-31639, Jet Propulsion Laboratory, Pasadena, California, 143 pp.
- ROSEN, P.A., HENSLEY, S., JOUGHIN, I.R., LI, F.K., MADSEN, S.N., RODRÍGUEZ, E. & GOLDSTEIN, R.M., 2000: *Synthetic Aperture Radar Interferometry*. Proceedings of the IEEE, Vol. 88, No. 3, pp 333 – 382.
- ROSENQVIST, Å., SHIMADA, M., CHAPMAN, B., FREEMAN, A., DE GRANDI, G., SAATCHI, S. & RAUSTE, Y., 2000: *The Global Rain Forest Mapping Project—a Review*. Int. J. Remote Sensing, Vol. 21, No. 6 & 7, pp 1375–1387.
- ROSENQVIST, Å., SHIMADA, M., CHAPMAN, B., McDONALD, K., DE GRANDI, G., JONSSON, H., WILLIAMS, C., RAUSTE, Y., NILSSON, M., SANGO, D. & MATSUMOTO, M., 2004: *An Overview of the JERS-1 SAR Global Boreal Forest Mapping (GBFM) Project*. Proc. of IGARSS'04, Fairbanks, Alaska.
- ROSENQVIST A., SHIMADA, M., WATANABE M., TADONO T. & YAMAUCHI K., 2004: *Implementation of Systematic Data Observation Strategies for ALOS PALSAR, PRISM and AVNIR-2*. IGARSS '04. Vol 7, pp. 4527- 4530.
- ROY, J., SAUGIER, B., MOONEY, H.A., 2001: *Terrestrial Global Productivity*. Academic Press, San Diego, CA.

- RUDANT, J-P., BEDIDI, A., CALONNE, R., MASSONNET, D., NESTI, G. & TARCHI, D., 1996: *Laboratory Experiments for the Interpretation of Phase Shift in SAR Interferograms*. Proceedings of the Fringe '96 Workshop, 30 Sept - 2 Oct 1996, Zurich, Switzerland.
- RUFINO, G., MOCCIA, A. & ESPOSITO, S., 1998: *DEM Generation by Means of ERS Tandem Data*. IEEE Transactions on Geoscience and Remote Sensing, Vol. 36, No. 6, pp 1905-1912.
- SAATCHI, S.S. & MOGHADDAM, M., 2000: *Estimation of Crown and Stem Water Content and Biomass of Boreal Forest Using Polarimetric SAR Imagery*. IEEE Transactions on Geoscience and Remote Sensing, Vol. 38, No. 2, pp 697-709.
- SANTORO, M., ASKNE, J. & DAMMERT, P.B.G., 2005: *Tree Height Influence on ERS Interferometric Phase in Boreal Forest*. IEEE Transactions on Geoscience and Remote Sensing, Vol. 43, No. 2, pp 207- 217.
- SARABANDI, K., 1997: *Δk -Radar Equivalent of Interferometric SAR's: a Theoretical Study for Determination of Vegetation Height*. IEEE Transactions on Geoscience and Remote Sensing, Vol. 35, No. 5, pp 1267-1276.
- SARABANDI, K., BROWN, C.G. & PIERCE, L., 1999: *Tree height estimation from the polarimetric and interferometric radar response*. Proc. IEEE Trans. Geosci. Remote Sensing Symp., Hamburg, Germany, 1999.
- SARABANDI, K., & LIN, Y.C., 2000: *Simulation of Interferometric SAR Response for Characterizing the Scattering Phase Center Statistics of Forest Canopies*. IEEE Transactions on Geoscience and Remote Sensing, Vol. 38, No. 1, pp 115-125.
- SCHUMANN, G., MATGEN, P., CUTLER, M.E.J., BLACK, A., HOFFMANN, L. & PFISTER, L., 2007: *Comparison of Remotely Sensed Water Stages from LiDAR, Topographic Contours and SRTM*. ISPRS Journal of Photogrammetry and Remote Sensing, Vol. 63, No. 3, pp 283-296.
- SEXTON, J.O., BAX, T., SIQUEIRA, P., SWENSON, J.J. & HENSLEY, S., 2009: *Comparison of LiDAR, Radar, and Field Measurements of Canopy Height in Pine and Hardwood Forests of Southeastern North America*. Forest Ecology and Management, Vol. 257, pp. 1136–1147.
- SIGNELL, P., 2001: *Electromagnetic Waves from Maxwell's Equations*. PHYSNET. Available online (Oct/2008: <http://www.physnet.org/modules/pdfmodules/m210.pdf>).
- SIMARD, M., RIVERA-MONROY, V.H., MANCERA-PINEDA, J.E., CASTAÑEDA-MOYA, E. & TWILLEY, R.R., 2008: *A Systematic Method for 3D Mapping of Mangrove Forests based on Shuttle Radar Topography Mission Elevation Data, Icesat/GLAS Waveforms and Field Data: Application to Ciénaga Grande De Santa Marta, Colombia*. Remote Sensing of Environment, Vol. 112, pp 2131–2144.
- SIMARD, M., ZHANG, K., RIVERA-MONROY, V.H., ROSS, M.S., RUIZ, P.L., CASTAÑEDA-MOYA, E., TWILLEY, R.R. & RODRÍGUEZ, E., 2006: *Mapping Height and Biomass of Mangrove Forests in the Everglades National Park with SRTM Elevation Data*. Photogrammetric Engineering & Remote Sensing (PE&RS), Vol. 72, No. 3, pp 299-311.
- SKIDMORE, A.K., 1989: *A Comparison of Techniques for Calculating Gradient and Aspect from a Gridded Elevation Model*. International Journal of Geographic Information Systems, vol. 3, 4, pp. 323-334.
- SKOLNIK, M.I. Ed., 1990: *Radar Handbook*, McGraw-Hill, New York, 1990.
- SLATER, J. A., GARVEY, G., JOHNSTON, C., HAASEN, J., HEADY, B., KROENUNG, G. & LITTLE, J., 2006: *The SRTM Data "Finishing" Process and Products*. Photogrammetric Engineering and Remote Sensing, Vol. 72, No. 3, pp. 237-247.
- SLATTON, K. C., CRAWFORD, M. M. & EVANS, B. L., 2001: *Fusing Interferometric Radar and Laser Altimeter Data to Estimate Surface Topography and Vegetation Heights*. IEEE Transactions on Geoscience and Remote Sensing, Vol. 39, No. 11, November 2001, pp 2470-2482.

- SMITH, B. & SANDWELL, D., 2003: *Accuracy and Resolution of Shuttle Radar Topography Mission Data*. Geophys. Res. Lett., Vol. 30, No. 9.
- SMITH, J. O., 2007: *Fourier Theorems for the DFT, in Mathematics of the Discrete Fourier Transform (DFT) with Audio Applications*. [electronic], 2nd ed., W3K Publishing, Menlo Park, Calif. Available at http://ccrma.stanford.edu/_jos/mdft/Fourier_Theorems_DFT.html.
- STONE, W.E., 2004: *ASPRS Guide to Land Imaging Satellites*. Available online (May 2009): <http://www.asprs.org/news/satellites>
- SOLAAS, G.A. & GATELLI, F., 1996: *Initial testing of ERS Tandem Quality for InSAR Applications; Examples from Taiwan, Madagascar, Zaire, Ivory Coast, Mali and Greenland*. Proceedings of the Fringe '96 Workshop, 30 Sept - 2 Oct 1996, Zurich, Switzerland.
- SOLBERG, S., WEYDAHL, D. & NÆSSET, E., 2008: Simulating X-Band Interferometric Heights and Canopy Penetration Using Airborne LiDAR. Proceedings of the 3rd TerraSAR-X Science Team Meeting, 25-26 Nov., DLR Oberpfaffenhofen, Germany. Available online: http://sss.terrasar-x.dlr.de/papers_sci_meet_3/paper/LAN0101_solberg.pdf
- STEININGER, M.K., 2000: *Satellite Estimation of Tropical Secondary Forest Above-ground Biomass: Data from Brazil and Bolivia*. Int. Journal. Remote Sensing, Vol. 21, No. 6 & 7, pp 1139–1157.
- SUN, G. & RANSON, K.J., 1995: *A three-dimensional radar backscatter model of forest canopies*. IEEE Trans. Geosci. Remote Sens., Vol. 33, No. 2, pp. 372–382.
- SUNE R.J.A, ERIKSSON, M. & HALLDIN, S., 1999: *Tree-heights derived from radar profiles over boreal forests*. Agricultural and Forest Meteorology, Vol. 98-99, pp 427-435.
- TANGKI, H. & CHAPPELL, N.A., 2008: *Biomass Variation across Selectively Logged Forest within a 225-Km² Region of Borneo and its Prediction by Landsat TM*. Forest Ecology and Management, Vol. 256, pp. 1960–1970
- TOWNSHEND, J.R.G., 1981: *Terrain Analysis and Remote Sensing*. George Allen & Unwin, London.
- TRINDER, J., CHENG, E. & GE, L., 2003: *Tests on Determining Digital Elevation Models from ERS Tandem Data*. Geomatics Research Australasia, 79, 59-74.
- ULABY, F.T. & EL-RAYES, M.A., 1987: *Microwave Dielectric Spectrum of Vegetation-Part II: Dual-Dispersion Model*. IEEE Transactions on Geoscience and Remote Sensing, Vol. GE25, No. 5, pp 550-557.
- ULABY, F.T., MOORE R.K. & FUNG, A.K. 1982: *Microwave Remote Sensing Vol. II*. Addison-Wesley, Reading, MA.
- UNFCCC, 2006: *Background Paper for the Workshop on Reducing Emissions from Deforestation in Developing Countries*. Workshop on reducing emissions from deforestation in developing countries. Working paper No. 1 (a) (2006), Part I. Available online (March 2007): http://unfccc.int/files/methods_and_science/lulucf/application/pdf/part_i_scientific_issues.pdf
- USGS, 2007: *The National Map Seamless Server*. Available online: <http://seamless.usgs.gov/>.
- USTIN, S.L., MARTENS, S.N. & VANDERBILT, V.C., 1991: *Canopy Architecture of a Walnut Orchard*. IEEE Transactions on Geoscience and Remote Sensing, Vol. 29, No. 6, pp 843-851.
- VAN NIEL, T.G., McVICAR, T.R., LI, L.T., GALLANT, J.C. & YANG, Q.K., 2007: *The Impact of Misregistration on SRTM and DEM Image Differences*. Remote Sensing of Environment, Vol. 112, pp 2430– 2442.
- WEGMÜLLER, U. & WERNER, C. L., 1996: *Applications Using ERS-1/2 Tandem Data*. Available online (March 2007): http://earth.esa.int/workshops/fringe_1996/wegmuell/

- WANG, Y., DAVIS, F.W., KASISCHKE, E.S., 1994: *Effects of Variation in Soil Moisture on ERS-1 SAR Backscatter*. Geoscience and Remote Sensing Symposium, IGARSS '94. Surface and Atmospheric Remote Sensing: Technologies, Data Analysis and Interpretation., International , Vol.3, pp.1475-1477.
- WARNER, T., BELL, R. & SINGHROY, V., 1996: *Local Incidence Angle Effects on X and C band Radar Backscatter of Forest Communities*. Canadian Journal of Remote Sensing, Vol. 22, No. 3, pp 269-279.
- WARNER, T. A., LEE, J., Y. & MCGRAW, J. B., 1998: *Delineation and Identification of Individual Trees in the Eastern Deciduous Forest*. International Forum on Automated Interpretation of High Spatial Resolution Imagery for Forestry. Victoria B.C. Available online (March 2007): <http://www.geo.wvu.edu/~warner/resume/victoria98.pdf>.
- WEISHAMPEL, J.F., BLAIR, J.B., KNOX, R.G., DUBAYAH, R. & CLARK D.B., 2000: *Volumetric LiDAR Return Patterns from an Old-growth Tropical Rainforest Canopy*. International Journal Remote Sensing, Vol. 21, No. 2, pp 409-415.
- WEN, B., TSANG, L., WINEBRENNER, D.P. & ISHIMARU, A., 1990: *Dense Medium Radiative Transfer Theory: Comparison with Experiment and Application to Microwave Remote Sensing and Polarimetry*. IEEE Transactions on Geoscience and Remote Sensing, Vol. 28, No. 1, pp 46-59.
- WERNER, M., ROTH, A., MARSCHALK, U., EINEDER, M. & SUCHANDT, S. 2005: *Comparison of DEMs derived from SRTM/X-and C-band*. Workshop: "The Shuttle Radar Topography Mission – Data Validation and Applications", June 14-16, 2005, Reston, Virginia, USA.
- WERNER, M., 2001: *Status of the SRTM Data Processing: When will the World-wide 30m DEM Data Be Available?* Photogrametric Week '01, (D. Fritsch – Editor), Herbert Wichmann Verlag, Heidelberg.
- WEST, R., TSANG, L. & WINEBRENNER, D.P., 1993: *Dense Medium Radiative Transfer Theory for Two Scattering Layers with a Rayleigh Distribution of Particle Sizes*. IEEE Transactions on Geoscience and Remote Sensing, Vol. 31, No. 2, pp 426-437.
- WILEY, C.A., 1965: *Pulsed Doppler Radar Methods and Apparatus*. US Patent No. 3,196,436.
- WIMMER, C., SIEGMUND, R., SCHWÄBISCH, M. & MOREIRA, J., 2000: *Generation of High Precision DEMs of the Wadden Sea with Airborne Interferometric SAR*. IEEE Transactions on Geoscience And Remote Sensing, Vol. 38, No. 5, pp. 2234-2245.
- WRIGHT, R., GARBEIL, H., BALOGA, S.M. & MOUGINIS-MARK, P.J., 2006: *An Assessment of Shuttle Radar Topography Mission Digital Elevation Data for Studies of Volcano Morphology*. Remote Sensing of Environment, Vol.105, No. 1, pp. 41-53.
- WULDER, M., 1998: *Optical Remote-Sensing Techniques for The Assessment of Forest Inventory and Biophysical Parameters*. Prog. Phys. Geogr. Vol. 22, pp 449–476.
- YA-QIU JIN; ZICHANG LIANG, 2004: *An Approach of Three-Dimensional Vector Radiative Transfer (3-D-VRT) Equation for Inhomogeneous Scatter Media*. IEEE Transactions on Geoscience and Remote Sensing, Vol. 42, No. 2 pp 355-360.
- YUEH, S.H., KONG, J.A., JAO, J.K., SHIN, R.T. & LE TOAN, T., 1992: *Branching Model for Vegetation*. IEEE Transactions on Geoscience and Remote Sensing, Vol. 30, No. 2 pp 390-402.
- ZEBKER, H.A. & VILLASENOR, J., 1992: *Decorrelation in Interferometric Radar Echoes*. IEEE Transactions on Geoscience and Remote Sensing, Vol. 30, No. 5, pp 950-959.
- ZEBKER, H.A., (Ed), 2004: *InSAR Workshop Summary Report*. October 20-22, Oxnard, California. Available online (March 2007): <http://solidearth.jpl.nasa.gov/PDF/InSARWorkshopReport.pdf>.

ZHAN, X., DeFRIES, R.S., LOS, S.O. & ZONG-LIANG YANG, 2000: *Application Of Vegetation Continuous Fields Data Inatmosphere-Biosphere Interaction Models*. Geoscience and Remote Sensing Symposium, Proceedings. IGARSS 2000. Vol. 5, pp 1948 – 1950.

ZIANIS, D., 2008: *Predicting Mean Aboveground Forest Biomass and its Associated Variance*. Forest Ecology and Management, Vol. 256, pp 1400–1407.

APPENDIX 1: Test Sites

A. The Nerang State Forest (NSF)

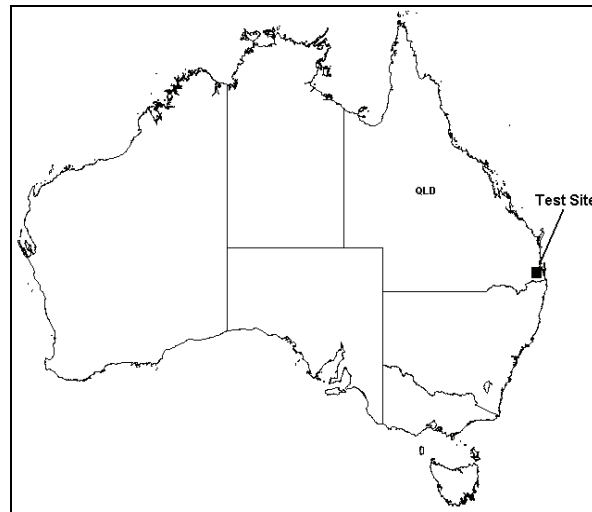


Figure A1: Location of the Nerang Forest test site.

The Nerang State Forest test site (NSF) is located in the South-East part of Queensland, Australia, as shown in Figure A1. It extends between 27°56'28.5"S, 153°15'52.5"E (top left), and 27°59'28.5"S, 153°19'22.5"E (bottom right) (WGS84) measuring roughly 5km by 6km. The main feature of interest is the Nerang State Forest Reserve. Total area of AOI is 3264 hectares, including 1329 hectares of the Nerang State Forest.

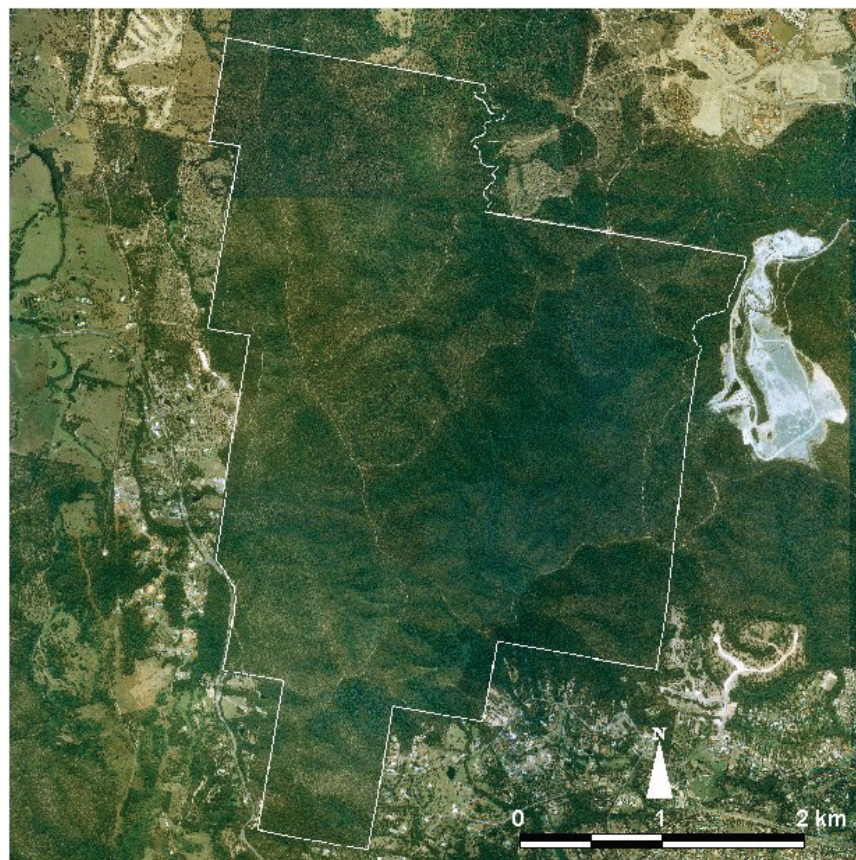


Figure A2: Mosaic of orthophotographs (0.15m by 15m pixel) produced using May 2002 aerial photos of the Nerang State Forest test site (NSF), including cadastral boundaries of the Nerang State Forest Reserve.
Source: Courtesy of the Gold Coast City Council.

Basic climate characteristics for the NSF site are the same as those found at a meteorological station located some 9km south from NSF at Hinze Dam (site number: 040584) (<http://www.bom.gov.au/jsp/ncc/cdio/cvg/au>), and are readily available from that station, as shown in Figure A3. Mean annual rainfall for the area is about 1302mm. The elevation of the Hinze Dam meteorological station is about 110m above mean sea level.

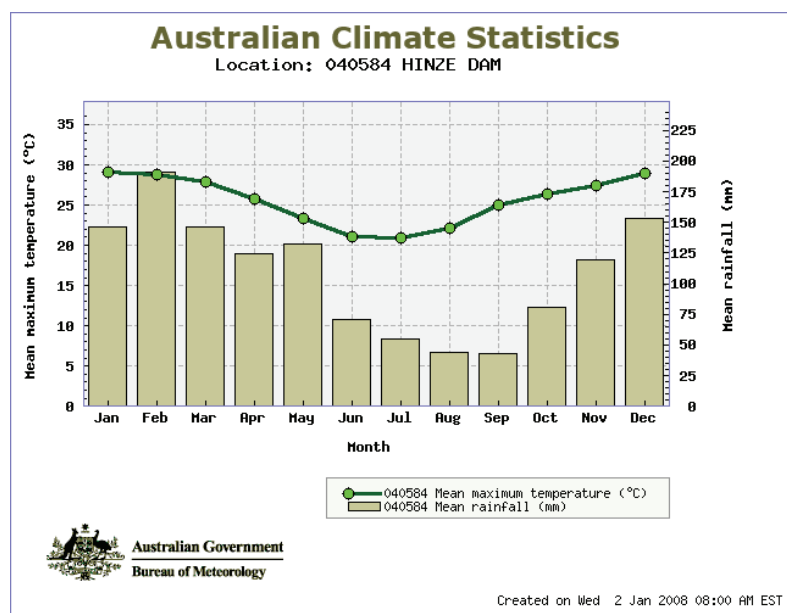


Figure A3: Basic climate data for the Nerang State Forest test site.

The Nerang State Forest is dry rainforest and open eucalyptus forests of grey gum (*Eucalyptus punctata*) open-crowned tree, blue gum (*Eucalyptus tereticornis*) and stringy bark and tallowwood (*Eucalyptus microcorys*) trees located in the hilly reserve. Open eucalypt forests occupy low to moderate soils with limited water infiltration and storage. The lower stratum of the open forest is dominated by short sub-canopy trees and drought-tolerant shrubs. Dry rainforests are often found on more fertile soils and reach into water valley floors (BEADLE, 1981). Some of the trees in the Nerang Forest display scars of fires which are a frequent occurrence in the Australian landscape. Figure A5 shows a typical scene within the Nerang State Forest Reserve.

The mean diameter of trees at breast height (DBH) is about 0.33m (0.18m – 0.66m). The height of a number of tree species was measured using trigonometrical levelling. Mean tree height is 20.5m ±1m. Crown cover for the open eucalypt forest is generally between 40%-70%, and 70%-80% for the dry rainforest (DNR, 1998). Currently, the Nerang State Forest Reserve is utilised as a recreation area.

Figure A4 shows a sample of leaves of the predominant tree species collected in the Nerang State Forest. Their striking feature is the very low width/length ratio varying between ~ 4 to ~13% .

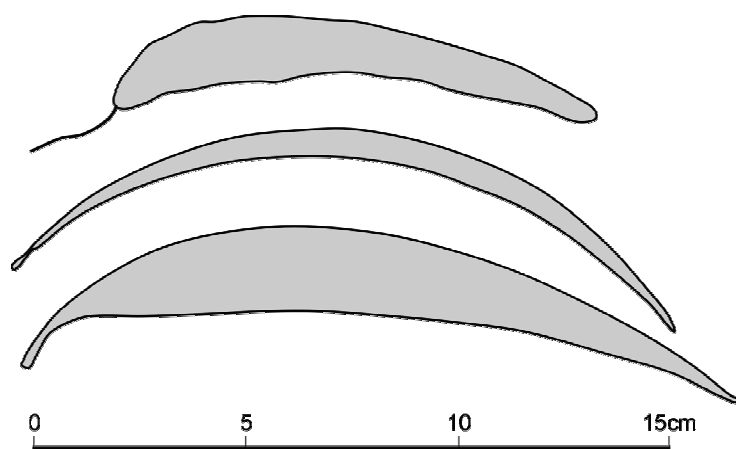


Figure A4: Sample of leaves of predominant tree species in the Nerang State Forest. The width/length ratio varies between ~ 4 to ~13% .



Figure A5: Open eucalyptus Nerang State Forest from the ground. The average trunk DBH is $0.33\text{m} \pm 0.15\text{m}$. The largest DBH encountered was 0.66m . The average tree height is $20.5\text{m} \pm 1\text{m}$. (Photo K. Becek, 27.5.2007)

The mean elevation of the test site is 120.9 m , with 29m and 240m for minimum and maximum elevation, respectively. The standard deviation of the terrain undulation is $\pm 42.5\text{m}$.

The sun-shadowed DTM over the NSF test site is shown in Figure A6.

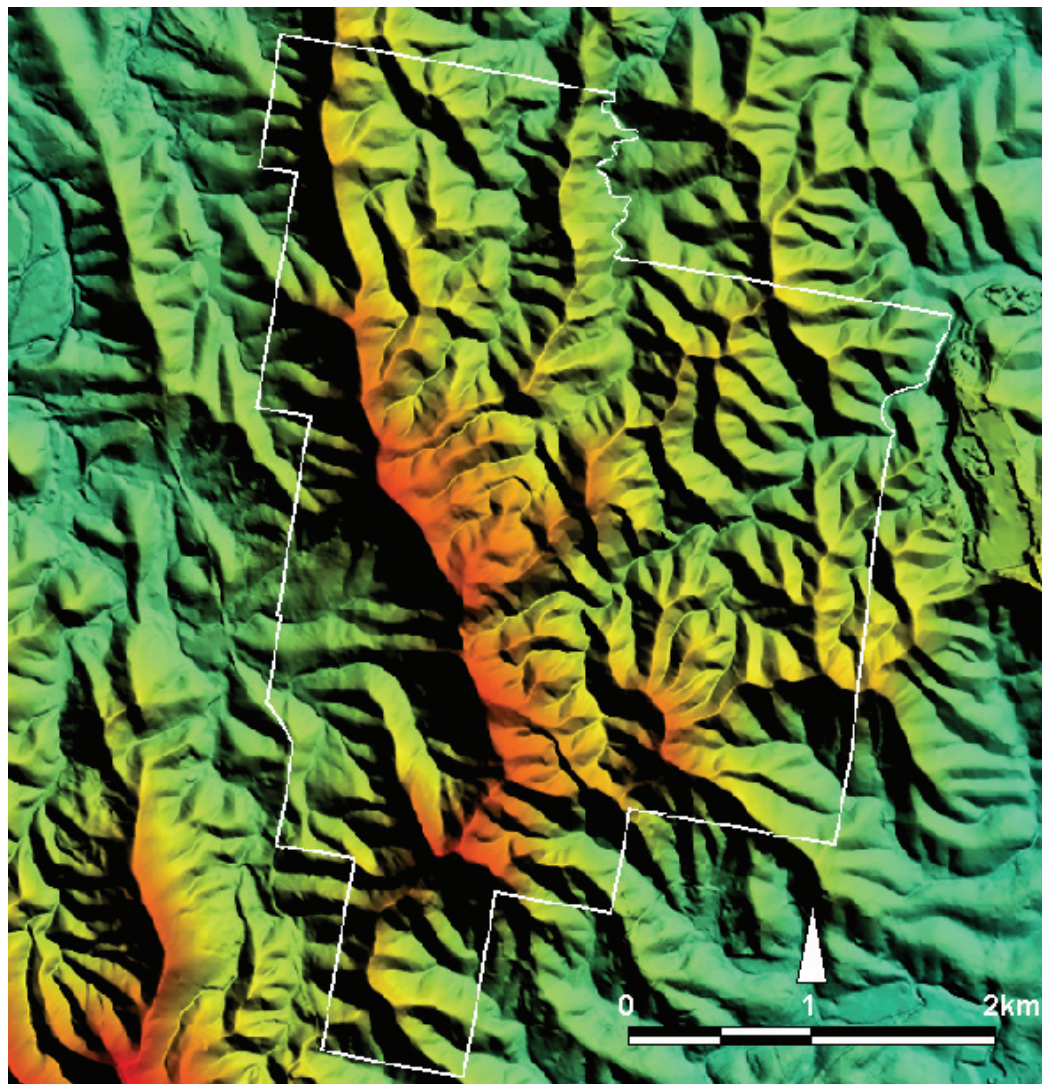


Figure A6: Sun-shadowed DTM over the Nerang test site including boundaries of the Nerang State Forest Reserve. Mean height $114.7\text{m} \pm 42.5\text{m}$. The minimum and maximum height is 29.3m and 234.9m , respectively.

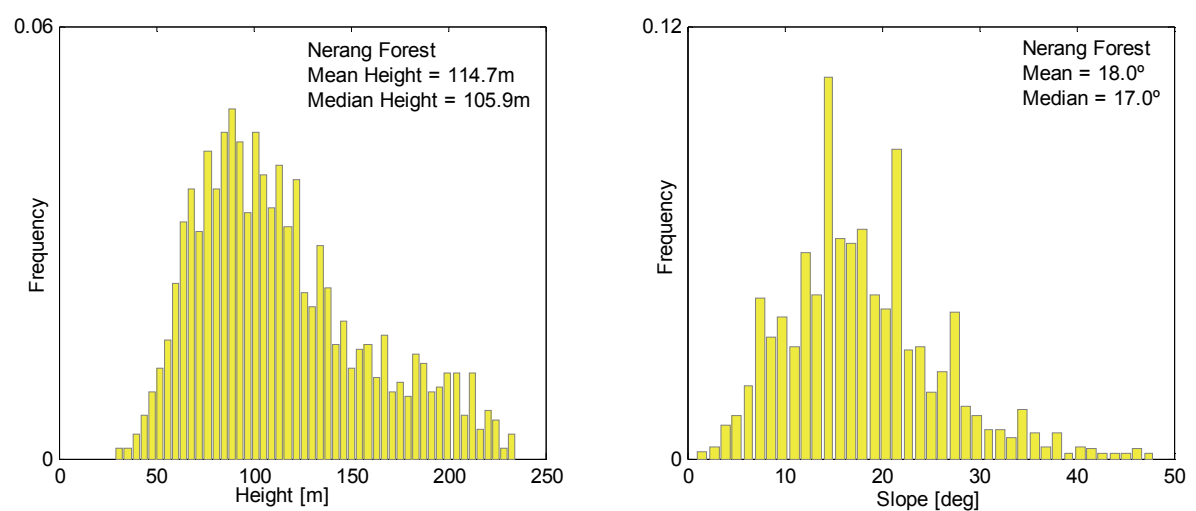


Figure A7: Histogram of elevations (left-hand pane), and slopes (right-hand pane) of the NSF site. Reference spot heights data were used to generate the histograms.

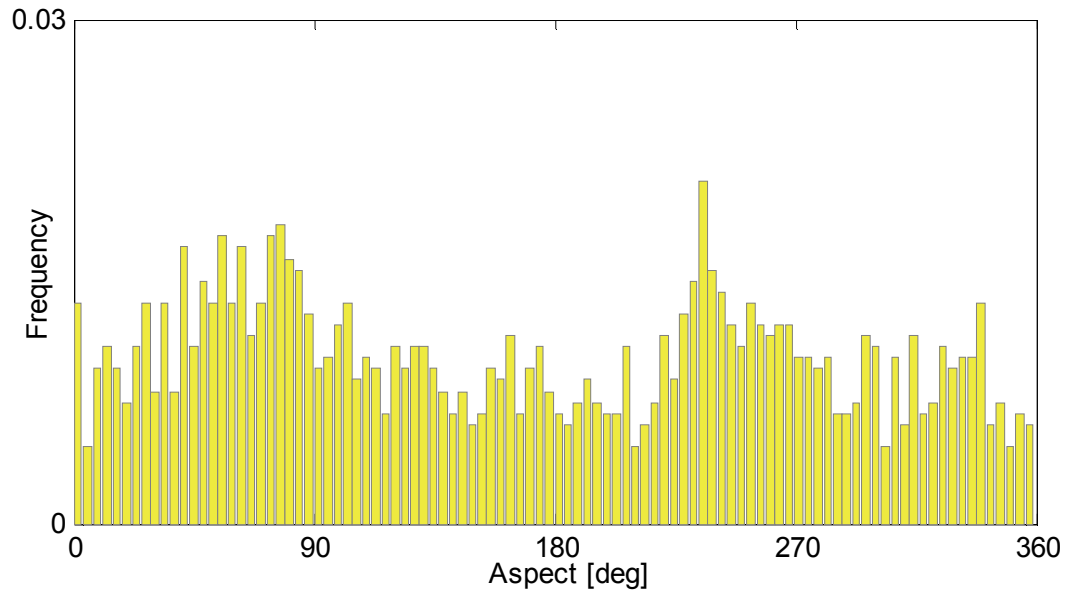


Figure A8: Histogram of aspects for the NSF site.

Figure A7 and A8 show the histograms of elevations, slopes and aspects calculated from the reference spot heights. Terrain with a mean slope of 18° is considered by FAO as “class c” terrain, i.e. “*steeply dissected to mountainous*” (<http://www.iiasa.ac.at/Research/LUC/GAEZ/>).

An interesting feature of the test site is revealed by the histogram of aspect shown in Figure A9. It is evident that the topography is predominantly oriented along a north-east/south-west bearing.

A basics comparison of the SRTM.X data against reference spot heights is provided in Table A1.

Table A1: Elevations of the Nerang Forest test site as calculated from various datasets.

| Dataset | Mean Height [m] | Min - Max Height [m] | STD [m] |
|------------------------|-----------------|----------------------|------------|
| Reference spot heights | 114.7 | 29.3 – 234.9 | ± 42.5 |
| SRTM.X | 127.8 | 36 – 245 | ± 42.6 |

Considerable differences between mean heights indicate an elevation bias or impenetrability caused by the presence of vegetation.

B. The Brunei Darussalam test site (Brunei)

The area of interest comprises the territory of Negara Brunei Darussalam (about $5,765\text{km}^2$), a country located on the island of Borneo in Southeast Asia (4.5° North of Equator, 114.5° East of Greenwich). It borders the South China Sea from the north (about 130km in length) and the Malaysian state of Sarawak from the other directions. The climate is described as wet tropical, with the monthly average temperature ranging between 26.7°C and 27.7°C , and the annual average rainfall varying from 2880 up to 4500mm in isolated mountainous areas. The area is influenced by two distinctive monsoons: weaker south-west (April-August) and stronger north-east (October-January). The topography of the country is mainly dominated by low, slightly undulating features with the south-eastern part described as mountainous areas – the Temburong Mountain Range – which belongs to a much larger geological structure – the Crocker Range. The topography culminates in the south-east corner of the country at Bukit Pagon (1850m) located in the Temburong district. Most of the country is covered by soft, tertiary sediments and alluvial soils, which are prone to erosion processes once exposed. A significant part of the western part of Brunei Darussalam, mostly the catchment of the lower part of the Belait river, is covered by peat land swamp, supporting peat land swamp forests, (JALI, 2003). Current geomorphology was formed during the last significant sea level subsidence some 5,000-6,000 years ago. The area of interest (AOI) is drained by four major rivers (‘Sungai’ in the Malay language means ‘river’): Sungai Belait (209km),

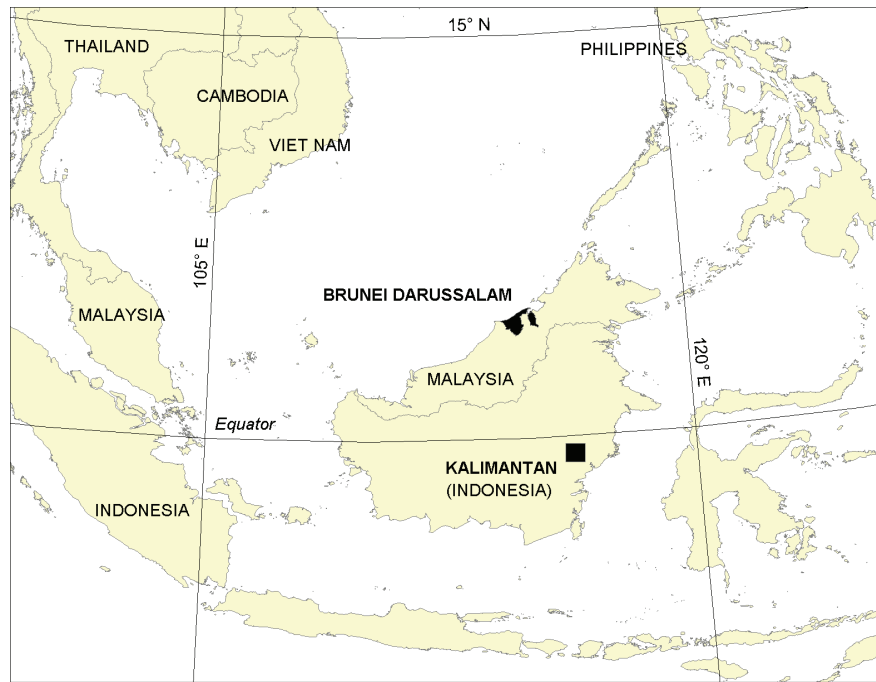


Figure A9: Location of the Brunei Darussalam and Kalimantan test sites.

Sungai Tutong (137km), Sungai Temburong (98km) and Sungai Brunei (41km). The total area of the natural inland waters is less than 0.25% or 15km². The eastern part of Brunei – the Temburong District – is detached from the rest of the territory by the Malaysian valley of Sungai Limbang.

According to the Forestry Department, Ministry of Development, Brunei Darussalam in 2005 some 48% and 28% of the total country area was covered by primary and secondary forest, respectively, FAO (2005b). The forests in Brunei are dominated by the Mixed Dipterocarp forest (46%) and Peat Swamp forest (18%). The average size of a forest stand is 492ha, varying between 5.9ha and 40,000ha. A detailed forest map and statistics are provided in APPENDIX 2.

The location of the country in the tropical belt, which is characterised by persistent cloud cover (on average 7 octas between 9 and 11am local time), precludes acquisition of passive remote sensing data. According to estimates done by the author, the probability of acquiring of satellite image having a given percentage of cloud cover equals the percent of cloud cover. This means that the chance of acquiring a cloud-free image is next to impossible, and there is a 20% chance of acquiring a 20% cloud covered image. The situation in this regard is also complicated by the haze conditions usually associated with forest fires in Borneo and Sumatra, which are frequently burning in the August/September period. The geographic context of the Brunei Darussalam test site is presented in Figure A9. The mean monthly temperature and rainfall at the Brunei International airport are shown in Figure A10.

Much attention in this work is given to the Badas Peat Swamp Forest, which is located in the north-western part of Brunei Darussalam (Figure A11). The southern and western and partially eastern border is constituted by Sungai Badas. The northern border is defined by the Kuala Belait-Muara highway.

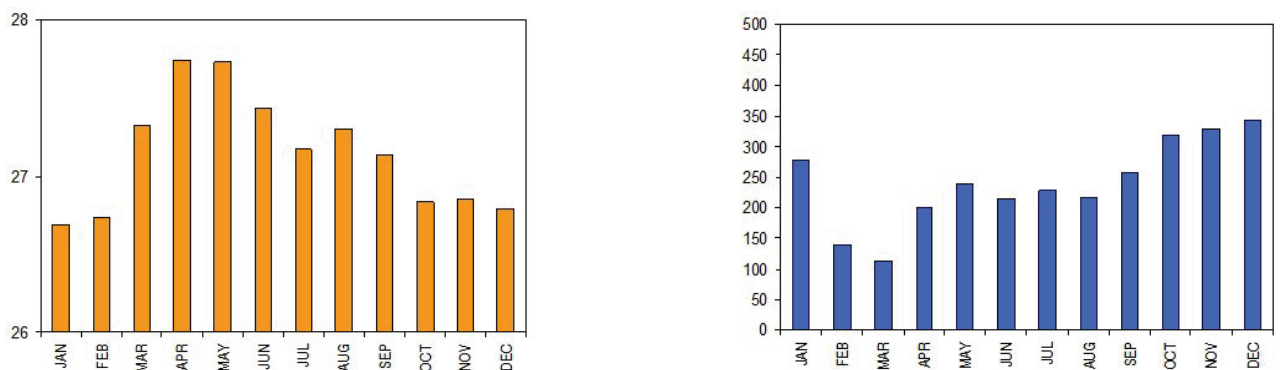


Figure A10. The mean monthly temperature (Celsius) and rainfall (mm) at the Brunei International airport (4°56' N, 114°55' E), left and right pane, respectively. Source: The Brunei Darussalam Meteorological Service.

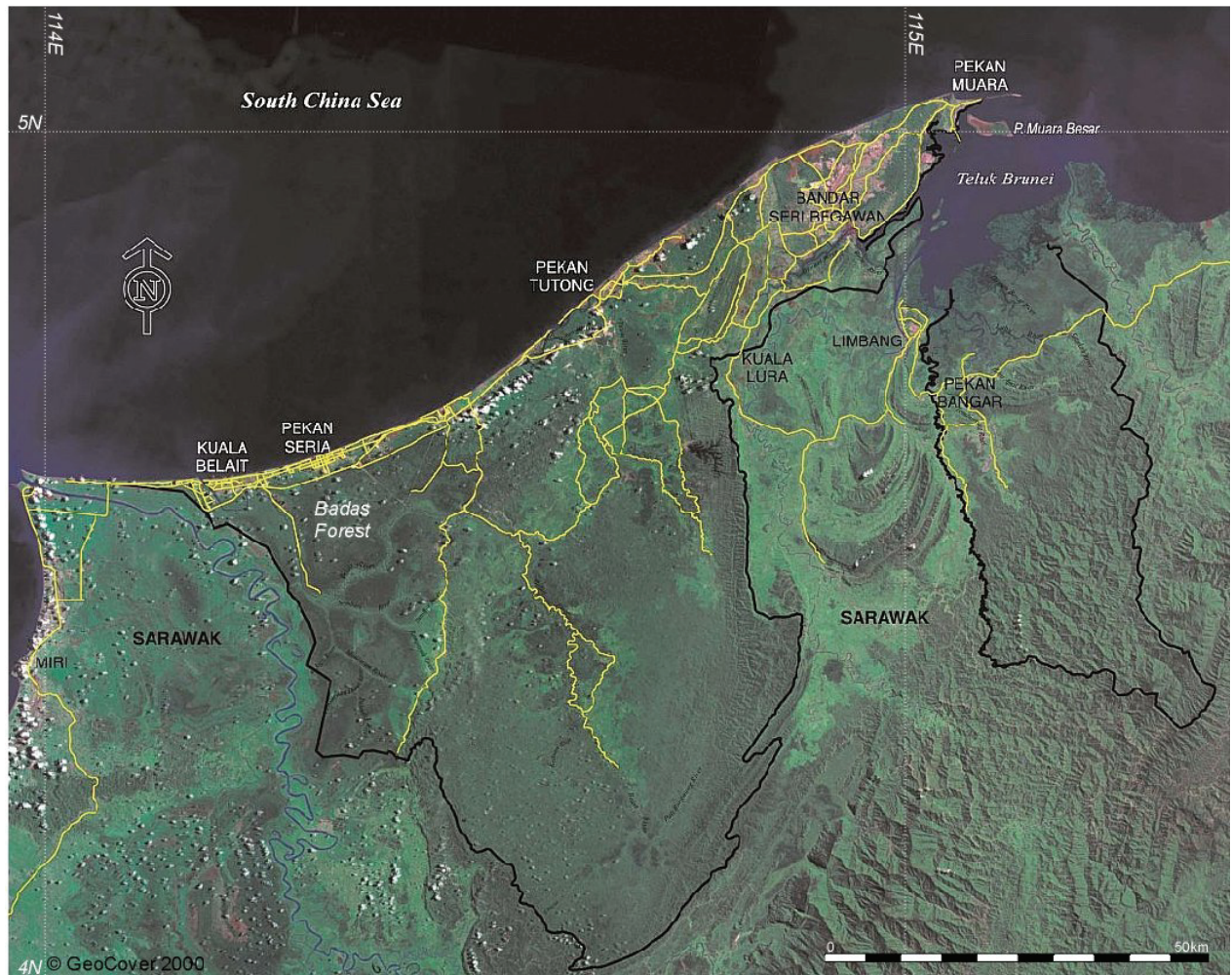


Figure A11: Geographical features of the Brunei Darussalam test site.

C. The Badas Peat Swamp Forest, Brunei Darussalam (Badas Forest)

The periphery of the Badas Peat Swamp Forest is dominated almost exclusively by very large trees called Alan (*Shorea albida*), up to 70 m tall, with 6 m girth. The centre is predominantly under the Alan Bunga trees not exceeding 40 m tall (ASHTON, 1964).

Peatland covers about 18% (101,500ha) of the country. It is a part of the world's tropical peatlands (about 35million ha in total), of which 60% occurs in Southeast Asia. The area of the Badas peatland forest is about 17,600 ha. The unique feature of the forest is the presence of the Alan tree *in* a pure stand, which is in contrast to the peat swamp forests found in Southeast Asia consisting of several mixed species with no distinguishing dominant species (JALI, 2003). Nevertheless, there are distinct signs that *Shorea albida* trees are on the verge of extinction not only in Brunei (JALI, 2003). The upper canopy stratum of the forest is about 50 – 60m above ground. The crown is cauliflower shaped, with dbh varies between 130 and 150cm. The second storey is composed mainly of *Diaospyros evena* and *Dyeri lowi*, which are 40-50m tall with a dbh about 50 to 60cm. Frequent gaps in the canopy are due to lightning strikes. Overall, the canopy is closed. Nevertheless, the undergrowth is thick, mainly with seedlings and saplings. Thorny stemless palms, *Pandanus andersoni*, are responsible for the impenetrable forest (JALI, 2003). The number of species in this peatland forest is about 242, compared to 2000 for a lowland mixed dipterocarp forest (JALI, 2003). Typical tree leaves found are shown in Figure A19. They have a much more oval shape compared to that found in NSF, Figure A4.

The forest floor is extremely uneven with frequent depressions and hummocks. However, the highest elevation reaches only 3 m (JALI, 2003). A digital elevation model produced using a SRTM.C dataset shown in Figure A11 discloses a rich 'topography' of vegetation cover. Low, regularly shaped objects are the remains of logging activity, whereas the low elliptic feature in the centre is a relic of the 1953/54 destruction done by an unidentified insect infestation (JALI, 2003).

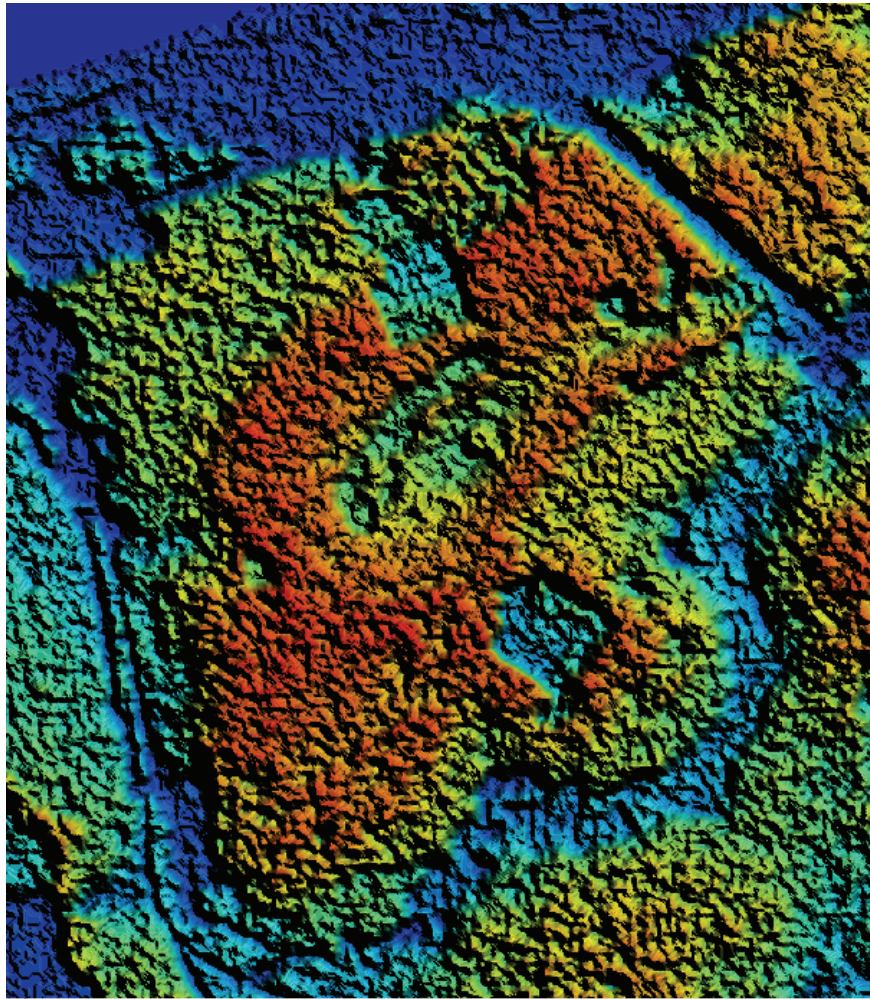


Figure A11: Sun-shadowed digital elevation model of the Badas Forest and its surroundings. A SRTM.C dataset was used to generate the ‘canopy trees’ DEM. The lowest point (top left corner) is the sea level; the highest point is just to the left from the square-like feature in the centre of the forest (60m). The model represents an area of 17.5km by 20km.

Badas Forest is classified as a production forest. However, because of a very restrictive logging policy it is not currently explored. Nevertheless, despite that policy which supposedly should limit deforestation, the northern part has been damaged by extracting sand underlying the uppermost layer of peat. This operation is associated with a drop in the ground water level, leading to oxidation of the peat, which is an irrevocable and destructive process.

Figure A12 shows the fringes of the forest, including a road built of trunks of trees to facilitate sand extraction operations. Two main tree species found in the forest, *Shorea albida* and *Diospyros evena*, are also visible.

Figure A13 shows the tree canopy as seen from orthorectified aerial photography taken in 2003. The approximate scale of the photos was 1:20,000. Using the photography, a manual tree count was performed on 21 randomly selected 4ha plots. It was found that the mean number of trees is 47.15 trees/ha \pm 22 trees/ha.

It has to be noted that the forest, at least in some areas, appears to be almost 100% closed, which contradicts observations made by JALI, (2003).

The last forest fire was recorded in August 2007. North-east to eastern fringes bordering transportation routes were affected. The latest observations made by the author indicate that the forest is not recovering from the event to the previous state. Instead, the damaged area has been mostly settled by ferns.



Figure A12: Fringes of the Badas Forest. Alan (*Shorea albida*), ~60m tall, and *Diospyros evena* ~40m tall trees species are shown here. Source: K. Becek, 25/3/2007.

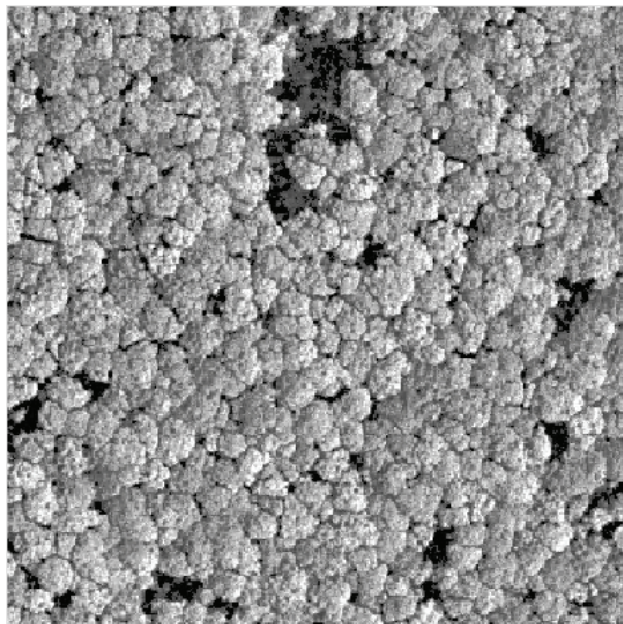


Figure A13: Aerial view of the canopy top of the Badas Forest. Dark spots are gaps caused most likely by lightning. The area shown is 200m by 200m (4 ha), and the number of trees is around 324 (81 trees ha⁻¹).

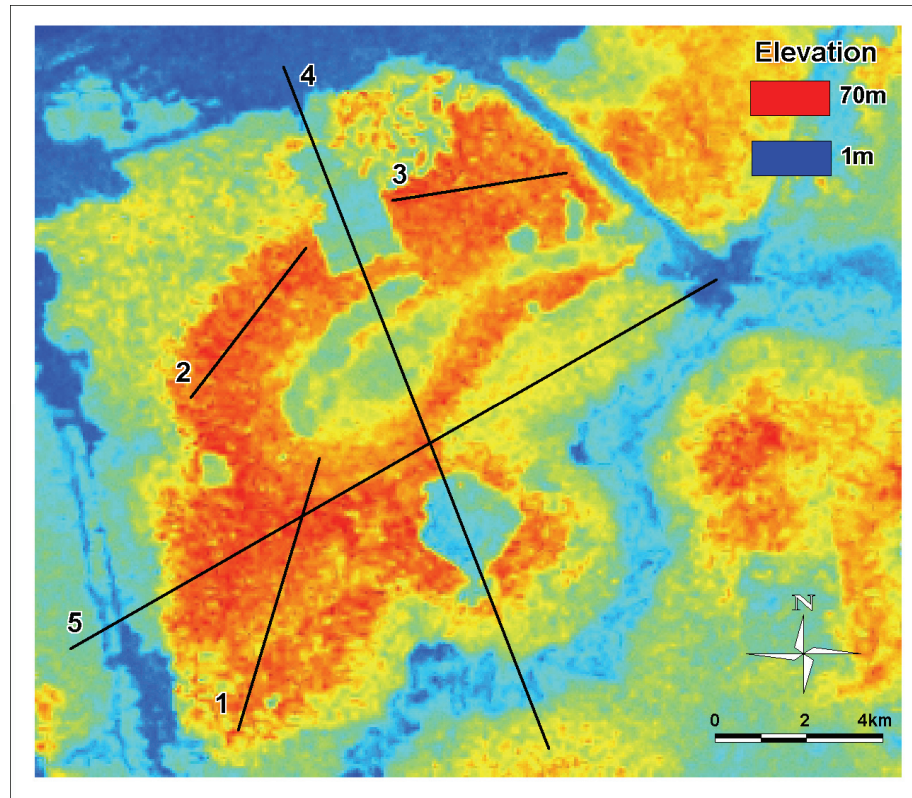


Figure A14: Location of transects over SRTM DSM in the Badas test site.



Figure A15: Cauliflower-like canopy of trees (*Shorea albida*) in the Badas test site.



Figure A16: Diebacks in Brunei Muara district. The cause of the destruction is unknown. Source: The author

C. The Kalimantan Site, East Kalimantan, Indonesia (Kalimantan)

The site is located on the island of Borneo in the Indonesian province of East Kalimantan, some 66 km north-west from the capital city, Balikpapan (Figure A9). Vegetation cover is diverse and comprises Dipterocarp forest, peat swamp forest and oil palm and rubber tree plantations. Typical leaf types found here are very similar to those of the Badas Forest (Figure A19). Cloud cover and other meteorological/climatological factors are comparable with those prevailing over Brunei Darussalam (see Section B above). Consequently, a cloud-free space-borne visible imagery was not available over the area for the purpose of this project. However, the GeoCover® 2000 image of the area is available but here not shown.

Topographic features of the area include lowland (roughly 120m a.s.l.) prevailing in the north-western quadrant, elevated plateau reaching some 750 m a.s.l., and heavily undulating hills reaching some 350 m a.s.l. in the southern section. Clearly visible in Figure A17 is a fault line separating the north-western corner of the lowland from the rest of the area. The histogram of aspect for the site shown in Figure A18 reveals the south-east to north-west dominant topography. The histogram was prepared using SRTM.C dataset.

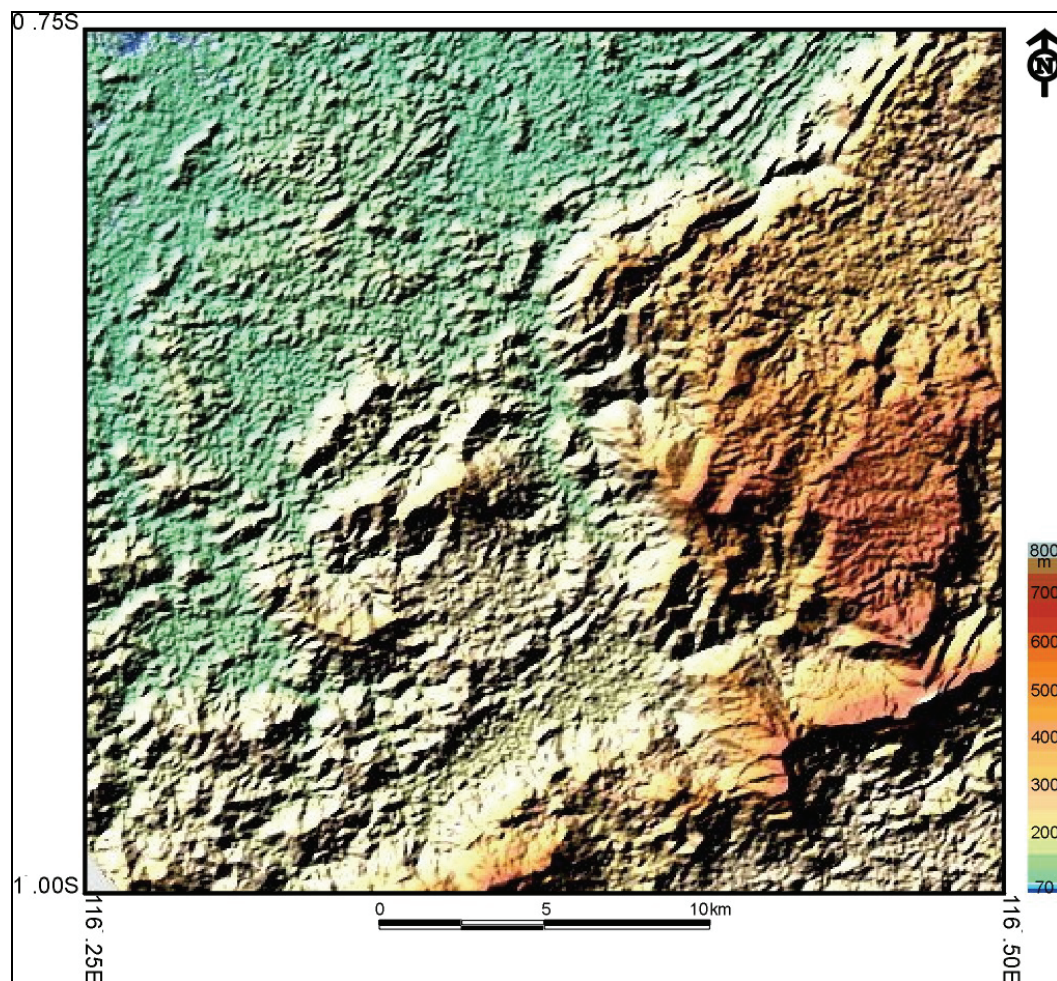


Figure A17: Topography of the Kalimantan test site based on the SRTM.X. Source: Image courtesy of DLR.

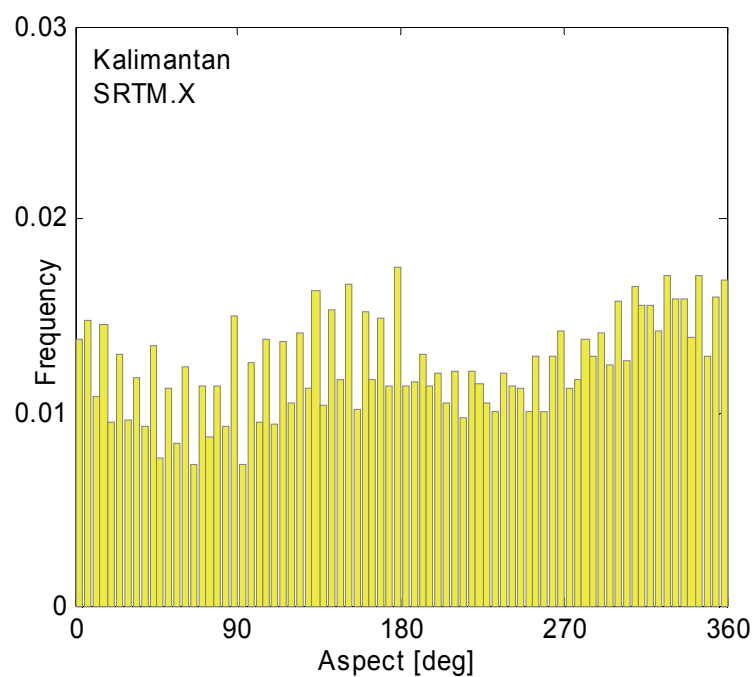


Figure A18: Histogram of aspect over the Kalimantan test site. SRTM.X data were used to generate the histogram.

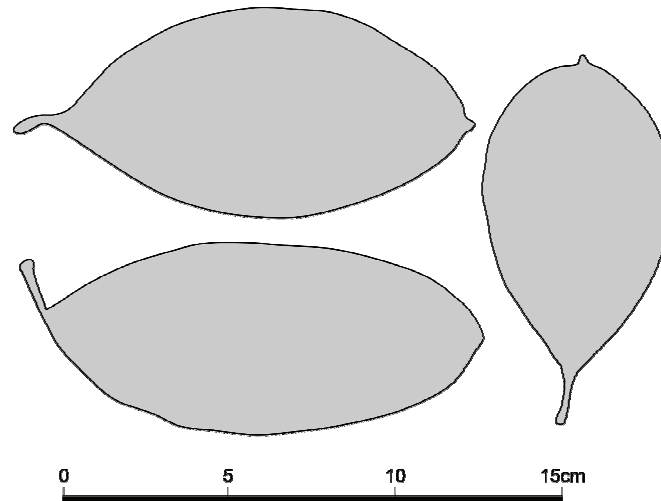


Figure A20: Sample of leaves of predominant tree species in the Badas Forest and Kalimantan test site. The width/length ratio varies between ~ 43 to $\sim 57\%$.

D. The USA Site, Washington State, USA

The USA test site is located in the Pacific Northwest region of the USA, within Capitol State Forest, Washington State. The coordinates of the area of interest are: top left: 123.750022° W, 47.750019° N, and bottom right: 123.624981° W, 47.624978° N. The elevation ranges from 230m to 1740m. This forest is composed of coniferous Douglas fir (*Pseudotsuga menziesii*) and western hemlock (*Tsuga heterophylla*) with insignificant presence of deciduous hardwoods such as red alder (*Alnus rubra*) and maple (*Acer spp.*) (ANDERSEN *et al.*, 2003). Figure 20 shows an orthorectified radar image (X-band, first return) of the site. The image reveals a very rough topography which is confirmed by the histogram of slopes of the sites shown in Figure 21. The average slope is 32° . Figure 22 shows a QuickBird image of a part of the site which was magnified to show details of the vegetation cover. The location of the enlarged part of the site is shown in Figure 20. Orthorectified large scale aerial photography of the general area of the Capitol State Forest is available from ANDERSEN, *et al.*, (2003).

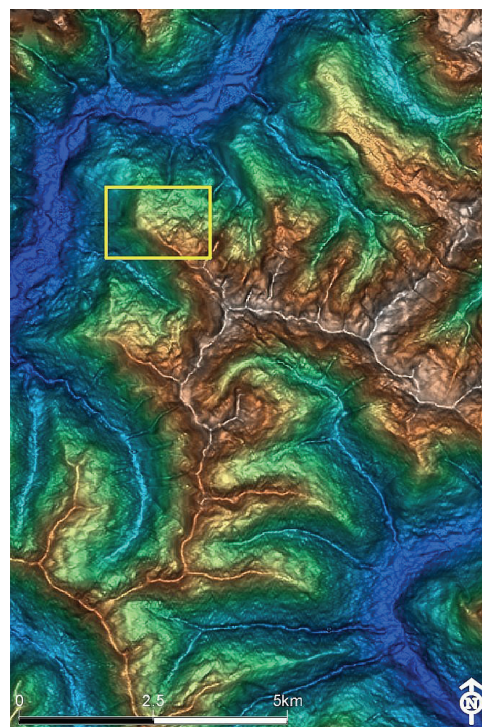


Figure A20: Sunshadowed IFSAR X-band dataset for the USA site. Source: Intermap Technologies Inc. USA.

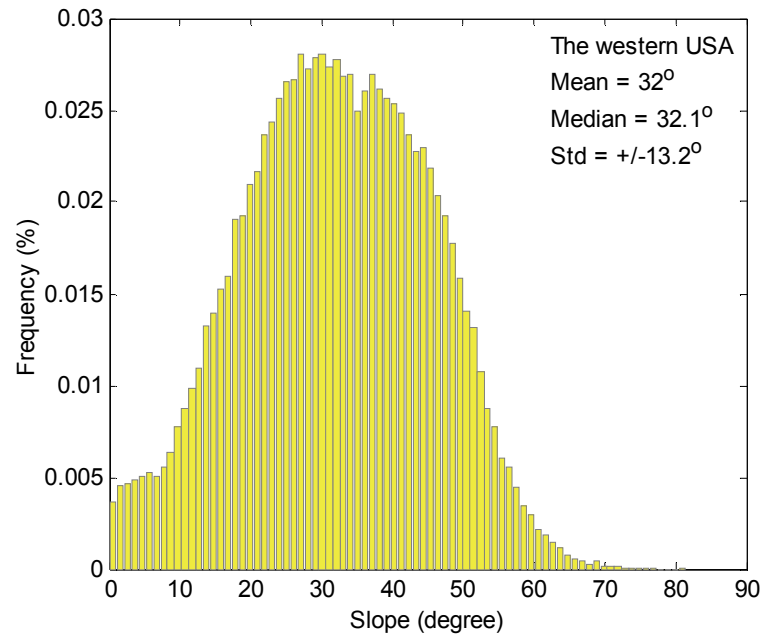


Figure A21: Histogram of slopes of the West USA test site. The Intermap Technologies Inc. The DTM data downsampled to 50m pixel were used for the calculations.

Figure A23 shows the most common tree species, e.g. Douglas fir (*Pseudotsuga menziesii*) and Western hemlock (*Tsuga heterophylla*), found in the test site. Rocky Mountain Douglas fir attains a height of about 35 – 35m. The mountain Western hemlock can reach upwards of 40 - 50m.

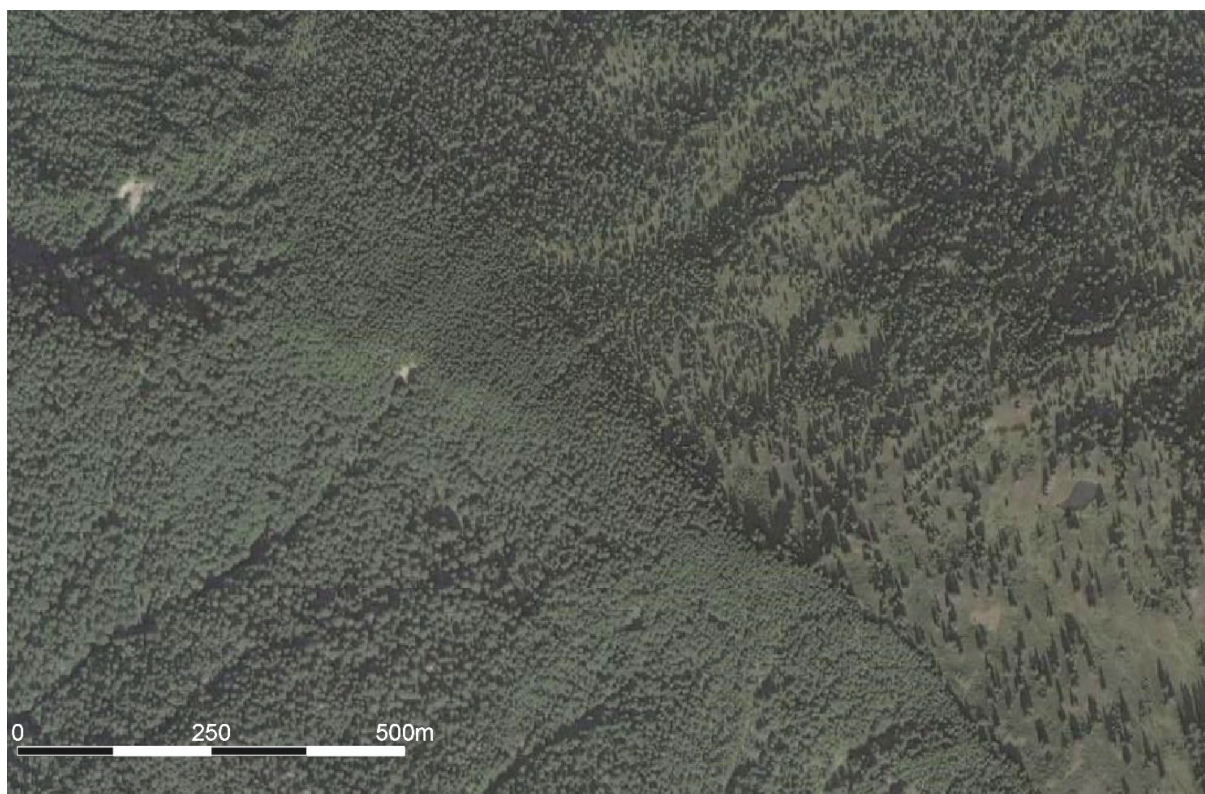


Figure A22: A QuickBird image of a part of the USA site. Various density coniferous forest is clearly visible. Approximate coordinates of the centre of the image are 123.71° W, 47.71° N. Approximate location of the area covered is shown in the radar image in Figure 20. Source: GogleEarth®, 2009; also DigitalGlobe®, 2009.



Figure A23: Douglas fir (*Pseudotsuga menziesii*) (left). Source: Walter Siegmund. Western Hemlock (*Tsuga heterophylla*) (right). Source: MPF/Wikipedia.

E. The German Site, Bavaria, Germany

The German test site forms a triangle with the following vertices: (1) 10.82°E, 48.25°N, (2) 11.0°E, 48.25°N, and (3) 11.0°E, 48.35°N. The largest town in the area is Königsbrunn (left from the centre), a municipality in the district of Augsburg, in Bavaria. The area features a mixed forest covering about 25% of the area. Trees reach about 17m in height. Urban areas cover about 20% of the landscape. The water bodies cover about 10% of the area. The remainder is farmland.



Figure A24: Ground view of the German site. Source: Baidl (left-hand) & Tranquility (right-hand).

Figure A24 shows a ground view of the site. Figure A25 shows a GoogleEarth® image of the test site. The bottom right hand side triangle is the actual test site.



Figure A25: The Germany test site. SRTM.X data are available for the south-east triangle of the scene. Source: GoogleEarth ®.

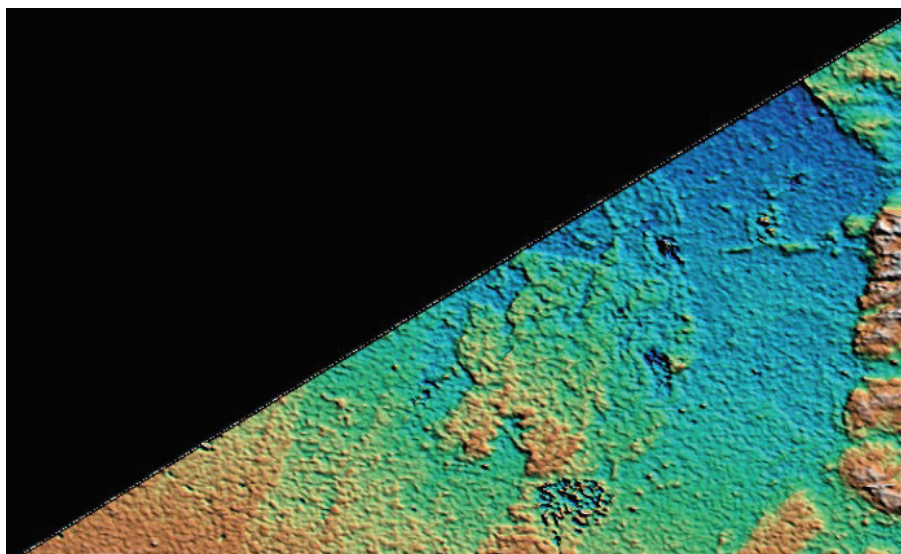


Figure A26 Sunshaded map of the German test site. The elevation falls between 525m and 600m above mean sea level. Source: SRTM.X data.

The topography of the area is dominated by flat areas with slopes up to 5°. A sunshadowed picture of the site is shown in Figure 26. A histogram of the elevations produced from SRTM.X data is shown in Figure 27.

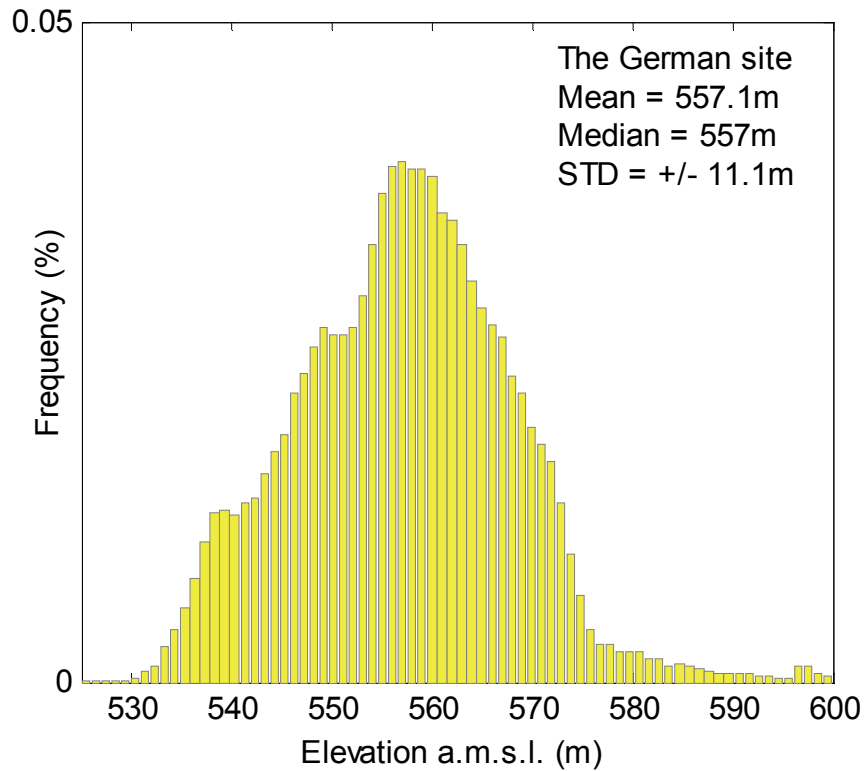


Figure A27: Histogram of elevations for the German test site based on the SRTM.X dataset.






APPENDIX 2: Description of Datasets Used



1. SRTM C-band Dataset

The Shuttle Radar Topography Mission or SRTM C-band digital elevation data product (SRTM.C) is available in a $1^\circ \times 1^\circ$ cells free of charge from JPL/NASA at <ftp://e0srp01u.ocs.nasa.gov>. Other sources of the SRTM.C datasets are not recommended because of the resampling procedure used to reduce the spatial resolution of the dataset from one arc-second to three arc-seconds. The procedure used for the downsampling was decimation, which is not the optimal procedure for downsampling. For more information on this topic see BECEK, (2007). The accuracy parameters for the dataset were estimated in BECEK, (2008b). The dataset was used in its original datum (WGS84) in a geographic coordinate system (ϕ, λ). Horizontal resolution of the dataset is three arc-seconds, but the dataset is also available at one arc-second resolution over the USA. Vertical reference is the mean sea level estimated from the EGM96 geoid model. The quantization level of the dataset is 1m. More information on the SRTM.C can be found from the above website or extensive literature sources on that topic.

A useful data regarding a particular pixel of SRTM.C is provided in Table A2. These data are provided through a facility located at the JPL SRTM Internet site (NASA, 2000). Both graphic and textual formats are used to represent some of the basics data acquisition parameters which are extracted from the SRTM mission timeline.

Table A2: Parameters of the data takes used in the investigations. Source: Extracted from mission timeline (NASA, 2000)

| No | Ground Track | Details | Notes |
|----|---|---|--|
| 1 |  | Data take: CX DT 30.141 MET: 01/19:55:01 Look angle: 39° Look direction: 54° Beam: 1 (CH) | Orbit: Descending Polarization: Horizontal Location: Nerang State Forest |
| 2 |  | Data take: CX DT 46.046 MET: 02/19:41:30 Look angle: 55° Look direction: 53° Beam: 4 (DH) | Orbit: Descending Polarization: Horizontal Location: Nerang State Forest |
| 3 |  | Data take: CX DT 131.251 MET: 08/02:24:47 Look angle: 51° Look direction: -54° Beam: 3 (CV) | Orbit: Ascending Polarization: Vertical Location: Nerang State Forest |
| 4 |  | Data take: CX DT 15.055 MET: 00/21:29:49 Look angle: 50° Look direction: 60° Beam: 3 (CV) | Orbit: Descending Polarization: Vertical Location: Kalimantan test site |
| 5 |  | Data take: CX DT 54.280 MET: 03/08:09:46 Look angle: 40° Look direction: -61° Beam: 1 (CH) | Orbit: Ascending Polarization: Horizontal Location: Kalimantan test site |

| | | | |
|---|---|--|--|
| 6 |  | Data take: CX DT 86.280 MET: 05/07:43:41 Look angle: 38° Look direction: -61° Beam: 1 (CH) | Orbit: Ascending Polarization: Horizontal Location: Badas test site |
| 7 |  | Data take: CX DT 158.053 MET: 09/17:54:44 Look angle: 41° Look direction: 60° Beam: 1 (CH) | Orbit: Descending Polarization: Horizontal Location: Badas test site |

Using the facility for a pair of coordinates (a pixel) the following parameters can be extracted: the data take ID, the time stamp of the acquisition, look angle, look direction and polarisation mode used. Also, a number of looks is provided and a simplified map of a particular acquisition strip.

2. SRTM X-band Dataset

The Shuttle Radar Topography Mission X-band digital elevation data product (SRTM.X) was developed by the German and Italian space agencies (DLR and ASI) from the interferometry SAR data acquired during the SRTM mission. A fixed-look angle construction of the X-band instrument is a source for the limited data coverage (grid-like pattern – see Figure 19 in the main text) achieved. Another constraint for the quality of elevation data was the number of data takes available for calculation of elevations. In fact, a single data take was used for that purpose, except for the areas covered by the ascending and descending orbits where two data takes were used. The initial requirements for the resulting elevation data product are shown in Table A3. They are coincidental with the SRTM C-band product requirements. Unlike SRTM.C which is available at three by three arc-second resolution for almost entire land mass of the earth, SRTM.X is provided at one by one arc-second, where available.

The final quality control verifications of SRTM.X have shown that the accuracy requirements have been significantly exceeded (WERNER *et al.*, 2005). In general, the difference in accuracy of SRTM.C and SRTM.X appears to be similar despite the coarser resolution of the SRTM.C. This is probably a combined effect of lower resolution of SRTM.C but larger number of datatakes available for calculation of elevations.

The SRTM.X elevation data product is available for a fee of €400 per 15' by 15' tile (excluding areas under water) (WERNER, 2001).

Table A3. Basic parameters of SRTM.X elevation data product.

| | |
|---|---|
| Raster size | 1"x1" Lon & Lat |
| Height quantisation level | 1m |
| Datum horizontal/vertical | WGS84/WGS84 |
| Data format | 16-bit Signed Integer |
| Horizontal/vertical accuracy (absolute) | ±20m 90% circular error/±15m 90% circular error |
| Horizontal/vertical accuracy (relative) | ±15m 90% circular error/±6m 90% vertical error |

3. Forest Map of Brunei Darussalam

Forest maps of Brunei Darussalam (ANDERSON *et al.*, 1984) were developed on the scale 1:50,000 (9 sheets), and as 1 summary sheet on the scale 1:200,000. The main data source was colour aerial photography 1975/76 (1:25,000), and grey-scale flown in 1981 (1:25,000). An extensive ground survey and ground truthing were also performed. On many occasions a helicopter was deployed. Figure A28 shows the summary sheet of the forest map of Brunei Darussalam.

The 1:200,000 forest map was manually digitized. Table A4 shows eight major forest types with 24 subtypes (Symbol). The map also shows parcels which are marked as a combination of two types of forest, for example 3.1/3.3. The mixed forest parcels were counted as a unique forest type. Hence, the total number of classes was equal to 64. Over 1100 individual forest parcels were identified.

Table A4: Forest types as identified on the 1:200,000 forest map of Brunei Darussalam (ANDERSON *et al.*, 1984). Note the omission of ‘Symbol’ ‘6’. This is an obvious mistake on the part of the author of map.

| Forest Type | Symbol | Description |
|-------------------------------------|--------|---|
| Mangrove | 1 | Undifferentiated, mainly mixed species |
| | 1.1 | Bakau (<i>Rhizophora apiculata</i>) |
| | 1.2 | Nyireh Bunga (<i>Xylocarpus granatum</i>) |
| | 1.3 | Linggadai (<i>Bruguiera gymnorhiza</i>) |
| | 1.4 | Nipa (<i>Nypa fruticans</i>) |
| | 1.5 | Nipa/Dungun (<i>Nypa fruticans</i> / <i>Heritiera globosa</i>) |
| Freshwater Swamp Forest | 2.1 | Levee alluvium (empran) |
| | 2.2 | Lower level alluvium |
| Peat Swamp Forest | 3 | Transitional between Mangrove & Peat Swamp Forest |
| | 3.1 | Mixed swamp forest (MSF) |
| | 3.2 | Alan Forest - Forest Dominated by Alan (<i>Shorea albida</i>) |
| | 3.3 | Alan bunga forest |
| | 3.4 | Padang alan forest |
| | 3.5 | Padang Forest (mixed species) |
| | 3.6 | Padang keruntum (<i>Combretocarpus ratundatus</i>) |
| Kerangas | 4 | Tropical Healthy Forest |
| Mixed Dipterocarp Forest | 5(1) | Dense even or semi-open canopy of mainly small-crowned trees |
| | 5(2) | Canopy uneven, or moderately open, some medium or large emergents |
| | 5(3) | Dense even canopy of medium crowns |
| | 5(4) | Dense uneven canopy of medium-sized and large crowns |
| | 5(5) | Dense uneven canopy, mainly large crowns |
| Montane Forest | 7 | Forest above 2500ft (762m) |
| Secondary Forest | 8 | Generally over 25 years old |
| Urban, cleared land and cultivation | 9 | Land under urban and industrial use is not distinguished from current and lapsed cultivation which includes wet rice, rubber plantations and forest plantations |

Parcel boundaries along with their attributes were used to establish a GIS layer. Some basic statistics on the forest types/plots are listed in Table A5.

Table A5: Basic Statistics of forest types in Brunei Darussalam calculated from the 1:200,000 forest map.

| Forest Type | Symbol | Area [ha] | Percentage of total forest areas |
|-------------------------------------|--------|----------------|----------------------------------|
| Mangrove | 1 | 18,487 | 3.2 |
| Freshwater Swamp Forest | 2 | 13,656 | 2.3 |
| Peat Swamp Forest | 3 | 105,994 | 18.2 |
| Kerangas | 4 | 9,506 | 1.6 |
| Mixed Dipterocarp Forest | 5 | 266,159 | 45.7 |
| Montane Forest | 7 | 7,160 | 1.2 |
| Secondary Forest | 8 | 56,958 | 9.8 |
| Total Forest | | 477,920 | 82.0 |
| Urban, cleared land and cultivation | 9 | 104,277 | 18.0 |
| Grand Total | | 582,197 | 100.0 |

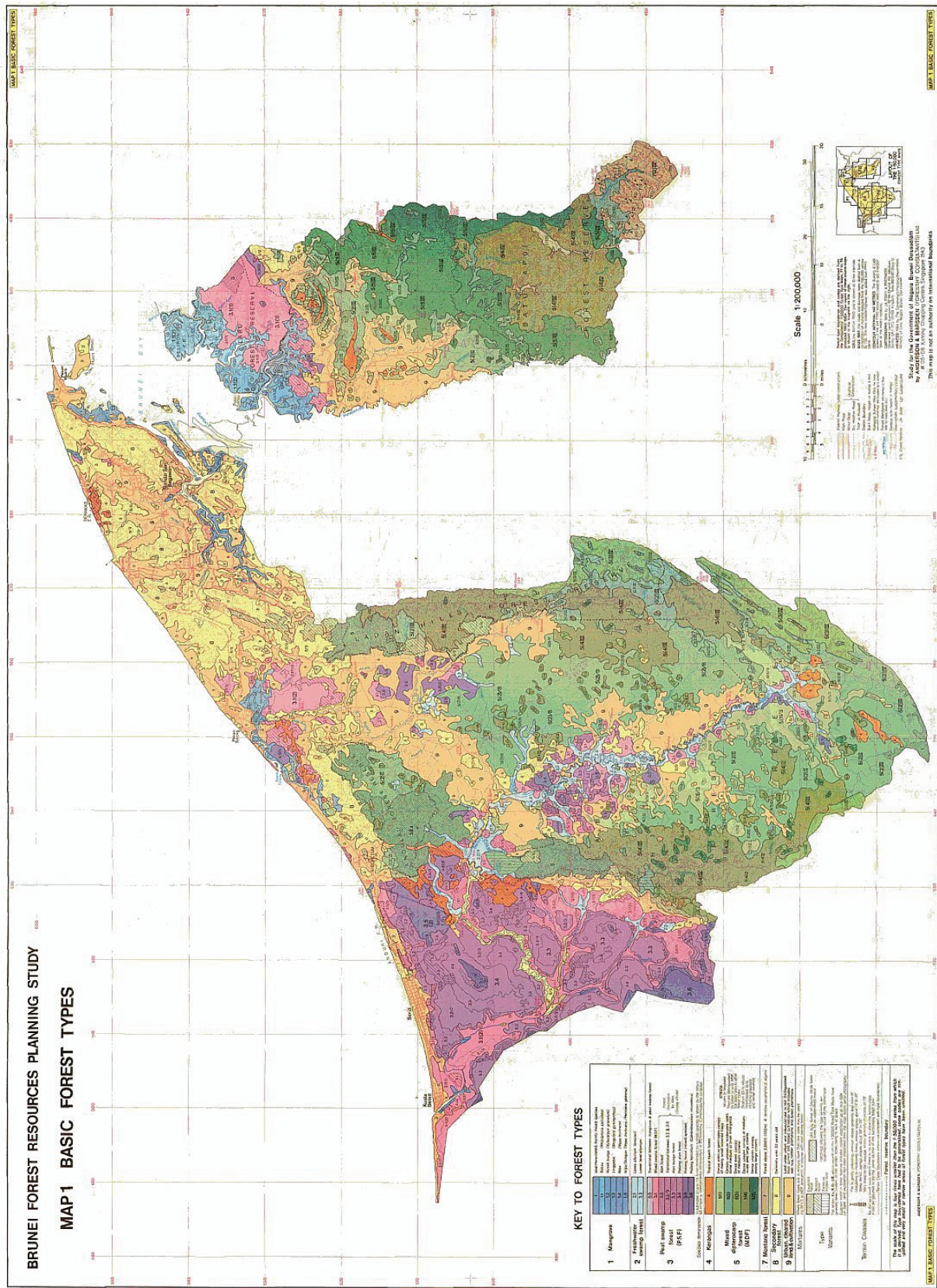


Figure A28: Forest Map of Brunei Darussalam. Source: ANDERSON & MARSDEN, 1984.

4. SPOT DEM

SPOT DEM and SPOT DEM Precision DEM are relatively new data products offered by the SPOT IMAGE Company. The DEM is produced from the SPOT images using an automatic image correlation (REINARTZ *et al.*, 2006).

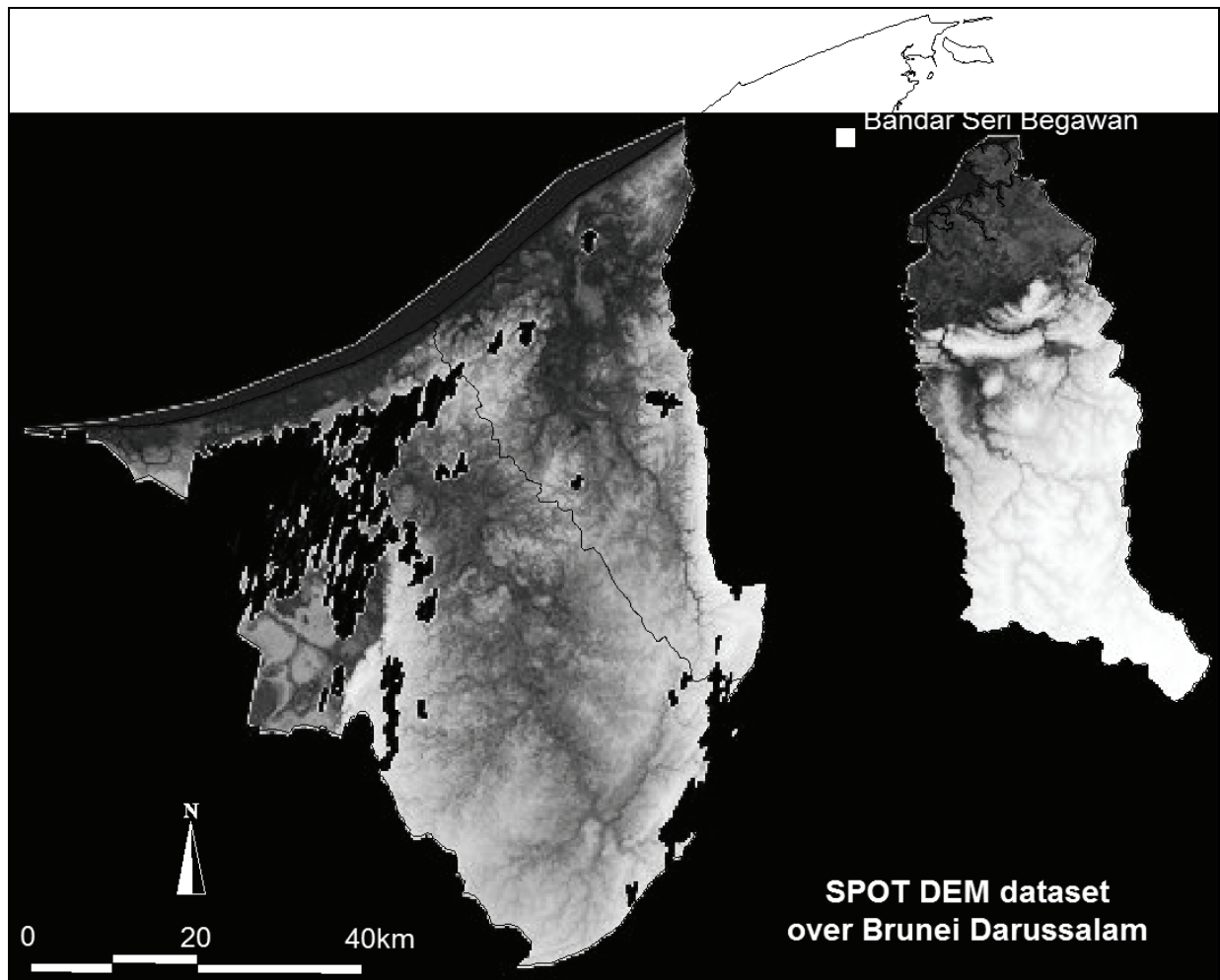


Figure A29: The SPOT DEM dataset used in this project. Missing data cells in the western part of the country are because of unsuccessful acquisition of high resolution imagery suitable for DEM production.

The SPOT DEM dataset used in this project is shown in Figure 24. It covers almost the entire country, except the northern district of Brunei Muara, which constitutes about 10% of Brunei's territory. A large number of the data cells in the western part of the country are missing. According to the supplier, this is due to the lack of imagery data (mainly because of cloud cover) and unsuccessful image correlation. In total, there were some 6000 cases of data voids. The DEM was produced from six stereopairs acquired between July 29, 2005 and June 26, 2008 by the SPOT 5 HRS instrument (*Source: The metadata file accompanying the SPOT DEM product*). The acquisition time of a stereopair for this system is about 90 seconds. It is suspected that some of the data voids may well be due to the temporal decorrelation between images of some stereopairs.

The pixel size of the dataset was 20 m by 20 m. According to the SPOT Company, there is a 90% confidence level that the vertical accuracy of the SPOT DEM is better than ± 20 m (slopes $< 20\%$), while the horizontal accuracy is listed as ± 30 m (<http://www.spotimage.fr/web/en/811-spot-dem.php>). However, some research results indicate that the accuracy is significantly better, for example, ± 6 m (REINARTZ *et al.*, 2005, 2006).

5. PALSAR Dataset

The PALSAR sensor is installed on board the newest Japanese satellite system, the ALOS (Advanced Land Observing Satellite). The PALSAR system is an L-band SAR, which is a successor to the JERS -1 satellite. The level 1.5 data product is a geo-referenced amplitude data sequencer with single polarisation. The dataset was supplied in HH

polarisation at a 6.25 m by 6.25 m pixel size. Figure 25 shows the coverage of the PALSAR dataset used in this project. It covers the northwestern part of Brunei Darussalam with the Badas Peat Swamp Forest in the centre.

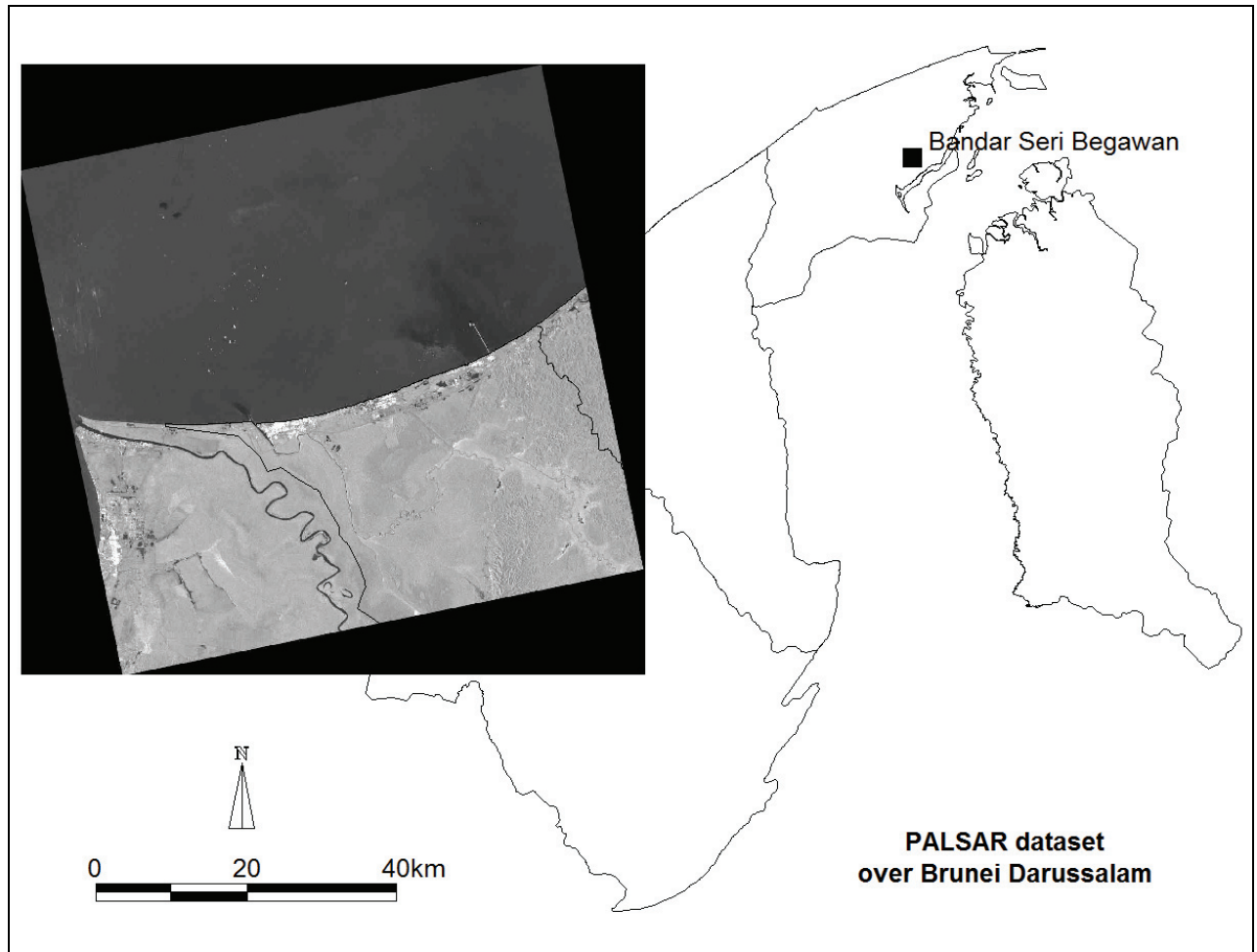


Figure A30: The coverage of the PALSAR dataset used in the project.

The image was acquired on January 1, 2007. The look angle was 34.3° and four looks were performed. The observation width in range/azimuth direction was 83 km /81 km, respectively. The data format was 16 bits per pixel.

6. TerraSAR-X Dataset

The TerraSAR X-band system (9.65GHz) is a German SAR satellite that was launched in mid-June 2007. Figure 26 shows the geographic extent of the dataset acquired for this project. The dataset covers almost the entire landmass of Brunei, except a small region in the western part of the country. The acquisition was carried out on January 15, 2009, in the scan mode with HH polarisation. The pixel size in this mode is 16 m by 16 m (http://www.dlr.de/en/desktopdefault.aspx/tabid-4219/8885_read-15979/).

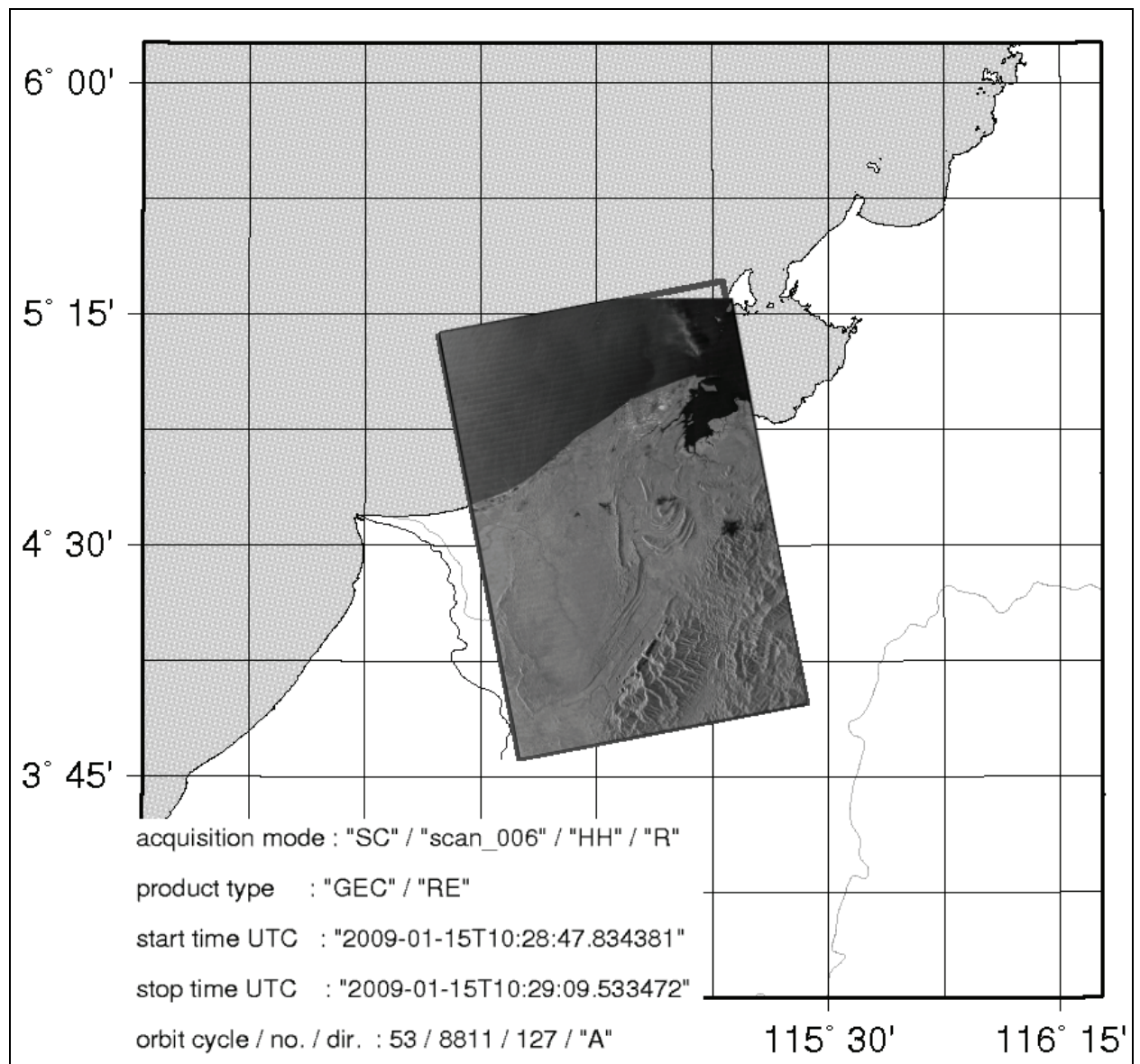


Figure A31: TerraSAR-X dataset used in this project. Source: The base map – DLR (a part of the deliverable data package).

The acquisition of the images was impaired by several local thunderstorms in the area of interest. The areas affected are clearly recognisable over other areas because of the significantly lower pixel values.

APPENDIX 3: Some Essential Mathematical Formulas

The Gradient Operator ($\vec{\nabla}$) takes a scalar field or function as an argument and produces a vector which is a tangent to that field in any allowed point of the field, which can be written for a field $f(x,y,z)$ as follows:

$$\vec{g} = \vec{\nabla} f \equiv \frac{\partial f}{\partial x} dx + \frac{\partial f}{\partial y} dy + \frac{\partial f}{\partial z} dz.$$

The Divergence Operator works on a vector function and produces a scalar function. The resulting value at a given point identifies to what extent the function has a minimum (sink) or maximum (source) at that point. For example, let \vec{g} be a vector field, then the divergence h can be expressed as follows:

$$h = \vec{\nabla} \cdot \vec{g} \equiv \frac{\partial g_x}{\partial x} + \frac{\partial g_y}{\partial y} + \frac{\partial g_z}{\partial z}.$$

The Curl Operator takes a vector field as an argument. The result is also a vector function representing circulation at a given point of the vector field. Let \vec{g} be a vector field, and then the curl of that function is given in a symbolic way by the determinant-like algorithm:

$$\vec{\nabla} \times \vec{g} \equiv \begin{vmatrix} dx & dy & dz \\ \frac{\partial}{\partial x} & \frac{\partial}{\partial y} & \frac{\partial}{\partial z} \\ g_x & g_y & g_z \end{vmatrix}.$$